Investigation of the Hall Thruster Breathing Mode

by

Ethan T. Dale

A dissertation submitted in partial fulfillment
of the requirements for the degree of
Doctor of Philosophy
(Aerospace Engineering)
in The University of Michigan
2020

Doctoral Committee:

Professor Alec Gallimore, Co-Chair
Assistant Professor Benjamin Jorns, Co-Chair
Professor John Foster
Dr. Wensheng Huang, NASA Glenn Research Center
Dr. Ioannis Mikellides, Jet Propulsion Laboratory

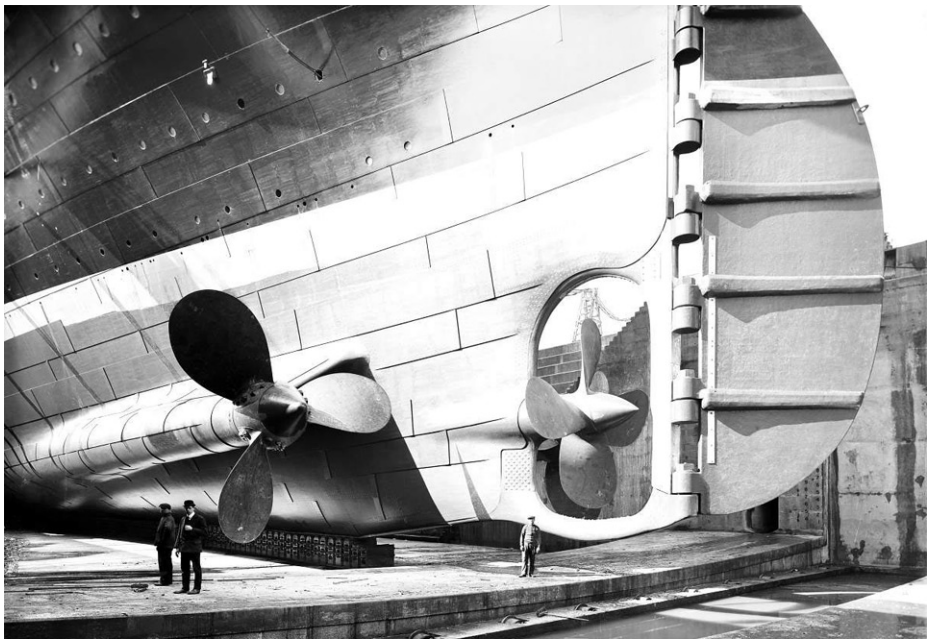

No amount of skillful invention can replace the essential element of imagination.

Edward Hopper

Ethan T. Dale

etdale@umich.edu

ORCID: 0000-0001-7720-1159

To my parents: for encouraging me in my education and supporting me in my aspirations.

ACKNOWLEDGMENTS

There are many people I must thank who have helped me throughout my graduate career and ultimately contributed to this document. First, all of those who have served as an advisor to me (a surprisingly long list): Ben Longmier, JP Sheehan, Prof. Ben Jorns, and Prof. Alec Gallimore. The guidance and advice of all of you has kept my dissertation work on track and shaped my research skills. And to those serving on my committee, Prof. John Foster, Dr. Ioannis Mikellides, and Dr. Wensheng Huang: I have learned much from you all, either through mentorship, classes, or collaboration, and I am grateful for the experience and insight you have shared with me.

To all of my labmates, I am greatly indebted. For those who have already graduated but shared time with me at PEPL, Mike S., Roland, Kim, Chris D., Frans, Scott, Tim C., and Sarah: working with and learning from you has been enriching and invaluable. In particular I thank Mike S. for providing an example of what a grad student *should* be, and Roland for providing an example of what a grad student sometimes *needs to* be. For the enduring figures of the lab, Dr. Tim Smith and Eric Viges: you provide continuity to an otherwise forgetful stream of grad students, and your invaluable know-how continually amazed me. For those students still at the lab, Marcel, Ben W., Shad, Zach, Matt, Josh, Chris, Leanne, and Thomas: I wish you all the best of luck in your continued research, and it has been a pleasure collaborating with you all. And for those just starting, Collin and Evan: I encourage you to savor the coming years, as I assure you they will go by quickly but will offer an academic experience like no other.

There are many others with whom I have interacted during my education that deserve thanks. Mr. David Silverman, my high school physics teacher, gave me an appreciation for the subject and an enduring desire to master it. As an undergrad, Prof. Mitchell Walker first guided me in my research on electric propulsion at Georgia Tech, turning my idle interest in spacecraft propulsion into an unexpected obsession, for which I am very grateful. Dr. Robbie Lobbia: I have never learned so much about electronics in so short a time as when I worked with you, and I will forever aspire to achieve your attention to detail. And within the Aerospace Engineering department at Michigan, Dave McLean, Tom Griffin, Terry Larrow, Cindy Collins, and Denise Phelps: although our direct interactions were usually when something went gravely awry, I sincerely appreciate all of the support you have given me and the rest of PEPL throughout the years.

Finally, I must profusely thank my family for supporting me no matter how far

from home my academic career took me. I also owe copious thanks to my girlfriend April (and our cat Lemon), who encouraged me when I was in research slumps, endured my weekend visits to the lab "for only an hour," and kept me humble when my results appeared to good to be true. But most importantly, she reminded me that there is a life to be had outside of work.

ETD
Ann Arbor, MI
2019

TABLE OF CONTENTS

LIST OF FIGURES

Figure

LIST OF TABLES

Table

LIST OF APPENDICES

Appendix

NOMENCLATURE

Latin

a	arbitrary polynomial coefficient
b	arbitrary polynomial coefficient
c	arbitrary polynomial coefficient
A	amplitude
A_{ch}	channel area, m^2
A_n	neutral gas plume area, m^2
A_p	probe area, m^2
B	magnetic field strength, T
c	speed of light in vacuum, m/s
C	capacitance, F
c_n	neutral gas sound speed, m/s
c_i	ion sound speed, m/s
e	elementary charge, C
E	electric field strength, V/m
$\mathcal{E}$	collisional electric field, V/m
$\mathbb{E}$	energy, J
f	velocity distribution function, $(m/s)^{-1}$
F_a	anomalous electron drag force, N
f_{iz}	ionization frequency, Hz
f_n	plasma density gradient frequency, Hz
g	gravitational acceleration, m/s^2
h	Planck constant, J-s
I_a	active probe current, A
I_d	discharge current, A
I_e	electron current, A
I_i	ion current, A
I_{sp}	specific impulse, s
I_n	null probe current, A
I_p	probe current, A
I_{sh}	sheath capacitive current, A

J	specific radiation power, W m^{-3}
j_e	electron current density, A m^{-2}
j_d	discharge current density, A m^{-2}
j_i	ion current density, A m^{-2}
k	wavenumber, rad/m
L	plasma length scale, m
$\mathcal{L}$	Lorentzian distribution
L^*	length scale ratio
L_c	line length, m
L_{ch}	effective channel length, m
L_{iz}	ionization region length, m
L_n	neutral density gradient length, m
m	mode number
$\dot{m}$	mass flow rate, kg/s
m_d	dry mass, kg
m_e	electron mass, kg
m_i	ion mass, kg
m_w	wet mass, kg
n	plasma density, m^{-3}
N	an integer
$\mathcal{N}$	complex amplitude
$\dot{n}$	ionization rate, Hz m^{-3}
n_a	near-anode plasma density, m^{-3}
n_e	electron density, m^{-3}
n_i	ion density, m^{-3}
n_n	neutral gas density, m^{-3}
$n_{n,0}$	injected neutral gas density, m^{-3}
$n_{n,a}$	near-anode neutral gas density, m^{-3}
p	null probability, %
P	facility pressure, Torr
$\mathcal{P}$	power, W
$\mathbb{P}$	branching ratio
p_e	electron pressure, J m^{-4}
q	charge, C
r	correlation coefficient
R_c	cathode coupling resistance
r_L	Larmor radius, m
t	time, s
T	thrust, N
T_e	electron temperature, eV
T_n	neutral gas temperature, eV
u	fluid velocity, m/s
$\hat{u}$	most probably velocity, m/s
u_B	Bohm velocity, m/s
u_d	drift velocity, m/s

u_e	electron velocity, m/s
$u_{e,a}$	near-anode electron velocity, m/s
u_{ex}	exhaust velocity, m/s
$u_{E\times B}$	E×B drift velocity, m/s
u_f	ionization front velocity, m/s
u_i	ion velocity, m/s
u_n	neutral gas velocity, m/s
u_{th}	electron thermal speed, m/s
V_a	accelerating potential, V
V^*	relative bias-to-plasma voltage, V
V_b	bias voltage, V
V_{c2g}	cathode-to-ground voltage, V
V_{cc}	cathode coupling voltage, V
V_d	discharge voltage, V
V_p	plasma potential, V
w_{acc}	acceleration region width, m
w_{ch}	channel width, m
w_{iz}	ionization region width, m
z	axial position, m
z_{acc}	acceleration region location, m
z_b	boundary location, m
z_{iz}	ionization region location, m

Greek

α	arbitrary scaling factor
β	arbitrary scaling factor
ϵ	electrical permittivity, F/m
ϵ_w	wall energy loss, J
ζ	damping ratio
η_e	electron resistivity, Ω m^{-2}
η_i	ion resistivity, Ω m^{-2}
γ	angular growth rate, rad/s
γ_{SEE}	secondary electron emission yield
θ	fluctuation phase, rad
κ	excitation rate coefficient, Hz m^{-3}
λ	wavelength, m^{-1}
Λ	effective electron energy relaxation frequency, Hz
λ_D	Debye length, m
μ	nominal distribution mean
μ_e	electron mobility, m^2/V-s
N	number of samples/points
ν	radiation frequency, Hz
ν_a	electron anomalous collision frequency, Hz

ν_{class}	electron classical collision frequency, Hz
ν_e	total electron collision frequency, Hz
ν_w	wall collision frequency, Hz
ξ_{iz}	ionization rate coefficient, Hz/m^{-3}
ρ	density ratio
σ	standard deviation
τ	settling time, s
ϕ_w	wall sheath potential, V
ψ	cathode flow fraction
χ	excitation cost factor
ω	angular frequency, rad/s
Ω	Hall parameter
ω_{ce}	electron cyclotron frequency, rad/s

ABSTRACT

Hall thrusters can support a wide range of instabilities, many of which remain poorly understood yet are known to play a critical role in the fundamental operation of these devices. In this work, the dominant low-frequency oscillation known as the "breathing mode" is investigated. The goal of this study is to use experimental data to inform a simple model of the breathing mode that could yield an intuitive physical and analytical description of the criteria for the onset and growth of the instability. These criteria could serve as invaluable tools in improving the reliability of Hall thrusters. Foremost, an intuitive physical description of the breathing mode can provide insight into the ramifications of operating with the breathing mode. Such a model can reveal where this instability derives energy and thus which part of the thruster's efficiency is suffering as a result of these oscillations. Additionally, growth criteria can potentially provide insight into the operating conditions and thruster design choices that can minimize these oscillations. That is, if a model can definitively relate the growth rate of the breathing mode to high-level operating parameters, thruster designs can be targeted toward quieter operating conditions. Collectively, this knowledge can be used to intelligently optimize new Hall thrusters.

The first objective in this work is to implement or develop experimental techniques for validating existing theories for the breathing mode. Various high-speed diagnostics are evaluated to find a reliable, non-perturbative solution for characterizing the near-field Hall thruster discharge during breathing oscillations. In doing this, optical emission spectroscopy, high-speed Langmuir probing, and time-resolved laser-induced fluorescence are studied. The first diagnostic is found to be easy to implement but too

complicated to interpret to yield reliable plasma measurements. The second diagnostic is simpler to execute and fundamentally has substantial heritage. However, it too became unreliable in the discharge regions of interest due to interactions between the probe and near-field plasma. The third method, time-resolved laser-induced fluorescence, is historically used to determine ion velocities, but in this work it is applied to characterize ion density, ionization rate, and electric field strength along the thruster axis over the course of a breathing cycle. The results are found to be realistic and constructive, which leads to the conclusion that this approach is most successful in characterizing the breathing mode.

In ensuing experiments, existing theories of the breathing mode are compared to the collected time-averaged and time-resolved laser data. In examining the scaling of the predicted breathing frequency, positive correlation between the experimental values and those predicted by theory is found, albeit with poor sensitivity. However, a comparison of the dynamic properties of the discharge to those assumed/predicted by theory reveal numerous discrepancies. Ultimately two leading theories for the breathing mode, the classical predator-prey model and a resistive instability, are determined to be incompatible with the measured oscillatory behavior. On the other hand, the data suggests a third possibility: a plasma-driven neutral gas instability. This is substantiated by the observation of neutral drift waves in the thruster channel.

The classical zero-dimensional predator-prey model is expanded by the inclusion of more fluctuation terms to increase its fidelity in an attempt to reconcile discrepancies with experiment. In particular, zero-dimensional models of the breathing mode are considered. Different permutations of the ion and neutral continuity, ion momentum conservation, and electron energy conservation equations are subjected to a linear perturbation analysis. Some systems are shown to be analytically unconditionally damped, while others require numerical evaluation. Of the models considered, none predict linear instability at self-consistent operating conditions. Two alternative

models are proposed that either assume the existence of fluctuations in the ionization region length out of phase with fluctuations in ion density, or assume modulation of the upstream neutral gas flow. Both models are shown to be unstable – an improvement over the traditional predator-prey model of the breathing mode.

Using this theoretical and experimental data, a modified theory of the breathing mode is derived in which coupled ionization instabilities lead to modulation of the neutral gas flow upstream of the traditional ionization region in the thruster. This physical description agrees qualitatively with experimental data. The model retains much of the same properties as the predator-prey model, which is widely accepted to be qualitatively correct. Numerical studies of this model are performed and the existence of unstable roots with reasonable real frequencies is verified. A simplified version of this model is derived to produce straightforward analytical expressions for the real frequency and growth rate of the breathing mode. The high-level trends implied by this simplified model are examined and found to be consistent with empirical scaling relationships.

CHAPTER I

Introduction

1.1 Problem Statement

Hall thrusters are increasingly being slated for deep space missions that require high reliability and high power. However, several aspects of the physical processes governing Hall thruster operation are still poorly understood and so empirical testing remains a vital tool in designing new thrusters and validating those intended for flight. But these tests do not provide a first-principles understanding of the operation of a thruster, which means they present an incomplete picture of its performance and reliability. Further, these tests can become logistically impractical especially as the need for greater duration and power throughput strains the capabilities of modern vacuum facilities.

Improving the design and test cycle for Hall thruster technology requires new tools that provide greater understanding of the fundamental physical processes governing these devices. Reduced-fidelity analytical models of Hall thrusters fill this role by providing exact reduced-order descriptions of these processes for use in guiding the design process. Alternatively, high-fidelity numerical simulation can provide more thorough and complicated predictions of the performance of a Hall thruster, which is indispensable in the testing phase of new designs. These two tools can also be used together, the high-fidelity models furnishing detailed plasma information that

the low-fidelity models can use for large-scale predictions.

For this collaboration between experimental, theoretical, and computational efforts to succeed, and thereby aid the proliferation of Hall thruster technology, models and simulations should be self-consistent. That is, even though a code may need to be tuned to replicate experimentally measured quantities, it should rely on first-principles descriptions of the physical processes occurring in the device rather than empirical quantities that are dependent on the thruster operating condition or configuration. If a code is not self-consistent, its predictive capabilities are severely limited. To make a code self-consistent, it must be able to accurately capture *ab initio* the important physical processes governing the operation of the thruster. Therefore, it is critical to understand the operation of a Hall thruster to enable the design and validation of new devices.

One area where the understanding of Hall thruster operation falls short is with regard to the low-frequency "breathing mode," a ubiquitous coherent oscillation of the thruster discharge current. Although this instability has been studied experimentally, numerically, and theoretically over several decades, there is still no universally-accepted description of the criteria for its onset and growth. Further, proposed theories for this instability either do not predict growth or do not provide an analytically tractable description of it (a full numerical solution must be found). Deriving the onset criteria for the breathing mode would demonstrate an accurate understanding of the nature of this instability, which would allow greater confidence in the reliability and performance of these devices.

1.2 Objectives

Our primary goal of for this work was to produce a set of analytical criteria for the growth of the breathing mode. As part of this, we had to develop a model to describe the instability, and then we conducted a stability analysis to describe the

conditions for the onset and growth of the breathing mode. To formulate this new model, we conducted experiments to characterize various plasma parameters in a thruster exhibiting the instability. However, definitive measurements of this type are not available in the literature, and so we had to find/develop an adequate diagnostic for making them. This involved implementing and applying various time-resolved near-field diagnostic techniques until a suitable one could be identified.

Contributions of this work include:

1. **Survey of existing zero-dimensional breathing models to determine stability.** Several zero-dimensional models of the breathing mode composed of ion, electron, and neutral fluid equations were investigated to determine their stability. A linear perturbation analysis complemented by numerical studies were used to explore the behavior of these reduced-fidelity models.

2. **Evaluation of high-speed diagnostics for characterizing the near-field Hall thruster plasma.** A xenon optical emission spectroscopy scheme was adopted from the literature and implemented using a high-speed camera and passive optical components. The technique was applied with a Hall thruster plume to determine time-averaged temperature measurements. It was also used to estimate the time-resolved electron temperature in the thruster channel. The effectiveness of this technique was assessed based on these preliminary results. Additionally, high-speed Langmuir probe measurements were made in the near-field discharge of a Hall thruster to evaluate the applicability of this technique to characterizing the breathing mode. In doing this, new methods for analyzing data from dual Langmuir probe configurations were developed. Further, limitations of this technique relating to sheath effects and near-field perturbation were identified. A time-resolved laser-induced fluorescence setup was also implemented and used to measure fluctuating ion properties in a Hall thruster exhibiting the breathing mode. Although similar approaches can be found in

the literature, the extent of the measurements and particular configuration in this study were unique.

3. **Development of the ion Boltzmann implicit solution method (IBIS) for diagnosing the near-field Hall thruster plasma with time-resolved laser-induced fluorescence.** An existing kinetic analysis technique was adapted for determining time-resolved electric field strength, ionization rate, and ion density using phase-averaged laser-induced fluorescence measurements and minimally-perturbative *in situ* probe measurements. The technique was applied to a Hall thruster and shown to successfully recover dynamic plasma behavior on the time scale of the dominant low-frequency oscillations.

4. **Demonstration of the inability of existing theories to predict experimentally observed breathing mode behavior.** The IBIS technique was used to infer the evolution of several plasma and neutral properties in a Hall thruster throughout a breathing cycle. The phases of fluctuations in these quantities were examined in context of the assumptions of existing models of the breathing mode. The applicability of these models was then evaluated where significant discrepancies between the model assumptions and experimental data were found.

5. **Development of an alternative breathing model.** Informed by the experimental and theoretical evidence gathered, a new model for the breathing mode based on the predator-prey description is formulated. The stability of this model is examined and used to gain physical insight into the driving mechanism for the breathing mode.

6. **Development of analytical instability expressions.** A simplified form of this new breathing mode theory is presented. An analytical description of the real frequency and growth rate of breathing oscillations is found using this sim-

plified model. The frequency scaling of the model is assessed using experimental data, and the predictive aspects of the model are explored.

1.3 Organization

In describing the work performed to meet these objectives, we start in Chapter II by contextualizing the problem, first by reviewing electric propulsion and Hall thrusters, then describing the wide range of instabilities supported in these devices, and finally detailing the breathing mode in particular. We discuss previous experimental, numerical, and theoretical studies of this instability, devoting attention in particular to a review of several mechanisms proposed in the literature. In Chapter III, we motivate the problem, explaining the gaps in the current understanding of the breathing mode and the importance of describing its growth and onset fully. After presenting our experimental methods in Chapter IV, we then experimentally evaluate existing theories of the breathing mode in Chapter V. First, we find a high-speed diagnostic capable of making the measurements needed for this evaluation; as part of this, we develop a minimally-invasive technique (IBIS) to diagnose the near-field and internal Hall thruster plasma. Then, we perform a correlational study between the predicted breathing frequency and measured values. We also measure the dynamic properties of a thruster exhibiting the breathing mode and compare the results to the fundamental assumptions of each theory. In Chapter VI, we use this experimental validation work to guide the modification of the predator-prey model of the breathing mode so as make it more consistent with experimental data. In doing this, we explore the stability of multiple models both analytically and numerically, and identify a few physical mechanisms that can drive the system unstable. Based on these findings, in Chapter VII we synthesize a new model based on a novel physical description of the breathing process. We examine the stability of this model and attempt to derive simple descriptions of the breathing frequency from it. Due to the complexity of the

model, we formulate a simpler version and find it to suitably describe the breathing behavior we experimentally observed. We then conclude with a summary of our accomplishments, the impact of this work, and possible avenues of continued research into the breathing mode.

CHAPTER II

Background

2.1 Introduction

In this section, we begin by introducing electric propulsion, including pertinent definitions and example technologies. We then focus the discussion to Hall thrusters, where we dwell on the fundamental physical processes governing their operation. We additionally consider the technological evolution of these devices, including their current role as an in-space propulsion solution and possible directions the technology is heading. In §2.4, we consider the stability of these devices, focusing mostly on the wide range of plasma oscillations that have been observed and characterized. We then hone in on the breathing mode in particular, discussing its experimentally recorded properties and an overview of the numerical and analytical attempts to describe it.

2.2 Electric Propulsion

2.2.1 Definition

Before defining electric propulsion (EP), first we will discuss a few fundamental aspects of in-space propulsion. Propulsion systems on Earth often rely on a medium or interface to impart momentum to a vehicle or other object. For example, an airplane pushes itself through the air and an automobile pushes against a road to move.

In space, however, the medium is often incredibly sparse and no interfaces are available, so momentum can only be imparted to a spacecraft by expelling a propellant. This is required by Newton's third law (which is also met by propulsion systems on Earth): momentum must be conserved. Further, since much of space is populated by extremely low-density gas and plasma, propellants generally are stored onboard the spacecraft. This means that the spacecraft only gains momentum by accelerating a propellant from rest. This can either be done by storing energy in the propellant in advance or putting energy into the propellant in flight. A propulsion system using the former approach will be energy-limited – a finite amount of energy is available for conversion to spacecraft momentum – while the latter approach will be power-limited – energy can be provided on the spot, but the rate that it is applied limits the rate of momentum imparted to the spacecraft. The simplest form of an energy-limited propulsion system is a cold gas thruster, where work is done to pressurize a gas before loading it onto the spacecraft. To accelerate the spacecraft once it is in space, the gas can be allowed to escape, converting potential energy in the form of pressure to kinetic energy. As an example of the latter, we begin our discussion of electric propulsion.

In general, electric propulsion is a class of devices that use electrical energy in flight to impart momentum to a spacecraft. They are typically classified as electrothermal, electrostatic, or electromagnetic. These categories simply describe how the electrical energy of the device is applied. For electrothermal thrusters, electrical energy is converted to heat, and this heat is converted to kinetic energy imparted to a propellant. For electrostatic thrusters, electricity is used to maintain a static electric field that resistively accelerates a propellant. For electromagnetic thrusters, electricity is used to generate electric and magnetic fields that accelerate a plasma via the Lorentz force; alternatively, electricity is used to generate EM waves that couple to the propellant for eventual conversion to kinetic energy.

2.2.2 Application

We now consider why and how electric propulsion is applied instead of traditional chemical solutions. All propulsion systems must abide by the rocket equation, derived by Konstantin Tsiolkovsky in 1897 and published soon after [1]:

$$\ln\left(\frac{m_w}{m_d}\right) = \frac{\Delta u}{u_{ex}} \ . \tag{2.1}$$

Here, m_w is the wet mass of the vehicle, m_d is the dry mass, Δu is the change in velocity ("delta-v"), and u_{ex} is the propellant exhaust velocity. The specific impulse $I_{sp} \equiv u_{ex}/g$ is sometimes used in place of u_{ex}, where it literally represents the amount of time it would take to reach the exhaust velocity with 1 g of acceleration. The exhaust velocity is often considered a measure of "fuel efficiency" in that it dictates how much Δu a propulsion system produces for a given mass of propellant. The change in velocity is more relevant here than, say, the acceleration on the spacecraft because a thruster applies a discrete force T to the spacecraft, and thus acceleration is dependent on the mass $m_w(t)$ which is varying over time t as propellant is expelled. It can be trivially shown that $d\Delta u/dt \propto \dot{m}\ {m_w}^{-1}$, where $\dot{m}$ is the propellant flow rate.

Equation (2.1) demonstrates several interesting and intuitive trends. First, as the amount of propellant onboard $m_w - m_d$ increases for a given u_{ex}, the Δu increases. Physically, if there is more propellant available and the propulsion system has a certain Δu per mass of propellant, the total Δu will increase. Second, regardless of mass fraction, a higher exhaust velocity will allow a greater change in spacecraft velocity. Together, these observations seem to imply that a thruster with a high u_{ex} will always give you more "bang for your buck." However as we mentioned before the acceleration achieved is proportional to the mass flow rate, thus the period of time over which the Δu occurs is inversely related to the mass flow rate.

Herein lies the performance balance that can sometimes be favorable for electric

propulsion. The relationship between $\dot{m}$ and u_{ex} can be simply defined in terms of the power input to the propellant: $\mathcal{P}_{in} = \dot{m}{u_{ex}}^2/2$. To achieve the largest Δu possible in the shortest time, both $\dot{m}$ and u_{ex} must be large, so the total power into the propellant must be even larger. For this reason, for a given $\mathcal{P}_{in}$ there tends to be a tradeoff: some propulsion system have high flow rates but low exhaust velocities, while others have the opposite. The former have high acceleration (high thrust) but are "fuel inefficient," while the latter have low acceleration but are efficient. In practice, it is difficult to energize the propellant in flight when $\dot{m}$ is high because of the limited available power, so electric propulsion systems tend to fall into the low thrust category. On the other hand, the power put into the propellant in chemical systems is limited by the reaction rate and material limitations of the combustion system. Since $\mathcal{P}_{in}$ scales as the square of u_{ex}, this tends to mean that chemical systems cannot achieve very high exhaust velocities. As a result, they fall into the high thrust category. Figure 2.1, after Ref. 2, compares the thruster and I_{sp} regimes of a few chemical and electric propulsion systems, reflecting these deduced trends.

In summary, chemical propulsion systems are energy-limited and have high thrust but poor economy (low I_{sp}). Electric propulsion systems are power-limited and have low thrust but excellent economy (high I_{sp}). As a result, for a certain amount of Δu, a chemical thruster will need more propellant but can deliver faster, while an electric thruster will need little propellant but will deliver slower. This typically means that electric thrusters are used when slow maneuvers are acceptable so that payload can be maximized. Alternatively, chemical thrusters are used when few but fast maneuvers are necessary.

2.2.3 Examples

We will now provide a few examples of different electric propulsion systems to demonstrate the variety of technologies and physical processes employed by this class

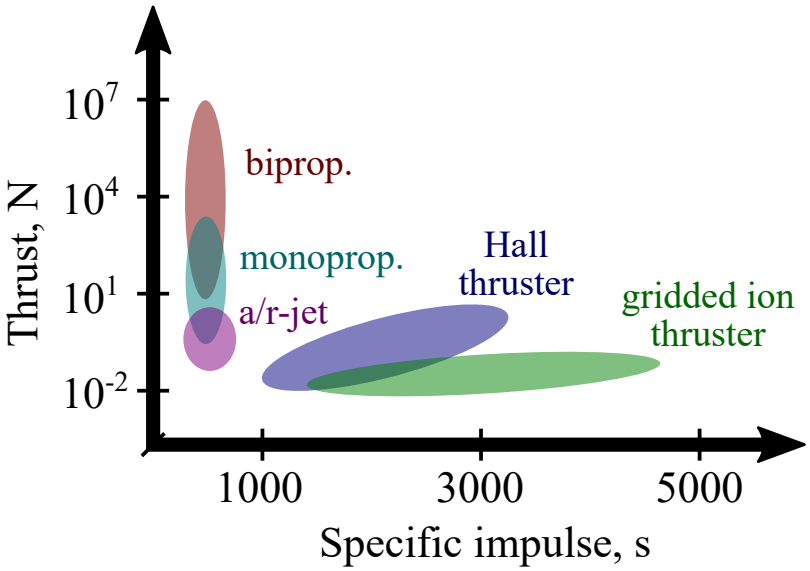

Figure 2.1: A comparison of the thruster versus specific impulse regimes for chemical and electric propulsion systems. The approximate levels of thrust and I_{sp} are for flight chemical and arcjet/resistojet systems, while the electric propulsion values include laboratory devices. These regions are meant to reflect a variety of devices and studies, and thus do nto portray constant-power trends in thrust as a function of I_{sp}.

of devices. Much of this summary is informed by Ref. 3, Robert Jahn's seminal text on electric propulsion. First we consider electrothermal thrusters, a classical example of which is the resistojet. This type of thruster resistively converts electrical energy to heat and applies this heat to a propellant that is exhausted through a nozzle. Just like in a chemical system, the nozzle converts the propellant's random thermal energy to directed kinetic energy. Since the heat is applied to the propellant externally rather than homogenously within it like in a combustion system, the flow rate is limited by the thermal conduction of the heater elements to the propellant, and the conduction within the propellant itself. In general, resistojets are mechanically and electrically simple but have low I_{sp}, only marginally improved from a cold gas thruster compared to other electric propulsion technologies.

An example of an electrostatic thruster is the gridded ion thruster. Here, an electric field is established between two semi-transparent electrodes (grids). Since the

propellant gas is itself weakly affected by electric fields, it must be converted into a plasma inside the thruster. The ions in this plasma are drawn out through the grids and accelerated by them. A separate cathode outside the thruster neutralizes the extracted ion beam. These devices can have incredibly high I_{sp} dictated mostly by the potential across the grids. For example, a 10 kV potential difference nominally produces a singly-charged xenon exhaust velocity of 121 km/s, an I_{sp} of over 12,000 s.

Finally, we provide examples of the electromagnetic class. Jahn further splits this category into steady and unsteady acceleration mechanisms. An example of the former is the magnetoplasmadynamic (MPD) thruster, which relies on the Lorentz force to accelerate a plasma. Typically, an arc is struck between a coaxial anode and cathode; an azimuthal magnetic field is generated by the current flowing into the central cathode; and the plasma conducting current radially from anode to cathode experiences an axial Lorentz force. These devices promise high I_{sp} and thrust but are often mired in cumbersome hardware or plagued with electrode erosion issues. An example of an unsteady electromagnetic device is a pulsed inductive thruster (PIT), in which a pulse of high current through a spiral antenna inductively ionizes nearby propellant and drives an azimuthal plasma current. The radial magnetic field induced by the antenna then leads to a Lorentz force applied to the plasma, accelerating it away from the antenna. Like MPDs, these devices have high I_{sp} and high thrust, and can be relatively propellant-agnostic due to the absence of electrodes. However, practical challenges in implementing high-power, pulsed electronics to allow continuous operation of these devices have limited their experimental exploration.

2.3 Hall Thrusters

We now describe in detail a specific electrostatic electric propulsion technology, the Hall thruster. These devices are sometimes referred to as Hall effect thrusters,

closed-drift thrusters, or Hall current thrusters; for brevity in this document we will refer to them as Hall thrusters or HETs. We begin by reviewing the basic design of these devices, including the major components and terminology. Next we discuss the underlying physical processes controlling their operation within the context of their physical design. We then outline a technical history of these devices, including trends in size, power, and design.

2.3.1 Physical Design

Hall thrusters are annular plasma propulsion devices that utilize crossed static electric and magnetic fields to generate and accelerate a plasma for the purpose of producing thrust. They consist of four main parts: (i) a circular electrode (anode) at the back of a (ii) ceramic channel, encased by (iii) a ferromagnetic circuit; (iv) an electron source (cathode) sits near the channel. Often the anode is hollow and serves as the propellant gas distributor. The magnetic circuit is composed of electromagnets to generate a magnetic field and magnetic iron to shape this field in the vicinity of the channel. Figure 2.2 shows a simple diagram of this configuration.

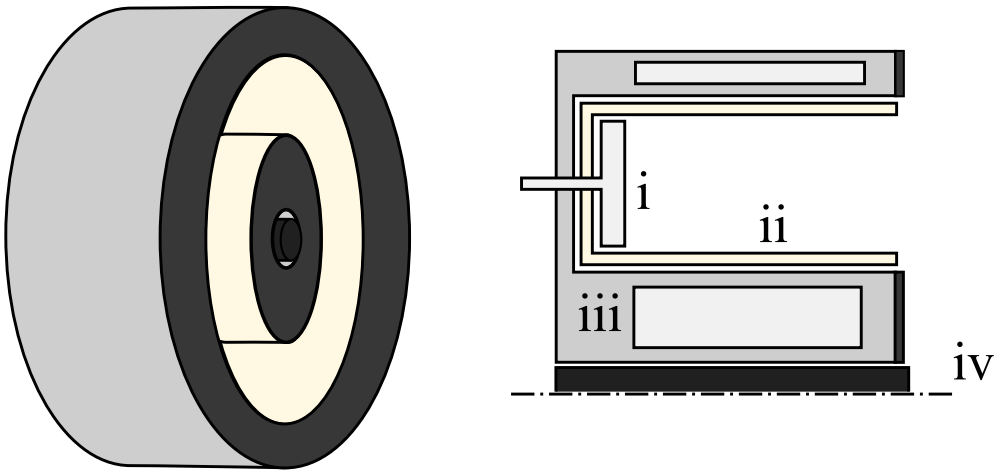

Figure 2.2: A notional diagram of a Hall thruster.

The magnetic field is mostly radial across the ceramic channel, peaking in strength

near the exit plane (front face) of the thruster. The magnetic field topography is usually not purely radial but can be lensed [4] in which the field lines bow concave, or shielded [5] in which the field lines dive deep into the channel. The motivation for both designs will be discussed further in the next section, although a diagram is included for reference now in Fig. 2.3.

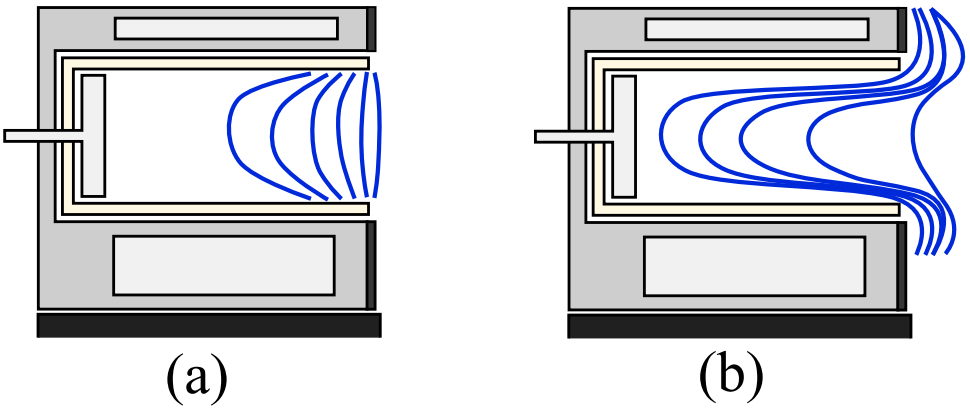

Figure 2.3: Examples of the plasma lens topography (a) and magnetic shielding (b).

2.3.2 Governing Physics

Just like in a gridded ion thruster, thrust is generated in a HET by electrostatic acceleration. In this case, though, the electric field is established self-consistently in the discharge; that is, the acceleration zone is not bounded by electrodes. Instead, a potential is applied between the anode and the cathode. Electrons emitted by the cathode are drawn toward the anode but they are impeded by the radial magnetic field applied in the channel. In this region, the axial electric field and radial magnetic field leads to a E×B drift of the electrons; the annular channel geometry allows this resulting "Hall current" to flow without terminating on a wall. Neutral gas – typically inert, heavy, and with low ionization energy, like xenon – streams from the anode and passes through this hot region of high electron resistance, ionizing vigorously. The resultant ions are accelerated out of the channel by the axial electric field. The

cathode, aside from sourcing electrons for the channel, also provides electrons to neutralize the ion beam. Figure 2.4 illustrates an overview of this process.

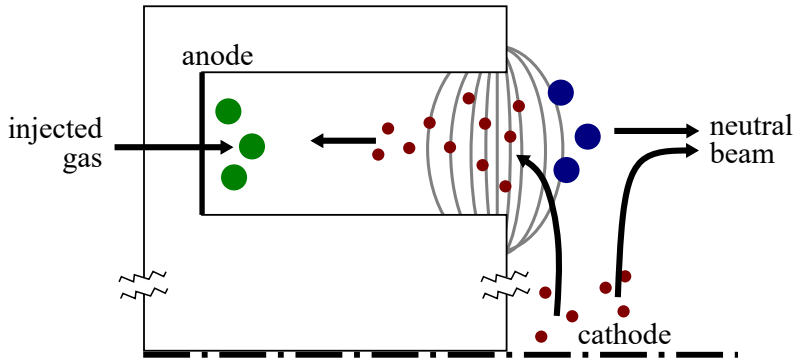

Figure 2.4: An illustration of the physical processes governing a Hall thruster. Neutral particles are shown in green, electrons in red, and ions in blue. Arrows indicate the flow of current unless otherwise labeled.

An important point to cover is how exactly momentum is transferred between the ions and the thruster. The ions are accelerated by an electric field, so in effect they are "pushing" off this field to accelerate. The apparent contradiction here is that a massless field exchanges momentum with the ions. However, the electric field is established by the electron resistance localized on the peak radial magnetic field. In this sense, the magnetic field anchors the electric field to the thruster magnetic circuit, and thus the ions are pushing against the magnetic field.

An alternative explanation is that the Hall current due to electrons leads to a Lorentz force with the radial magnetic field, and thus the ions are experiencing an opposite force to keep the electrons (axially) stationary. The direction of the force on electrons for an axial electric field strength E_z, radial magnetic field strength B_r, and fundamental charge e is given by $-e(\vec{E_z} \times \vec{B_r})/{B_r}^2 \times \vec{B_r} = e\vec{E_z}$, and thus the ions are accelerated with the electric field. Again, here the magnetic field is the intermediary in transferring momentum to the thruster, but now a Lorentz force is applied between the Hall-circulating plasma and the thruster's electromagnetic coils.

Regardless of the physical explanation, the resulting discharge tends to be divided

into the near-anode, ionization, acceleration, and plume regions. Neutral gas drifts through the near-anode zone until it reaches the ionization region, where most ions are produced. The resulting ions drift into the acceleration region where the strong electric field accelerates them rapidly. They then depart form the thruster into the plume. These zones are shown, along with notional ionization rate $\dot{n}$ and axial electric field strength E_z curves, in Fig. 2.5. The ionization and acceleration regions are thought to overlap somewhat to explain the non-monoenergetic ion beams measured in the plume.

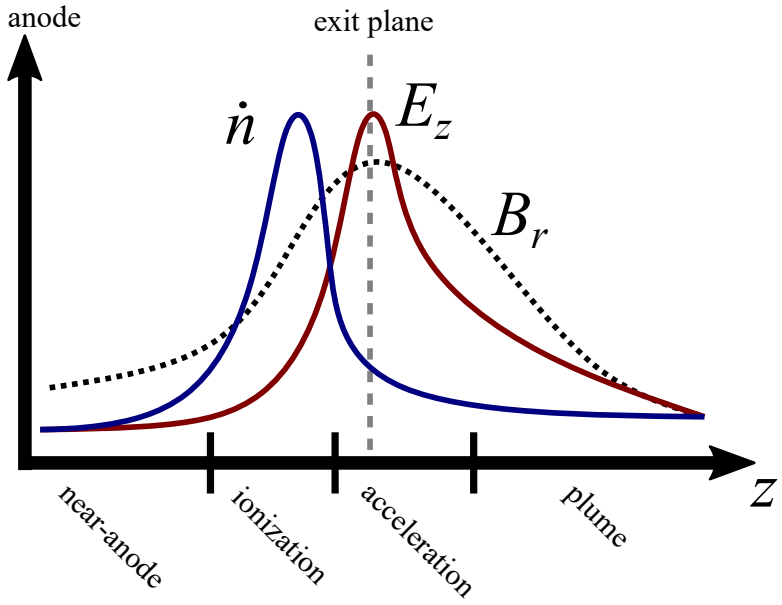

Figure 2.5: The regions of the Hall thruster discharge, defined by the axial electric field strength E_z and the ionization rate $\dot{n}$. Also shown in the radial magnetic field strength B_r for reference.

Also shown in Fig. 2.4 is a diagram of currents in the thruster. For perfect ionization, ideally very little electron current escapes the acceleration/ionization zone. Some current *must* flow to allow steady state operation though. This current is not entirely classical, a point that will be touched upon throughout this work, especially in Appendix H. Also note that some electron current from the cathode is diverted to neutralize the beam. The remainder sustains the electron population in the acceler-

ation/ionization zone.

2.3.3 Trends in HET Technology

Hall thrusters were developed extensively in the Soviet Union and flown in both technology demonstration and practical missions in the second half of the 20th century[6]. At this time, these devices were low power ($\lesssim$1 kW), low thrust (<100 mN), and relatively short-lived due to erosion of the channel walls. For this reason, they were mostly relegated to stationkeeping of satellites: performing minute orbit adjustments to maintain a satellite's trajectory. After Hall thrusters were introduced to the West in the early 1990s following the collapse of the Soviet Union, higher power devices were gradually developed. Optimizing the magnetic field shape to "lens" the plasma also increased efficiencies from about 50% for the SPT-100 [7] to nearly 70% for shielded and unshielded variants of the H6 [8]. The first Western-built Hall thruster was flown in 2006 [6].

As the thrusters were scaled to higher power and numerical simulation of them matured, the lifetime of the devices became an increasing focus of research. Specifically, ion sputtering of the ceramic channel walls would eventually lead to failure of the thruster once the thermal and electrical isolation provided by the wall weakened. However, studies showed that the magnetic field topography could be designed to reduce potential gradients near the channel walls by having field lines dip deep into the channel [9]. Very quickly these magnetically-shielded thrusters were found to have orders of magnitude less erosion with minimal changes in performance [8]. This promises to extend the mission space for Hall thrusters to long-duration operations.

2.4 Hall Thruster Stability

We now review several aspects of the stability of Hall thrusters. In particular, we examine the wide range of plasma instabilities supported in HETs. Formally, a

plasma instability is a physical process that drives a plasma into a non-equilibrium state. For example, a two-stream instability involves a non-equilibrium distribution of particle velocities that can give rise to plasma waves. These processes can be characterized with a frequency ω and wavenumber k, the real components of which are the observed frequency/wavenumber of oscillations of the system, and the imaginary components the temporal/spatial growth of the oscillations. Instabilities can also exhibit dispersion given by some eponymous relation $\omega(k)$, where $\partial\omega/\partial k$ is a function of k such that the group velocity of a wave is dependent on its wavelength.

Plasma instabilities in Hall thrusters have been reviewed thoroughly in the literature, c.f. Ref. 10, so here we will present only a brief overview. We present a non-exhaustive summary ordered by frequency regime, starting with low-frequency oscillations (<100 kHz) and progressing to high-frequency oscillations (>1 MHz). Finally, we narrow our discussion even further to the particular low-frequency oscillations known as the "breathing mode." We begin by giving them a thorough phenomenological description. Then we outline the experimental, numerical, and theoretical studies of this instability, highlighting the unique physical mechanisms governing the breathing mode that have been proposed in the literature.

2.4.1 $\omega <$ 100 kHz Regime

Roughly a decade ago, the first studies of Hall thrusters with high-speed cameras began, and soon after the nature of rotating azimuthal features was characterized [11]. In general, isolated regions of enhanced light emission in the discharge – "spokes" – were observed to propagate azimuthally around the channel. This instability was distinguishable at multiple azimuthal wavenumbers ("modes"), in which many distinct spokes were observed propagating together. The rotational frequency is typically $\sim$10 kHz, although some modes could have non-harmonic peak frequencies that would bleed over to other modes. By operating with a segmented anode, McDonald et al.

found that the spokes can carry up to 50% of the discharge current [12]. Parametric studies by Sekerak et al. showed that spokes tended to dominate at high magnetic field strengths, corresponding with low I_d and high thrust-to-power [13]. Similar work on a magnetically-shielded thruster indicated that spokes were suppressed until the magnetic field shape distorted in such a way that promoted plasma impingement on the walls [14].

Early work by Janes and Lowder observed spoke-like features in a Hall thruster [15]. They used *in situ* probe measurements to discriminate azimuthal density fluctuations from background high-frequency turbulence. They suggested this as an electron transport mechanism following the work of Yoshikawa and Rose [16], who found that electron diffusion across magnetic field lines could follow a B^{-1} scaling when there are density fluctuations. In line with this description, several decades later it was loosely proposed that spokes constituted a traveling density fluctuation whose potential perturbation could drive an axial E×B drift, and thus partly contribute to electron transport in the channel [12]. More recent simulation work [17] has suggested that spokes are unrelated to ionization and are in fact a result of the collisionless Simon-Hoh instability [18], in which azimuthal charge separation produces an electric field that can enhance density perturbations.

Cathode spokes are an unrelated gradient-driven instability observed near the cathode of a Hall thruster and proposed to influence anomalous electron resistivity in that region. This instability is composed of an azimuthally-propagating region of high light emission centered on the cathode but extending radially outside the orifice, with rotational frequencies between 10 and 100 kHz. Assuming an axial magnetic field, a radial density gradient, and an electrostatic oscillation frequency between the ion and electron cyclotron frequencies, Jorns and Hofer showed that this mode can be described as anti-drift waves in which oscillations follow the diamagnetic drift of electrons and grow due to the phase delay electrons incur from axial collisional drag

[19]. This instability is limited to the vicinity of the cathode, and in fact the theory of Jorns and Hofer breaks down at large radii. They speculated that there is a transition from the m=1 azimuthal mode to a global (m=0) mode closer to the channel, which explains why these seemingly local cathode oscillations are observable in the discharge current signal.

Work on rotating structures in Hall thrusters tends to focus on anode spokes but occasionally tenuous connections are made between them and the gradient-driven cathode spokes. However, it has been questioned whether the Simon-Hoh instability is compatible with the theory of Jorns and Hofer, which may limit the comparability of these two instabilities [20]. A recent parametric study on a high-power magnetically-shielded thruster involved an examination of cathode spokes and found that trends with magnetic field strength, background pressure, and cathode flow fraction roughly agreed with the anti-drift wave description [21].

2.4.2 100 kHz $< \omega <$ 1 MHz Regime

Transit-time, or "transient-time," oscillations are an axial ion instability that has variously been attributed to resonant ion acoustic waves. Esipchuk et al. experimentally and theoretically explored this instability, describing it as a mostly-axial gradient-driven magnetosonic wave [22]. According to their work, this mode is only unstable for regions of positive radial magnetic field gradient. Experimentally, they found that these oscillations were present in otherwise "quiet" operating conditions, increasing in strength with increased magnetic field. They were characterized as mostly turbulent, although some coherence was observed. They were generally $\sim$100 kHz, close to the estimated transit rate of ions through the channel.

These oscillations have also been reproduced numerically; for example, in the work of Bareilles et al. a 2D hybrid particle-in-cell (PIC) code exhibited an instability related to the ion beam that appeared at similar frequencies. However, here it was

related to reciprocation of the acceleration region such that high- and low-velocity ion populations form that upset the steady-state potential structure [23]. This is described as a "surf-riding" effect: when the acceleration region is moving with ions, the ions "ride" this region and reach higher velocities. Barral et al. performed a linearized short-wave analysis to study this mode and found that it corresponded to resonance of ion acoustic waves [24]. They were able to reproduce the eponymous transit time scaling and related the growth of the oscillations to the ion current fraction and the ionization rate.

2.4.3 $\omega > 1$ MHz Regime

Many studies of Hall thruster stability focus on the frequency content of the discharge current signal I_d. Although much of the spectral power in I_d is focused in low frequencies, often there are distinguishable characteristics above 1 MHz, and further there exist many local modes that are not captured by I_d. Although there are a wide variety of high-frequency modes that could exist in a Hall thruster plasma, here we provide as examples two types: gradient drift instability (GDI) and electron drift instability (EDI).

The former instability was predicted and measured by Esipchuk and Tilinin several decades ago [22] and has been occasionally studied thereafter. This long-wavelength instability derives its energy from the azimuthal electron drift in the presence of axial density and magnetic field gradients. For ballistic ions and ignoring axial electron drift, the dispersion relation found by Esipchuk and Tilinin becomes

$$(\omega - k_x u_i)^2 + \frac{k^2 {u_i}^2}{k_y(u_{E\times B} - u_d)}\omega - \frac{k^2 {u_i}^2}{k_y(u_{E\times B} - u_d)} k_y u_{E\times B} = 0 \ , \tag{2.2}$$

where u_i is the ion axial velocity, k is the wavenumber, ω is the frequency, u_d is a "magnetic drift velocity," and $u_{E\times B}$ is the E×B drift velocity. One of the conditions

for instability given ${u_{E\times B}}^2 \gg {u_i}^2$ is $dB/dz > 0$, which relegates this instability to the channel plasma.

The EDI is a limit of the GDI in which it is not assumed that the electron drift velocity is much smaller than the thermal velocity u_{th} or that the wavelength is large. Typically this corresponds with frequencies 1-10 MHz. Physically, as summarized by Cavalier et al. [25], extant Bernstein waves (slow electrostatic electron cyclotron waves perpendicular to the radial magnetic field) are Doppler-shifted to frequencies close to ion acoustic turbulence due to the large azimuthal drift velocity of electrons. The instability arises as these waves merge, typically yielding resonances in azimuthal wavenumber k_y that correspond to multiples of the cyclotron frequency ω_{ce}. These resonance can smooth out with increasing $u_{th}k_z/\omega_{ce}$, where k_z is the radial wavenumber, in which case they appear as ion acoustic turbulence. Recent theoretical work [26] has suggested that the EDI appears as an electron-ion drag force F_a that may depend on the plasma density n, electron temperature T_e, and ion sound speed c_i. The EDI has recently been investigated as a possible source of anomalous electron transport in HETs. For this reason, formulations for F_a are actively pursued for inclusion in inexpensive fluid simulations that cannot resolve the kinetic EDI self-consistently.

2.5 Hall Thruster Breathing Mode

We now discuss the low-frequency instability that is the focus of the present work, the breathing mode. We begin by reviewing the experimental and numerical investigations that have been conducted on this phenomenon. We then describe a diverse range of hypotheses put forth for the breathing mode. In the next chapter we will return to this summary as motivation for continued study of the breathing mode.

2.5.1 Historical Study

Strong low-frequency oscillations in Hall thruster discharge current were observed in early Russian studies of these devices [27]. These investigations indicated that the fluctuations were exacerbated by slight increases in magnetic field strength, such that the optimal ("quiet") operating condition existed at a relatively low B_r. Further, the oscillations seemed sensitive to the thruster electrical circuit and could be suppressed with a well-designed filter.

The presence of these oscillations was well-known as research on Hall thrusters picked up in the West in the 1990s. A numerical investigation with a 1D hybrid-PIC code by Boeuf and Garrigues first reproduced these oscillations, proving that external circuitry was not necessary to support them [28]. Further, the authors connected the instability to a cyclic depletion and refilling of neutral gas in the channel. The rhythmic ebb and flow of the neutral front was described as "breathing." Fife et al. similarly resolved these oscillations with a hybrid-PIC code and proposed that a predator-prey process was responsible [29]. A simple continuity-based linear perturbation analysis suggested that the transit time of neutrals and ions through the channel controlled the breathing process.

An early parametric study of the breathing mode was conducted on a low-power linear Hall thruster, where it was found that the frequency and amplitude of the oscillations increased with magnetic field strength [30]. High-speed electrostatic probing and optical emission spectroscopy on a traditional coaxial thruster indicated that the low-frequency oscillations were centered on the ionization region [31, 32]. This experimental evidence agreed well with the modeling work of Boeuf et al. and Fife et al., and at this time it was felt that the instability was at least qualitatively well understood.

However, inconsistent numerical reproduction of low-frequency oscillations, stifled insight from the predator-prey model, and the emergence of new hypotheses for the

breathing mode from theoretical studies shook this certainty. Chable and Rogier suggested that low-frequency oscillations could actually be due to a resistive instability, and they found encouraging agreement between their theory and numerical simulations [33]. Further, different interpretations of the deceptively simple predator-prey description led to the investigation of the breathing mode as a higher-order ionization instability by Barral, Ahedo, and Perazdynski [34, 35].

During this time, investigations of anomalous electron transport in Hall thrusters began to peripherally intersect with the study of the breathing mode. In particular, studies of anode spokes in this context led to high-speed video characterization of the breathing mode where it was found that the discharge current oscillation amplitude decreased with increasing discharge voltage and magnetic field strength [36]. This latter finding contrasts with early Russian work. Additional parametric studies focused on the transition between the breathing and spoke modes, in which it was found that, as breathing amplitude decreases with increasing magnetic field strength, the discharge current and thrust-to-power decrease [13].

Aside from these dedicated studies of the breathing mode, the presence of these oscillations has been noted offhandedly in a variety of different types of Hall thrusters and similar plasma devices. Low-frequency oscillations similar to the breathing mode have been observed in the following devices (where italicized entries are unconfirmed):

- cylindrical Hall thrusters [37]
- linear Hall thrusters [30]
- anode layer thrusters [38]
- state-of-the-art low-power Hall thrusters [39]
- high-power Hall thrusters [14]
- wall-less Hall thrusters [40]

- external discharge thrusters [41]
- *sputtering magnetrons* [42]
- *end-Hall thrusters* [43]

The consistency of the observed oscillations across different geometries and power levels seems to indicate that they are fundamental to E×B devices. This could serve as evidence that the breathing mode should be described by a single straightforward process rather than the handiwork of multiple interacting mechanisms, as it is doubtful that multiple processes would exist and interact identically in such different devices. The proposed mechanisms described in §2.5.2 inherently embrace this concept.

Yet with this wide repertoire of experimental evidence, recent developments continue to muddle the modern understanding of the breathing mode. Namely, different models based on incongruent assumptions can all predict oscillations that are qualitatively consistent with the breathing mode. First, hybrid-kinetic and full PIC models have been shown to resolve breathing fluctuations, reinforcing the traditional predator-prey interpretation [44, 45]. Further, Hara et al. adapted the zero-dimensional predator-prey model to include electron energy conservation to examine mode transitions [46, 47]. Meanwhile, Koshkarov et al. returned to a resistive description [48]. Recent 1D full fluid simulations suggested that a wide variety of parameters, including neutral gas properties and near-anode properties, influence the strength and frequency of low-frequency oscillations [49], which entirely exceeds the purview of the universally-accepted predator-prey model. Finally, aside from direct studies of the breathing mode, there has also been mounting evidence that this instability correlates with anomalous electron transport [50] – itself a poorly understood phenomenon – and may play a role in the erosion of pole covers, which is more pronounced in magnetically-shielded Hall thrusters and may be a life-limiting factor for long duration missions [51].

2.5.2 Proposed Mechanisms

Many hypotheses for the breathing mode exist. Historically, low-frequency Hall thruster oscillations were proposed to be a circuit effect related to the filtering electronics used to operate the thruster [52]. However, similar oscillations were resolved by hybrid-PIC codes, which pointed toward an ionization instability. In particular, Fife et al. proposed that a cyclic depletion and refill of neutral gas in the channel could lead to a predator-prey process that would explain the breathing mode [29]. These authors also produced a zero-dimensional model encapsulating this process that predicted realistic breathing frequencies.

Although this predator-prey description was intuitive and seemingly analytically successful, its unclear growth mechanism led to further investigation of the low-frequency oscillations in Hall thrusters. Barral, Ahedo, and Perazdyński performed one-dimensional modeling that indicated the breathing mode is a higher-order ionization instability, with both a standing and traveling component [53, 35]. In this way, they found that the predator-prey explanation is not entirely incorrect, but rather it is driven by spatial effects that could not be captured with Fife et al.'s 0D framework.

Similarly, Chables and Rogier suggested that a resistive instability could drive a predator-prey cycle [33]. Again, this involved a 1D description of the discharge, but here a kinetic instability gives rise to fluctuations that sustains the predator-prey cycle.

2.6 Summary

In this chapter, we started by reviewing some fundamental aspects of propulsion through the rocket equation, and then gave an overview of electric propulsion. From there, we focused specifically on Hall thrusters, introducing their design, governing principles, and trends. Next we discussed the wide range of instabilities observed in

these devices, ranging from low-frequency azimuthal fluctuations to high-frequency gradient-driven processes. We gave special attention to low-frequency oscillations, examining anode spokes, cathode spokes, and transit-time effects. Finally, we narrowed the discussion to the breathing mode. We presented a summary of the experimental and numerical investigations of this instability, spanning the foundational Russian work nearly half a century ago to recent sophisticated simulations that continue to illustrate the complexity of the breathing mode. While briefly reviewing a few breathing mode hypotheses, we highlighted purported energy sources for the instability. A more quantitative discussion of each theory is reserved for the next chapter.

CHAPTER III

Motivation

3.1 Introduction

In this section, we will motivate the present investigation of the Hall thruster breathing mode. First, we outline the challenges in characterizing Hall thrusters exclusively with experimental techniques. In this way, we establish the importance of their theoretical study. We then describe the high-level impact of the breathing mode on thruster behavior to further motivate theoretical study of this particular phenomenon. Finally, the shortcomings in existing breathing mode theories are reviewed, followed by the challenges in improving upon these limitations.

3.2 Engineering Challenges in Hall Thruster Development

Hall thrusters are exclusively an in-space propulsion technology: they cannot operate properly at atmospheric pressure, nor suitably even at rough vacuum. Since thruster performance can vary dramatically with facility pressure, there are guidelines developed within the Hall thruster community for the upper limit of operating pressure before performance measurements are suspect [54]. This requires that Hall thrusters are tested in vacuum vessels with high pumping speed, but even so space-like pressures are still at least three to four orders of magnitude lower than can be

achieved. Further, modern thrusters are designed for exceedingly long lifetimes, near 10,000 hours [55]. Duration tests on the ground, then, potentially require a thruster to be operated in a vacuum facility for years to characterize its performance and stability over time. Although the plasma processes in Hall thrusters presumably reach an equilibrium quite rapidly, there are still subtle material effects that act on long time scales, e.g.: channel erosion [56], pole cover erosion [57], cathode keeper erosion [58], and hardware outgassing. Figure 3.1, following Ref. 10, gives an order of magnitude overview of these time scales.

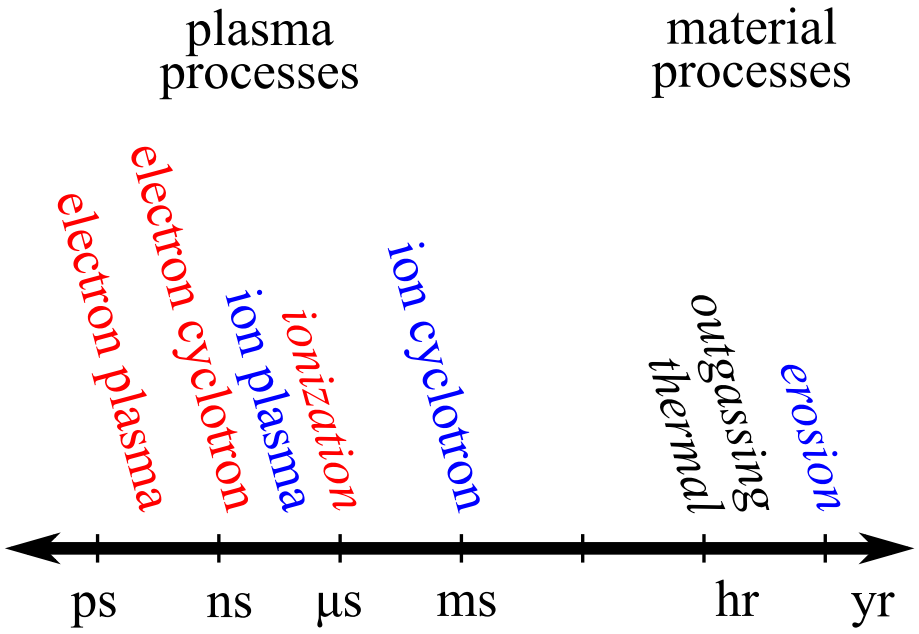

Figure 3.1: Characteristic time scales for Hall thruster processes, including electron (red), ion (blue), and material phenomena. Irreversible and periodic processes are both included, with the former italicized.

As a result, Hall thruster ground testing cannot fully replicate the in-space environment and full life tests are logistically impractical. Therefore, experimental work on Hall thrusters has only a limited capacity for characterizing them throughout an entire mission envelope. The theoretical understanding of these devices, especially their stability and performance, is thus critical for their successful design, development, and application in space missions.

3.3 Influence of the Breathing Mode

The theoretical study of plasma instabilities in Hall thrusters is of particular interest due to the variety of ways in which these phenomena can impact the high-level behavior of the device, as well as the often unintuitive manner in which they form, grow, saturate, and dissipate. The breathing mode is a strong and macroscopic instability that interacts intricately with the thruster, varying with voltage, background pressure, and many other quantities as described in §2.5.1.

Although the breathing mode visibly influences the thruster discharge, it is not trivial to qualify its effect because oscillations cannot be "turned off" without varying other operating parameters. As a result, it is difficult to distinguish the effect of low-frequency oscillations from intentional changes in operating condition. For example, the parametric investigations of Sekerak et al. revealed positive correlation between the discharge current and breathing amplitude, as well as negative correlation between thrust-to-power and breathing amplitude [13]. However, a causal relationship was not established: the magnetic field strength was varied to induce changes in oscillations, and it is conceivable that this could be the primary driver of performance changes, not the oscillations.

Clarifying this relationship is somewhat difficult since the breathing mode is often identified with qualitative or high-level measurements, such as light intensity or discharge current, but there does exist some direct experimental evidence in the literature. We now present a few examples where unambigious, quantitative indications of the breathing mode's influence on thruster operation have been found. Lobbia et al. used a high-speed Langmuir probe in a Hall thruster plume to measure plasma density, electron temperature, and plasma potential during breathing, and found significant fluctuations, on average a root-mean-square (RMS) around 50% of the mean value [59]. Huang et al. examined the possibility of low-frequency oscillations leading to the acceleration region oscillating spatially and found it plausible [60]. Vaudolon

et al. and Mazouffre et al. performed time-resolved laser measurements on a thruster with coerced oscillations and indeed found that the potential structure varied significantly over the course of a cycle [61, 62]. Similar measurements by Fabris et al. showed consistent fluctuations of ion velocities with thruster oscillations [63].

This experimental evidence verifies that the breathing mode can alter several fundamental processes in Hall thrusters. For instance, experiments on displacement of the acceleration region have indicated that the divergence angle of the beam is dependent on the acceleration region location [64], and thus the presence of low-frequency oscillations can drastically change the divergence efficiency of a thruster. Further, variations in plume temperature and density may indicate significant changes in the production of ions and in electron resistivity in the near-field discharge. This is related to the fact that there is no guarantee a steady-state plasma condition is identical to an oscillating condition with the same average properties. That is, a steady thruster with a certain electron temperature $\overline{T}_e$ is not necessarily identical to a breathing thruster with the same average temperature $\langle\tilde{T}_e\rangle$: $\tilde{T}_e \neq \overline{T}_e$. This is simply a statement of the fact that an unsteady system can have the same average properties as a steady system while involving markedly different physical processes. As a result, simply verifying that plasma properties like T_e and n are fluctuating implies that there may be large-scale changes in the physical operation of the thruster.

Finally, there is evidence that instabilities are sensitive to facility conditions, which suggests that thruster performance observed on the ground may vary from that demonstrated in space due to oscillations. Pressure studies by Diamant et al. showed that the breathing frequency varied non-monotonically with background pressure [65]. Walker et al. found that the location of the cathode and the presence of nearby conducting walls also correlated with changes in oscillation amplitude and frequency [66]. This may mean, for example, that a thruster may be more oscillatory in space than on the ground, and thus will experience concomitant changes in

performance as a result of these oscillations.

In summary, the breathing mode is sensitive to many operational and environmental parameters, and the development of this instability corresponds to fundamental changes in the operation of the thruster. As a result, even if a thruster is designed to perform "quietly" in ground tests, the environmental differences of in-space operation may strengthen the breathing mode and, both simultaneously and consequently, lead to unanticipated changes in performance. By highlighting how intimately the breathing mode is tied to Hall thruster operation, we therefore motivate a better understanding of this phenomenon.

3.4 Existing Models and Their Limitations

Given that the breathing mode can have such a large effect on thruster operation and a theoretical understanding of it is critical for successful deployment of this technology, we now examine known limitations of these existing models or otherwise the obstacles faced in validating them. In essence, we explore the reasons why each extant model is not universally embraced within the Hall thruster community as an accurate description of the breathing mode. We review in depth the theories for the breathing mode outlined in §2.5.2. The details of how each type of instability is derived will not be included in favor of highlighting the testable features of the hypotheses. We then discuss their shortcomings, limited to those already found in the literature; we will expand on some of them in an original discussion in Chapter V. We define "shortcomings" based on what we desired in a successful theory: strong physical sense; clearly-defined energy source; tractable, predictive analytical expression for frequency; and experimentally-evaluable predictions.

3.4.1 Circuit Effect

Early work on low-frequency oscillations in Hall thrusters distinguished between an ionization-related mode and a "contour" mode due to the thruster electrical circuit, both exhibiting frequencies ∼10 to ∼100 kHz [52]. Laboratory Hall thrusters are often operated with electrical filters to help off-the-shelf power supplies cope with transients in discharge current, and these filters can couple reactively to the thruster. Presumably, the oscillation behavior can vary for an unchanging filter in response to changes in the plasma impedance. Physically, the energy source for the oscillation would be from the discharge power supply itself: extra electrical energy is stored in the circuit and delivered to the plasma so as to drive low-frequency oscillations. Little analytical work has been devoted to understanding this coupling, and thus no quantitive criteria to validate it are available, but it is physically plausible due to the coherent and tank-like nature of the discharge current oscillations. Studies have shown that filter design can influence current and voltage fluctuation amplitude [67, 68]. However, the prevalence of low-frequency oscillations in numerical simulations – in which typically the power supply is treated as an ideal voltage source – suggests that circuit effects alone are not responsible for the breathing mode. A recent study by Brieda et al. included the electrical harness in a hybrid-PIC model and showed that the oscillations vary as the harness length changes, but the oscillations remained qualitatively unchanged even for a zero-length harness [69].

The circuit effect explanation of the breathing mode has a few shortcomings that first became clear with the work of Boeuf and Garrigues [28]. In that work, low-frequency oscillations were successfully resolved in a one-dimensional hybrid-PIC code that did not account for external thruster circuitry. Since this numerical investigation – as well as many similar ones that have followed it – was otherwise realistic and in good agreement with experiment, this work suggests that a circuit effect is not the primary driver of the breathing mode. Second, the fact that breathing frequen-

cies correlate with plasma and neutral properties, where the latter population plays a minimal electrical role, again makes it seem unlikely that a circuit interaction is dominant. Finally, the oscillation frequency can be arbitrarily coerced by applying an alternating voltage on a thruster electrode [70], which again implies that a fundamental circuit resonance is not dictating the breathing frequency. Specifically, the resonant frequencies of the thruster electronics are fixed, so arbitrary manipulation of the breathing frequency is inconsistent with a circuit effect. However, all of this evidence is circumstantial and cannot rule out that there is at least some circuit effect at play in the breathing process, although the success of other modeling work that ignores external circuitry suggests it is secondary.

3.4.2 Predator-Prey

One of the first self-consistent explanations of the breathing mode was provided by Fife et al. as part of a numerical study that resolved low-frequency oscillations [29]. Fife proposed a zero-dimensional description based on the Lotka-Volterra, or "predator-prey," model. Conceptually, the thruster ionization region is reduced to a 0D box of putative length L in which neutral particles are prey and electrons are predators. Physically, this is captured with ion and neutral continuity equations,

$$\frac{dn}{dt} = \xi_{iz} n n_n - n\frac{u_i}{L} \tag{3.1}$$

and

$$\frac{dn_n}{dt} = -\xi_{iz} n n_n + n_n\frac{u_n}{L} \ . \tag{3.2}$$

Here, the plasma and neutral densities are given by n and n_n, and the respective velocities by u_i and u_n. The constant ionization rate coefficient ξ_{iz} is a function of electron temperature. A linear perturbation analysis yields zero growth rate and a real frequency that is the geometric mean of the neutral and ion transit frequency

through the box:

$$\Re(\omega) = \frac{\sqrt{u_i u_n}}{L} \ . \tag{3.3}$$

Barral and Ahedo corrected Eq. (3.3) by nothing that it does not capture all relevant aspects of the physical configuration; specifically, it disregards the constant neutral inflow from the anode and finite outflow of neutrals [34]. Hara et al. similarly reformulated both equations to include neutral inflow with density $n_{n,0}$ and radial ion flow, and produced the following real frequency and growth rate $\gamma \equiv \Im(\omega)$ [46]:

$$\Re(\omega) = \sqrt{n n_n \xi^2 - \gamma^2} \ , \tag{3.4}$$

$$\gamma = -\frac{1}{2} \frac{n_{n,0}}{n_{n,0} - n_n} n\xi \ . \tag{3.5}$$

The real frequency predicted in this way generally agrees with experimental measurements but by construction γ cannot be positive, indicating that there is no linear growth due to the proposed predator-prey action. As a result, oscillations due to this process should not exist in a real thruster, and so at best the predator-prey model must be incomplete. As a result of this lack of growth, this model does not clearly indicate from where the oscillation would draw energy – in fact, it indicates that any initial energy in the form of increased plasma or neutral density (available ionization energy) is either perfectly conserved or advected out of the system.

Adding additional physics (more conservation equations) to the zero-dimensional formulation often complicates the model enough to preclude exact analytical predictions. This was the case for work by Hara et al., in which T_e was allowed to linearly fluctuate. Some roots of a resulting quartic polynomial in ω were shown numerically to grow, but the complexity of the analytical solution was such that the physical understanding of the instability was limited to a balance of electron energy terms highly dependent on the transport of electrons in the ionization-acceleration region [47]. Further, Hara et al. did not show that the growing roots coincided with the

physical steady-state solution implied by the governing zero-dimensional equations. In total, even more intricate study of the predator-prey model is plagued by a major limitation: there is no physically intuitive growth mechanism presented by this model, and the simplest forms like that of Fife et al. explicitly predict no growth.

3.4.3 Resistive Instability

A description of the breathing mode that downplays the role of ionization is as a resistive instability. Fundamentally, this is a Buneman instability [71]: counter-streaming ions and electrons experience a two-stream instability, modified by the presence of a perpendicular magnetic field, that gives rise to fluctuations in the local electric field. These counter-streaming populations in a Hall thruster lead to an increasing electric field, which is followed by enhanced ionization as electron temperatures rise. Eventually the neutral gas is depleted, and as the plasma thins the instability breaks and the electric field is reduced, allowing the cycle to repeat as the neutral gas refills the channel. In this way, the low-frequency oscillations are not an ionization instability in the sense that the process is driven by the Buneman instability, and predator-prey-like ionization fluctuations are merely a response.

As applied to Hall thrusters, this instability was first discussed by Litvak and Fisch [72] for high-frequency azimuthal fluctuations. Chables and Rogier [33] derived the dispersion equation for a low-frequency axial form of this instability and related it to the breathing mode by speculating that it could drive ionization oscillations. A simplified kinetic model for only the Buneman component yields the following complex frequency expression:

$$\frac{\omega}{ku_i} = -\frac{i}{2\tau} + 1 \pm \sqrt{-\frac{1}{4\tau^2} - \frac{i}{\tau}}\ , \tag{3.6}$$

where $\tau \equiv \frac{m_i}{e} k u_i \mu_e$ is like an electron-ion residence time ratio, m_i is ion mass, k is

axial wavenumber, and μ_e is electron mobility. In arriving at this result, Chables and Rogier assumed constant electron energy, a known and spatially constant neutral distribution function, no ionization, and constant electron mobility (including an empirical anomalous component).

Different approaches to deriving and analyzing this instability have been taken since the work of Chables and Rogier. Fernandez et al. used a fluid approach [73]: ion and electron continuity, ion momentum conservation, and a simplified Ohm's law. Assuming quasineutrality, ignoring elastic collisions or kinetic effects, and including ionization, a dispersion relation similar to Eq. (3.6) results [73]. It is important to note that Eq. (3.6) only captures the two-stream aspect of the resistive instability, while the work of Fernandez et al. encompasses the entire process of ionization oscillation. A practical approximation for the high-frequency limit of ω is presented in Ref. 73 as

$$\omega \approx k u_i \mp \sqrt{\frac{1}{2}\nu_e k (u_i - u_e)}(1 \pm i) \ , \tag{3.7}$$

where u_e is electron velocity and $\nu_e \equiv e/m_i\mu_e$ is the electron collision frequency. Koshkarov et al. followed a similar approach but also explored damping of the mode at short wavelengths and the mode's nonlinear development [48].

Both dispersion relations depend on the difference in u_i and u_e, where the latter is dictated in some fashion by the electron cross-field collision frequency. Physically, this suggests that kinetic energy from the drift of ions and electrons fuels the instability. Qualitatively, this seems to be a plausible mechanism for the breathing mode: the electron current increases toward the anode and the ion current increases toward the plume, so there is a region in/near the channel in which there is a significant counter-current between electrons and ions. However, there remains no quantitative theory connecting the resistive driving mechanism to large-scale ionization instability, and moreover no attempts at experimental validation of this instability have been made.

The resistive instability has not been extensively examined as a potential expla-

nation of the Hall thruster breathing mode. One reason for this, which also serves as a limitation of this hypothesis, is that a resistive instability depends on plasma quantities that are difficult to measure or estimate. Most notably, as shown in Eq. (3.6), the electron mobility is involved, which means that oscillations may depend on the poorly-understood anomalous electron transport. Additionally, the work of Chables and Rogier only qualitatively connected a resistive instability to the breathing mode – it was merely postulated in Ref. 33 that the resistive instability could fuel a low-frequency ionization instability. Koshkarov et al. does provide a more comprehensive derivation with regard to low-frequency oscillations, but again the dependence on electron properties makes it hard to evaluate the usefulness of this model [48]. Further, in that work it appeared that most oscillation time scales were close to the lower hybrid frequency, which in general would be much too high to correspond to breathing oscillations. In total, then, this proposed physical mechanism may be promising but there is simply not enough experimental and theoretical development of it to determine if it is realistic.

3.4.4 Higher-Order Ionization Instability

The predator-prey model is a zero-dimensional instance of an ionization instability in which a global instability is confined to a specific region and presumably advects away. However, other ionization fluctuations with higher-order spatial dependence can arise that may correspond to the breathing mode. In particular, Barral et al. have expanded the predator-prey approach to consider a local instability with a spatial dependence [53, 35]. They used one-dimensional fluid equations for electrons, ions, and neutrals to analyze fully time-dependent and quasi-steady fluctuation behavior, and further examined linear and nonlinear behavior analytically.

Physically, Barral et al. proposed that breathing was a result of a two superimposed waves. One is a standing wave solution, in which plasma density fluctuates

in phase with discharge current; the other a traveling wave solution, in which the neutral density lags the discharge current. Barral et al. summarized these as follows:

$$\frac{\partial n}{n} \approx \frac{\partial I_d}{I_d} \tag{3.8}$$

and

$$\partial n_n \approx i\frac{\partial I_d}{\omega}\left[f_{iz}n_n - f_{iz,0}n_{n,0}\mathrm{Exp}\left(-i\omega\frac{x}{u_i}\right)\right] \ . \tag{3.9}$$

This behavior is a result of a competition between avalanche ionization and neutral advection, leading to a "slow progression and fast recession of the ionization front" [35]. An order of magnitude analysis produced a real frequency of

$$\omega_r = \frac{u_i}{L_{iz}}\mathcal{O}\left(\sqrt{\frac{n_n}{n}}\right) \ , \tag{3.10}$$

but no growth rate was readily available due to the complexity of the analysis. Physically, the apparent success of this model suggests that a coupling between these standing and traveling waves is important in driving the breathing mode unstable. In theory, the standing wave is the instantaneous reaction of the discharge to a change in current – in the form of a fluctuation in ionization – while the traveling wave is the propagation of this reaction with the neutral gas. As a result, the energy for the breathing mode may come from electrons (via ionization) but is inertially mediated by the neutral gas.

The main shortcoming of the higher-order ionization instability models of Barral, Ahedo, and Perazdyński is that they cannot be simplified sufficiently to allow for a predictive description of breathing behavior [74]. For example, only an order of magnitude estimate of the real frequency could be determined, and it was found to essentially scale identically to the predator-prey model [34]. This description of the breathing mode is therefore not necessarily incorrect but does not readily yield any

predictive or testable criteria on ω. Further, the authors suggest that the oscillations are largely following a predator-prey cycle, but it is unclear from this work where the higher-order instability gains its energy. And because the simplified result for $\Re(\omega)$ derived in Ref. 34 is nearly identical to that of the 0D predator-prey model, it appears that any key 1D physical processes included in the model are lost in the simplification process.

Also, due to the presence of local and non-local effects in this model, it is likely that any second-order features, such as those that might contribute to the growth of the oscillations, may depend on quantities that are difficult to estimate. Specifically, plasma properties upstream of the ionization region are somewhat unclear, as this region is generally inaccessible to probing and often poorly approximated in simulations. As a result, it would again diminish the predictive capabilities of this model if these ill-defined quantities must be known *a priori* to estimate ω. For example, if this model dictated that ω depends on the near-anode electron mobility – a quantity that is hard to determine, especially from high-level operating parameters – there is little predictive use for the model because a high-fidelity numerical simulation would be required beforehand to estimate that property. Even so, examination of Barral et al.'s model by Sekerak found good qualitative agreement with a predator-prey process but physical discrepancies with plasma measurements [75].

3.5 Obstacles to Investigating the Breathing Mode

Theoretical and numerical studies of a hypothetical breathing mode mechanisms can provide *verification* – ensuring that the physical picture is internally consistent – but only experimental data can be used for *validation* – ensuring that the physical picture is realistic. So many hypotheses for the breathing mode proposing wildly different physical processes exist because this final step of validation is difficult. We now discuss the specific challenges in it, so as to highlight the manifold avenues of

research that could be taken to improve the modern understanding of the breathing mode.

3.5.1 Thruster Optimization

Perhaps the largest challenge in characterizing the Hall thruster breathing mode is a procedural one: because the breathing mode is so sensitive to magnetic field strength, and it typically correlates with low thrust, often the magnetic field topography of a thruster is optimized to minimize the oscillation amplitude. Specifically, the nominal magnetic field strength is often designated as that at which the discharge current is low and low-frequency oscillations are weak, as discussed in Ref. 4. As a result, most experimental data for laboratory Hall thrusters is tabulated at "quiet" conditions, so wide-ranging trends in oscillation frequency and amplitude are unavailable.

As a result, the findings of most oscillation studies are applicable only to a certain thruster in either an off-nominal operating condition or a weakly-oscillating one. In turn, it is difficult to correct for incidental differences (e.g. differing background pressure [65]) between facilities or devices that may impact oscillatory characteristics. Existing hypotheses for the breathing mode that require estimates of many low-level plasma parameters are therefore hard to test universally.

3.5.2 Complexity

Another fundamental issue in studies of the breathing mode is that Hall thrusters are highly complex devices governed by intricate and tightly-coupled physical processes. This means it is often difficult to perform true *ceteris paribus* parametric studies: when one independent parameter is changed, there are multiple dependent properties that also change. However, we presume that a given thruster has unique operating states, such that although one parameter may influence several others, ev-

ery set of parameters is unique. If this is true, the most rigorous way to investigate trends in low-frequency oscillations without *a priori* knowledge of its dependencies is to completely characterize the plasma state. This concept is illustrated in Fig. 3.2 (and defined formally in Ref. 76) where the breathing frequency ω is proposed to depend on mass flow rate $\dot{m}$, radial magnetic field strength B_r, and acceleration region location z_{acc}. In this example, B_r is a confounding variable: it influences both independent (z_{acc}) and dependent (ω) quantities. To avoid spurious associations in any parametric studies in lieu of *a priori* knowledge, all quantities must be measured to understand trends in breathing frequency *a posteriori*.

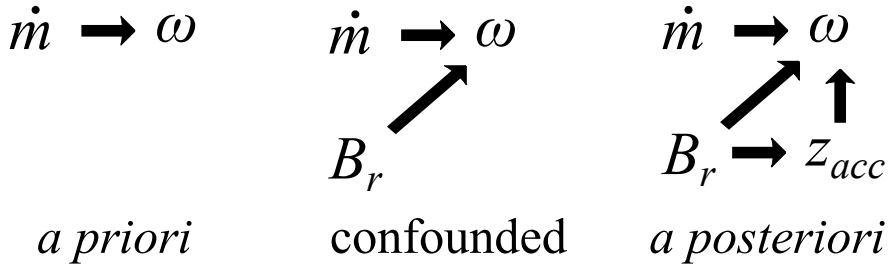

Figure 3.2: Examples of three parametric studies of the mass flow rate $\dot{m}$, radial magnetic field strength B_r, and acceleration region location z_{acc}.

3.5.3 Parameter Definition

Aside from the inherent complexity of Hall thrusters, there are also conceptual deficiencies that stymie the investigation of the breathing mode. Many models of low-frequency oscillations leverage reduced dimensionality for greater predictive capabilities but often this introduces uncertainty in the modeled parameters. For example, the predator-prey model relies on a length scale variously associated with the channel length [29, 28] or a characteristic ionization length [77, 46]. On top of that, the distinct regions of a Hall thruster discharge are known to overlap [78] and can likely vary over time [60]. In applying an existing breathing mode theory like the predator-prey model to experimental data, there is often enough uncertainty in

the definition of the relevant quantities that higher-order numerical simulations are needed for more precise evaluation of the theory. For instance, Hara et al. formulated a zero-dimensional model that showed linear growth over a wide parameter space [46] but examination of the trends predicted by this theory required more extensive one-dimensional hybrid-kinetic simulations [47].

3.5.4 *In Situ* Probing

Finally, even if a relevant operating condition is found (§3.5.1), a parametric study can successfully be designed (§3.5.2), and the relevant modeled parameters are well-defined (§3.5.3), actually performing the necessary measurements may be challenging, as motivated in Ref. 79. To characterize plasma properties in a thruster exhibiting breathing, the channel plasma must be interrogated [31], which in a traditional *in situ* diagnostic approach requires a robust yet small electrostatic probe. Measurements must also be made at high-speed, $\sim$100 kHz, to capture meaningful temporal detail. Finally, unambiguous quantities are desired; for instance, instead of only measuring the discharge current, the constituent ion current and electron current are more insightful. Achieving this specificity can be challenging because, per the discussion of §3.5.2, the full plasma state may need to be defined to adequately capture the dependencies of the oscillatory behavior. We will now consider these three criteria: accessibility, speed, and ambiguity.

3.5.4.1 Accessibility

The simplest way to access the thruster channel is to inject an electrostatic probe into it with a reciprocating high-speed motion stage. These setups have been explored at multiple institutions [79, 80, 81, 82, 21] and generally found to be practical. Considerable effort has been put toward designing and implementing robust probe injection systems [83, 80]. Although this technique can yield a wealth of information

in a physically complex region of the thruster, multiple studies have shown that probe injection fundamentally perturbs the thruster [81, 82].

Alternatively, there are several non-invasive techniques for characterizing the channel plasma or the near-field plume. These include microwave interferometry [84], optical spectroscopy [31], laser-induced fluorescence [60, 85], and Hall current tomography [86]. All of these techniques are potentially fast enough to resolve the breathing mode but they have varying levels of ambiguity. Most interferometric or passive techniques only provide line-averaged data and may require an energy level model to yield the desired quantities. Laser-induced fluorescence readily yields the ion velocity distribution function but cannot easily be extended to quantifying other parameters without probing multiple populations or relying on a model of plasma optical density. Hall current tomography, although quite sophisticated, still only yields Hall current density which is dependent on multiple inseparable plasma parameters [86].

3.5.4.2 Speed

As mentioned in the previous section, many non-invasive techniques are fast enough to resolve low-frequency oscillations. However, most electrostatic probes are more difficult to operate in a time-resolved manner. Lobbia and Gallimore developed a high-speed Langmuir probing technique with which they could measure breathing behavior in a Hall thruster plume [59]; however, they applied it neither in the near-field nor inside the channel, and it is unclear from their studies of the bandwidth limits of the technique [87] whether it is feasible. Retarding potential analyzers (RPA) and Wien filters are typically too large to inject toward the thruster without unacceptable perturbation, and in fact little literature is available describing their near-field use, although the RPA may work in theory since it relies on ion dynamics which will be unaffected by the strong radial magnetic field in the channel. Emissive probes can be operated at high-speed to measure the plasma potential but generally carry substan-

tial uncertainty ($\sim T_e$) unless more sophisticated (slower) operating techniques are employed [88] and likely would be affected by the near-field thruster magnetic field.

3.5.4.3 Ambiguity

The theory of Langmuir probes has been studied for nearly a century, and as a result a wealth of information can be gleaned from this diagnostic, including plasma density, electron temperature, and plasma potential. In fact, it is also possible to estimate the electron energy distribution function (EEDF) with a Langmuir probe [89], which is a unique and highly insightful measurement. However, many non-invasive diagnostic tools tend to be ambiguous, as mentioned in §3.5.4.1, yielding not only fewer properties than an electrostatic probe but less specific ones as well. However, Pérez-Luna et al. demonstrated that moments of the Boltzmann equation for ions can be solved using laser-induced fluorescence data to yield the axial electric field strength and ionization frequency [90] in a one-dimensional ion beam. This improves the utility of these laser measurements, which otherwise are typically used to only determine the mean ion velocity and temperature. It is possible that similar complementary modeling techniques could be used to expand the repertoire of measurements provided by other non-invasive diagnostics, but given the sensitivity of Pérez-Luna et al.'s method to uncertainty in the raw data, it remains to be seen whether it can be extended to high-speed measurements. At least one instance [91] of it being used successfully outside of Ref. 90 exists, but we can find no examples of equiavlent methods applied to other diagnostics in the electric propulsion literature.

3.6 Summary

Developing Hall thrusters without a complete understanding of their stability is an expensive, time-consuming, and unreliable process. Even though Hall thrusters are already a flight-proven technology, as greater numbers and more exotic variations of

these devices are flown in the coming years, failures as a result of this incompletely-informed design process will emerge. A device under test must be operated in a vacuum facility, and due to the designed lifetime of modern thrusters and the long timescales of some processes, they must be tested for impractical lengths of time. To improve the reliability of this technology and forego extensive ground testing, it is of paramount importance that the stability and performance of Hall thrusters is well-understood from a theoretical perspective.

The former aspect – stability – is of particular importance. Low-frequency oscillations, which are typically dominant in Hall thrusters, can have a wide impact on thruster behavior. Aside from correlational trends with performance, fluctuations of plasma properties in the plume and acceleration region have been measured. Yet existing hypotheses for the breathing mode all suffer from practical shortcomings, ranging from lack of a clear growth mechanism [29], to analytically-restrictive complexity [34, 46], to physical inconsistencies. As a result, there exists no intuitive yet predictive description of the breathing mode that can be used to aid design or at least explain empirical trends.

Even though some existing breathing mode theories remain prominent despite blatant deficiencies, definitive progress toward improving these descriptions of the instability has been hindered by the inherent difficulty in experimentally characterizing it. To measure low-frequency plasma properties, a diagnostic must be able to access the thruster channel, it must be fast enough to sufficiently resolve fluctuations, and it must unambiguously measure the plasma state. Although many diagnostics fulfill some of these requirements, very few meet all of them, which has historically limited the clarity and generality of breathing mode experiments.

In total, a physically-accurate, experimentally-validated, and analytically-tractable theory of the Hall thruster breathing mode is needed to improve the modern understanding of the stability of these devices, which is nec-

essary for successful proliferation of this technology.

CHAPTER IV

Experimental Methods

4.1 Introduction

In this chapter we present the experimental techniques used to characterize the breathing mode. We begin by summarizing the diagnostic approaches evaluated for this purpose, including optical emission spectroscopy, high-speed Langmuir probing, and time-resolved laser-induced fluorescence. For the former two, in §4.2 we describe the limitations that prevented us from using them to study the breathing mode. In §4.3, we focus on the last approach, describing the underlying experimental techniques and deriving new methods for inferring plasma parameters. We finish by reviewing the facilities and thrusters involved in the present work in §4.4, followed by a summary of this chapter.

4.2 Traditional Diagnostics Considered

We initially explored two traditional diagnostic techniques for characterizing the breathing mode: optical emission spectroscopy (OES) and high-speed Langmuir probing (HSLP). We explain in detail their implementation and evaluation in Appendices A and C, respectively. In the following, we summarize our findings and highlight the major limitations that ultimately prevented us from applying them in studying the

breathing mode.

4.2.1 Optical Emission Spectroscopy

Optical emission spectroscopy involves measuring the spectrum of emissions from a plasma and relating the ratios of different line intensities to properties of the plasma itself. Typically, a collisional-radiative model is used to describe the relationships between the emitted lines and plasma parameters. In this way, the accuracy of OES depends greatly on the model employed. Aside from that, though, this technique is non-invasive and the upper limit on the rate at which measurements can be made depends on the lifetimes of the transitions being observed, which may dictate a bandwidth in the megahertz or higher.

In Appendix A we demonstrate that OES is possible with a high-speed camera but several issues are apparent. Fundamentally, the collisional-radiative model used in this study becomes less sensitive as T_e increases, which means that these measurements become more uncertain as temperature rises. Since we expect $\sim$10 eV electrons in the thruster channel, this issue would be relevant to any ionization region studies. Further, all OES measurements are line-integrated in different planes, so the inverse Abel transform [92] – often used to infer radial data from integrated measurements of axially-symmetric two-dimensional information – would not be immediately applicable. Beyond even these inherent limitations, we found that the characteristic oscillations in light intensity of a HET discharge exhibiting breathing were not strongly recovered with our OES system, suggesting that other assumptions of the KCD model or our implementation of the system are preventing us from resolving the breathing mode fully.

4.2.2 High-Speed Langmuir Probing

In situ electrostatic probing of plasmas is historically and theoretically a well-founded diagnostic technique. In particular, Langmuir probes can reveal a wide range of plasma parameters with relatively simple operation. One possible method for characterizing an oscillatory Hall thruster plasma is with a high-speed Langmuir probe. As we detail in Appendix C, one manner to do this is by measuring the differential current between capacitively-matched probe electrical lines. In such a setup, typical Langmuir probe theory can readily be applied, such that unlike OES the biggest obstacles to implementation are hardware-related.

As we describe in Appendix C, the high-speed Langmuir probing we performed was more encouraging than OES in that we were successful in characterizing the near-field plasma of a low-power HET at rates sufficient to capture breathing oscillations. However, it has been identified in the literature that probe injection into a Hall thruster channel can subtly impact the discharge, such that even if the injected probe is operating normally, the plasma parameters being measured are influenced by the presence of the probe. We found considerable evidence of this effect in our own experiment. Aside from that, we found the spectral behavior of the thruster, in terms of both the discharge current and cathode-to-ground voltage, exhibited a sudden transition as the probe entered the channel. And further, the low-frequency spectral structure of the discharge current signal remained altered even as the probe was being retracted, implying that the probe injection "snaps" the thruster into another mode where it continues to reside for at least $\sim$1 s. Although each mode may still have strong low-frequency oscillations, we found that the frequency and intensity of the post-injection oscillations were significantly different from those pre-injection. As a result, this technique would likely be incompatible with any very-near-field studies of a Hall thruster like those needed to characterize the breathing mode.

4.3 Time-Resolved Laser-Induced Fluorescence with Ion Boltzmann Implicit Solution

Since we found the traditional diagnostic options insufficient, we had to explore (and in part develop) a more sophisticated approach. This eventually became the primary diagnostic method we relied upon in our experiments: time-resolved laser-induced fluorescence paired with an ion Boltzmann implicit solution technique (developed as part of this work), collectively referred to as TRLIF-IBIS. In the following, we describe the theoretical and practical aspects of laser-induced fluorescence as applied to the study of Hall thrusters. We similarly review the extension of this technique to time-resolved data collection. Finally, we discuss the ion Boltzmann implicit solution method, including its time-averaged and time-resolved application, additional data that can be inferred with it, and the uncertainty we anticipate with it. A preliminary experiment evaluating the practicality of TRLIF-IBIS is detailed in Appendix F, in which we successfully apply it on time scales meaningful for characterizing the breathing mode, and discuss refinements made to the technique as a result of that work.

4.3.1 Laser-Induced Fluorescence

The TRLIF-IBIS method is fundamentally a form of laser-induced fluorescence (LIF), a minimally-invasive diagnostic employed widely in electric propulsion research. We start by describing the theory underpinning this technique, followed by our practical implementation. We describe our analysis procedure and the specific data processing strategies we used to produce accurate plasma measurements.

4.3.1.1 Theory

LIF is a well-established technique for determining the velocity distribution function of an excited population [93]. In principle, a metastable state is non-resonantly excited with a laser at wavelength λ and the resulting fluorescence is collected as a measure of that metastable population density. If the laser is detuned from the nominal transition wavelength λ_0, the Doppler effect dictates that only particles moving at a certain fraction of the speed of light c will excite and fluoresce, given by

$$\frac{u_i}{c} = \frac{\lambda - \lambda_0}{\lambda_0} \ . \tag{4.1}$$

By detuning the laser over a wide range, the relative density of the excited population is determined as a function of particle velocity. Assuming that the excited state total density is proportional to the ground state density – which is true for negligible laser line width compared to the transition's broadening, steady-state population densities, negligible collisional excitation, and unsaturated laser excitation [94] – the velocity distribution function (VDF) is determined. Figure 4.1 is a diagram demonstrating this process, in which a laser is detuned to a higher frequency, given by $\mathbb{E}_0 + \delta\mathbb{E}$, such that particles at a specific velocity will see it blue-shifted by $\delta\mathbb{E}_0$ and fluoresce.

Although this process is straightforward, there are many practical aspects of it that make its implementation challenging. First, the fluorescence signal is usually very faint compared to the background light emission, so it is common to employ homodyning: modulating a signal to distinguish it from undesired noise. In particular, phase-sensitive detection methods like lock-in amplification are used to this end. Second, the laser wavelength must be known precisely, as typical velocity sweeps for a near-infrared transition require detuning $\sim$1 GHz for a nominal frequency of $\sim$100 THz. As a result, a very precise and stable wavemeter is required in the LIF setup. Finally, even if the fluorescence can be detected, the measured lineshape is not al-

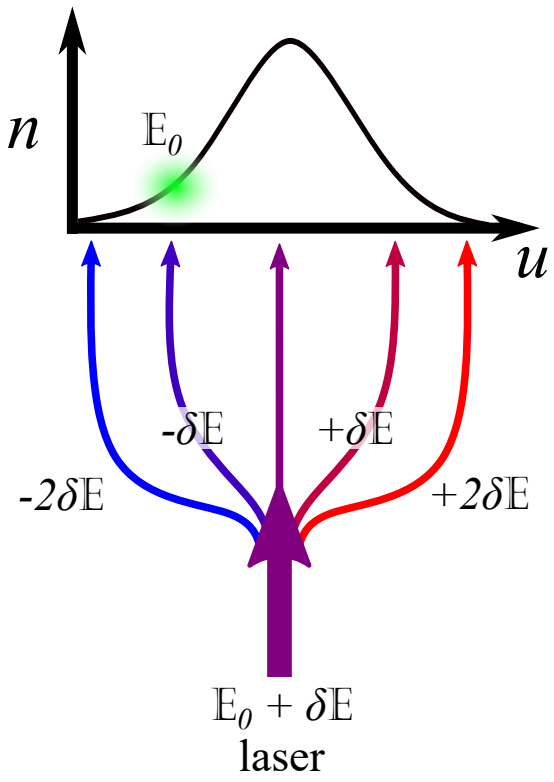

Figure 4.1: An illustration of the operational principle of LIF. Laser light is injected with some energy detuned from a nominal transition energy $\mathbb{E}_0$. A slight blue-shifting of particles moving away from the laser leads to fluorescence of those particles.

ways a true representation of the VDF. For example, there are several broadening mechanisms (discussed in §4.3.1.4) that can obscure the distribution. Additionally, saturation can occur when the excited state is pumped faster than it can fluoresce, broadening the lineshape.

4.3.1.2 Implementation

The LIF setup used in his work is fairly typical for Hall thruster research. We excited the $5d[4]_{7/2}$–$6p[3]_{5/2}$ (834.72 nm in air) transition for singly-charged xenon (Xe II), which fluoresces at 541.91 nm in air (green), and the $6s^2[1/2]^0_1$–$6p^2[3/2]_2$ (834.68 nm in air) transition for neutral xenon (Xe I), which fluoresces at 473.41 nm (blue). Figure 4.2 shows an energy level diagram for these excitation-fluorescence schemes, and Fig. 4.3 shows a diagram of the physical configuration. We will now give a brief

description of the hardware involved. First, laser light detuned from the stationary transition wavelength is produced by a Newport TLB-6700 diode laser and TA-7600-LN tapered amplifier, chopped with a SR540 mechanical chopper, fiber-coupled and fed into the vacuum chamber, and focused axially to a roughly 1 mm^3 point in the discharge. The wavelength is measured precisely with a HighFinesse WS-7 wavemeter. At the interrogation point inside the discharge, the laser wavelength Doppler shifts to the stationary wavelength in the frame of reference of ions at a specific velocity. These ions are excited by the laser, and the subsequent fluorescence is collected with optics offset from the thrust axis by 60°. The fluorescence is filtered with either a Spex 500M spectrometer or a set of dielectric bandpass filters (±4 nm band), amplified with a Hamamatsu E717-500 photomultiplier tube (PMT) and an Oriel 70710 trans-impedance amplifier (TIA), and finally homodyned with a SRS 810 lock-in amplifier (LIA) to discriminate the fluorescence from background light. The LIA uses the voltage output of the mechanical chopper as a reference signal and digitally determines the magnitude of the fluorescence signal at the same chopping frequency. The SRS 810 LIAs used in the present experiments are capable of automatically determining the phase of maximum amplitude; that is, the fluorescence signal at the chopping frequency may have a slight phase delay, and the LIA will automatically find it. In practice, we are interested in the magnitude of the signal, which tends to introduce an offset in the data due to noise. The LIA can also output the maximum amplitude phase (in degrees) at each velocity, although this information is often ignored. We will discuss a use for the phase data in §4.3.1.3.

The optics inside the vacuum chamber consisted of 50 mm achromatic doublet lenses coupled to 50-μm fibers for laser injection, and a 75 mm achromatic doublet lens coupled to a 1000-μm fiber for collection. The lenses are protected with borosilicate sacrificial glass, and all lens tubes and mounting structures are covered in flexible graphite foil sheets. The injection optics are attached to short two-axis fine position-

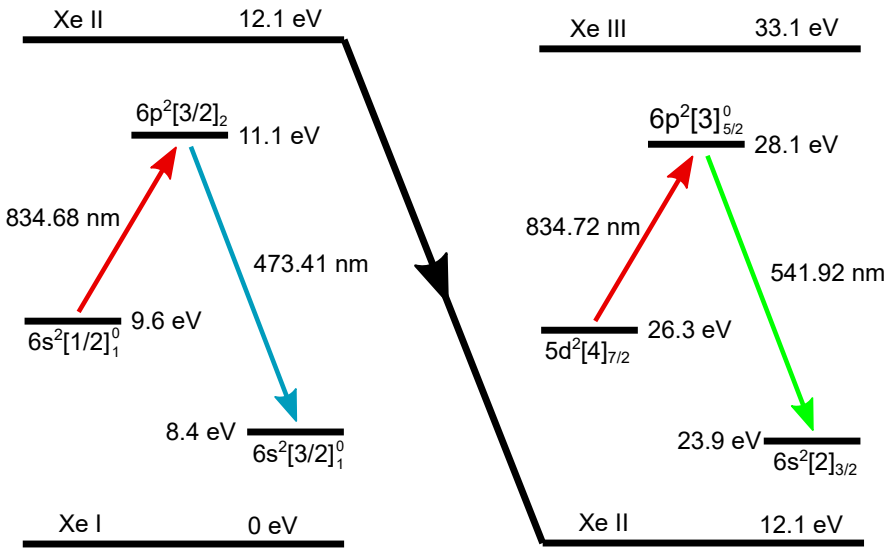

Figure 4.2: Energy level diagrams of the Xe I scheme spanning the first ionization energy 12.1 eV (left) and Xe II scheme spanning the second ionization energy 21.0 eV (right), with state terms and transitions labeled.

ing stages for alignment but are otherwise kept stationary. When aligning the optics, we couple low-power visible lasers to the injection and collection fibers. Before pump-down, we use an autocollimation technique to ensure that the beams are squared up to thruster surfaces: first we mount a plane mirror to a thruster surface; we then roughly align the injection laser spot so that it falls on the mirror; we then adjust the injection angle until the reflection from the mirror falls on top of the injection lens itself. During pumpdown, we check hourly that the alignment lasers coincide with an alignment point – typically a dab of ceramic paste – located at a precise position on the thruster. In practice, the mounting hardware in the chamber will expand/flex in response to heating from the plasma plume, so often ± 2 mm corrections are needed to bring the beams back into alignment. By translating the thruster using a set of stepper-driven motion stages with $\sim$50-μm resolution and 10-μm accuracy, spatial maps of VDFs can be acquired without large-scale translation of the optics.

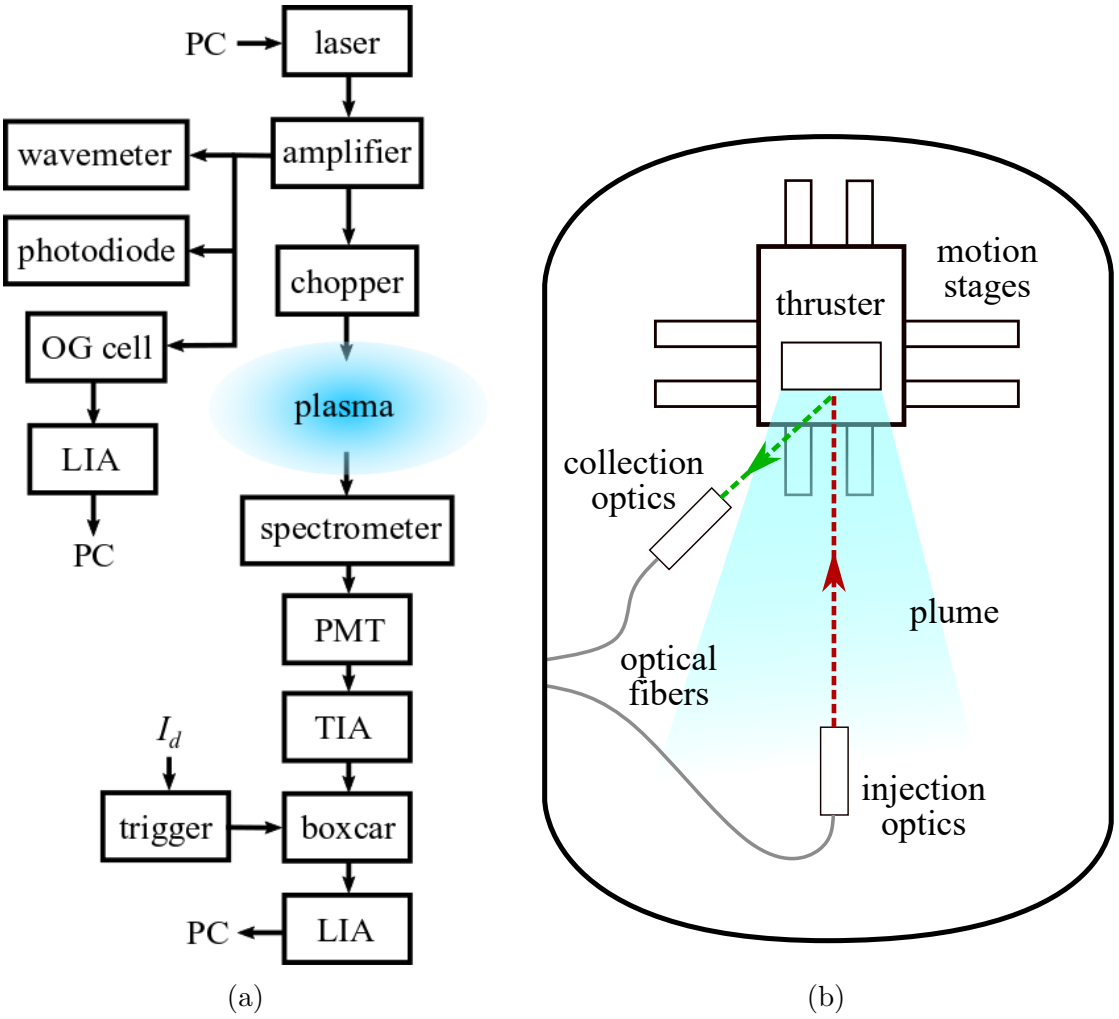

Figure 4.3: A diagram of the external LIF setup (a), and a birds-eye view of the internal setup (b), showing the placement of optics relative to the thruster.

4.3.1.3 Analysis

Like that of many other diagnostics, the analysis of LIF data is a balance between fidelity and simplicity. We begin here by describing the general procedure for processing VDFs into typical quantities of interest. In the following sections, we detail the specific procedures needed depending on the species being probed.

The mean and most probable velocities of a population are usually the quantities of greatest interest from LIF data. The latter is simply the velocity of peak intensity, and thus it can be determined to within the wavelength resolution of the laser scan,

often ∼100 m/s, which is small compared to typical Hall thruster beam velocities, ∼10 km/s. The former requires the first moment of the probability distribution $f(u)$ to be taken, where the i$^{\text{th}}$ moment is given by

$$\overline{u^i} = \int_{-\infty}^{+\infty} u^i f(u)\, du\ . \tag{4.2}$$

When there is random noise of variance σ^2 in the normalized signal, the uncertainty of a moment is given by $\overline{u^i}\sigma^2$. However, if the data has an offset Δf, the moment then depends on the bounds of the data set $\{u_1,u_2\}$, such that the error becomes $({u_2}^{i+1} - {u_1}^{i+1})\Delta f/(i+1)$. Although removing such an offset may seem trivial, the presence of random noise can often obscure its true value if too few samples are available. Clearly the calculation of moments from the raw data could lead to significant error if the signal-to-noise ratio (SNR) is too low. Moreover, the uncertainty due to random error could be much larger than anticipated if too few measurements are available, as there will be no guarantee that the noise will be symmetrically distributed. There are several approaches to overcoming this SNR issue, including simply smoothing the raw data, fitting multiple Gaussians, and a combination of the two. In the present work, a new phase approach is taken for smoothing VDFs. All of these methods will now be discussed.

Smoothing

Smoothing the raw data – essentially low-pass filtering $f(u)$ in u space – can help eliminate random noise. However, it does not correct offset of the data, and it will unavoidably broaden the distribution. Further, it can be difficult to determine an appropriate amount or type of smoothing to apply. Binning and averaging, which involves splitting the data into equal segments and averaging within each segment, makes no assumptions about trends in the data and reduces the uncertainty of each

measurement point considerably. The cost of this approach is that it reduces the size of the data set; since LIF measurements are often time-consuming, data sets are usually sparse, making it impractical to bin and average. Alternatively, Savitzky-Golay smoothing [95] sequentially applies a polynomial fit to a subset of points. In this case, the number of data points is not reduced but an assumption must be made about the trends in the data, which dictates the order of the polynomial used for smoothing. The number of local points to fit the polynomial ("frame length") must also be decided. For this reason, there are many assumptions made to smooth in this manner, and thus an unquantifiable uncertainty is contributed to any moment calculations. Figure 4.5 shows a sample VDF with smoothing applied, resulting in considerable (and apparently non-uniformly distributed) residuals with the raw data.

Gaussian Fitting

Since the ion population in Hall thrusters typically remains quite cold, often <1 eV [96], it is usually assumed that the distribution is not far from Maxwell-Boltzmann, as it may be for the weakly-collisional neutral population. This implies that the raw data will be Gaussian-shaped, and thus a single-Gaussian fit could be successfully applied to avoid smoothing. However, the distortion of a VDF due to uniform acceleration of particles (kinematic compression) can make an originally Gaussian profile asymmetric [96]. For a distribution of variance σ^2 accelerated through a potential V_a, the variance becomes dependent on velocity: $\sigma^2 u^2/(u^2 + eV_a)$. This means the distribution narrows toward low velocities and approaches the original width at high velocities – thus producing a high-velocity tail, and perhaps justifying fitting two Gaussians to capture this effect. Further, Huang et al. showed that oscillations in bulk velocity can naturally lead to a saddle-shaped distribution [60], which may also justify a double-Gaussian fit. The presence of multiple populations produced by kinetic effects could require fitting with even more Gaussians, although properly pre-

dicting and verifying these populations is difficult. In general, using many-Gaussian fits is dangerous because a VDF composed of N points can be near-perfectly fit with the sum of (at most) N Gaussians, since they are square integrable. This means any VDF can be successfully fit with enough Gaussians but doing so does not imply the VDF is composed of multiple Maxwellian populations.

In fact, with certain assumptions we can estimate the number of Gaussians needed to match a random data set of N points within some percentage X of the range of the data set. A single Gaussian is guaranteed to coincide with one data point but the probability of matching the rest is given by X^{N-1}. For two Gaussians, each one only needs to match $N/2$ random points, which have $N!/(N/M)!(N - N/M)!$ combinations. As a result, the total probability of reconstructing the random data with Gaussians is given by an expression like $\{N!X^{N/M-1}/(N/M)!(N - N/M)!\}^M$. For typical LIF parameters of $N = 50$ and $X = 10\%$, only five Gaussians are required to fit the data within the specified tolerance. To further illustrate this point, Fig. 4.4 shows the number of required Gaussians (fits) as a function of sample size for three $1 - X$ values. We expect this is an underestimate, as we have not accounted for the fact that the total combinations of points each Gaussian must match decreases as M increases, but nonetheless it demonstrates that very few Gaussians are needed to fit an arbitrary LIF data set, and thus relying on the physical meaning of multi-Gaussian fits can be perilous.

Regardless of the hazards, this method has the advantage that it is strongly resistant to noise and can easily reject non-physical features in a VDF. Conversely, this fitting technique will produce unreliable results if the VDF does contain non-Gaussian features or is mostly composed of noise. Additionally, good initial guesses for the Gaussian parameters are needed for a meaningful fit, and one needs to know in advance how many Gaussians to fit and the relationship between them. However, once a good fit is made the velocity moments are easily calculated. Figure 4.5 shows a three-

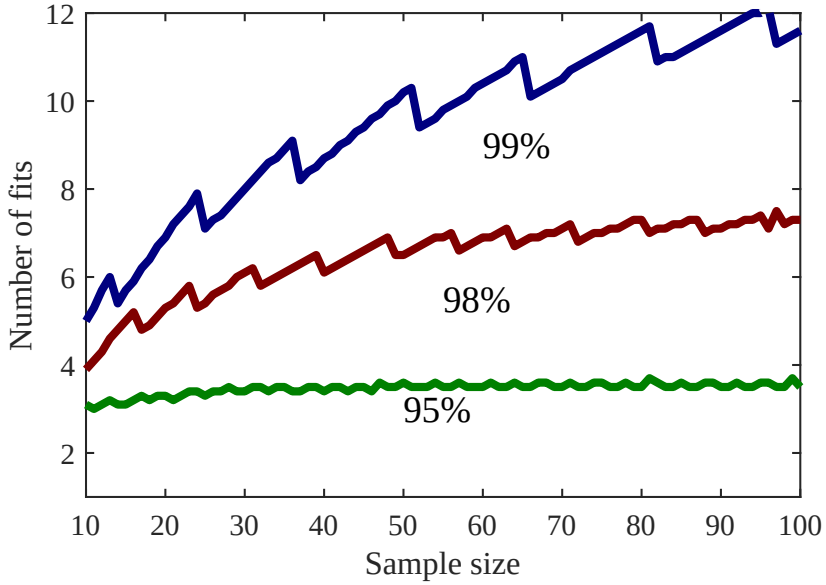

Figure 4.4: The required Gaussian fits to match a random data set of a given sample size with 99%, 98%, and 95% tolerance. The jaggedness of the data reflects that the fact that the possible fit combinations is a function of factorials and thus there are unavoidable rounding errors in these curves.

Gaussian fit applied to a sample VDF, producing more uniformly-distributed residuals and reducing deviation from the raw data compared to Savitzky-Golay smoothing.

Given the foreknowledge needed to effectively Gaussian fit a VDF, certain aspects of this approach can be combined with typical smoothing techniques to compensate for deficiencies in both. For example, a single-Gaussian fit can be performed on the raw fluorescence data to determine any offset, and then smoothing can be applied to minimize random noise. The single-Gaussian fit can also be used as a windowing function to minimize noise in the wings of the VDF. Combined, these methods account for random noise, offset, and small sample sizes. However, it may obscure tails or discrete high-energy populations, and the windowing fundamentally skews the shape of the VDF. And for higher velocity moments, the reduction of noise in the wings achieved in this manner may still not be sufficient to prevent erroneous calculations.

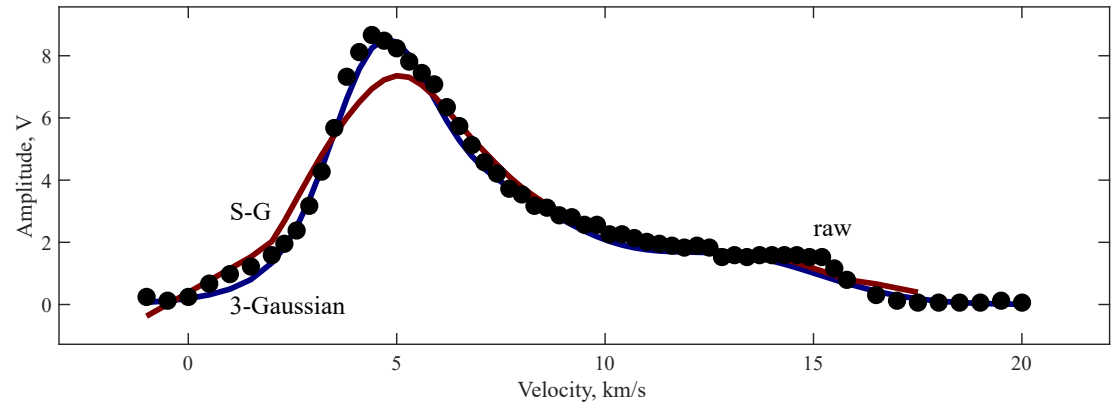

(a)

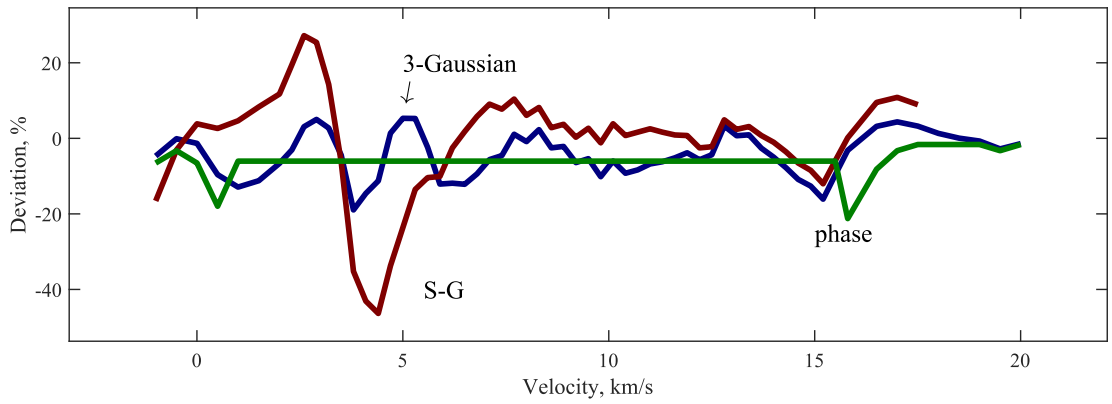

(b)

Figure 4.5: A raw VDF compared to smoothed and Gaussian-fit curves (a). A comparison of the relative residuals of the smoothed, Gaussian-fit, and phase-analyzed distributions compared to the raw data.

Phase Analysis

When taking LIF measurements, we typically only consider the laser wavelength and the locked-in fluorescence amplitude, allowing for little insight into the nature of the noise in the measured VDF. However, the phase of maximum amplitude at each wavelength can also be recorded from the LIA without difficulty. For a given signal of amplitude A, the LIA measures an in-phase component X and a 90° component Y such that $A^2 = X^2 + Y^2$ and the phase θ is given by $\tan^{-1} Y/X$. It can be shown with circular statistics that normally-distributed noise (due to e.g. Johnson noise) in Y and X approximately produces uniformly distributed noise in θ [97]. This suggests

that the fluorescence signal will have a definite characteristic phase while the noise-dominated signal will be uniformly distributed from -180° to 180°. Figure 4.6 shows sample amplitude and phase curves, where the fluorescence amplitudes are clearly delineated from noise based on the phase.

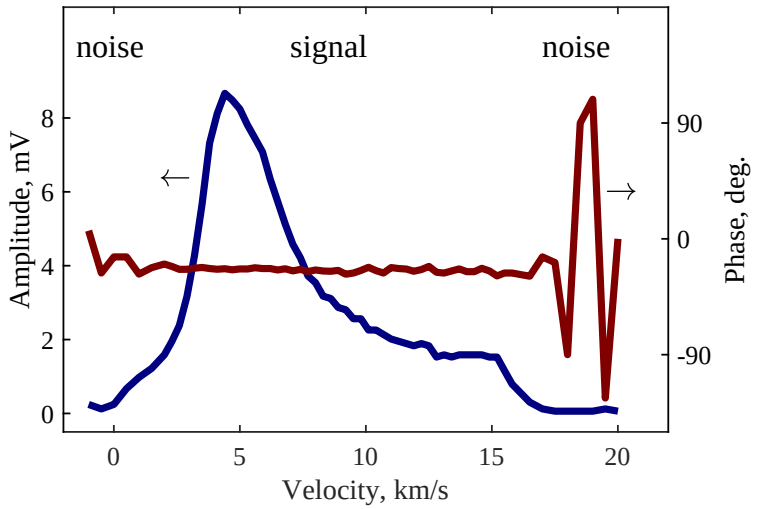

Figure 4.6: A sample of the variation in signal phase between noisy regions and signal-dominated regions.

Given that both the Gaussian fitting and smoothing approaches to VDF analysis are challenged by separating noisy measurements from reliable ones, the signal phase can be leveraged as a better technique for calculating moments. A simple implementation of this utilized in some parts of the present work will now be described and is shown conceptually in Fig. 4.7. First, it is assumed that the measured data includes some amount of pure noise, and that if the data is sorted by intensity, the first data point is due to fluorescence and the last is due to noise. The probability of a uniform distribution of the phases of all data points above (i.e. higher intensity than) a given one is then calculated (Fig. 4.7c). In effect, this is measuring the probability of all points above a given intensity being due to noise, as judged by the range of phases for those points. The minimum probability point presents an intensity threshold below which the data becomes increasingly consistent with random noise. In this

way, we have found a threshold below which the data can be considered noise and ignored when calculating moments. Further, this data can be averaged to estimate any constant offset in the VDF. This technique therefore presents a clear criterion for separating noisy points from meaningful ones, which provides an algorithmic yet physically-inspired approach to reducing noise when calculating moments. Figure 4.5b includes the residuals for a phase-analyzed sample distribution, where there is constant deviation for most of the velocity range (accounting for an offset) and varying deviation toward the wings where the raw data is most likely noise.

4.3.1.4 Data Processing

Aside from the general analysis procedure for LIF data just reviewed, there are corrections to the measured lineshape specific to the species being probed. The two main effects we consider are hyperfine splitting and Zeeman splitting. There is also natural line broadening due to the necessary uncertainty in energy levels but we neglect this as it is typically small compared to the desired Doppler broadening [98]. We also experimentally explored saturation broadening by varying laser power and examining the change in fluorescence intensity for our typical LIF setup (probing a high-power Hall thruster discharge), and the response was found to remain linear throughout the range of laser powers tested, so likewise we neglect this effect. We now describe the pertinent splitting effects as well as how we account for them in processing raw LIF data. To reiterate, we utilized the $5d[4]_{7/2}$–$6p[3]_{5/2}$ (834.72 nm in air) transition for singly-charged xenon (Xe II), which fluoresces at 541.91 nm in air (green), and the $6s^2[1/2]^0_1$–$6p^2[3/2]_2$ (834.68 nm in air) transition for neutral xenon (Xe I), which fluoresces at 473.41 nm (blue). Others have found this Xe II transition to be relatively strong even deep inside a Hall thruster channel [99] as well as into the near plume [100]. The chosen Xe I transition, on the other hand, is relatively weak and may not be usable far from the anode where neutral density begins to fall off [98].

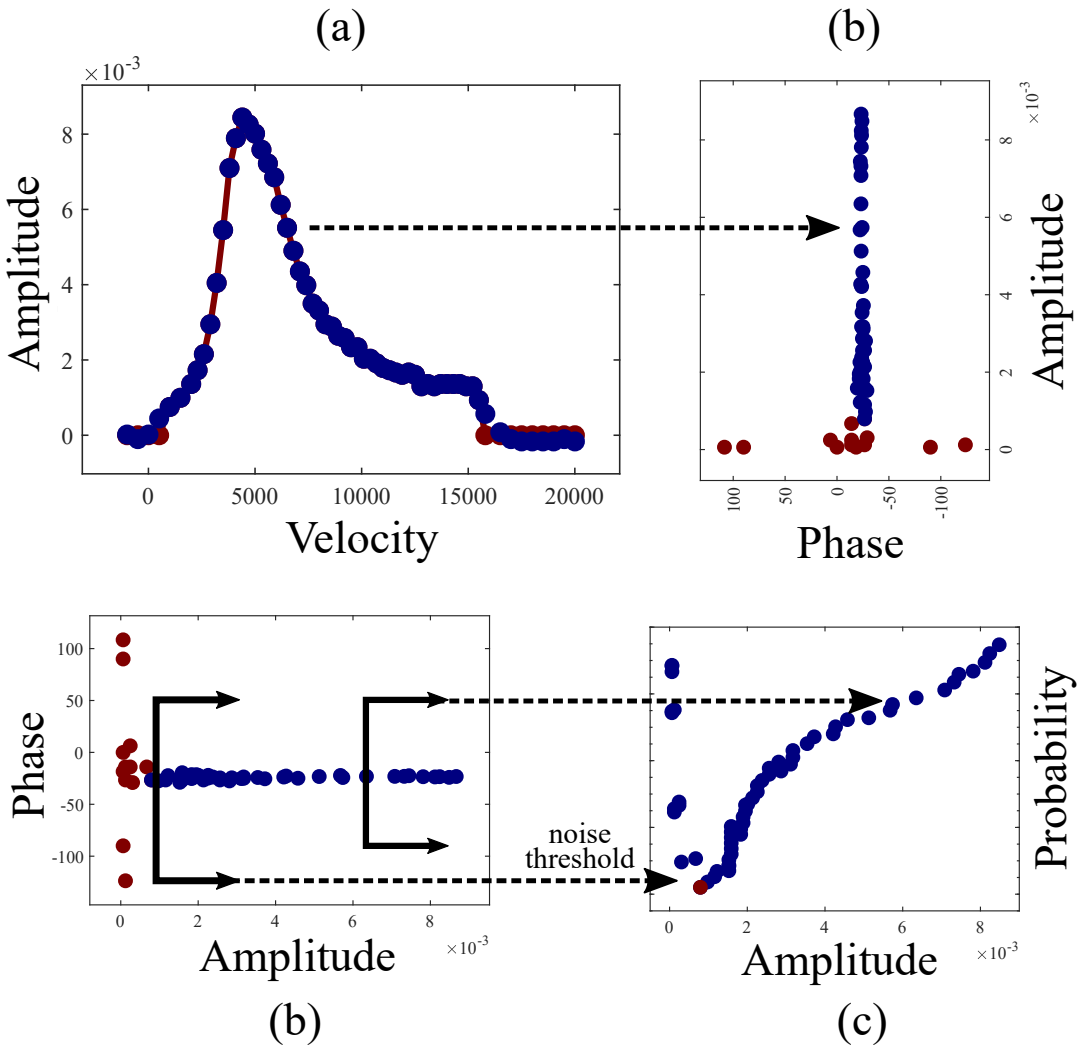

Figure 4.7: A sample of the phase analysis process: starting with a raw VDF (a), the amplitude as a function of phase (b) shows a clear delineation between signal (blue) and noise (red); the probability of the phases above a given amplitude being due to noise can be calculated as a function of amplitude (c), where a minimum occurs at some noise threshold below which the data should be ignored.

Other transitions are available that are much stronger but at least one other common one is resonant [101] and thus cannot be used to find the VDF. For this reason, in the present work Xe II LIF was performed on both sides of the exit plane, while Xe I LIF could only be done in the channel.

Hyperfine Structure Splitting

Hyperfine structure encompasses the shifting of energy levels in an atom due to

interaction of the nucleus and electrons. The two forms of this interaction of interest in this work are isotopic and nuclear spin splitting, the latter of which only affects odd isotopes (non-zero nuclear spin). For Xe II, this splitting is minimal and symmetric [93], so in this work it is ignored. For Xe I, particle velocities and temperatures in a Hall thruster are quite low, so hyperfine splitting becomes more significant. The rules for this splitting are described in general in atomic physics texts [102] and in the context of LIF as part of many studies [96, 101], so we will forego an identical review. Instead, we present Figs. 4.8 and 4.9, which show our predicted cold spectrum, as well as the specific line splitting we calculated for Xe I based on data from Refs. 103, 104, 105, and 106. The shape of Fig. 4.8 differs slightly from that shown elsewhere (cf. Ref. 107), which could be due to using different hyperfine constants or misapplication of the selection rules, but it generally follows the same splitting.

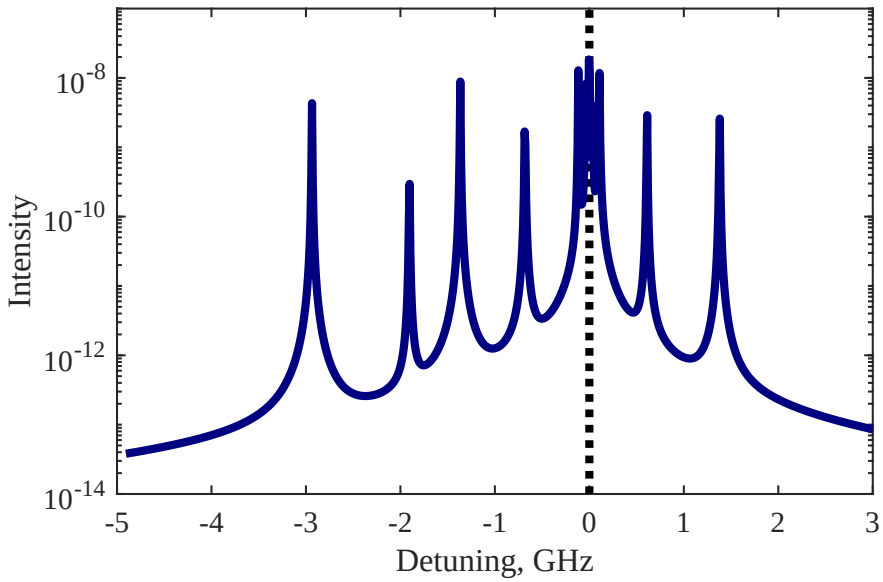

Figure 4.8: The theoretical cold hyperfine spectrum for the Xe I transition used for LIF.

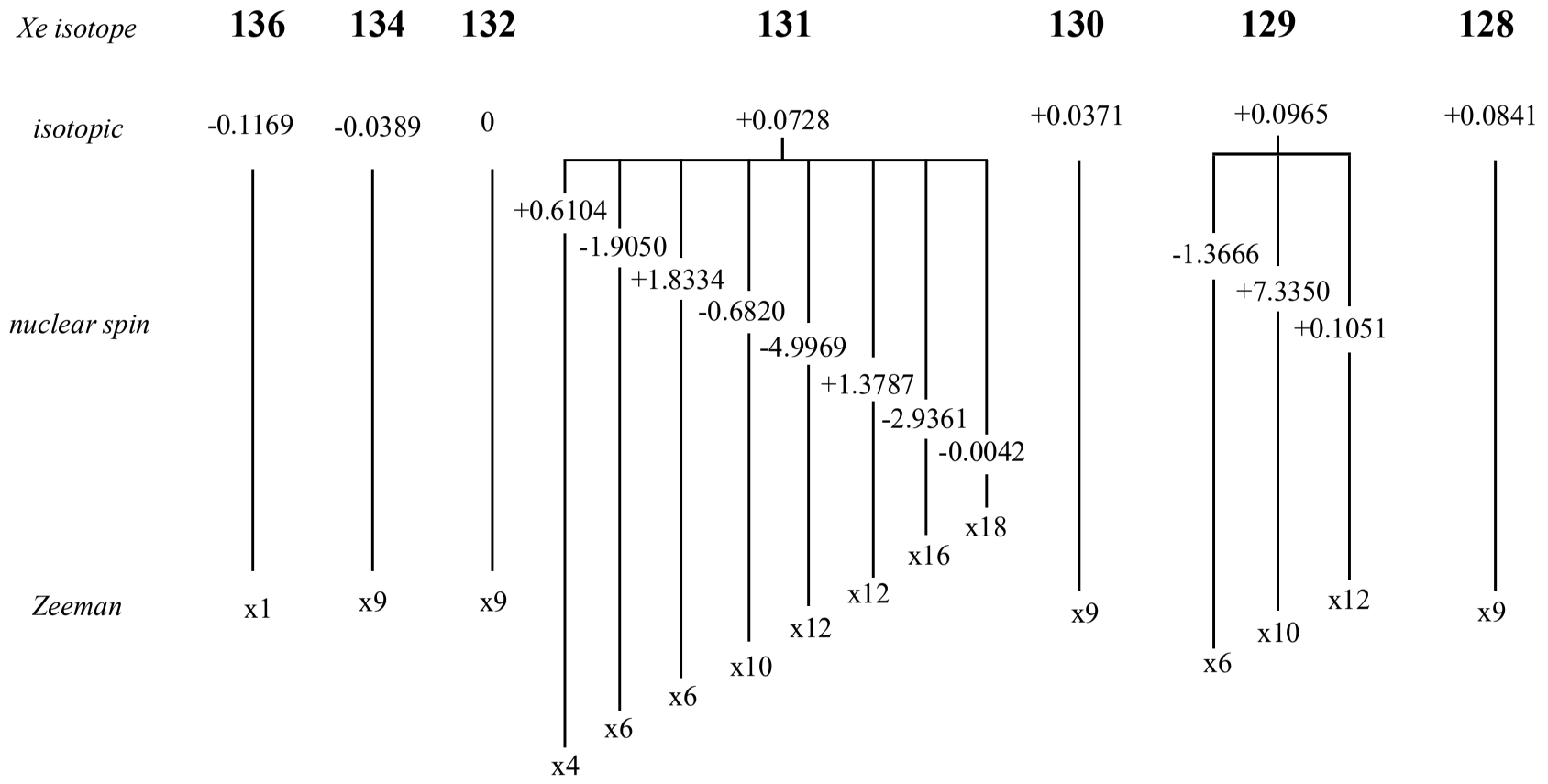

Figure 4.9: The splitting of Xe I lines due to isotopic, nuclear spin, and Zeeman splitting. Changes in wavelength are enumerated in nm.

This line splitting is accounted for in analyzing raw Xe I VDFs by deconvolving the measured spectrum with the theoretical one. Smith explored various deconvolution strategies, eventually settling on an inverse Gaussian filter as the most effective [96]. Others have explored more sophisticated methods like Tikhonov regularization, although the benefits are arguable [101]. Alternatively, Mazouffre et al. fit multiple warm (Gaussian) theoretical spectra to their measurements, which avoids the numerical difficulties of deconvolution but necessarily assumes the population is Gaussian and/or can be described with a chosen number of Gaussians [98]. As part of the present work, we developed a simpler approach to the Gaussian-fitting of Mazouffre et al., in which we can determine the VDF moments from the theoretical spectrum and measured spectrum without any fitting. With this method, which we will describe next, we do not resolve the VDF itself and still must assume it can be described as a sum of Gaussians, but the correction is algebraic and thus computationally-inexpensive and less sensitive to initial fitting guesses.

First, we assume a given warm lineshape is the convolution of the cold spectrum and a Gaussian velocity distribution. Due to natural broadening (uncertainty in energy levels), the cold spectrum is not simply a series of peaks but is a sum of Lorentzians [102]. In velocity-space, then, the cold spectrum may have a non-Lorentzian shape, and thus the form of the convolution of the cold spectrum with a Gaussian is unclear. Given the Doppler relation of Eq. (4.1) and for frequency ν such that $c = \lambda\nu$, it can be shown that a Lorentzian $\mathcal{L}$ in frequency space

$$\mathcal{L}(\nu) \propto \frac{1}{1 + \left(\frac{\nu - \nu_0}{\Delta\nu}\right)^2} \tag{4.3}$$

is also approximately Lorentzian in velocity space since ion velocities are at most

$\sim$ 10 km/s and thus u/c$\ll$1,

$$\mathcal{L}(u) \underset{\sim}{\propto} \frac{1}{1+\left(\frac{\nu_0 u}{c\Delta\nu}\right)^2} \ . \tag{4.4}$$

The convolution of a Lorentzian and a Gaussian is the Voigt profile, which although common in spectroscopy is defined by a complex transcendental function and often can only be evaluated numerically. However, the FWHM of $\mathcal{L}(u)$ is given by $c\Delta\nu/\nu_0$, which is approximately 8 m/s for the Xe I transition of interest, whereas the FWHM of a room temperature xenon Maxwellian population is about 200 m/s. The limit of an infinitely thin Lorentzian can be approximated as a delta function, and thus a warm lineshape convolved from such thin Lorentzians can be approximated as simply a Gaussian.

With that established, we assume that a warm stationary lineshape can be described by a sum of Gaussians, and by measuring such a lineshape we can estimate the mean velocities μ_i, variances ${\sigma_i}^2$, and relative amplitudes α_i of the associated cold spectrum. This is represented in Fig. 4.10a. An arbitrary ("unknown") measured lineshape is therefore composed of a sum of stationary lineshapes with means velocities μ_j and amplitudes β_j, such as in Fig. 4.10b. The first velocity moment of the lineshape $\overline{u}_L$ can then be described as

$$\overline{u}_L = \int_{-\infty}^{+\infty} u \sum_j \sum_i \frac{\alpha_i \beta_j}{\sqrt{\pi}\sigma_i} \exp\left[-\frac{(u-\mu_i-\mu_j)^2}{{\sigma_i}^2}\right] du = \sum_j \beta_j(\overline{u}+\mu_j) \ , \tag{4.5}$$

such that

$$\overline{u} = \frac{\overline{u}_L - \sum_j \beta_j \mu_j}{\sum_j \beta_j} \ . \tag{4.6}$$

As a result, the true first moment is related linearly to the measured first moment, where the relationship is a function of the cold spectrum mean velocities and amplitudes, which can be measured separately. In fact, if the cold spectrum amplitudes

are normalized, Eq. (4.6) indicates that there is simply a subtractive correction $\Delta\overline{u}$ required to find the first moment: $\overline{u} = \overline{u}_L - \Delta\overline{u}$. A similar analysis for the second moment assuming normalized cold spectrum amplitudes yields

$$\overline{u^2} = \overline{u^2}_L - 2\overline{u}\sum_j b_j\mu_j = \overline{u}_L{}^2 - 2\overline{u}_L\Delta\overline{u} + 2\Delta\overline{u}^{\,2} \ . \tag{4.7}$$

In this way, by simply measuring the cold spectrum in advance, the velocity moments can be determined from measured lineshapes without any ambiguous fitting or sensitive deconvolution techniques. Appendix G presents the quantitative application of this technique for the work described here; any reference to Xe I velocity moments hereafter are assumed to be corrected in a similar manner.

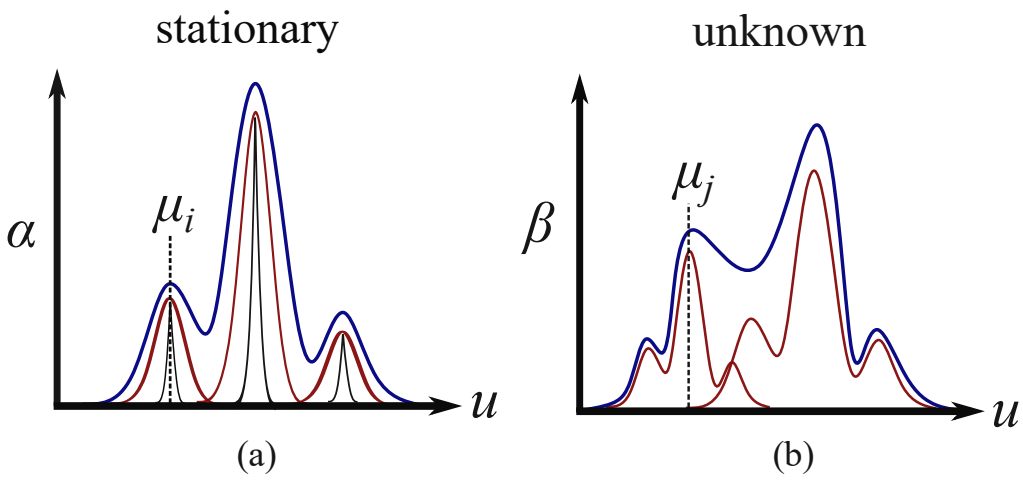

Figure 4.10: An illustration of fitting Gaussians to a stationary lineshape (a), and the fitting the stationary lineshape to an unknown VDF (b).

Zeeman Splitting

The Zeeman effect is the splitting of spectral lines due to the presence of a magnetic field. This effect comes into play for Hall thrusters in the near-field region and inside the channel, where the magnetic field may be around 10,000 times stronger than the Earth's magnetic field. Unlike with hyperfine splitting, the Zeeman effect

is more important for Xe II than Xe I LIF in the present work because the latter is performed deep in the channel where the magnetic field strength is low. The uncertainty due to this effect for Xe II can be calculated in the fashion of Huang et al. [101] and Jorns et al. [57]. Assuming Gaussian normalized VDFs we found it to characteristically contribute <10% uncertainty to the computed velocity moments at all times within the entire LIF domain, <1% at the exit plane, and even less downstream for typical conditions in our experiments.

In some neutral xenon LIF studies the laser is polarized to reduce the impact of the Zeeman effect, as its influence on line splitting is much greater for σ polarization (laser perpendicular to magnetic field) than π polarization (laser parallel to magnetic field) [101]. However, in general the Zeeman effect for the targeted Xe I line has been shown to be minimal for relevant field strengths in an optogalvanic cell [108]. In fact, our most downstream Xe I LIF points corresponds to a B_r of about 60 G, which when investigated in a stationary reference cell in Ref. [108], produced lineshapes nearly indistinguishable from those in the absence of a magnetic field. To explore this further, we can use our theoretical Xe I spectrum to demonstrate the influence of the Zeeman effect for our maximum anticipated magnetic field of 60 G. This is shown in Fig. 4.11. Note that the warm spectra are nearly identical, and so we neglect the Zeeman effect for neutral LIF in this study.

4.3.2 Time-Resolved Laser-Induced Fluorescence

Following our discussion of LIF, we now detail its time-resolved execution. As the theory and practical application are the same as with typical LIF, here we only discuss previous work, particularly the different approaches taken for time-resolved LIF. We also describe our implementation, including our efforts to optimize the acquisition parameters.

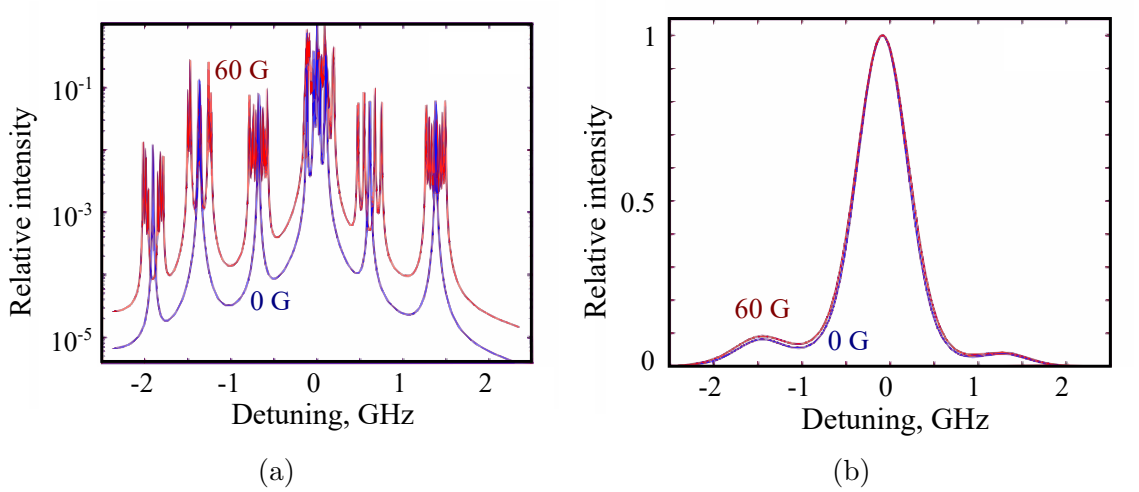

(a) (b)

Figure 4.11: The theoretical cold spectrum due to the Zeeman effect (a), and the theoretical warm spectrum for room-temperature neutral xenon (b).

4.3.2.1 Previous Work

In traditional LIF, the lock-in-amplifier works with the frequency-domain fluorescence signal, which means many chopper cycles must be available for integration. Naturally, the LIA treats all cycles identically, so ideally there is no change in the plasma chop-to-chop. Together, this means any plasma oscillations must be much faster than the chopping frequency, which itself must be much faster than the integration rate of the LIA. In practice, this corresponds to frequencies on the order of 10 kHz, 1 kHz, and 10 Hz, respectively. It is clear from this reasoning that the LIA sets a hard limit on the rate of LIF measurements. Each measurement takes ∼100 ms, and each VDF trace may be composed of 10-100 points, so full VDFs are only measured at < 1 Hz – much too slow to resolve low-frequency plasma oscillations according to the Nyquist sampling theorem [109]. However, several techniques are available to overcome this limitation.

Although many different methods are available for performing time-resolved laser-induced fluorescence (TRLIF), most of them apply some form of frequency-space averaging while still homodyning the fluorescence signal. One of the first implementations for Hall thruster research was performed by Mazouffre et al. using a novel

photon-counting technique [110]. Here, photons are detected with a PMT and converted to pulses with a high-speed discriminator; a lock-in counter then temporally bins the pulses after being triggered with an external signal; and finally background pulse counts are subtracted from the signal in real-time using slow modulation of the laser. In the initial application of this technique, the thruster discharge power was rapidly cycled as the counter was triggered to minimize noise due to spectral dispersion of the breathing oscillations [85]. Using a heterodyning technique, Diallo et al. similarly coerced the natural oscillations to a more coherent frequency by modulating the discharge voltage slightly [111].

A similar technique involves using a sample-and-hold circuit (SHC) with a LIA to measure VDFs phase by phase [112]. Here, the discharge current signal is used to trigger the SHC, which will sample and output the fluorescence signal (as transduced by a PMT) according to a programmable delay and gate width. Traces are taken sequentially for a range of delays until an entire breathing cycle has been characterized. This technique is sometimes referred to as boxcar averaging, where it is implied that not only is the fluorescence sequence sampled and held, each sample is a running average within a chop. However this can be difficult to achieve in practice, as many samples would need to be taken per chop, which requires the SHC to trigger at $\gtrsim$100 kHz, or for the chopper to be phase-locked with the trigger signal.

Finally, more data-intensive methods exist in which the frequency-space characteristics of relatively long and high-speed samples of the fluorescence, laser modulation, and relevant reference signal (e.g. the discharge current) are manipulated [113]. After homodyning the fluorescence signal, transfer functions between subsets of the fluorescence and the reference are computed based on the Fourier transforms of these signals. The average transfer function is then convolved with the reference signal to yield the time-resolved fluorescence intensity. More sophisticated interpolation schemes exist instead of simply averaging the transfer functions [114], with improved reconstruction

of transient features.

4.3.2.2 Implementation

As part of the present work we elected to use the sample-and-hold approach as it is the simplest. A SRS SR250 gated integrator filtered the fluorescence signal before it was homodyned with a lock-in amplifier, as shown in Fig. 4.3a. The discharge current was measured with a 15 MHz Tektronix TCP303 Hall current sensor and monitored with a Tektronix DPO2014 100 MHz oscilloscope. The gated integrator was triggered off of this signal using a custom high-speed monostable multivibrator circuit. Once triggered, the integrator outputs the fluorescence signal within a 10 μs gate after a computer-controlled delay below 100 μs. By varying the gate delay throughout a breathing period, the fluorescence at specific phases of a breathing cycle were sampled. We evenly sampled between seven and ten phases from 0 to 65 μs of delay. The chosen gate width dictated a Nyquist frequency of 50 kHz, which was sufficient to resolve the breathing frequency in all the present experiments. Figure 4.12 gives notional examples of the signals involved in this TRLIF setup, in which the SHC gate triggers off of the discharge current signal, and the fluorescence fluctuates with the discharge current (natural) and the chopper (induced).

Given the length of time required to make TRLIF measurements – seven to ten times that of time-averaged LIF – considerable effort was spent in optimizing four TRLIF parameters: (i) gate width, (ii) chop averaging, (iii) trigger rate, and (iv) chopping frequency. A small gate width (i) is more susceptible to noise (frequency dispersion) but eliminates "motion blur" due to the temporal evolution of the VDF, while a large gate width suppresses noise. If samples can be averaged (ii) within a chop, the signal will be cleaner, but if not enough samples are available the exponential averaging of the SR250 will attenuate the signal. A faster trigger rate (iii) allows more unique samples per LIA integration, but since the SR250 can only trigger as

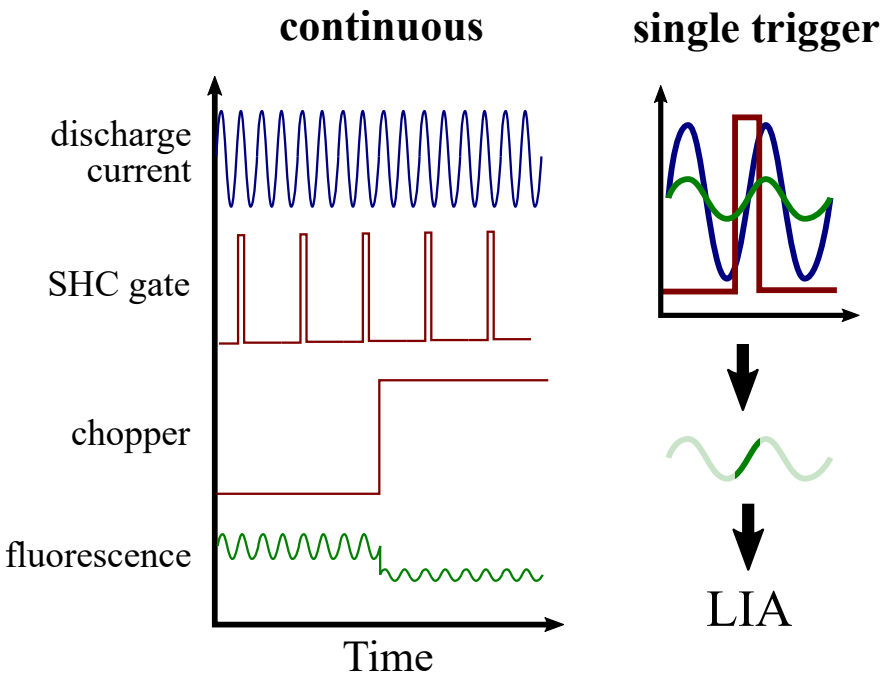

Figure 4.12: Notional examples of the discharge current, SHC gate, chopper, and fluorescence signals ("continuous"), and an demonstration of the extraction of a fluorescence measurement during ("single trigger").

high as 20 kHz, the triggering becomes less consistent such that some gate delays will permit fewer unique samples than others. Even if no chop averaging is performed, the chopping frequency (iv) can still influence the TRLIF performance. If chopping is too slow, the LIA will not be able to homodyne effectively and the SNR will decrease. If the chopping is too fast, there may be an imbalance in the sampling of "on" and "off" chops, which will attenuate the LIA signal. In fact, the beat frequency between the trigger rate and the chopping frequency must be large to prevent this, although it is difficult to predict in advance an optimal value for this ratio.

In practice, we found that reducing the gate width (i) led to better SNR but since the transimpedance amplifier had a bandwidth of only 100 kHz, reducing it below 10 μs did not change the performance of the TRLIF system. With a trigger rate of 10 kHz and a chopping frequency of 1 kHz, we estimated that we could chop average (ii) at most ten samples per trigger of the SHC. In practice though, the

exponential averaging always greatly attenuated the signal because the chopper was not phase-locked with the trigger signal, which meant that typically only around five samples were averaged. In theory this should only attenuate the signal by 0.7%, but in practice it appears to be much greater, and thus we found chop averaging to be detrimental. Raising the trigger rate (iii) did indeed lead to less consistent SNR phase to phase, so it was kept as large as possible while still remaining consistent, which was found to be ∼5 kHz. The chopping frequency (iv) was indeed found to influence the TRLIF results, with the best performance near 800 Hz. It is interesting that noticeable differences were observed even when chopping only 200 Hz faster, a 5:1 rather than 6.25:1 ratio of triggering to chopping. This suggests that there may be other effects dictating the optimal chopping frequency but eking them out was outside the scope of this work.

4.3.3 Ion Boltzmann Implicit Solution

Laser-induced fluorescence data by itself only gives insight into a few plasma parameters. However, it is well-known that the velocity moments yielded by LIF can be paired with a kinetic ion model to infer other quantities of interest. Pérez-Luna et al. outlined a method for determining E_z and the ionization frequency f_{iz} from LIF data for a few plasma sources [90]. The purpose of that study was to demonstrate that determining E_z from LIF data without accounting for ionization – by assuming conservation of energy using the most probable velocity $\hat{u}$ such that $\hat{u}(d\hat{u}/dz) = (e/m_i)E_z$ – can be inaccurate. However, Pérez-Luna et al.'s method can be extended for the purpose of inferring many important plasma parameters from LIF data. We now describe our contributions to this technique, which we refer to as the ion Boltzmann implicit solution method, or IBIS.

4.3.3.1 Time-Averaged

We begin by describing this technique in a time-averaged sense. On the centerline of a Hall thruster channel, the ion dynamics are largely one-dimensional. Further, the ion-ion collision mean free path is long throughout the channel and near-plume, roughly 0.1 m in these studies, and for much of this region they are very cold compared to the drift velocity $\overline{u_i}$, so they are assumed to move ballistically. By ignoring all collisions except for electron impact ionization and assuming quasi-neutrality, the centerline ion Boltzmann equation becomes

$$\frac{\partial f}{\partial t} + u_i \frac{\partial f}{\partial z} + \frac{e}{m_i} E_z \frac{\partial f}{\partial u_i} = \left(\frac{\partial f}{\partial t} \right)_{iz}, \tag{4.8}$$

where the righthand side is the time rate of change in the IVDF due to ionization. Taking the first three velocity moments of this equation yields the familiar fluid Eqs. (4.9), except instead of a single fluid velocity u_i there appears up to the third velocity moment $\overline{u_i{}^3}$ because we have not assumed an ion distribution.

$$\frac{\partial n}{\partial t} + \frac{\partial \overline{u_i} n}{\partial z} = n f_{iz} \tag{4.9a}$$

$$\frac{\partial \overline{u_i} n}{\partial t} + \frac{\partial \overline{u_i{}^2} n}{\partial z} - \frac{e}{m} n E_z = 0 \tag{4.9b}$$

$$\frac{\partial \overline{u_i{}^2} n}{\partial t} + \frac{\partial \overline{u_i{}^3} n}{\partial z} - 2\frac{e}{m} n E_z \overline{u_i} = 3\frac{e}{m} T_n n f_{iz} \tag{4.9c}$$

Here we have expressed the righthand side of Eq. (4.8) as the product of the ion density and ionization frequency f_{iz}, which itself represent the ionization events per unit time per electron. In the third moment there appears the neutral temperature T_n that represents the temperature of newborn ions.

For steady ion behavior, the temporal terms in these moments drop out, reducing Eqs. (4.9) to a system of ordinary differential equations, implicit in the ion density n. However, this system can be solved explicitly for E_z, f_{iz}, and $d\ln(n)/dz$ as functions

of the velocity moments. Given a condition for density at some spatial boundary z_b, $n(z_b)$, the density can be found via

$$n(z) \propto \exp\left[\int_z^{z_b} \frac{d\ln n}{dz} dz\right] \quad , \tag{4.10}$$

where $n(z_b)$ dictates the constant of proportionality.

To acquire the boundary value $n(z_b)$, we typically used a small (∼3-mm diameter) planar Faraday probe with a foil guard electrode to measure j_i in the near-plume. The probe was injected with a high-speed motion stage to minimize thruster perurbation, as in §4.2.2. The measurement point was coincident with our most downstream LIF point such that the relation $n = j_i/eu_i$ could be used assuming all ions are singly-charged; this configuration is shown in Fig. 4.13. The collector and guard were usually biased to -40 V to ensure ion saturation. The probe current was measured with a 1-Ω shunt fed into an AlazarTech ATS9462 16-bit, 180 MHz digitizer card. In some cases the probe was also biased with a Kepco BOP-1000M amplifier to acquire full I-V sweeps. Alternatively, we could have used a far-field Langmuir probe to determine the density and extrapolated it to the near-field, but as Eq. (4.10) shows, the inferred $n(z)$ profile is proportional to the boundary density, and so we strove to minimize its error by performing *in situ* measurements.

In this way, n, E_z, and f_{iz} can all be inferred exclusively from LIF measurements and a single downstream density reading furnished by an electrostatic probe. However, there are many challenges in implementing this technique despite its conceptual simplicity. First of all, calculating higher-order velocity moments from measured IVDFs can be difficult due to the exaggerated effect of noise in such calculations, as we described in §4.3.1.3. Second, as noted by Pérez-Luna et al. in their similar derivation [90], the Boltzmann equation moments applied in this way can be prone to singular solutions in E_z or f_{iz}, which means the consequences of inaccurate velocity

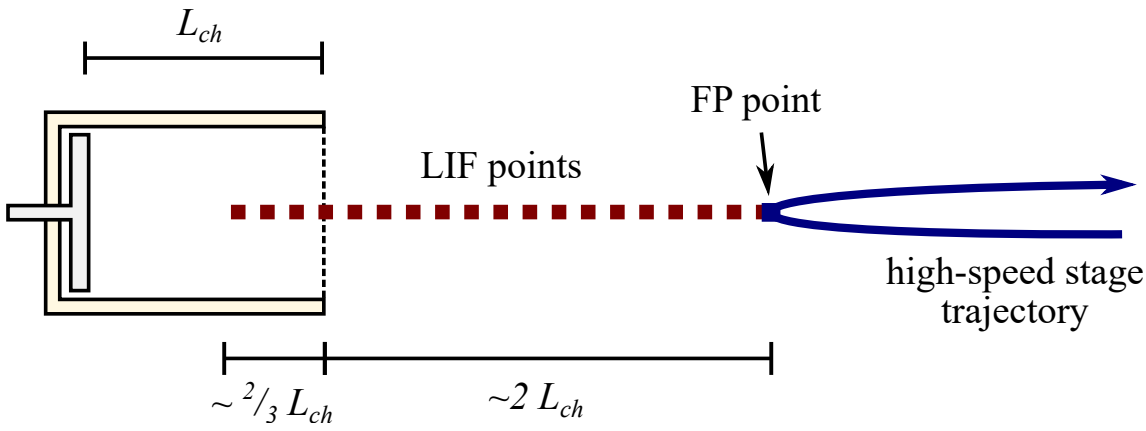

Figure 4.13: A diagram of the measurement configuration, where LIF points are taken inside the channel and in the near-plume, and a single Faraday probe point is taken coincident with the most downstream LIF measurement.

moments can be dire. Altogether, we find that although the calculation of n, E_z, and f_{iz} is computationally simple, the results may be meaningless if the inputs are noisy. Since it is impossible to completely eliminate noise in the LIF measurements, the strategy we took to overcome this issue was to develop a more robust numerical method for solving Eqs. (4.9).

First, we present the raw solutions for E_z, f_{iz}, and f_n, where for simplicity we define the plasma density gradient frequency $f_n \equiv \overline{u_i}\ (d\ln n/dz)$ and we assume that the righthand side of Eq. (4.9c) is negligible:

$$f_{iz} = \frac{d\overline{u_i}}{dz} + \overline{u_i}\left(\frac{-\frac{d\overline{u_i{}^3}}{dz} + 2\overline{u_i}\frac{d\overline{u_i{}^2}}{dz}}{\overline{u_i{}^3} - 2\overline{u_i}\,\overline{u_i{}^2}}\right) , \tag{4.11a}$$

$$f_n = \frac{d\overline{u_i}}{dz} - f_{iz} , \tag{4.11b}$$

$$E_z = \frac{m_i}{e}\left(\frac{d\overline{u_i{}^2}}{dz} - \frac{\overline{u_i{}^2}}{\overline{u_i}} f_n\right) . \tag{4.11c}$$

In practice, we find that the numerator and denominator of the second term in Eq. (4.11a) have a coincident zero-crossing near the peak in f_{iz}. As a result, if any velocity moment is too noisy, f_{iz} can become singular. However, assuming that $\overline{u_i{}^3}$ is

close to its Maxwellian equivalent $3\overline{u_i}\overline{u_i{}^2} - 2\overline{u_i}^2$, we can reformulate f_{iz} as

$$f_{iz} = \frac{- \overline{u_i}\frac{dD}{dz} + N}{D} \tag{4.12}$$

where

$$D \equiv 2\overline{u_i}\overline{u_i{}^2} - \overline{u_i{}^3} \ ,$$

$$N \equiv \frac{d\overline{u_i}}{dz}\left(2\overline{u_i}\overline{u_i{}^2} + D\right) \ .$$

In this form, the numerator is the sum of the gradient of the denominator D and an additional term N. Although this reformulation does not preclude f_{iz} becoming singular, relating the numerator and denominator by D clarifies its non-singular zero crossing as $D = 0$ and $dD/dz = 2\overline{u_i{}^2}(d\overline{u_i}/dz)$. With this information, it is easier to determine what quantity is contributing to singular behavior and smooth it as necessary. With this new formulation for f_{iz}, f_n and E_z remain the same as in Eqs. (4.11b) and (4.11c). Note that the assumption we made on $\overline{u_i{}^3}$ is not physically inspired, but rather it accounts for the fact that $\overline{u_i{}^3}$ is often the noisiest moment calculated and thus tends to be the source of unphysical f_{iz} values.

4.3.3.2 Time-Resolved

For time-resolved ion behavior, note that Eqs. (4.9), being a system of partial differential equations, is implicit for n in t and z. As a result, they cannot be solved explicitly for $d\ln n/dz$. One way to solve these equations is by marching upstream starting with the known downstream boundary density $n(z_b, t)$ and a spatial resolution Δz: for a known $n(z_i, t)$, calculate $dn(z_i, t)/dt$; solve Eqs. (4.9a)-(4.9c) non-conservatively as in §4.3.3.1, yielding $dn(z_i, t)/dz$; calculate $n(z_{i-1}, t) = n(z_i, t) + \Delta z\{dn(z_i, t)/z\}$; repeat at z_{i-1}. This method is easy to implement but is inefficient and can be numerically unstable, as error in upstream measurements can amplify downstream until

the results are nonphysical, especially if any gradients are large over Δz.

Alternatively, Eqs. (4.9) can be written once more as a system of ordinary differential equations that can be solved identically to §4.3.3.1 if we again assume $\overline{u_i{}^3}$ is nearly Maxwellian and that $\partial n/\partial t(\overline{u_i{}^2} - \overline{u_i}^2) \ll n f_{iz} \overline{u_i{}^2}$:

$$f_{iz} = \frac{- \overline{u_i} \frac{dD}{dz} + N + T}{D} \tag{4.13a}$$

$$f_n = \frac{D\overline{u_i}}{Dz} - f_{iz} \tag{4.13b}$$

$$E_z = \frac{m_i}{e} \left(\frac{\partial \overline{u_i}}{\partial t} + \frac{\partial \overline{u_i{}^2}}{\partial z} - \frac{\overline{u_i{}^2}}{\overline{u_i}} f_n \right) \tag{4.13c}$$

where

$$T \equiv \overline{u_i} \frac{\partial \overline{u_i{}^2}}{\partial t} - 2\overline{u_i{}^2} \frac{\partial \overline{u_i}}{\partial t} \ .$$

Notice here that f_n is in terms of the total derivative D/Dz, and thus f_n is defined in a Lagrangian sense. As a result, Eq. (4.10) must be solved along ion trajectories. Here becomes apparent the cost of this technique compared to the iterative solution: the ion trajectories must be determined from $\overline{u_i}(z,t)$ by tracing streamlines in $\{z,t\}$ space, and Lagrangian and Eulerian quantities must be interpolated back and forth between grids. In this way, we have traded numerical instability in the marching scheme for numerical uncertainty due to interpolation. Fortunately, it is easy to implement fairly sophisticated interpolation algorithms that are first-order continuous, which keeps this approach feasible.

Before continuing with this discussion, we should first examine the assumption mentioned previously, $\partial n/\partial t(\overline{u_i{}^2} - \overline{u_i}^2) \ll n f_{iz} \overline{u_i{}^2}$. This is necessary to decouple f_{iz} and E_z from $\partial n/\partial t$ so that the system is ordinary. However, there is little *a priori* insight into whether this assumption is justified. We argue though that when f_{iz} is large, the ionization rate $n f_{iz}$ will be $\sim 10^{23}$ m^{-3}/s, while $\partial n/\partial t$ is at most $\sim 10^{21}$ m^{-3}/s, and thus the inequality holds. When f_{iz} is small, $\overline{u_i}$ tends to be large compared

to the ion temperature such that $\overline{u_i{}^2} \approx \overline{u_i}^2$, and thus the inequality holds for non-zero f_{iz}. In this way, we expect this assumption to be reasonable.

Additionally, we should note that in Eq. (4.13a) we empirically found $N \approx \overline{u_i} dD/dz$, which meant that the change in D over the LIF domain could be approximated as $\int N dz/\overline{u_i}$. This relationship is only exact for cold Maxwellian ions, but even so it provides another way to address singular results other than blindly smoothing noisy velocity moments.

4.3.3.3 Additional Quantities

Aside from n, E_z, and f_{iz}, other plasma and neutral information can be estimated using the IBIS technique. The methods with which these properties are found are not new, but rather the minimally-invasive access to their constituent quantities in the ionization and acceleration regions of a Hall thruster is largely unprecedented. Since proposed breathing mode mechanisms variously involve neutral and electron behavior, it is important to be able to resolve these features aside from the readily-available ion information yielded by IBIS.

Of great interest is the time evolution of neutral density during breathing oscillations. Since the neutral population is anticipated to be mostly Maxwellian, using moments of the Boltzmann equation as described previously is not entirely necessary. Instead, Lagrangian quasi-1D fluid mass and momentum conservation equations are solved, where A_n is the neutral plume cross-sectional area estimated based on semi-hemispheric expansion of neutrals past the exit plane:

$$\frac{Du_n}{Dt} = \frac{nf_{iz}}{n_n} \ , \tag{4.14a}$$

$$\frac{Dn_n}{Dt} = -2nf_{iz} - \frac{u_n n_n}{A_n}\frac{dA_n}{dz} \ . \tag{4.14b}$$

Two boundary conditions are available: the upstream neutral velocity, measured with

Xe I LIF; and the downstream neutral density $n_n(z_b, t)$. This latter value is difficult to measure, as most techniques are too slow and bulky, as in the case of an ionization gauge or heat flux probe [115].

The intensity of the LIF fluorescence signal could be used as a proxy for neutral density if the average density is known somewhere within the LIF measurement domain. The relative emission intensity of fluorescence is a function of the excited state density, which can be related to the ground state density by a constant degeneracy ratio using a two-level excitation model [94]. However, the opacity of the plasma may vary in time as a function of its density and temperature so this approach is expected to be inaccurate. Instead, we estimated our boundary n_n as $f_{iz}/\xi_{iz}(T_e)$, where T_e comes from a phase-averaged HSLP (§4.2.2), ξ_{iz} is tabulated for Maxwellian electrons (cf. Ref. 78), and f_{iz} comes directly from IBIS. Since f_{iz} becomes vanishingly small downstream of the exit plane, this approach can lead to estimates for neutral density that become unphysically small in the near field. In order to provide a lower bound for the estimate, we introduce an offset $\delta f_{iz}/\xi_{iz}$ to the calculated boundary density $n_n(z_b, t)$ such that its average matches that implied by a far-field ionization gauge assuming the neutral gas is accommodated to the chamber walls. Inherently in this correction, we are assuming that the fluctuations in temperature resolved with the Langmuir probe are accurate and only an offset in f_{iz} is present. This assumption is encapsulated with Eq. (4.15):

$$n_{n,b} \approx \frac{f_{iz} + \delta f_{iz}}{\xi_{iz}} \text{ where } \delta f_{iz} = \frac{\langle n_{n,b} \rangle - \langle f_{iz} {\xi_{iz}}^{-1} \rangle}{\langle {\xi_{iz}}^{-1} \rangle} \ . \tag{4.15}$$

Once our boundary value was determined we chose to use a shooting method in calculating n_n: start by guessing a downstream u_n and marching upstream, then repeat this process with new guesses until the upstream u_n matches the values measured with Xe I LIF.

Given the ion information of IBIS and the neutral information discussed in the preceding section, we are also able to estimate several electron properties. Foremost, the temperature T_e can be solved numerically using tabulated values for $\xi_{iz}(T_e)$, where $\xi_{iz} = f_{iz}/n_n$ is inferred from IBIS. If we assume a radially-uniform distribution of discharge current throughout the plasma column, we can also estimate the electron velocity as $u_e = u_i + I_d/(enA_{ch})$ by current continuity, where A_{ch} is the plasma ("channel") cross-sectional area and u_e is defined positive in the upstream direction. It is also possible to estimate the total electron collision frequency with this information, as described in Appendix H.

4.3.3.4 Uncertainty

With a method so heavily dependent on high-order velocity moments and numerical derivatives as IBIS, the uncertainty must be considered. We now present a limited error analysis for the time-averaged IBIS technique (§4.3.3.1), though we suspect the results will be similar for the time-resolved variant.

First, we assume that the uncertainty is dominated by that of the highest velocity moment, $\delta\overline{u_i^3}$, and that the uncertainty of that moment's gradient is given by the second-order finite difference to be $\delta\{d\overline{u_i^3}/dz\} = \delta\overline{u_i^3}/\sqrt{2}\delta z$ where δz is the spatial resolution. We can then simply find the following uncertainties:

$$\delta f_{iz} \approx \left|\frac{\delta\overline{u_i^3}}{D}\right| \sqrt{\left(f_{iz} - \frac{d\overline{u_i}}{dz}\right)^2 + \frac{1}{2}\left(\frac{\overline{u_i}}{\delta z}\right)^2} \tag{4.16a}$$

$$\delta f_n \approx \delta f_{iz} \tag{4.16b}$$

$$\delta E_z \approx \left|\frac{m_i}{e}\frac{\overline{u_i^2}}{\overline{u_i}}\delta f_{iz}\right| \tag{4.16c}$$

We see from these equations that the uncertainty in each quantity is dependent on many velocity moments and their gradients. To make these expressions practically useful, we assume that $f_{iz} \gg d\overline{u_i}/dz > \overline{u_i}/\delta z$ on the grounds that ionization occurs

much faster than ions transit the discharge. Further, for cold Maxwellian ions, we finally find

$$\delta f_{iz} \approx \left| f_{iz} \frac{\delta \overline{u_i^3}}{\overline{u_i^3}} \right| \tag{4.17a}$$

$$\delta E_z \approx \left| \frac{m_i}{e} \overline{u_i} \delta f_{iz} \right| \tag{4.17b}$$

and Eq. (4.16b) still holds. The relatively uncertainty of f_{iz} – and thus E_z and f_n as well – is therefore proportional to that of $\overline{u_i^3}$. The uncertainty of individual velocity moments, touched upon in §4.3.1.3, can be estimated by jackknifing a set of data: iteratively removing single data points and calculating the moment, and then characterizing the width of the resulting moment distribution. Figure 4.14a show an example of $\delta\overline{u_i^3}/\overline{u_i^3}$ for a typical LIF study on a high-power Hall thruster operating at 300 V. Near the exit plane where velocities are lower, the uncertainty can be in excess of 20% but it rapidly drops to $< 1\%$. Reflecting this trend, applying IBIS to similar LIF data from the exit plane to 0.08 L_{ch} downstream we find $\delta f_{iz}/f_{iz}$=9.2%, $\delta E_z/E_z$=4.7%, and $\delta f_n/f_n$=55%. This last uncertainty is unexpectedly high, but in this case it is due to the fact that f_n has a zero crossing and thus $\delta f_n/f_n \to \infty$ even though δf_n is finite.

We have not discussed the uncertainty in n, which requires additional measurements and integration of f_n to compute. Based on the formula of Eq. (4.10), and assuming the only Faraday probe measurement error comes from $\delta\overline{u_i}$ of the coincident LIF acquisition, the uncertainty of n at some point z_i is given by

$$\delta n(z_i) \approx \sqrt{\left(n\delta f_n \sum_{z_b}^{z_i} \frac{\delta z}{\overline{u_i}} \right)^2 + \left(n\delta\overline{u_i} \sum_{z_n}^{z_i} \frac{\delta z f_n}{\overline{u_i}^2} \right)^2 + \left(\delta\overline{u_i} \frac{n(z_b)}{\overline{u_i}} \right)^2}. \tag{4.18}$$

Given that δf_n is a strictly increasing function of $\delta\overline{u_i}$, we expect the first term in the square root to dominate. In this case, $\delta n/n$ is proportional to $\delta f_n = \delta f_{iz}$ as well as

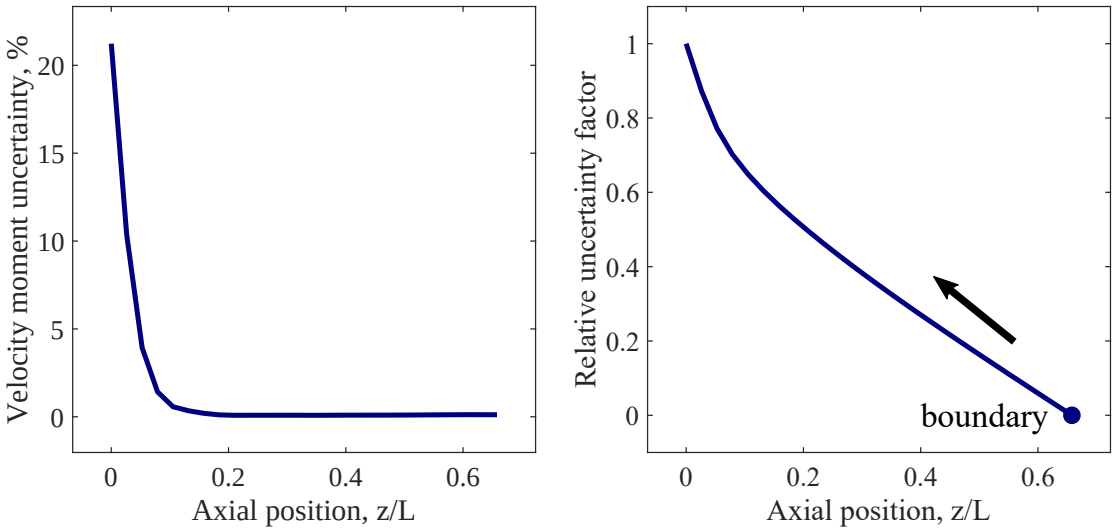

Figure 4.14: The relative uncertainty in the third velocity moment for a sample set of LIF data (a), and the ion transit time uncertainty factor (normalized to unity) for the computation of density (b), where integration is performed upstream from the boundary point near 0.7 L_{ch}.

the ion transit time through the integration domain (given by the summation). The spatial importance in this latter factor is shown in Fig. 4.14b for the same sample LIF data. This factor steadily grows in the plume and rises suddenly closer to the acceleration region. This indicates that the uncertainty in n will continually rise from the downstream boundary point and particularly worsens once u_i drops near the exit plane.

4.3.4 Limitations

The preliminary TRLIF experiment we performed on the H9 as described in Appendix F not only verified that we could measure time-resolved IVDFs fast enough and cleanly enough to capture breathing oscillations without coercing the thruster, but that IBIS could successfully be applied to determine E_z, f_{iz}, and n profiles that appear physically realistic and match anticipated shapes [83]. The main limitations of this technique appear to be practical. In particular, the SNR of the LIF signal can

vary drastically over axial position, breathing phase, and operating condition, so the feasibility of IBIS – especially the reliability of its results – can be hard to predict in advance. Further, others have shown that depletion of the targeted metastable ion population in time-resolved Xe II LIF can lead to spurious attenuation of the fluorescence signal [116]. Finally, in contrast to the OES and HSLP approaches which make "real-time" measurements, our TRLIF implementation is phase-averaged, and thus any transient features will be immeasurable or may even skew the TRLIF results.

4.4 Facility and Thruster

Having described the major diagnostic techniques leveraged in our experimental work, we now review the facilities and thrusters involved. For both we describe typical operating conditions and capabilities. We additionally note any deviations from nominal operation as part of our experiments.

4.4.1 Facility

A majority of our experiments were conducted in the Large Vacuum Test Facility (LVTF) at the University of Michigan. The LVTF is a 6-m diameter, 9-m long stainless steel-clad vacuum vessel. The chamber reaches rough vacuum using four 400-cfm mechanical pumps and two 2,000-cfm blowers. High vacuum is attained with a series of cryogenic pumps. Over the course of this work, the facility was upgraded from an initial seven CVI TM1200i re-entrant cryopumps with LN_2-cooled baffles, to a total of thirteen of these baffled cryopumps and five cryopanels. The maximum pumping speed for LVTF attained during the course of these experiments is approximately 500 kL/s on xenon. The cryopanel pumps were designed in-house [117] following the work of Garner et al. [118]. A sixth cryopanel was installed in an adjoining facility but was not used in any of these experiments. The LVTF is also equipped with a 144 ft^2 louvered graphite beam dump, coolant lines fed by a

recirculating 5-kW 1.5 HP chiller, and several acrylic and quartz viewports for visual access. Figure 4.15 is a photograph of the facility and a diagram of the layout.

(a)

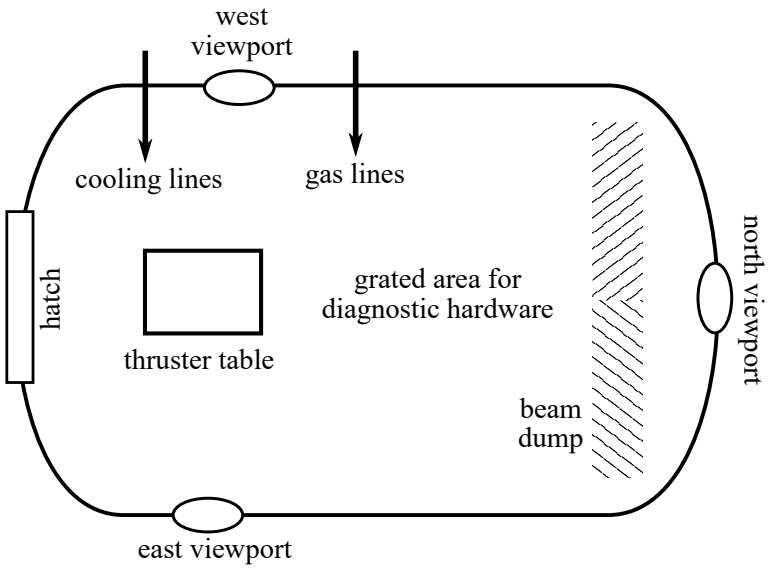

(b)

Figure 4.15: A photograph of the LVTF (a) and a birds-eye diagram of the interior (b).

In this facility, pressure was monitored with a MKS Stabil-Ion hot-cathode Bayard-Alpert ionization gauge, with a specified accuracy on N_2 of 4% and repeatability of 3% (likely similar for Xe). It is well-known that there are multiple sources of error in hot ionization gauges [119], ranging from material to electronic to geometric, with

some reports of as high as 50% repeatability [120], so it is likely these reported values for the Stabil-Ion gauge are underestimates. In LVTF, the gauge was equipped with a "snorkel" and placed roughly 1 m away from the thruster centerline and in the exit plane; this is in agreement with standard practices for electric propulsion testing [121].

4.4.2 Thruster

Nearly all of this investigation was conducted on the H9, a 9-kW magnetically-shielded Hall effect thruster designed by the Jet Propulsion Laboratory, the Air Force Research Laboratory, and the University of Michigan. The design and performance of this thruster are detailed in Refs. 122 and 123, and further it has at the time of writing been the subject of one dissertation [124] as well as a dedicated study of its shielding [125]. As part of this work, it was operated exclusively at 300 V and power levels from 3.5 kW to 6 kW with a cathode flow fraction (CFF) of 7%. At all nominal conditions, the peak-to-peak oscillation amplitude was $\leq$100% the mean discharge current, and these oscillations tended to be broadband but still with significant power at frequencies characteristic of the breathing mode. In many cases, the thruster was operated in an off-nominal but not atypical condition (reduced magnetic field strength) to produce more coherent breathing oscillations. In some studies, the CFF was varied from 5% to 15% to induce changes in oscillatory behavior. The thruster body was set to cathode potential to keep the thruster circuit isolated from ground but also prevent the body from floating too negative and experiencing undue erosion, based on the study of Ref. 126. The thruster was always run in this manner as it is expected that the breathing mode is sensitive to the electrical configuration [126]. Gas flow to the thruster was accomplished with a series of Alicat MC series mass flow controllers, calibrated with a Drycal Bios Definer finite-volume measurement unit, and fed with 99.9995% pure xenon. For most experiments in this work, the operating

pressure in LVTF for the H9 was <5 μTorr-Xe. In a pressure study accompanying the CFF experiment, the pressure was raised to 20 μTorr-Xe by turning off some cryopumps and flowing extra xenon into the chamber downstream of the thruster (directed toward the beam dump). A photograph of the H9 installed in the chamber and in operation is shown in Fig. 4.16.

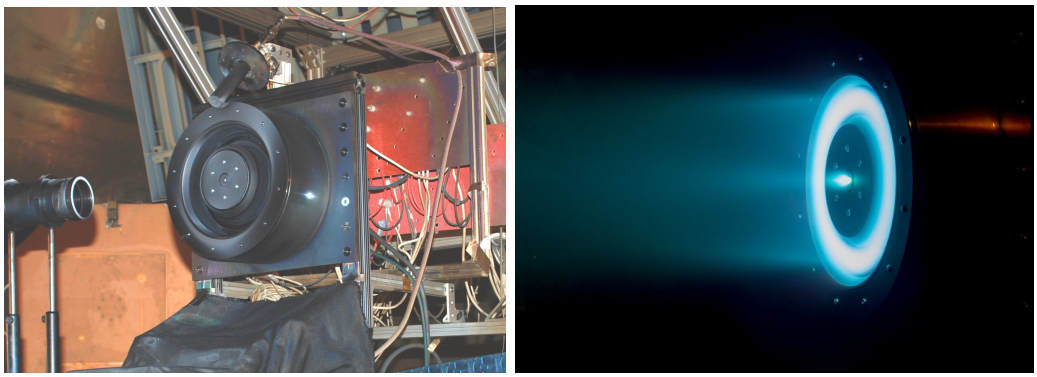

(a) (b)

Figure 4.16: The H9 installed in LVTF for an LIF experiment (a) and firing (b).

4.5 Summary

In this chapter, we presented the theoretical and practical aspects to our implementation of a time-resolved laser-induced fluorescence technique paired with an ion Boltzmann implicit solution method. As part of this, we discussed the anticipated uncertainty and limitations of this tool and elaborated further based on preliminary experimentation in Appendix F. We also summarized our evaluation of two other high-speed diagnostic techniques to determine if they were suitable for characterizing the breathing mode. Optical emission spectroscopy was found to be too insensitive, and high-speed Langmuir probing too perturbative. Time-resolved laser-induced fluorescence paired with IBIS was shown to overcome both of these issues, as well as allow many more plasma and neutral parameters to be inferred.

CHAPTER V

Evaluation of Existing Theories

5.1 Introduction

In this chapter, we will present the experimental efforts taken in the present investigation of the breathing mode. The aim of this work was to evaluate the physical accuracy of existing descriptions of this instability. We present the results of preliminary time-averaged data collection with the TRLIF-IBIS technique developed in the previous chapter. This experiment was aimed at testing the frequency scaling of the models discussed in §3.4. The insights gained by that experiment were then used for more extensive time-resolved testing, as described in §5.4. In §5.5 we summarize our experimental findings so as to motivate the analytical studies in the following chapter.

5.2 Methodology

To understand the successes and failures of existing breathing mode theories, we proceed to characterize the breathing mode experimentally. Given the challenges discussed in §3.5, the goal of this part of the present investigation was to apply a chosen diagnostic to furnish the information needed to evaluate existing theories. But since diverse mechanisms are attributed to the breathing mode in the literature, it was important to afford some flexibility in our experimental approach, and thus we

conducted both time-averaged and time-resolved experiments. The following are the major steps taken in our experimental work:

(i) *Time-averaged data collection*: Preliminary data was collected to evaluate the frequency scaling of existing models. Specifically, we made time-averaged measurements of the thruster in different oscillatory conditions, and then compared the predicted breathing frequencies to those measured. In this way, we evaluate the predictive power of the existing theories.

(ii) *Time-resolved data collection*: Time-resolved data is collected for a single operating condition to compare the dynamic properties of the plasma to those dictated by existing theories. In this way, we investigate the fundamental assumptions of these theories to determine if any are physically realistic. In particular, we examine which quantities fluctuate, the spatial extent of fluctuations, and the phase relationships between quantities.

5.3 Time-Averaged Study

Haven previously chosen and refined the TRLIF-IBIS technique for characterizing the breathing mode, we first apply it to evaluate the frequency scaling of various theories of these oscillations. In particular, we focus on the predator-prey model and the resistive instability. This selection provides a diverse representation of breathing mode hypotheses: the predator-prey model is the most prominent breathing mode description, and the resistive instability is a less-studied but still quantitative hypothesis that stands in stark physical contrast with the predator-prey model. In §5.3.3.3, we also discuss the possibility of a neutral gas instability, which is a strictly qualitative hypothesis that is unstudied but physically intuitive. To evaluate the scaling of these existing breathing mode theories, we determine steady-state plasma and neutral quantities as a function of breathing frequency, and then use these parameters to

predict the frequency according to each model. The accuracy of each theory can be assessed by comparing the predicted frequencies to the measured values. By doing this for multiple operating conditions, the frequency trends dictated by each theory can also be evaluated. This allows us to explore the predictiveness of the considered theories, which is of prime interest for a practical understanding of the breathing mode.

In this experiment, we performed time-averaged Xe I and Xe II LIF in the LVTF on the H9 at 300 V, 4.5 kW with nominal magnetic field strength. Unlike the typical configuration, here the cathode was mounted externally at the 12 o'clock position for reasons unrelated to this experiment; this should not be germane to our oscillation studies, as previous work did not reveal a consistent trend in oscillation amplitude with varying cathode position [127]. The LIF domain for Xe I was the upstream half of the channel, and for Xe II it was from the exit plane into the near plume. We varied the cathode flow fraction ψ from 5% to 15% to induce changes in the breathing frequency, and LIF data and discharge current telemetry was taken at each ψ condition. We chose here to vary the CFF because previous studies have shown that changes in near-field pressure affect the discharge [64], yet we expect only subtle variation in large-scale thruster operation compared to if we varied, e.g., discharge voltage or magnetic field strength [13].

5.3.1 Approach

With this time-averaged LIF data, the breathing frequency as a function of CFF can be estimated based on the predator-prey model and the resistive instability of Chables and Rogier. These values can then compared to the measured breathing frequency at each CFF condition to evaluate how well each mechanism describes the instability in terms of magnitude and trend. In this way, we either identify an existing theory to use as we continue our investigation, or we gain insight into what

mechanisms should be ignored.

To quantify the scaling fidelity of each model, we determine the correlation coefficient and null probability between predicted frequencies $\omega(\psi)$ and the corresponding measured values $\omega_0(\psi)$. The correlation coefficient r is here defined as the ratio of the covariance of the two frequencies to the product of their standard deviations σ and σ_0,

$$r = \frac{\sum(\omega - \overline{\omega})\sum(\omega_0 - \overline{\omega_0})}{\sigma\sigma_0} \ , \tag{5.1}$$

where the sums are over all samples of ω or ω_0. As an example, when $\omega = \omega_0$ such that there is perfect correlation, the numerator of Eq. (5.1) becomes ${\sigma_0}^2$; since $\sigma = \sigma_0$ in this case, the correlation coefficient is therefore 1. In general, r can be: positive, suggesting a theory is accurate; negative, indicating a theory is inaccurate; or near zero, suggesting the instability was absent or the measurements were too insensitive to yield a trend in the breathing frequency. We also consider the p-value of the correlation,

$$p = 2\int_{t^*}^{\infty} \frac{\Gamma\left(\frac{N}{2}\right)}{\sqrt{\pi(N-1)}\Gamma\left(\frac{N-1}{2}\right)} \left[1 + \frac{x^2}{N-1}\right]^{-\frac{N}{2}} dx \text{ for } t^* = \frac{\overline{\omega - \omega_0}}{\sigma} \ , \tag{5.2}$$

where x is the integration variable, Γ is the gamma function, and N is the number of samples of ω and ω_0. This quantity represents the probability of observing the same correlation by random chance according to a t-distribution.

With so few data points, it is arguable whether the correlation coefficient and null probability are meaningful. They clearly have little statistical significance with such a small data set but we contend they are still representative of the correlation between the measured and predicted frequencies. It can be shown that the absolute correlation coefficient $|r|$ is equal to unity when there are only two data points available. However,

with only three points r becomes

$$r = \frac{16{c_1}^2(\Delta x)^2 + 30c_1c_2\Delta x + 15{c_2}^2}{15{c_2}^2} \tag{5.3}$$

where $2c_1$ is the curvature of the ω data and c_2 is its slope. In this way, r is sensitive to trends in the nonlinear data and is still a meaningful measure of the linear correlation. Likewise, the null probability p is still reflective of the likelihood of the correlation being due to chance, although with fewer points we expect to rarely refute the null hypothesis. For this reason, $p > 5\%$ may be ignored in the following analyses, while $p < 5\%$ is indicative of good correlation. The standard 5% significance level is used for this threshold.

5.3.2 Results

We now present the results of this time-averaged experiment. First we show the discharge current telemetry and Faraday probe measurements. The TRLIF-IBIS results supplemented by those diagnostics is then presented. Finally, we consider the measured discharge current spectra more carefully, investigating the possibility of a mode transition as CFF was varied.

5.3.2.1 Discharge Current and Electrostatic Probe

Figure 5.1 shows a discharge current spectrum for the nominal ψ=7% condition, as well as the variation in peak frequency and spectral width with CFF. Also shown is the variation in breathing frequency with background pressure for the 7% condition. A similar trend is apparent in both cases, implying that variation of ψ is mostly a pressure effect. In contrast, if changing the CFF led to profoundly different cathode operation – as we wished to avoid by choosing CFF as our independent parameter – we might expect the two trends to differ. We observed that the dominant low-frequency

peaks in the spectra tended to be log-triangular, and so assuming there was a single breathing peak, the breathing frequencies were found by performing a two-line fit to the relevant portion of the power spectrum. This spectral shape also implies that the waveform has a cnoidal shape, which is often associated with nonlinear solitary waves [128]. However, as the breathing frequency decreases the spectral width also decreases, indicating that the waveform is broadening toward a sine-like shape. A high-frequency peak ∼50 kHz is also apparent in the discharge current spectrum; this is likely a cathode mode [19].

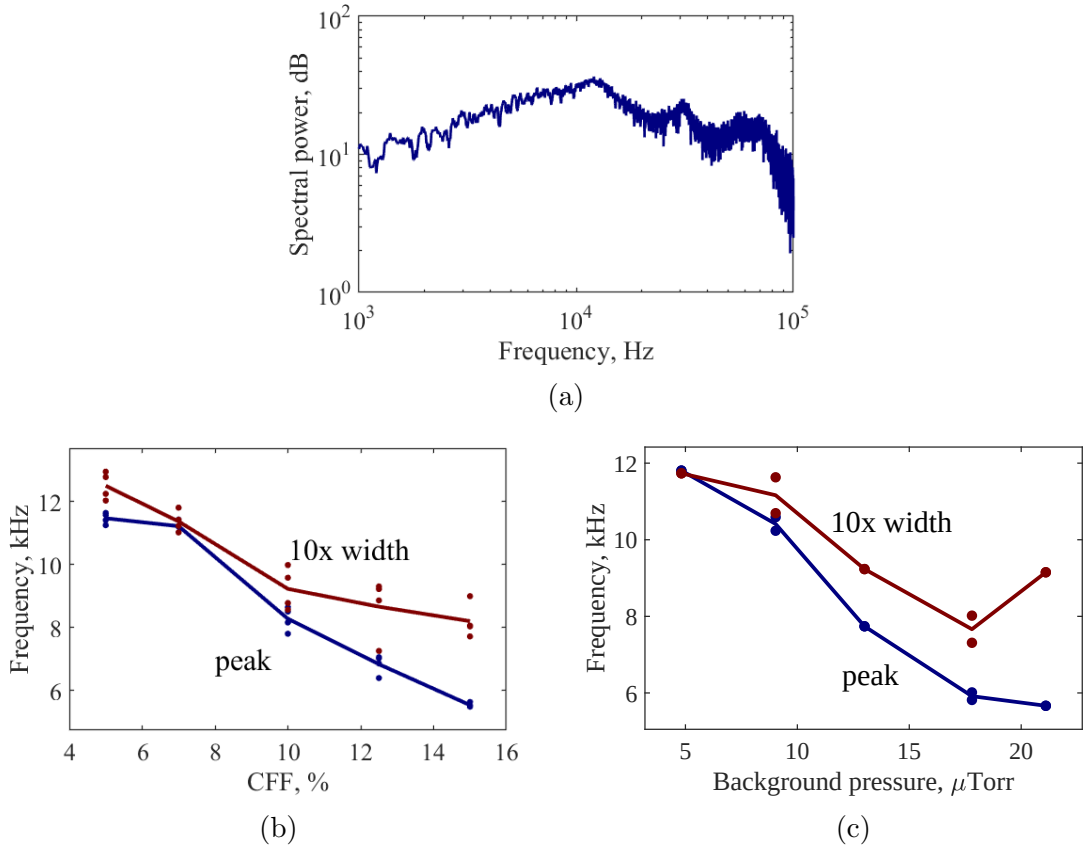

Figure 5.1: The nominal discharge current spectrum (a) and the variation of peak frequency (blue) and width (red) with CFF (b) and background pressure (c).

In the time-averaged experiments, only (relatively) far-field Faraday probe data was collected, so extrapolation was performed to provide a boundary measurement for IBIS. Figure 5.2 shows the ion current density j_i on channel centerline as a function

of axial position, as well as an extrapolation to the most downstream LIF acquisition point in this experiment. The extrapolation is performed assuming z^{-2} scaling, which corresponds to the ion beam expanding conically. The extrapolated value is found to be 124 mA/cm^2. The "anode limit" – that is, the nominal uniform discharge current density at the anode – is included for reference, where exceeding that limits implies that current is concentrated on channel centerline, as anticipated.

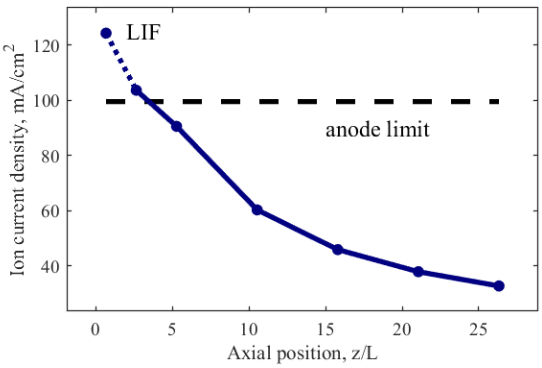

Figure 5.2: The ion current density measured with the Faraday probe as a function of axial position.

5.3.2.2 TRLIF-IBIS

Figure 5.3 shows the mean velocities for ions and neutrals as measured with LIF. The profiles for a few different ψ conditions are shown. It appears that the ion velocity increases almost uniformly as ψ increases, while a trend in the neutral profiles is harder to discern. The shift in the ion profiles agrees with a previous study that concluded the changes in neutral density as a result of varying the CFF are responsible for shifts in the acceleration region location [64]. Altogether, these profiles suggest that the discharge is indeed changing with the breathing frequency as cathode flow fraction is varied.

The result of applying IBIS is shown for 5%, 10%, and 15% CFF in Fig. 5.4. As ψ increases, the location of peak f_{iz} and E_z both shift upstream, and a somewhat similar trend is apparent in f_n. Similarly, f_{iz} and E_z become narrower with increasing

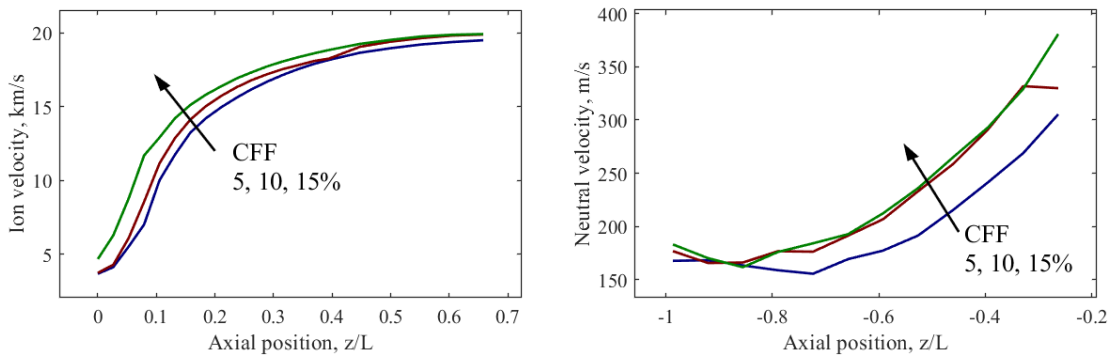

(a) (b)

Figure 5.3: Mean velocity profiles for ions (a) and neutrals (b) for a few different CFFs.

ψ. Using LIF, Faraday probe, and far-field ionization gauge measurements together, downstream boundaries for n and n_n are computed to be 3.9×10^{17} and 1.4×10^{18} m^{-3} respectively; with this information, both density profiles can be inferred. The computed density profiles are shown for the same CFFs in Fig. 5.5. The neutral density profiles are included merely for the sake of comparison; they are not used in any further analyses and we expect them to be slightly inaccurate since they do not account for changes in gas flow with increasing ψ.

5.3.2.3 Mode Transition

The f_{iz} and E_z profiles in Fig. 5.4 suggest that both the ionization and acceleration zones, as judged by the peak locations of f_{iz} and E_z, shift slightly upstream with decreasing frequency (increasing ψ), and that the spacing between them also appears to diminish. In this way, all available length scales are decreasing as ω increases, which means to retain any semblance of the conventional predator-prey scaling of Eq. (3.3) – which is held to be qualitatively true in the literature – u_n must be increasing with ω. However, we observed a decrease in u_n and an increase in T_n almost uniformly throughout the Xe I LIF domain as ω increased. In the absence of kinetic effects, we imagine that the neutral flow should be dictated by the anode temperature (initial ve-

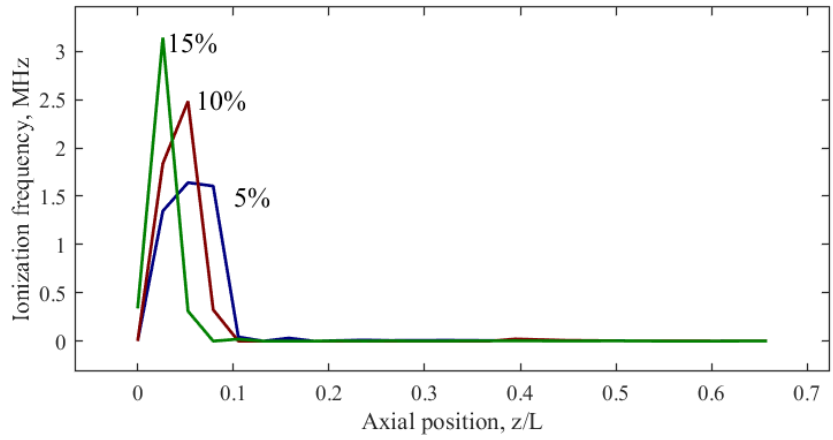

(a)

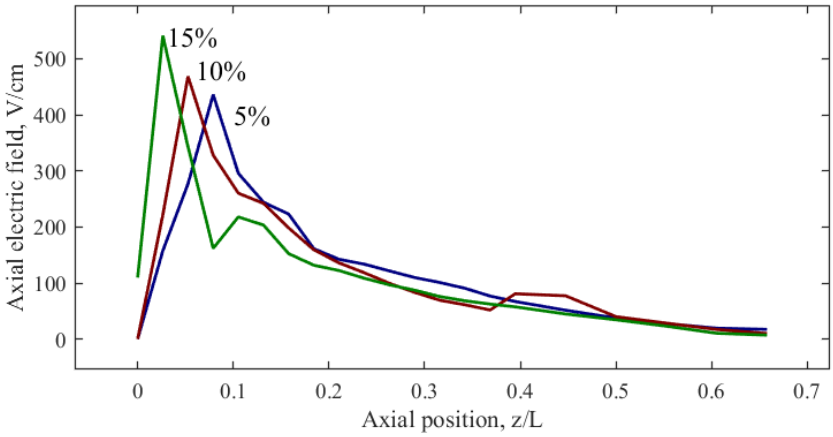

(b)

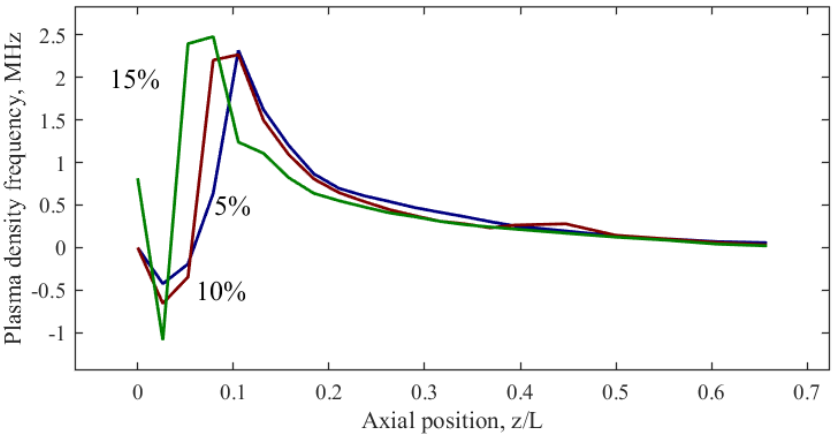

(c)

Figure 5.4: The quantities determined from the Boltzmann moment analysis, including ionization frequency (a), axial electric field strength (b), and plasma density frequency (c) for a few CFFs.

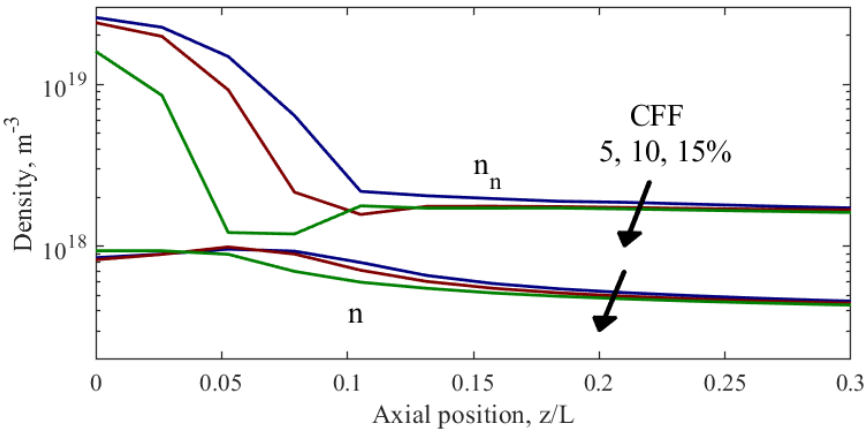

Figure 5.5: The ion and neutral density profiles for a few CFFs.

locity), wall temperature (Rayleigh acceleration), and background pressure (Bernoulli acceleration). When examining the standard thermal telemetry collected during this experiment, we found no evidence of a consistent change in thruster temperature with CFF. Further, we expect that there should be a shrinking pressure differential across the channel as ψ increases, which means u_n should decrease. Since none of these hydrodynamic effects are consistent with our measurements, the evolution of u_n with CFF must be dictated by kinetic effects. For example, with increasing cathode flow one might expect more warm neutrals to enter the channel, which would reduce the neutral velocity by introducing a negative (anode-ward) population to the velocity distribution, in agreement with dedicated neutral flow studies that have demonstrated a deceleration of the neutral "jet" emerging from the channel [98]. However, Fig. 5.3 does not reflect this trend either, which may indicate that a more complicated effect is controlling u_n.

Instead of exploring the kinetic aspects of the neutral flow further, upon closer inspection of the neutral velocity curves shown in Fig. 5.3 we find there are two distinct flow regimes: a low-velocity one at low ψ, and a high-velocity one at high ψ. In the former, ω appears to be insensitive to ψ, while in the latter it decreases as ψ increases. Interestingly, the transition between these modes corresponds to changes

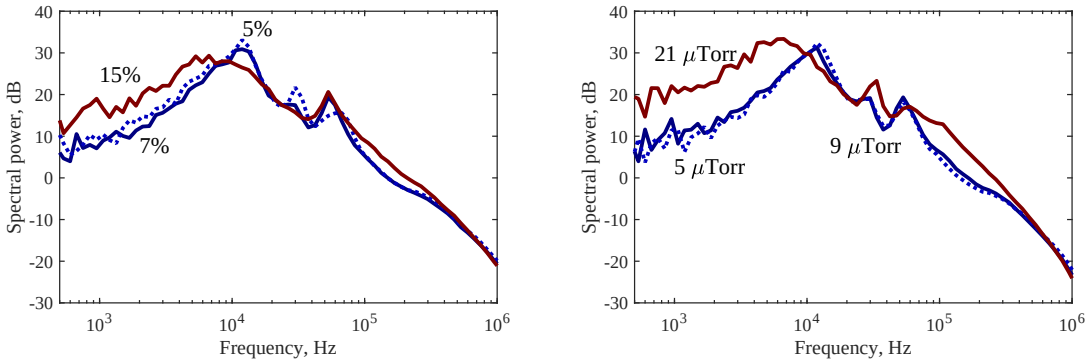

(a) (b)

Figure 5.6: The discharge current spectrum for varying CFFs (a) and background pressure (b), where the blue curves represent one mode and the red another. The dotted blue curve is "deeper" into the first mode than the solid one, such that transition occurs between the two solid curves.

in the discharge current spectrum. Figure 5.6a shows the spectrum at 7% and 15% CFF, acquired 20 minutes apart during an hours-long campaign. There is significant broadening of the dominant peak for high ψ, with slightly greater low-frequency (<1 kHz) and high-frequency (0.1-1 MHz) power. Also shown in Fig. 5.6a is the 5% CFF spectrum, which demonstrates an evolution of the high-frequency content even before this transition point. Specifically, at low ψ there is a non-harmonic peak between the breathing mode and cathode mode but as ψ increases this peak diminishes. Figure 5.6b shows the discharge current spectrum for various background pressures, where similar spectral changes are apparent, suggesting that this is largely a pressure effect. Comparing the 7% and 15% CFF spectra, the total power in the breathing mode, defined as the power within the cnoidal FWHM of the dominant peak, does not change much: 57 to 54 dB, respectively. However, there is clearly a significant loss of coherence and a shift of spectral power strongly toward lower frequencies and weakly to higher frequencies. The power below 1 kHz increases by 18% compared to that in the breathing mode, and the high-frequency power increases by about 11%.

It is difficult to reconcile these spectral changes with the marked transition in the neutral velocity profile, although we have at least established that it is likely a kinetic

effect. One possibility is that the changes in u_n are mediated by selective ionization in the channel (c.f. Ref. 101), which is itself a function of the ionization rate throughout the channel and thus dependent on the plasma. As a result, changes in the near-field neutral environment can be communicated to the internal neutral flow via the plasma. For example, changes in T_e as the local pressure increases can affect the ionization rate deeper in the channel as electrons stream toward the anode, which could alter the amount of selective ionization and thus apparently accelerate/decelerate the neutral gas. We have neither enough data from this experiment nor insight into this suggested process to confirm it, but we do believe that there is at least a correlational relationship between spectral changes and the transition in u_n.

In total, although we originally hoped to have five CFFs at which we could compare the measured ω to the value predicted by various breathing mode theories, there is evidence to suggest that the 5% and 7% cases and the 10%-15% cases represent separate modes that cannot be equally compared. Further, ω for the former cases shows little sensitivity to CFF, so we focus on the 10%-15% cases. However, if we examine these high-ψ spectra closely as in Fig. 5.7, we see that the broadening of the breathing peak is actually a bifurcation of the dominant solitary peak observed at low ψ. If we programmatically locate these two constituent peaks using a three-line fit (double-cnoidal), we find that the higher-frequency one apparently continues the trend of the low ψ spectra, as also shown in Fig. 5.7. For this reason, we consider these higher-frequency peaks when examining the frequency scaling of breathing mode theories. Note that this means we now have the opposite trend of Fig. 5.1: the breathing frequency is steadily increasing with ψ, not decreasing.

5.3.3 Discussion

Now that the raw results have been reviewed, we systematically apply them to existing breathing mode theories and evaluate the scaling relationship in ω that re-

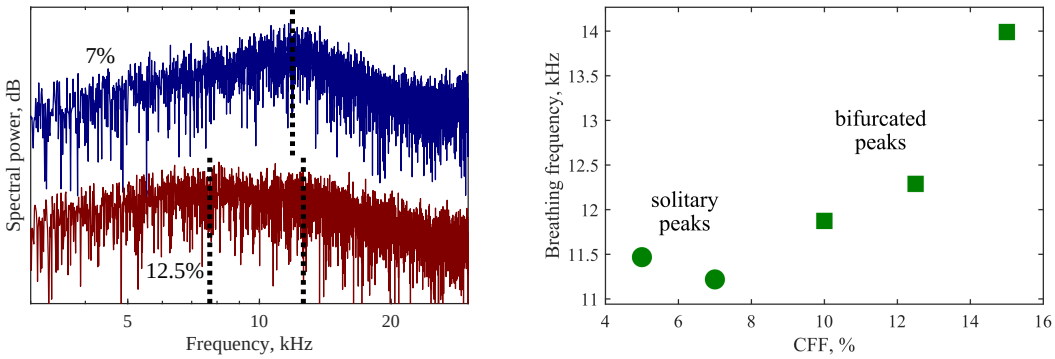

(a) (b)

Figure 5.7: A comparison of the 7% and 12.5% discharge current spectra (a), where a bifurcation into two peaks appears in the latter, and the variation of breathing frequency with CFF (b) where the higher-frequency peak is used for high CFFs.

sult. We begin with the classical predator-prey model, where we consider two possible length scales. We then examine the resistive instability description, in which the growth rate throughout the LIF domain is calculated. Finally, we consider the possibility of a neutral gas instability.

5.3.3.1 Classical Predator-Prey

To evaluate the frequency scaling of Eq. (3.3), realistic choices for u_i, u_n, and L must first be made. For L, the characteristic length of the discharge, we consider two possible and physically reasonable definitions: the total channel length and the length of the combined ionization-acceleration region.

The exact definitions of the ionization and acceleration regions are vague, so in this work we identify them based on the f_{iz} and E_z profiles, since both of these typically have a defined peak and diminish to zero on either side of it. Several different techniques were used to characterize the mean location and width of the ionization and acceleration zones based on these quantities. In some cases, the LIF data did not capture the upstream edge of a region, so the peak in f_{iz} or E_z was used as the nominal location of their respective regions. When greater extents of LIF data

were available, the spatial mean for either could be used; for instance, the location of the acceleration region z_{acc} can be calculated as

$$z_{acc} = \frac{\int z E_z dz}{\int E_z dz} \ . \tag{5.4}$$

Alternatively, the location at which half of all ions are produced and the location where half of the potential drop has occurred can be used to identify the ionization and acceleration zones, respectively. As an example of the latter case, for a measurement domain $\{z_1,\, z_2\}$ the acceleration region location $\overline{z}_{acc}$ is defined by

$$\frac{1}{2}\int_{z_1}^{z_2} E_z dz = \int_{z_1}^{\overline{z}_{acc}} E_z dz \ . \tag{5.5}$$

For the ionization region, E_z is replaced with nf_{iz}/u_i. The fundamental difference between z_{acc} and $\overline{z}_{acc}$ is that the former is based on the spatial distribution of potential energy density while the latter is based on non-specific potential energy. We therefore do not use the $\overline{z}_{acc}$ definition much in this work because we suspect it is less sensitive to the shape of E_z.

The width of the regions were calculated either as the FWHM when LIF measurements were limited, or as the spatial RMS otherwise. Again for the acceleration region, the RMS width w_{acc} can be found as

$$w_{acc} = \sqrt{\frac{\int (z - z_{acc})^2 E_z dz}{\int E_z dz}} \ . \tag{5.6}$$

Like before, one could also define $\overline{w}_{acc}$ as the axial region centered on $\overline{z}_{acc}$ that contains 50% of the potential drop, such that $\overline{w}_{acc} = w_{acc,2} - w_{acc,1}$ where

$$\frac{1}{4}\int_{z_1}^{z_2} E_z dz = \int_{z_1}^{w_{acc,1}} E_z dz \tag{5.7}$$

and

$$\frac{3}{4}\int_{z_1}^{z_2} E_z dz = \int_{z_1}^{w_{acc,1}} E_z dz \ . \tag{5.8}$$

But as before, we do not rely on this definition much because it is less sensitive to the shape of the f_{iz} and E_z spatial profiles.

Figure 5.8a shows both the ionization and acceleration regions as measured with the LIF based on the techniques we just described. Displayed are the mean location of f_{iz} (which tends to coincide with the peak in f_{iz}), z_{iz}, and the range between the peak in E_z and its mean location z_{acc}. Note that the two regions are quite close together relative to the extent of the acceleration region. In practice, we define the combined ionization-acceleration region to extend from $\overline{z_{iz}} - w_{iz}/2$ to $\overline{z_{acc}} + w_{acc}/2$.

Using these definitions, Eq. (3.3) can be compared to the observed breathing frequency. This is shown in Fig. 5.9 where L is either the channel length ("long," ∼10 mm) or the ionization-acceleration region length ("short," ∼1 mm). Also included is a dashed line of perfect correlation. The calculated magnitudes for the "long" case are quite reasonable but for "short" they are an order of magnitude too large. For the short and long predator-prey model the correlation coefficients are 0.73 and 0.93 with null probabilities of 48% and 24%, respectively. This means that both length scales produce good correlation, especially using the channel length ("long"). But the predator-prey model is fairly insensitive to CFF, the slope for the "long" case only 0.3 Hz/Hz, and as expected it is difficult to say that these trends are statistically significant. In total, though, the frequency scaling dictated by the predator-prey model can be consistent with the experimental data when L_{ch} is used as the characteristic length.

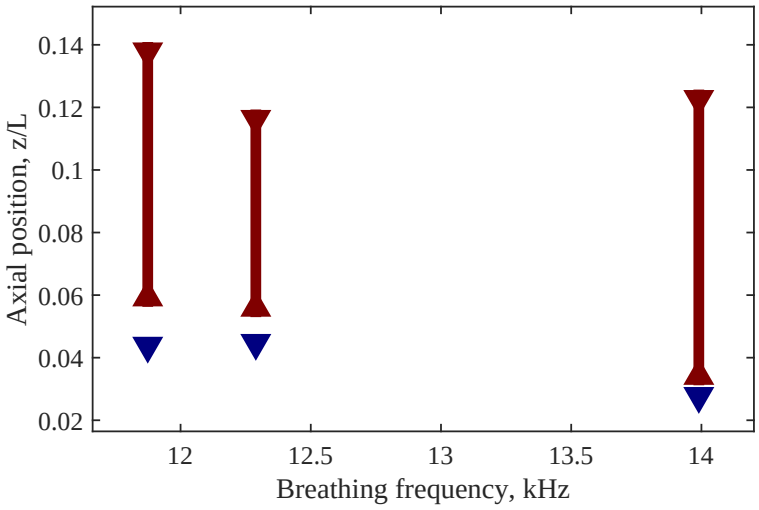

(a)

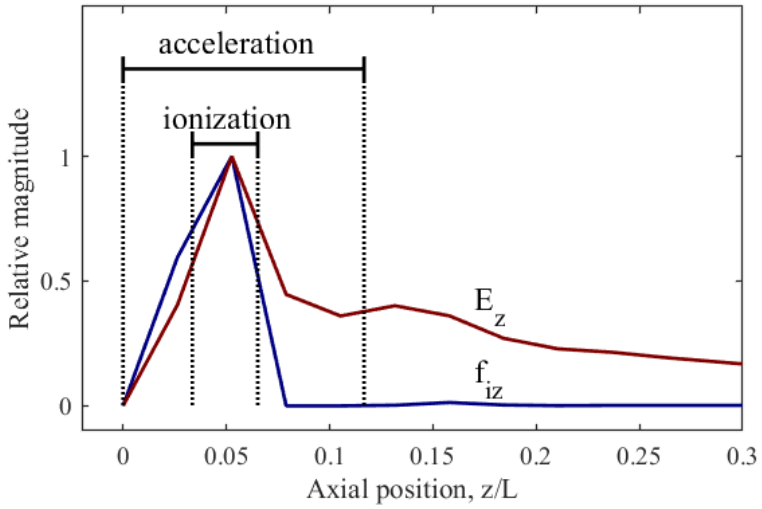

(b)

Figure 5.8: (a) The ionization and acceleration regions, where in the latter the location of peak E_z and mean E_z are delineated. (b) An example of determining the width of the ionization and acceleration regions, here for the nominal 7% CFF condition.

5.3.3.2 Resistive Instability

Unlike the predator-prey model, the dispersion for the resistive instability has a spatial dependence such that it is sensible to evaluate Eq. (3.6) at all points throughout the measured domain. Figure 5.10a shows the growth rate predicted by this model for a few CFF conditions. The growth peaks in the near plume, weakening

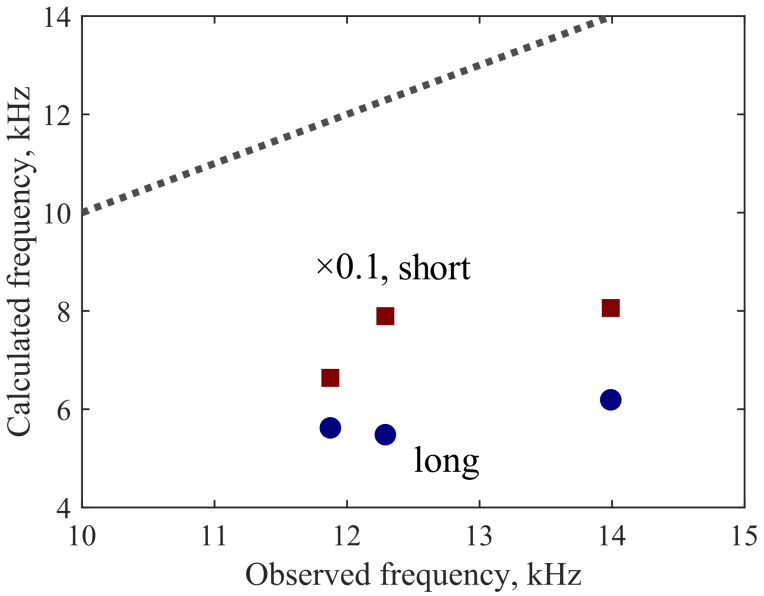

Figure 5.9: A comparison of the frequency predicted with the predator-prey model using a long and short length scale.

farther downstream and in the ionization-acceleration region. This is in agreement with Chables and Rogier's assessment that this mode should stabilize when electron mobility is very high (downstream) or very low (upstream). Instead of comparing the real part of Eq. (3.6) to the breathing frequency, we argue that it is more physically meaningful to examine correlation with the growth rate of the resistive instability. This is because, as Chables and Rogier implied in their work, the resistive instability merely drives a much slower ionization instability. We propose here though that the growth rate of the resistive instability does in some way dictate the breathing frequency: if the resistive instability grows quickly, predator-prey-like thickening of the plasma and depletion of neutrals can occur faster. Figure 5.10b shows the relative peak growth rate of the resistive instability as a function of the observed breathing frequencies. As Fig. 5.10a indicates, the growth rates tend to be much higher than the measured breathing frequencies, so in Fig. 5.10b they have been normalized to the mean breathing frequency, and a line of perfect correlation has been included. There is weak correlation between the growth rate and the measured breathing frequency,

r=0.59. Likewise, the null probability is calculated to be 60%, which would normally indicate that it is highly likely that any correlation measured is spurious. In total, the resistive instability, although potentially supported in a Hall thruster, correlates only fairly well with measured ω and thus likely does not set the pace of breathing oscillations.

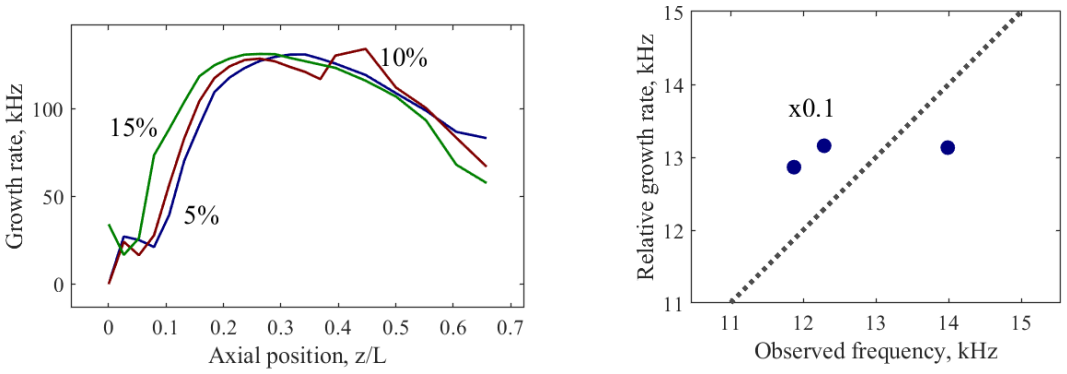

(a) (b)

Figure 5.10: The growth rate (a) and the 0.1x peak growth rate versus breathing frequency (b) for the resistive mode. A line of perfect correlation is shown in the second plot for reference.

5.3.3.3 Neutral Gas Instability

A more qualitative hypothesis for the origin of the breathing mode, which we neglected to discuss in Chapter III because it is relatively unstudied, is a neutral gas instability. That is, the transitional neutral gas flow in the thruster channel may inherently support an instability that couples to the plasma for growth. The primary intuition behind this explanation is that the scaling of the breathing frequency often seems to relate to the neutral transit time across the channel, implying that neutrals play some strong role in the process. Further, even the earliest Western studies of Hall thrusters [129] indicated that these devices often slowly hopped between stable and unstable (breathing) operation, on the order of minutes or tens of minutes, which most likely corresponds to a thermal effect. This implies that the oscillations are

either controlled by neutrals that thermally accommodate to the channel walls and anode, or by electrons via temperature-dependent secondary electron emission from the channel walls. The latter possibility is unlikely given that the breathing mode is observed in magnetically-shielded thrusters, where electron flux to the walls is small. This leaves the neutral population as the more probable participant in governing low-frequency oscillations. Some existing theories of the breathing mode, such as a higher-order ionization instability (§3.4.4), may involve neutral gas waves propagating in the thruster channel, but in those cases they are coupled to an ionization instability, whereas here we suppose that fluctuations in ionization are exclusively a result of neutral oscillations.

A possible candidate for a neutral gas instability would be the thermoacoustic instability, described analytically by Lord Rayleigh [130]. These oscillations are found in a wide variety of combustion systems where standing acoustic waves are supported by the device geometry. Physically, this mode involves the evolution of a standing sound wave with an anti-node located at a heat source. If the heat flow into the working gas is in phase with the sound wave, the wave amplitude will grow until nonlinear saturation. In this way, the energy for low-frequency oscillations would derive from heat transfer from the electron population to the neutral gas. Although the thermoacoustic instability is only one example of a wide variety of hydrodynamic fluctuations potentially supported in Hall thrusters, there has been little experimental study of the neutral population. Perhaps this is justified, as the neutral gas population in a Hall thruster has been shown to demonstrate little time-dependent behavior [63].

The fact that so little quantitative work has been done exploring neutral gas instabilities in Hall thrusters is itself the first obstacle in embracing this explanation of the breathing mode as there are no criteria with which to validate it against experimental data. Aside from that, there are still some qualitative aspects of this hypothesis that discredit it. First, the neutral population in the thruster channel is known to

be transitional [101] and thus the continuum instabilities studied extensively in combustion systems are not necessarily applicable. Further, the evolution of the neutral flow is heavily influenced by kinetic effects [98], yet fluid codes can still resolve low-frequency fluctuations. Even further, some codes use a reduced set of fluid equations for the neutral population and still find breathing-like features [28]. Even if those inconsistencies are ignored, a time-resolved laser study of the neutral population in a Hall thruster found very little fluctuation of the mean velocity [63], which limits the modes by which the neutral gas could support an instability. However, this does not rule out the possibility of a neutral gas instability, especially since no studies have verified these findings.

Another point that strains the likelihood of this model is that a neutral gas instability presupposes that *all* of the known relationships between plasma properties and low-frequency oscillations are correlational and not causal. That is, to influence the breathing mode any changes in plasma properties must primarily influence neutral properties. For example, decreasing the magnetic field strength influences how well electrons are trapped in the acceleration region, but this must also somehow change the neutral flow so as to induce the changes in oscillation amplitude that are well known to occur with diminishing B_r [13]. Some relationships are indeed expected to be correlational – for instance, changes in the ionization rate will influence the density of the neutral population – but in general these relationships are unclear. For example, Mazouffre et al. numerically verified the influence of facility background pressure on the evolution of the neutral gas flow in a Hall thruster but did not experimentally validate this effect, leaving the relationship between the two opaque [98]. As a result, even though it is possible that the relationship between low-frequency oscillations and the thruster plasma is exclusively correlational, there is insufficient study of this topic to verify this fact.

Determining the viability of a neutral gas instability as an explanation of the

breathing mode is difficult because there is no quantitative theory for comparison with the experimental data. However, there are a few neutral properties that can be examined. Figure 5.11a shows the neutral transit frequency from anode to ionization region compared to the observed breathing frequency. Also included are estimates of the bounds of this curve due to the fact that the Xe I LIF data does not extend to the ionization region. The correlation is high, $r > 0.99$ and $p < 2\%$, and the frequencies are the correct order of magnitude. However, the trend is not very sensitive, with a slope of only 0.17 Hz/Hz. Figure 5.11b shows the acoustic frequency for continuum neutral sound waves compared to the observed breathing frequency, with bounding curves as in Fig. 5.11a. Again the magnitudes are nearly correct, but here the correlation is strongly negative, -0.98, and the null probability higher, 11%. The neutral acoustic transit rate is therefore a poor description of the breathing frequency.

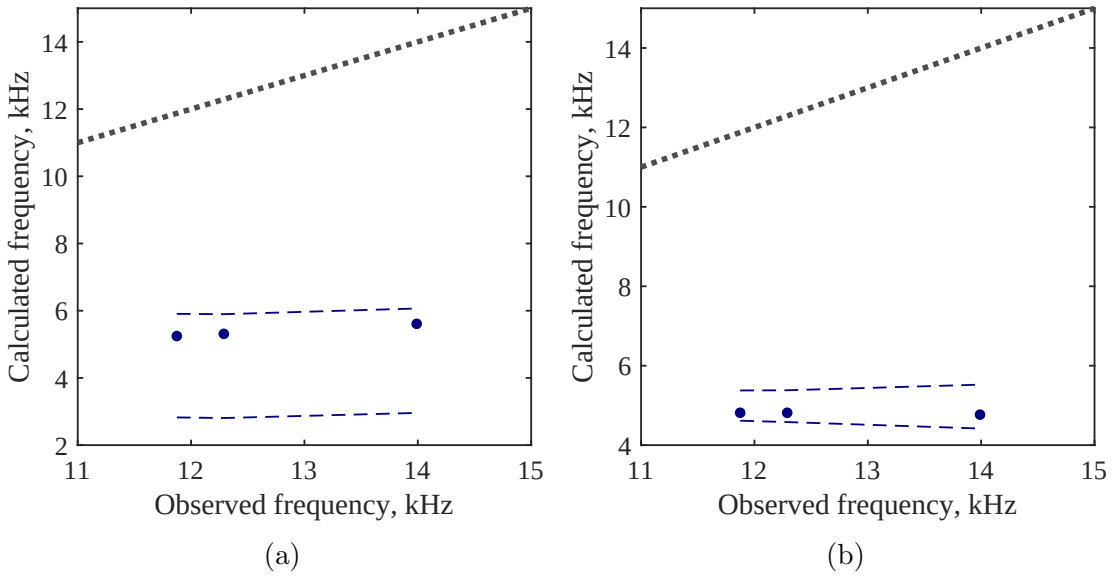

Figure 5.11: The calculated neutral transit frequency (a) and acoustic frequency (b) compared to the observed frequency. The dashed bounding curves account for the fact that Xe I LIF was not performed all the way to the ionization region.

At first glance, this is an encouraging result: the breathing behavior observed experimentally is described well by a neutral drift wave traveling from the anode to the ionization region. However, the origin of these waves is unclear – some unan-

ticipated upstream process must be occurring to produce neutral gas perturbations. As it stands, then, there is some evidence of an inherent neutral gas instability (as understood within the scope of this experiment), and in particular the strong neutral drift scaling confirms the important role the neutral population likely plays in the breathing process, but the details of this process are still unclear.

5.4 Time-Resolved Study

For a more in-depth investigation of breathing behavior, time-resolved LIF was performed in the LVTF on the H9 at 300 V, 3 kW, and 75% magnetic field strength. Unlike in §5.3, all data is taken at a single operating condition but over a greater spatial extent. Xe I LIF is performed roughly in the range z/L_{ch}={-1, -0.25}, and Xe II LIF in z/L_{ch}={-0.25, 0.75}. In this way, the two LIF schemes nearly overlap each other, and the Xe II domain extends far enough downstream for a practical overlap with electrostatic probes.

5.4.1 Approach

Whereas we only considered the frequency scaling of the predator-prey, resistive instability, and neutral instability descriptions of the breathing mode in §5.3, we are now able to examine the dynamic properties of these hypotheses. First, we must outline the major testable predictions and assumptions of each model. For the predator-prey model, we consider three main criteria: the presence of plasma density fluctuations in the ionization region, at most a 90° lag between plasma and neutral density, and spatial independence of the oscillations. By this last criterion we mean that, as a zero-dimensional model, the predator-prey mechanism supposes that the oscillation is born in the ionization region and advects downstream through the acceleration region. It therefore requires that any spatial dependence of low-frequency oscillations are secondary to this process anchored in the ionization zone.

For the resistive instability, due to the qualitative coupling between Chables and Rogier's Buneman instability and the much slower ionization instability, there are few criteria to identify. However, their hypothesis requires that electric field fluctuations lead those of the ionization rate. It is also implied, given that they describe a dispersive wave, that the maximum resistive growth rate should occur near the ionization region. In addition, the fluid resistive derivation of Koshkarov et al. suggests that ion current must lag electron current to support the instability.

A neutral gas instability has not been explored thoroughly in the literature, and so there are no quantitative criteria available. However, at a minimum it requires fluctuations in neutral properties, presumably upstream of the ionization region. Further, a characteristic neutral frequency – like the rate of neutral sound wave propagation across the channel – should align with the breathing frequency.

5.4.2 Results

First we present trends in breathing frequency from high-speed discharge current measurements. Next, the electrostatic probe results – to provide boundary conditions for IBIS – are presented. Finally, time-resolved LIF results for both Xe I and Xe II, and the accompanying IBIS computations, are shown.

5.4.2.1 Discharge Current

Figure 5.12 shows characteristic discharge current waveforms and frequency spectra at the nominal 300 V, 15 A operating condition and the more oscillatory mode used in this study. For all LIF measurements, the frequency varied from 16.0 to 16.6 kHz and the spectral peak width varied from 0.2 to 0.6 kHz. The breathing frequency was closer to 17.7 kHz for Faraday probe measurements, the difference likely owing to perturbation of the thruster by the proximity of the probe. However, the discharge current waveforms were similar with and without the probe, and the change

in the mean discharge current due to the probe's presence was below 1%, so this discrepancy does not portend a fundamental change in breathing behavior. As in Appendix F, to overcome any changes in breathing frequency between data sets, all results are considered in terms of phase of a breathing cycle. All probe quantities are phase-averaged using the discharge current signal, yielding probe results as a function of phase. Similarly, the TRLIF data is presented as a function of the phase of the discharge current signal (from which the gated integrator was triggered).

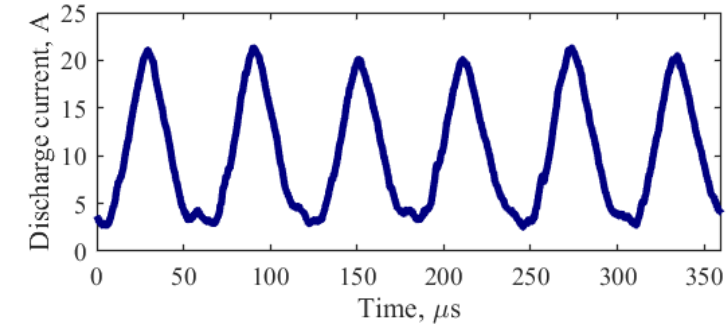

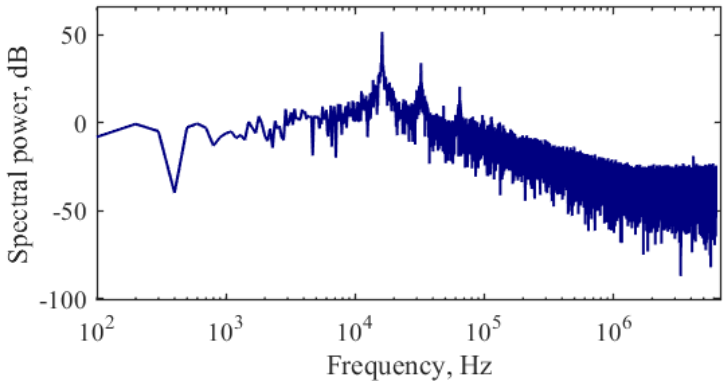

(a)

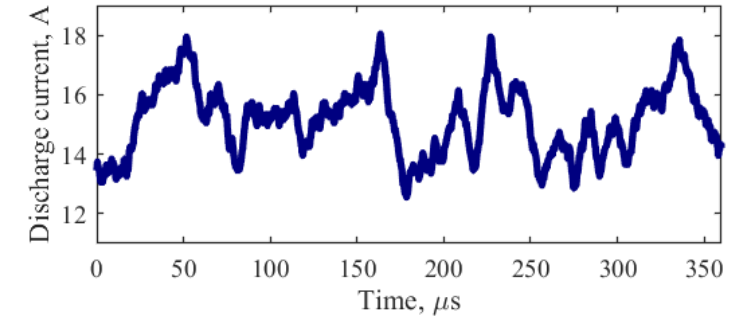

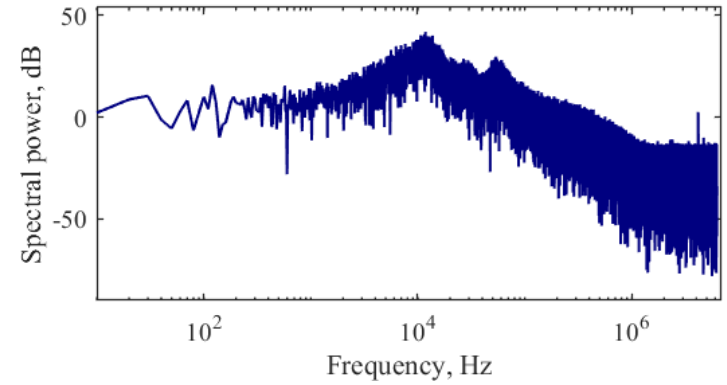

(b)

Figure 5.12: Representative waveforms (top) and spectra (bottom) at reduced magnetic field strength (a) and at nominal strength (b) for the H9.

5.4.2.2 Electrostatic Probe

A sample raw and phase-averaged Faraday probe signal is shown in Fig. 5.13. Also included is the phase-averaged discharge current signal as a function of breathing cycle phase, which acts as the reference signal. An equivalent raw probe current and phase-averaged temperature while operating as a Langmuir probe are also shown in Fig. 5.13. High-speed probe current measurements were made at a range of voltages and synchronized to produce time-resolved I-V traces, from which electron temperature was estimated, even though the probe was collecting ram current in this configuration [131]. For both the Faraday and Langmuir probe cases, the raw data is fairly noisy but eventually phase-averages to a smooth curve that has clear correlation with the discharge current.

5.4.2.3 Time-resolved LIF

Figure 5.14 shows the instantaneous mean velocity profiles for ions and neutrals yielded by TRLIF, with the discharge current as reference. We show three representative phases, which correspond to the discharge current increasing, decreasing, and bottoming out (i,ii, and iii) in Fig. 5.14c. The ion velocity profile changes markedly in shape and amplitude throughout a breathing cycle, while the neutral velocity profile does not change significantly or consistently.

5.4.2.4 IBIS

By applying the methodology described in §4.3, the ionization frequency, axial electric field, plasma density, neutral density, and electron temperature can all be estimated. Figure 5.15 shows these quantities at the same phases identified in Fig. 5.14c. Several important features can immediately be recognized. There is intense ionization in the discharge current trough (*iii*), with a corresponding spike in electric field strength, spike in electron temperature, and flattening of the plasma density

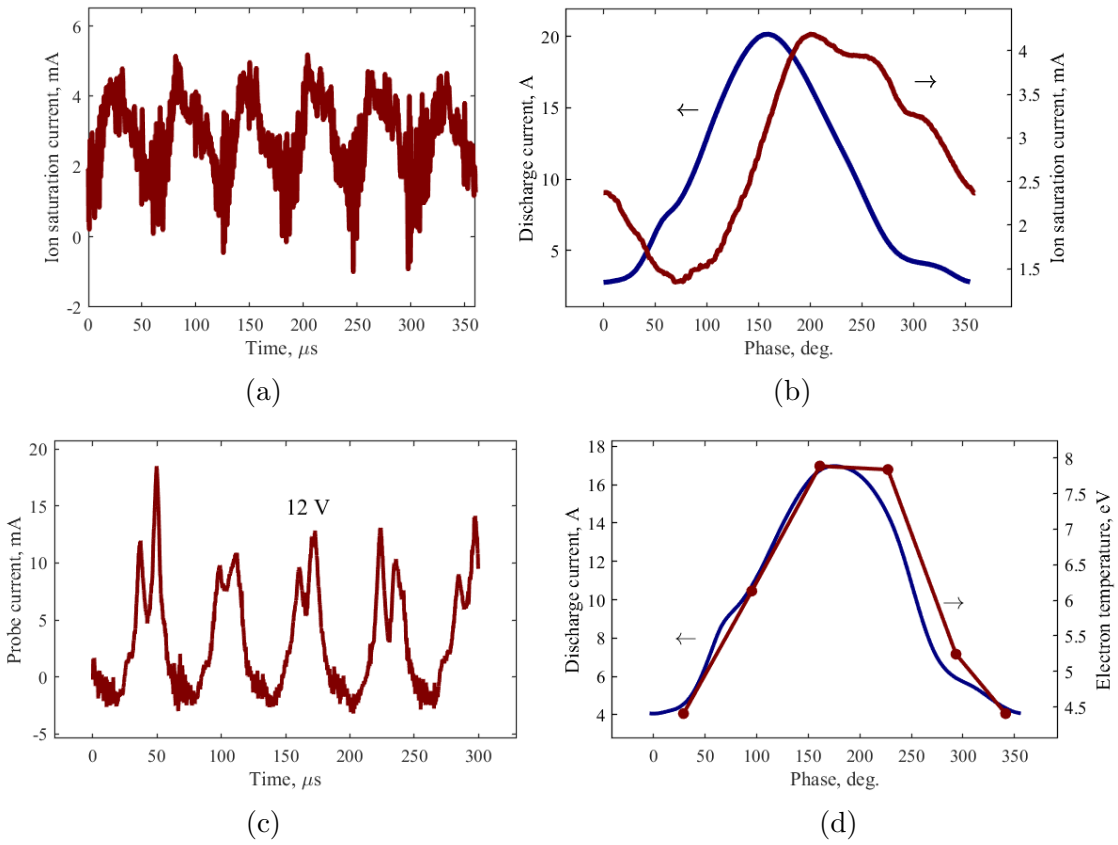

Figure 5.13: A representative Faraday probe current waveform (a) and the phase-averaged signal (b); and a sample Langmuir probe current waveform (c) and phase-averaged temperature resulting from synchronized I-V traces (d).

profile. Additionally, the neutral density profiles – inferred from IBIS, not measured directly with LIF – clearly show a perturbation traveling downstream with the neutral gas. The waves appear triangular downstream owing to the relatively broad (5-10 mm) spatial resolution of LIF measurements there.

Near the crest in the discharge current signal (*i* and *ii*), the ionization frequency, electric field, and electron temperature profiles are all low and wide. Due to the sensitivity of the method used to estimate T_e, this flattening leads to noisy temperature profiles at some phases, barely showing any semblance of the characteristic peak in temperature that typically coincides with the peak in E_z [78]. Altogether, Fig. 5.15 indicates that the discharge is dense but cool at the crest in discharge current and hot but sparse at the trough.

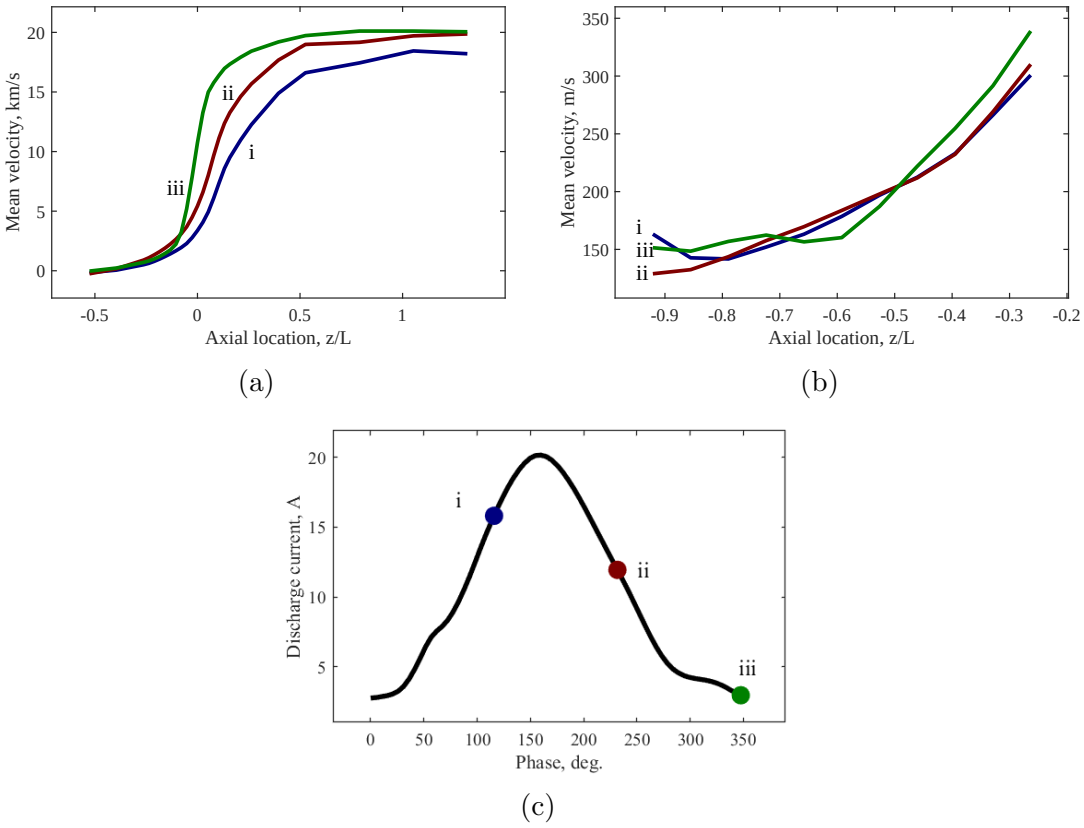

Figure 5.14: The ion (a) and neutral (b) mean velocity profiles at select phases of the discharge current (c).

Given the profiles in Fig. 5.15, the ionization and acceleration regions can be defined as the spatial mean of the ionization frequency and electric field, respectively, as discussed in §5.3.3.1. Figure 5.16 shows the position of these regions over a breathing cycle, again with Fig. 5.14c as a reference. Also shown is the width of each region identified as the weighted standard deviation of each quantity from the mean location. Both regions move outward and widen toward the peak in the discharge current. Of the quantities shown in Fig. 5.15, their average value within the acceleration and ionization regions can be computed and tracked over a breathing cycle; as a sample, Fig. 5.17 shows the normalized neutral density in the ionization region versus f_{iz} (a) and the normalized plasma density in the acceleration region versus E_z (b).

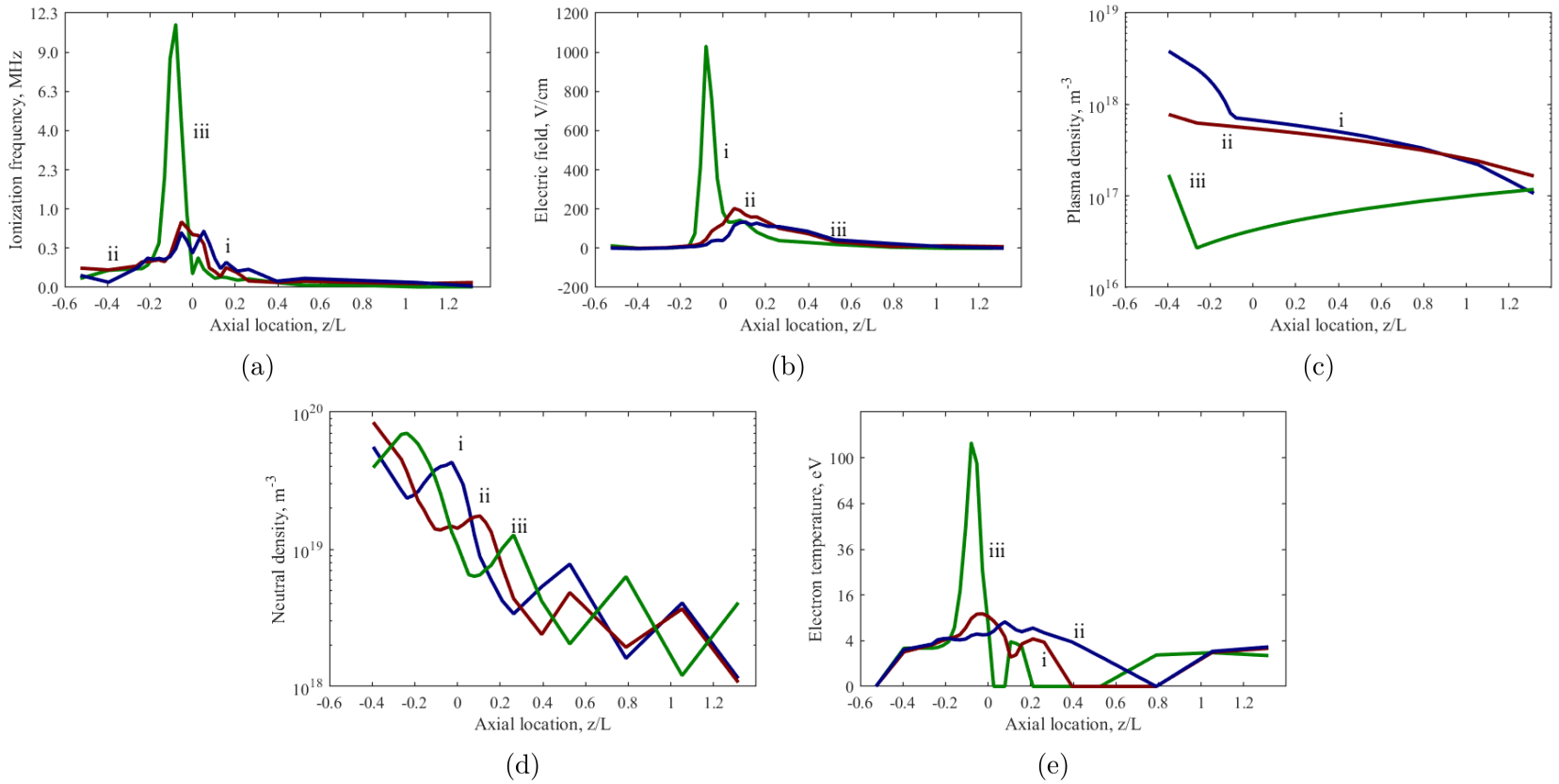

Figure 5.15: The ionization frequency (a), axial electric field strength (b), plasma density (c), neutral density (d), and electron temperature (e). Note that b and e have an ordinate power scale.

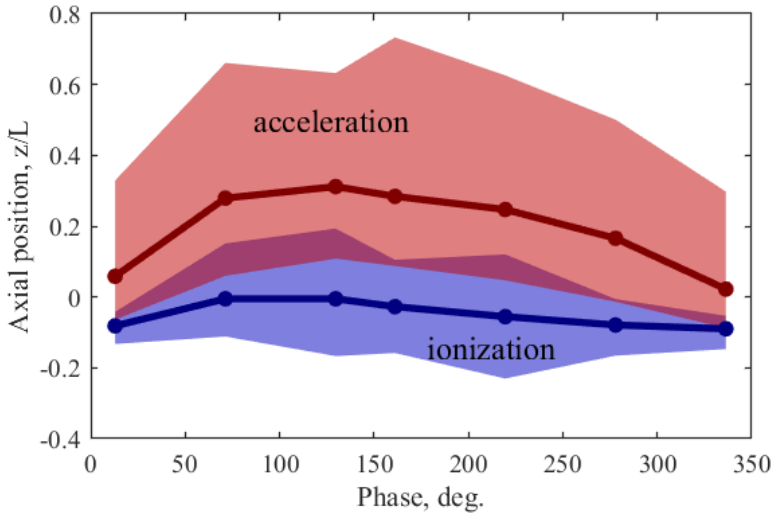

Figure 5.16: The fluctuation in ionization and acceleration region location with breathing phase.

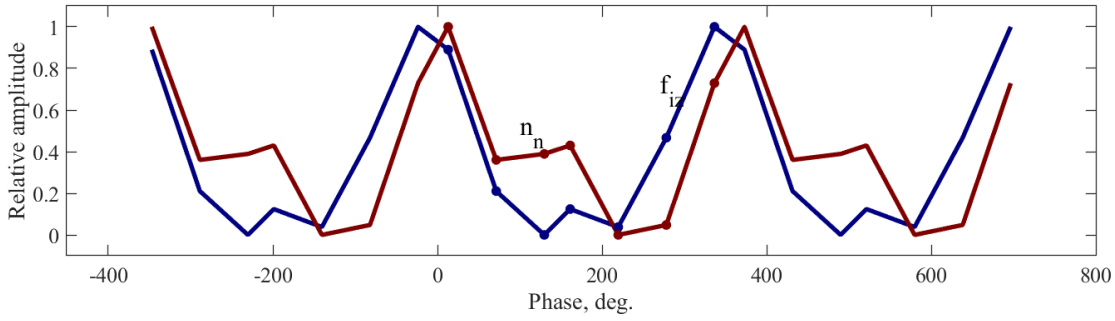

(a)

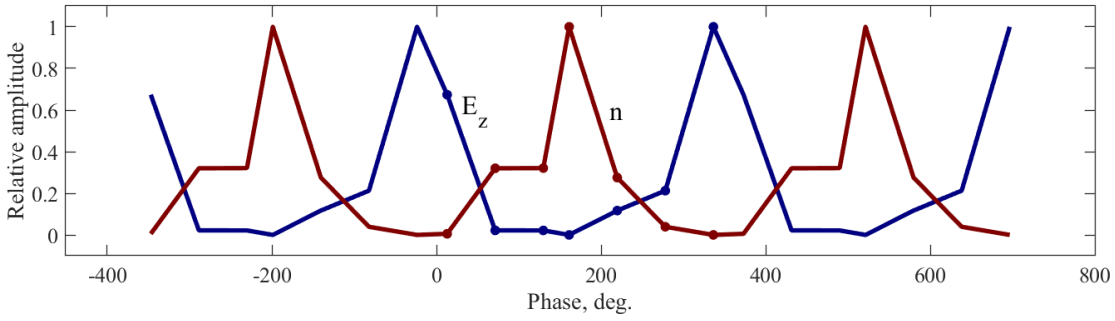

(b)

Figure 5.17: Relative fluctuations in plasma and neutral properties in the ionization region (a) and the acceleration region (b). The data from a single cycle (0 to 360°) is repeated three times (-360 to 720°) to convey the periodicity of the signals.

5.4.2.5 Phase Relationships

The strength and phase offset between the fluctuations in the calculated plasma and neutral parameters are plotted in Fig. 5.18. The phase lag relative to f_{iz} in the ionization region and E_z in the acceleration region is determined by comparing the lowest-frequency phase angles of the Fourier transforms of the waveforms. The rudimentary uncertainty for these phases $\delta\theta$ relies on the following expression, shown e.g. with n, where Δz is the discrete spatial uncertainty in the LIF measurements and $\mathcal{F}$ denotes the Fourier transform:

$$\delta\theta = \tan^{-1}\left[\frac{\Delta z \sum \frac{\partial n}{\partial z}}{\mathcal{F}(n)(\omega)}\right] \quad . \tag{5.9}$$

Similarly, the relative amplitude of the fluctuations is evaluated as the ratio of the lowest-frequency amplitude to the DC amplitude of the Fourier transform. Figure 5.18a indicates that there are a variety of phase relationships observed between these quantities, including: n and u_i are in phase in the ionization region but not the acceleration region; n is completely out of phase with f_{iz} and E_z; T_e is in phase with E_z; and n_n has some small phase lag behind f_{iz}. Figure 5.18b shows that f_{iz} has the relatively strongest fluctuation followed by n in both regions, while u_i had the weakest fluctuation in both.

5.4.3 Discussion

We now compare our time-resolved measurements to the criteria we outlined in §5.4.1. We start with the classical predator-prey model, which involves the examination of phase speeds and relationships between densities. Next, the resistive instability is assessed. Finally, a neutral gas instability is revisited, where the physical implications of the neutral drift waves detected in this experiment are considered.

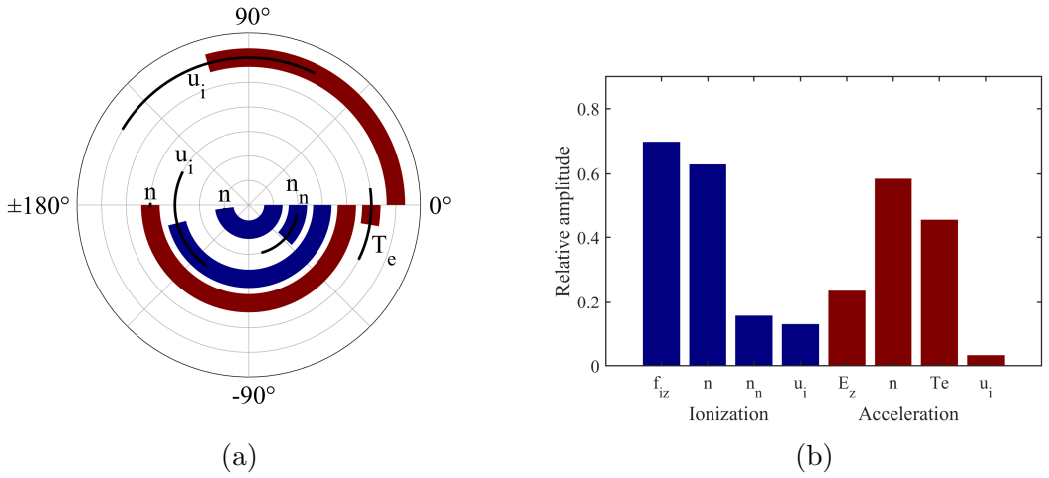

(a) (b)

Figure 5.18: Phase lag of various quantities in the ionization region (blue) versus f_{iz} and in the acceleration region (red) versus E_z (a), and the amplitude of fluctuations relative to the mean for these regions (b).

5.4.3.1 Classical Predator-Prey

Given the phase information presented in §5.4.2.5, we can now quantitatively evaluate the physical assumptions of the predator-prey model. Having clearly found that all measured plasma parameters fluctuate during a breathing cycle, we are left to examine two main features of the model: that it is spatially-independent, and the phasing of the plasma and neutral density.

To evaluate the spatial independence of the observed oscillations, the plasma density phase speed (given by $\omega d\theta_n/dz$ for the plasma density phase θ_n) can be investigated as a function of axial position. Figure 5.19 shows the spatial evolution of this quantity. The predator-prey model anticipates the oscillations originating from a single region – presumably near the ionization and acceleration zones – and propagating downstream with the ions. Thus also included in Fig. 5.19 is the mean ion velocity, which should be identical to the phase speed of any spatially-independent fluctuations. There are several significant features of this plot. First, the phase speed of n greatly exceeds u_i over a large range. Second, the trends in the speeds do not agree – the density phase speed reaches a peak near the acceleration region and then

slows down rapidly. Finally, the phase speed varies unexpectedly upstream of its peak. Altogether, the discrepancies between the two curves suggest that the oscillation is not spatially independent. This is incompatible with a zero-dimensional model, though it is in agreement with the work of Barral and Ahedo discussed in §3.4.4.

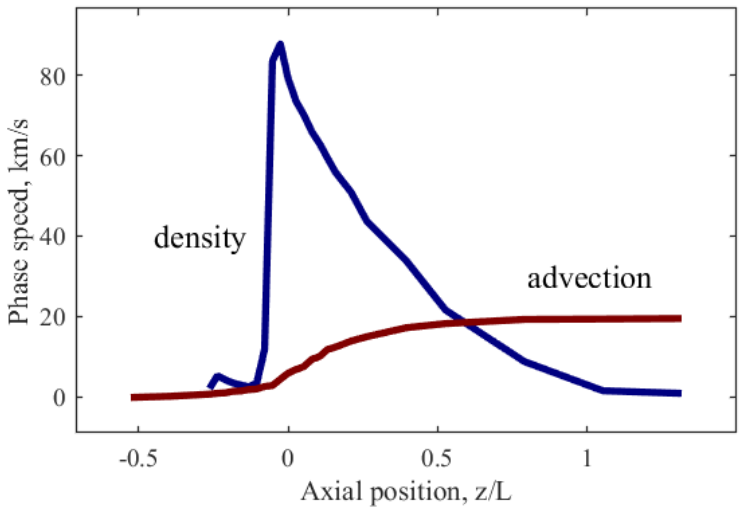

Figure 5.19: The variation in plasma density phase speed versus the axial position compared with the anticipated advection phase speed.

Next, the phase relationship between plasma and neutral density can be examined. Although Fig. 5.18a shows the phases of both quantities in the ionization zone, we acknowledge that the definition of this region is vague. It could be represented by (1) the spatial mean of the ionization frequency profile, (2) the spatial mean of the electric field strength profile, or the location of the peak in (3) f_{iz} and (4) E_z. In order to be comprehensive in our comparison, we consider the phase delay between the relevant plasma properties at all four locations. It is also of interest to consider their relationship throughout the entirety of the ionization and acceleration zones since the 0D predator-prey model combines these areas together and only distinguishes between quantities entering and inside this singular tract. Figure 5.20 shows the representative spatial evolution (relative to the mean ionization-acceleration location) of the lag of n_n behind n. We find that n_n leads n in the ionization region but slightly lags as

acceleration peaks. This is largely incompatible with the neutral and ion continuity equations of the predator-prey model, which assume constant ionization rate and a 90° phase delay in densities.

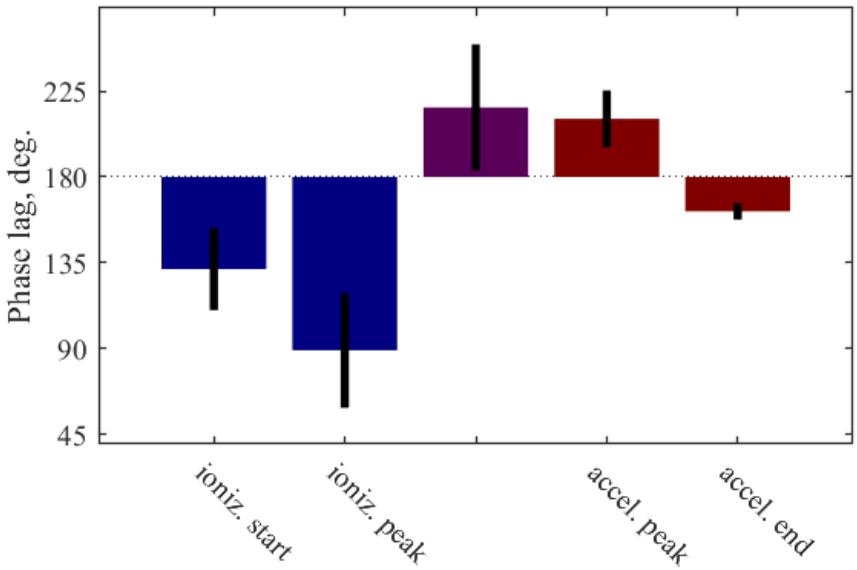

Figure 5.20: The evolution of the phase difference between neutral density and plasma density fluctuations throughout the ionization-acceleration region. Bars are shown as lags relative to a 180° offset (completely out of phase).

In summary, the predator-prey model does not agree with measurements in terms of its spatial dependence or the phase relationship between densities. As a result, we find that the zero-dimensional predator-prey mechanism as it is typically formulated does not accurately portray the dynamics of the breathing mode.

5.4.3.2 Resistive Instability

Next we evaluate the resistive instability description of the breathing mode, which downplays ionization. To reiterate the discussion of §3.4.3, this is a Buneman instability: counter-streaming ions and electrons experience a two-stream instability, modified by the presence of a perpendicular magnetic field, that gives rise to fluctuations in the local electric field. In a fluid derivation by Koshkarov et al., the resistive

instability can be identified by ion current lagging j_e [48] or E_z for negligible electron inertia. In physical terms, this represents that the resistive instability primarily drives fluctuations in E_z, with changes in current only following in response. The three main criteria that we have identified for the resistive instability are as follows: ionization fluctuations lag those in E_z, j_i lags j_e, and the growth rate maximizes near the ionization zone.

First, the growth rate profiles shown in Fig. 5.10a of §5.3.3.1 have already indicated that the resistive instability is strongest downstream of the ionization region. Specifically, we computed γ as maximizing near 0.2-0.3 L_{ch} downstream of the exit plane, while Fig. 5.8a shows the ionization region centered on 0.03-0.06 L_{ch} and the acceleration zone extending to only as far as 0.16 L_{ch}. This seems to indicate that the resistive instability would tend to develop in the near-plume, while the breathing mode is expected to originate in the ionization zone.

Next, by comparing fluctuations in f_{iz} in the ionization region to those of E_z in the acceleration region, we find that they are nearly in phase, with E_z lagging by about 6°. As a result, increases in electric field strength actually occur after those in ionization frequency, whereas a resistive instability would drive oscillations in E_z that then produce fluctuations in ionization.

Figure 5.18a indicates that n lags E_z by 180° ± 13° and u_i lags by 254° ± 54°. Given that $j_i = nu_i$, the phase offset between E_z and j_i can be judged on inspection knowing the identity $\mathcal{F}[n(t)u_i(t)] = \mathcal{F}[n(t)] \circledast \mathcal{F}[u_i(t)]$. Since the fluctuation strength of u_i is much lower than that of n according to Fig. 5.18b, it is expected that j_i should be almost completely in or out of phase with n, and in fact we find it lags E_z by roughly 182° ± 12°. So while a 90° lag between j_i and E_z might evince the presence of a resistive instability, the experimental data indicates the quantities are completely out of phase. This suggests that the inertial lag of the ions necessary for the resistive instability is not present.

In summary, the resistive instability does not correspond to experimental data in terms of phase relationships. A more direct evaluation would require resolving plasma properties on the time scale of Eq. (3.6), which we anticipate to be much higher than the Nyquist frequency of the TRLIF technique used in this study. We conclude that the resistive instability, like the predator-prey model, is not an accurate dynamic description of the breathing mode.

5.4.3.3 Neutral Gas Instability

The propagating neutral density waves of Fig. 5.15d are a surprising and significant finding of this study. Although no consistent evidence of velocity fluctuations were discernible from the Xe I LIF measurements, the waves in the n_n profiles inferred with IBIS are quite pronounced. The presence of these waves seems to indicate that a neutral gas instability is occurring, especially given the strong frequency scaling of neutral drift waves identified in §5.3.3.3. And in fact the waves of Fig. 5.15d propagate at the local neutral speed such that $k \approx \omega_b/u_n \sim 400$ m^{-1}, and they appear upstream of the ionization region. Figure 5.21 shows the peak-to-peak strength of these waves relative to the ionization zone, demonstrating that they originate upstream of it and gradually diminish undisturbed through it.

We suspect that these waves are a result of either a neutral-driven process or a plasma-driven process. In the former, the neutral waves would be present even in the absence of plasma; in the latter, the neutral waves are strictly a result of interaction with the plasma. We now argue that the former is unlikely; the latter is discussed in Chapter VII. If the waves are neutral-driven, presumably they originate inside the anode and are a fundamental gas instability, possibly related to the constriction of flow out of the anode and the heating of the gas as it passes through. A neutral-driven origin seems unlikely because the breathing frequency can both be identical for thrusters of vastly different geometry yet significantly different for similar thrusters. For exam-

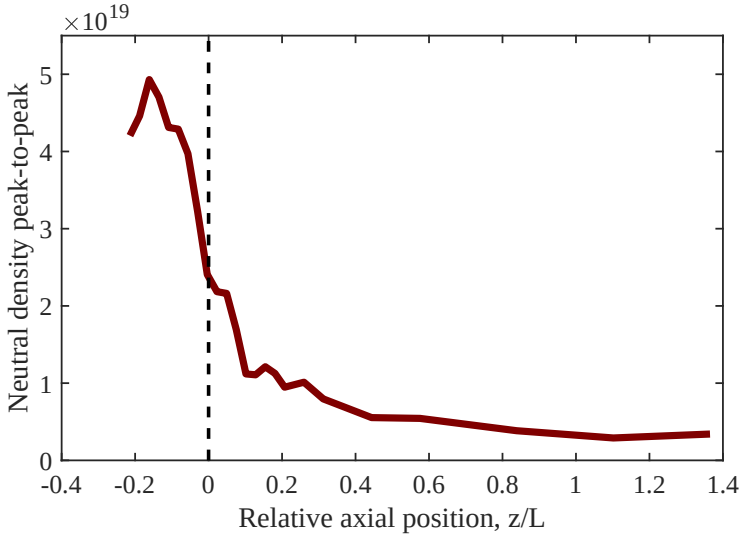

Figure 5.21: The peak-to-peak amplitude of neutral density fluctuations as a function of axial position relative to the ionization zone, with the ionization zone itself (z/L=0) denoted with a vertical dashed line.

ple, experiments performed on magnetically-shielded and unshielded configurations of a 6-kW thruster – where the anode was unchanged – exhibited breathing at two distinct frequencies: 8 kHz and 14 kHz, respectively [8]. Conversely, thrusters of diameter ∼10 cm and ∼30 cm can both exhibit 20 kHz breathing oscillations [32, 36]. Further, the breathing amplitude is very sensitive to the magnetic field strength [13], which should have little effect on the neutral population. Some of these observations could be obfuscated by secondary plasma effects on the neutral population, but even if that were true, it is undeniable that many Hall thruster codes can reproduce low frequency oscillations without simulating the gas distributing geometry of the anode. As a result, it is most likely that the neutral waves we measured are the result of a plasma process acting upstream of the ionization zone.

5.5 Summary

In this chapter, we first describe a frequency scaling study using time-averaged data for the H9 operating with a range of cathode flow fractions. We found that the

scaling dictated by a traditional predator-prey process and a neutral gas instability agreed with the measured frequency trends, although somewhat insensitively. By far, the neutral drift transit frequency correlated the best with our measurements. We then continued with a time-resolved experiment to characterize the dynamic properties of the plasma while the thruster exhibited low-frequency oscillations. From the resulting data, we showed that the zero-dimensional aspect of the predator-prey model is incongruent with an experimental characterization of density fluctuations, and that the phase relationship between plasma and neutral density was mostly inconsistent with this model. Although previous studies [46] have identified limitations in Fife et al.'s 0D predator-prey formulation, the shortcomings revealed presently have not be considered before. Similarly, phase criteria based on Koshkarov et al.'s fluid resistive instability were not met. Interestingly, fluctuations in neutral density appeared to propagate through the channel, which although not strictly anticipated for a neutral gas instability, suggests that some upstream process related to the neutral population could be contributing to the breathing mode. We propose that this is a plasma-driven effect, and thus not explained by an inherent neutral gas instability.

There are a few major lessons learned from the experiments discussed in this chapter. First of all, none of the existing theories considered are completely consistent with our measurements. The predator-prey model captured the scaling of ω adequately but was dynamically flawed, while we observed strong evidence for the presence of neutral drift waves propagating in the channel but without any indication of the source of these waves. Together, this information may imply that there is a spatial aspect to the predator-prey cycle, possibly involving the neutral population, that may need to be invoked to accurately describe the breathing mode. This may indicate that a zero-dimensional model of this phenomenon is inappropriate. However, we believe that our experimental investigation as presented in this chapter poses the possibility that more physical relationships – potentially those capturing spatial

effects – may be included into the traditional zero-dimensional predator-prey model to make it more consistent with our experimental findings. In this way, the following chapter is devoted to exploring what must be added to the predator-prey model to sufficiently capture the missing dynamic behavior identified presently. Primarily, we are interested in finding a model that captures the phasing of quantities in the ionization region and is consistent with the neutral drift waves we observed – both features that elude the traditional predator-prey model.

CHAPTER VI

Modification of Existing Theories to Agree With Experimental Measurements

6.1 Introduction

In this section, we describe the analytical and numerical efforts taken to modify the baseline predator-prey model to better agree with our experimental data. Specifically, we aim to correct the inconsistencies identified in the previous chapter. Our findings there suggested that one-dimensional effects may need to be considered to accurately capturing the breathing mode. However, we did observe that some features – like neutral drift waves – propagate with constant speed, such that the oscillations may still be modeled zero-dimensionally so long as the appropriate phasing is incorporated. In general, we presume that the predator-prey mechanism is a natural mode of the Hall thruster plasma and our goal is to identify the driving mechanism for this process. Previous authors have approached the problem similarly, attempting to increase the fidelity of the 0D predator-prey framework to induce growth. However, in the present study we leverage our experimental measurements to guide our modification of the classical 0D predator-prey model and identify several plausible growth pathways. In doing this, we start by presenting the analytical and numerical techniques at our disposal for evaluating the stability of these models. We then

discuss modifications of the traditional predator-prey model and explore their stability in an effort to understand what must be added to the system to achieve linear growth. Based on these results, we identify important quantities or features that could possibly drive low-frequency oscillations or otherwise are critical for the success of a predator-prey-like model. Finally, we summarize these results so as to motivate the following theoretical development of a new model.

6.2 Methodology

6.2.1 Approach

In the previous chapter, we identified that the traditional predator-prey mechanism is not an accurate description of the breathing mode. However, we did find evidence that the neutral population may play a significant role in this instability. We now attempt to modify the baseline predator-prey model, directed by our experimental studies, to more accurately capture the breathing mode. Specifically, the following steps were taken:

(i) *Baseline model selection*: We began by choosing the predator-prey model as the baseline model for this investigation. There are several aspects of the predator-prey theory that makes it attractive as a starting point. First, the real frequency predicted by this theory, such as with the formulation of Fife et al. [29], provides estimates that compare favorably with experimental and numerical studies. Second, the zero-dimensional framework of this description makes it analytically flexible, such that predictive results are easier to obtain than in higher-order models like that of Barral and Ahedo [35]. Finally, the predator-prey physical picture is commonly cited in the literature and is thus well-studied at this point.

(ii) *Expanding the model*: The predator-prey model was modified to more faithfully capture the breathing mode as characterized in our experimental work.

Two distinct routes were taken in doing this. First, following the work Hara et al. [46], additional 0D hydrodynamic relationships were added to the typical continuity equations of the predator-prey model, Eqs. (3.1) and (3.2). By introducing more equations, more terms could be allowed to fluctuate in a linear perturbation analysis, which generally allows for new coupling pathways between the equations, and thus more potentially unstable roots for the system. Physically, we expect that many plasma parameters fluctuate during breathing oscillations, and so adding more fluctuating terms within the simple 0D predator-prey framework allows the model to more closely approximate reality. Second, we defined new fluctuation relationships between parameters in the predator-prey system without adding new fluctuating terms. That is, we relate fluctuations of a given quantity to $\tilde{n}$ or $\tilde{n}_n$ such that the system rank does not change. In this way, new physical relationships are added to the model without increasing its complexity. Generally, these new fluctuation relationships come from perceived spatial effects not otherwise captured by the 0D framework.

(iii) *Examination of expanded models*: The stability of these new models is then assessed via linear perturbation analysis supplemented with Routh-Hurwitz criteria as necessary. Additionally, the predicted linear oscillation frequencies can be evaluated numerically by applying reasonable steady-state parameters to the model. The full nonlinear system of equations can also be modeled numerically to assess periodic trends not evinced by the linear analysis. In doing these studies, we primarily assess whether the system can be unstable (oscillations grow) and whether the real frequency is reasonable.

(iv) *Identification of important quantities*: Based on the analysis of the modified predator-prey systems, we try to gain insight into what parameters may be of interest for further theoretical study. For example, if allowing a certain quantity

to fluctuate produced less stable results than the baseline predator-prey model, we might deign that quantity worthy of theoretical inclusion so that we may better incorporate its evolution spatially and temporally in a model.

We will now describe some of the techniques used to accomplish these steps. In particular, we review the linear perturbation analysis applied in Step (ii) to derive expressions for ω, and the Routh-Hurwitz stability criteria used to evaluate these expressions for more complicated models.

6.2.2 Linear Perturbation Analysis

The linear perturbation analysis applied throughout the present work follows the typical exponential formulation. Fluctuating quantities, such as of plasma density $\tilde{n}$, are assumed to follow the form

$$\tilde{n} = \mathcal{N}\exp(\text{-}i\omega t) \ , \tag{6.1}$$

where ω is the complex angular oscillation frequency with an imaginary component γ, and $\mathcal{N}$ is a complex amplitude. If this form is expanded with Euler's identity, fluctuating quantities can be expressed as

$$\tilde{n} = \Re(\mathcal{N})\left[\exp(\gamma t) + \cos\omega t\right] + \Im(\mathcal{N})\sin\omega t + i\left\{\Im(\mathcal{N})\left[\exp(\gamma t) + \cos\omega t\right] - \Re(\mathcal{N})\sin\omega t\right\} \ . \tag{6.2}$$

Since only the real component is physically meaningful, fluctuations are described with a growing component, an in-phase component, and a 90° lagging component. The first two are scaled by the real part of $\mathcal{N}$ while the lagging component is scaled by the imaginary part. In this way, all fluctuations are only a function of time, they oscillate at $\Re(\omega)$, they grow at rate γ, and they have a phase $\arg(\mathcal{N})$. Interactions or dependencies between quantities are lost in assuming that small fluctuations can

be described linearly, i.e. $n(t) \approx n + \tilde{n}$.

Once a system of equations is linearized in terms of fluctuation quantities in vector $\vec{x}$, it can be represented as a matrix M where $M\vec{x} = 0$. The roots of the system are equivalent to the eigenvalues of this matrix, such that $\det M = 0$. As a result, solving for ω is a matter of finding the roots of a polynomial of order equal to the rank of M.

6.2.3 Routh-Hurwitz Stability Analysis

Closed-form solutions for polynomial roots exist up to fourth-order but even then they are so unwieldy as to be useless in judging the stability of a system. Analyzing the location of roots in the complex plane is commonly done in the design of control systems, where a routine tool is the Routh-Hurwitz theorem [132]. It provides a series of criteria for judging whether the roots of a polynomial are in the left half of the complex plane, and thus whether the polynomial is stable. However, in a linear perturbation analysis we are interested in whether the roots are in the upper or lower half of the complex plane. Thus in any polynomials for ω we substitute with $i\omega$, in which case the Routh-Hurwitz criteria judge whether the system is stable. That is, if the criteria are met then -$\gamma > 0$ so that $\gamma < 0$ and thus the system is stable. If the criteria are not met, the system is unstable or metastable. This difference in application of the Routh-Hurwitz theorem stems from the fact that it is common in control system theory to treat derivatives or integrals of a quantity as discrete variables rather than introducing imaginary units.

The criteria for a polynomial of order v comes from the following matrix:

$$\begin{matrix} a_v & a_{v-2} & a_{v-4} & \dots \\ a_{v-1} & a_{v-3} & a_{v-5} & \dots \\ b_1 & b_2 & b_3 & \dots \\ c_1 & c_2 & c_3 & \dots \\ \vdots & \vdots & \vdots & \dots \end{matrix} \tag{6.3}$$

where the iterative quantities b and c are given by

$$b_i = \frac{a_{v-1}a_{v-2i} - a_v a_{n-2i-1}}{a_{n-1}} \,, \tag{6.4a}$$

$$c_i = \frac{b_1 a_{n-2i-1} - a_{n-1} b_{i+1}}{b_1} \,. \tag{6.4b}$$

The number of sign changes in the first column (Routh array) indicates the number of non-stable roots.

As an example, for a second-order system $x^2+a_1x+a_0 = 0$, the criteria for stability are $a_1 > 0$ and $a_0 > 0$. A mass-spring-damper system of mass m, specific stiffness k, and specific damping d is such a second-order system, where $\omega^2 + id\omega - k = 0$. After rotating the complex plane, the Routh-Hurwitz criteria easily show that the system is unstable/metastable for $d \leq 0$ and stable for $d > 0$. This is physically sensible: an undamped system will oscillate continuously (metastable), a damped system will diminishingly oscillate (stable), and a negatively-damped system will increasingly oscillate (unstable).

6.3 Predator-Prey Modifications

In this section, we outline the framework with which we modify the traditional predator-prey model. First, the complete set of governing equations are presented.

Next, the general approach with which different subsets of these equations are explored is described. Finally, the specific numerical setup used in the simulation of different subsets of equations is detailed.

6.3.1 Governing Equations

As in the predator-prey model of Fife et al. with corrections implemented by Hara et al., we consider a 0D Hall thruster discharge channel, encompassing the ionization and acceleration regions. This is illustrated in Fig. 6.1, where particle fluxes are shown at the boundary of the 0D system. The fundamental equations are neutral continuity, ion continuity, ion momentum conservation, and electron energy conservation, shown as Eqs. (6.5).

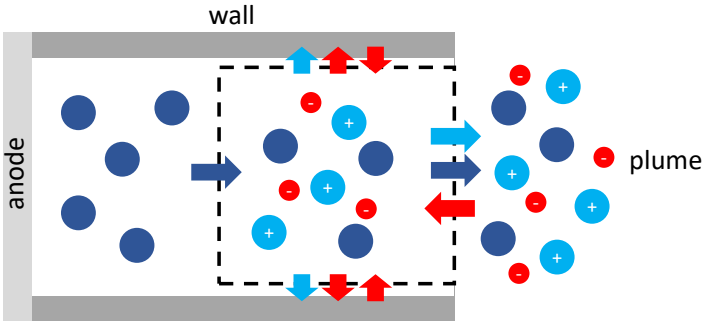

Figure 6.1: A physical picture of the temperature-dependent model, where the 0D system is contained within the dashed box. Neutral (dark blue), ion (light blue), and electron (red) fluxes are shown at the borders of the 0D box.

$$\frac{dn}{dt} = \xi_{iz} n n_n - \frac{u_i n}{L_{ch}} - \frac{2u_w n}{w_{ch}} \tag{6.5a}$$

$$\frac{dn_n}{dt} = -\xi_{iz} n n_n - \frac{u_n n_n}{L_{ch}} + \frac{u_n n_{n,0}}{L_{ch}} \tag{6.5b}$$

$$\frac{dnu_i}{dt} = \frac{e}{m_i} n E_z - \frac{{u_i}^2 n}{L_{iz}} \tag{6.5c}$$

$$\frac{d}{dt}\left(\frac{3}{2} n T_e\right) = -\frac{5}{2}\frac{n T_e u_e}{L_{iz}} - n u_e E_Z - n\epsilon_w \nu_w - n n_n \xi_{iz} \epsilon_{iz} \chi \tag{6.5d}$$

The ion continuity equation accounts for convection out of the thruster, radial losses to the walls, and ionization. The neutral continuity equation includes inflow from the anode, convection out of the thruster, and ionization. The ion momentum equation considers acceleration by a constant electric field, E_z, and convection out of the thruster. In the steady state, this equation dictates that the ion velocity is equal to the beam velocity (the ion velocity after acceleration through the entire discharge volage). The electron energy equation includes convection of electrons into the thruster, Joule heating, wall collision losses, and inelastic collision losses. The final term considers only ionization collisions but can be scaled by a cost factor χ to proportionally account for excitation as well. The wall collision frequency ν_w, the electron energy lost to the wall per collision ϵ_w, and the wall sheath potential ϕ_w follow forms used by Barral and Ahedo [53] involving the secondary electron emission yield γ_{SEE} and are given by:

$$\nu_w = \frac{u_w}{w_{ch}} \frac{1}{1-\gamma_{SEE}} \tag{6.6}$$

$$\epsilon_w = 2T_e + (1-\gamma_{SEE})\phi_w \tag{6.7}$$

$$\phi_w = -T_e \log\left(\frac{1-\gamma_{SEE}}{\sqrt{\frac{2\pi m_e}{m_i}}}\right) \tag{6.8}$$

Additionally, an effective ionization length is defined by comparing Eq. (6.5b) to Fife et al.'s model [29], and this definition is shown in Eq. (6.9), where all quantities are steady. As a result, L_{iz} has a dependence on T_e and u_i, which in the steady state are themselves dependent on other operating parameters.

$$L_{iz} = L_{ch}\left(1 + 2\frac{u_B}{u_i}\frac{L_{ch}}{R}\right)^{-1} \tag{6.9}$$

To capture fluctuations in E_z, a simple Ohm's law ignoring pressure terms can be included in the model:

$$E_z = \eta_e \Omega^2 j_e = \frac{-e u_e {B_r}^2}{\nu_e m_e} \ . \tag{6.10}$$

The collision frequency is the sum of electron-neutral, Coulomb, and anomalous collisions, where the last contribution is Bohm-like and scaled with parameter α. In this way, α and either E_z or u_e can act as independent variables for the model.

Finally, we can also account for changes in the ionization region length. To do this, first it is assumed that the breathing mode occurs in the ionization region, which oscillates over time in density and spatial extent. We assume that the width of the ionization region is strongly dictated by one-dimensional effects but changes in size due to the breathing mode can be modeled separately. Allowing the ionization region to deform may also be used to capture spatial effects although in this implementation it does not depend on any steady-state plasma gradients except for that of neutral density.

To model changes in ionization length, one can imagine the ionization region being an isolated block of plasma, where the upstream edge ("ionization front") is characterized by a transition from pure neutral gas to a mixture of plasma and neutrals. This is depicted in Fig. 6.2, where there is a front that merges the ion and neutral populations. A 0D neutral continuity equation can be written in the frame of reference of this upstream ionization edge. However, the transformation to this new frame of reference must first be considered. The edge is expected to accelerate since it presumably oscillates back and forth, and thus this frame of reference is non-inertial. As a result, a Galilean transformation is not appropriate. The transformation required to describe the time rate of change of scalar quantity x in the ionization front frame of reference (denoted with subscript "f") can be shown as,

$$(dx)_f = dt \frac{\partial x}{\partial t} + dt \frac{dz}{dt} \frac{\partial x}{\partial z} \ , \tag{6.11}$$

$$\left(\frac{dx}{dt}\right)_f = \frac{\partial x}{\partial t} + u_f \frac{\partial r}{\partial z} \ . \tag{6.12}$$

Intuitively, this transformation indicates that all gradients are material: the rate at which a quantity changes is a combination of the laboratory frame rate (the first term on the righthand side) and the change due to moving through the laboratory frame gradient (the second term on the righthand side).

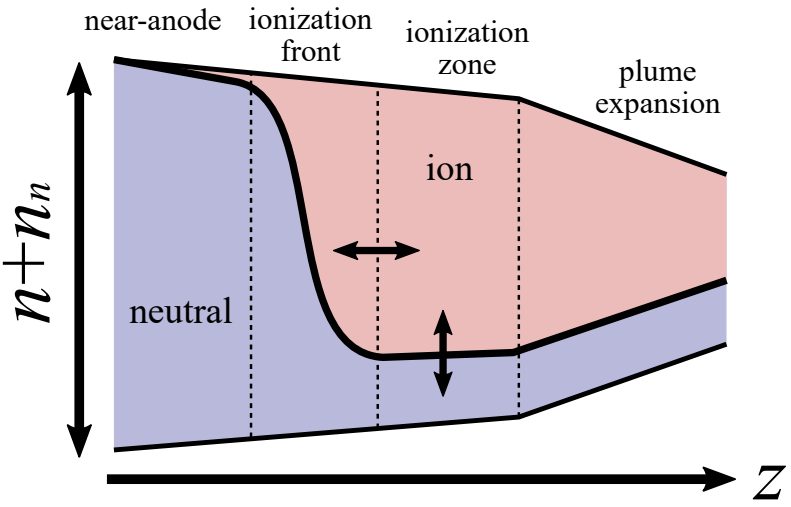

Figure 6.2: A notional diagram of the imagined variation in neutral density throughout the channel, where the edge of the ionization region and n_n within that region can oscillate.

In the frame of reference of the ionization front, the time rate of change of neutral density can be expressed as

$$\left(\frac{dn_n}{dt}\right)_f = \frac{\partial n_n}{\partial t} + u_f \frac{\partial n_n}{\partial x} = 0 \ . \tag{6.13}$$

Given that neutral continuity in the laboratory frame Eq. (6.5a), Eq. (6.13) becomes

$$\left(\frac{dn_n}{dt}\right)_f = -u_n \frac{\partial n_n}{\partial x} - n n_n \xi + u_f \frac{\partial n_n}{\partial x} = (u_f - u_n)\frac{\partial n_n}{\partial x} - n n_n \xi = 0 \tag{6.14}$$

which (ignoring radial diffusion) represents neutral continuity in the ionization front frame. Since the front is imagined traveling along an undisturbed stream of neutrals,

the first term is zero. If the drop in neutral density across the front is assumed to be exponential, a gradient length L_n can be assigned, simplifying the second term. The front velocity can be solved for explicitly, yielding

$$u_f = u_n - n\xi n_n \left(\frac{\partial n_n}{\partial x}\right)^{-1} \approx u_n - n\xi_{iz} L_n \ . \tag{6.15}$$

This form for the front velocity has a simple physical interpretation. The speed at which the ionization region moves upstream is the difference between the speed at which "fuel" enters, u_n, and the speed at which it is consumed by ionization, $n\xi_{iz}L_n$.

The ionization length L_{iz} can be described as

$$L_{iz} = L_{iz,0} - \int u_f dt \approx L_{iz,0} + \int \tilde{n}\xi_{iz} L_n dt = L_{iz,0} + i\frac{\xi_{iz} L_n}{2\omega}\tilde{n} \ , \tag{6.16}$$

where it is assumed that small perturbations in plasma density are sinusoidal in time such that $n = n_0 + \tilde{n}$. In the steady state, $u_f = 0$ and $u_n - L_n n\xi_{iz} = 0$. The perturbed form of the inverse of the ionization length, which is of more practical interest, is given by

$$\widetilde{L_{iz}^{-1}} \approx -i\frac{\xi_{iz} L_n}{{L_{iz,0}}^2 \omega}\tilde{n} \ . \tag{6.17}$$

Whereas Eq. (6.9) provides only a steady description of L_{iz}, here we have derived an expression for its fluctuations in terms of steady-state parameters.

Physically, these equations imply that changes in the ionization region length lag behind changes in ion density by 90°. In a linear sense, perturbations in the inverse of L_{iz} lead changes in n by 90°. Qualitatively, this can be understood as the ionization region stretching or compressing in response to variations in bulk ion density, with a lag occurring because this stretching is a function of these variations.

Table 6.1: A summary of the predator-prey cases examined here, broken down by the fluctuation quantities included in each model.

Case	$\tilde{n}$	$\tilde{n}_n$	$\tilde{u}_i$	$\tilde{T}_e$	$\tilde{E}_z$	$\tilde{L}_{iz}$	$\tilde{n}_{n,0}$
I	✓	✓					
II	✓	✓	✓				
III	✓	✓	✓	✓			
IV	✓	✓	✓	✓	✓		
V	✓	✓				✓	
VI	✓	✓					✓

6.3.2 General Approach

In this work, several subsets of the governing equations outlined in the previous section are examined in terms of stability. These cases are summarized in Table 6.1. A common procedure is followed in evaluating the stability of these systems. First, numerical simulations of the system are conducted for a limited set of input parameters to qualitatively identify any trends in the response. This includes examining whether each time-dependent quantity damps and whether the damping behavior between them is different. Next, a map of damping behavior is produced from numerical simulations over a wide range of input parameters to evaluate the breadth of the conclusions on stability made from the preliminary simulations. Finally, a linear perturbation analysis is performed on the system as an even broader assessment of stability.

6.3.3 Numerical Setup

The numerical simulations we performed used input parameters for the SPT-100 [129] except where otherwise noted. The choice of thruster was driven by similar numerical investigations in the literature, particularly Ref. 46. The channel length and width are 2.5 and 2 cm, respectively. A discharge current and voltage of 4.5 A and 300 V were assumed, which corresponds to the nominal 1.35 kW operating condition for this thruster. A current utilization efficiency between 50% and 100% is

assumed to allow the estimation of u_e/u_i, following Hara et al. [46].

6.4 Model Stability

6.4.1 Case I

The simplest subset of the governing equations is the neutral and ion continuity equations alone. For simplicity, the radial ion losses are disregarded and L_{ch} is more appropriately treated as L_{iz}. Because the linearized matrix determinant is only second order, it is sufficient to judge stability from a linear perturbation analysis. It has been shown in the literature [46] that the growth rate is,

$$\gamma = -\frac{1}{2}\frac{n_{n,0}}{n_{n,0} - n_n} n\xi_{iz} \ , \tag{6.18}$$

and thus all physical solution are damped. As others have concluded, this indicates that the traditional predator-prey model is a poor description of the breathing mode in terms of growth.

6.4.2 Case II

Next, the ion momentum conservation equation Eq. (6.5c) can be included in the model of Case I. Again, the system is simple enough that numerical simulations are unnecessary and the Routh-Hurwitz method can be used to judge linear stability. The determinant of the linearized matrix of this system is a third-order polynomial in ω, shown in Eq. (6.20). The condition for stability is given by,

$$u_i < L_{iz} n_{n,0} \xi_{iz} \ , \tag{6.19}$$

which is guaranteed by the construction of the system. Thus, the system is always damped. This result suggests that the ion momentum equation either has little im-

pact on the system or contributes damped poles to it. The former agrees with the observation that the breathing frequency is typically much slower than the ion transit time through the channel, and thus ions respond almost instantly to changes in the plasma during breathing oscillations.

$$\frac{2u_i u_n(-u_i + L_{iz} n_{n,0} \xi_{iz})}{L_{iz}^2 L_{ch}} + \frac{u_n(-u_i + 2L_{iz} n_{n,0} \xi_{iz})}{L_{iz} L_{ch}} \omega + \left(\frac{u_i}{L_{iz}} + \frac{L_{iz} n_{n,0} u_n \xi_{iz}}{L_{ch} u_i} \right) \omega^2 + \omega^3 = 0 \tag{6.20}$$

6.4.3 Case III

By adding the electron energy conservation equation Eq. (6.5d), the time-dependent parameters of the system now include n_n, n, u_i, and T_e. The determinant of the linearized matrix for this system is fourth order in ω, and thus is too complicated to examine by a linear perturbation analysis alone. As described previously, investigating the system's stability will begin with numerical simulations, which will then be compared to a a slightly broader numerical linear analysis.

6.4.3.1 Preliminary Numerical Simulations

The full nonlinear equations are evaluated for a few values of u_e/u_i between 0.5 to 5 and the results over 0.5 ms are shown in Fig. 6.3. The response is damped for all cases examined. In Fig. 6.3 the T_e plot is normalized by the steady state value so that the shape of the response can be compared for different inputs, and from this it is clear that T_e fluctuates very little compared to other quantities. This implies that the electron energy equation may be poorly coupled to the rest of the system since there are many conditions where T_e remains nearly steady or is only weakly perturbed. If the electron energy equation is playing such a limited role in the time response of the system, this model may be unconditionally stable since we proved in

§6.4.2 that the continuity equations together with the ion momentum conservation equation are always damped.

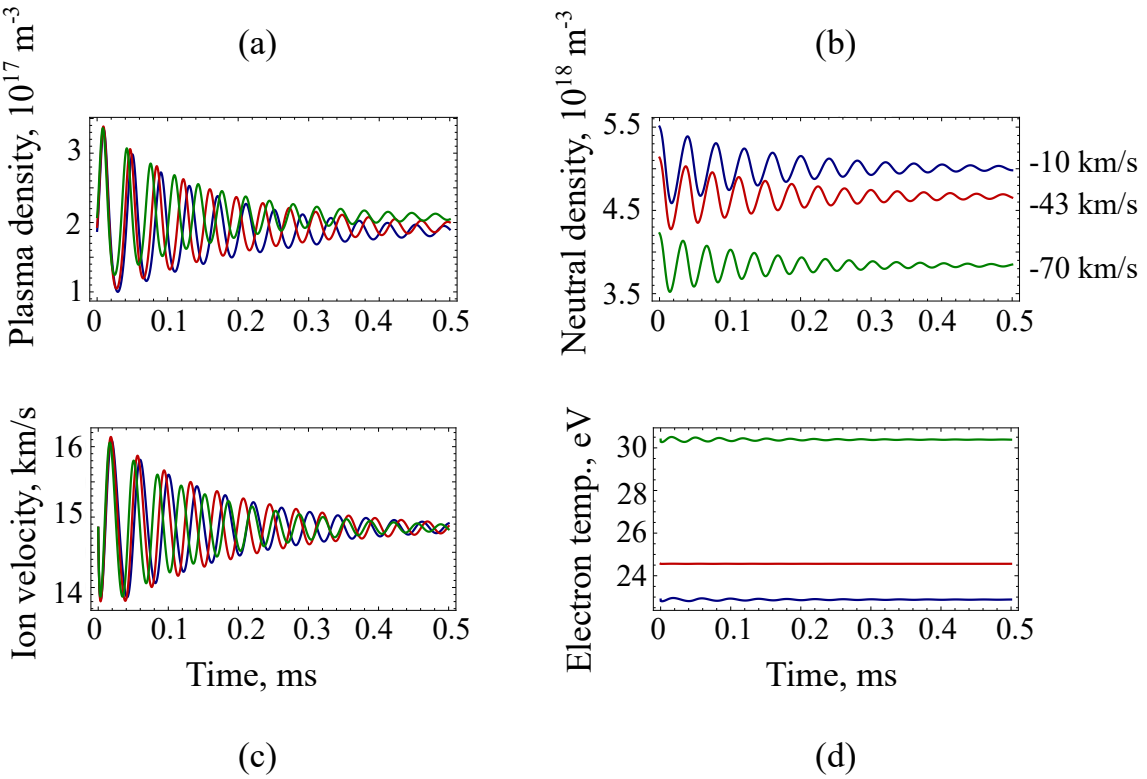

Figure 6.3: The time response of the plasma density (a), neutral density (b), ion velocity (c), and electron temperature (d) for various electron velocities denoted in (b).

6.4.3.2 Extensive Numerical Map

To verify these trends, numerical simulations are performed for a wide range of input parameters and the stability is summarized with the damping ratio of the ion density time response. The damping ratio ζ, defined as

$$\zeta = (\tau\omega_n)^{-1} \approx (\tau\omega)^{-1} \ , \tag{6.21}$$

is calculated for a 10% initial perturbation of the neutral density, where the natural frequency of the system was approximated with the observed frequency for simplicity.

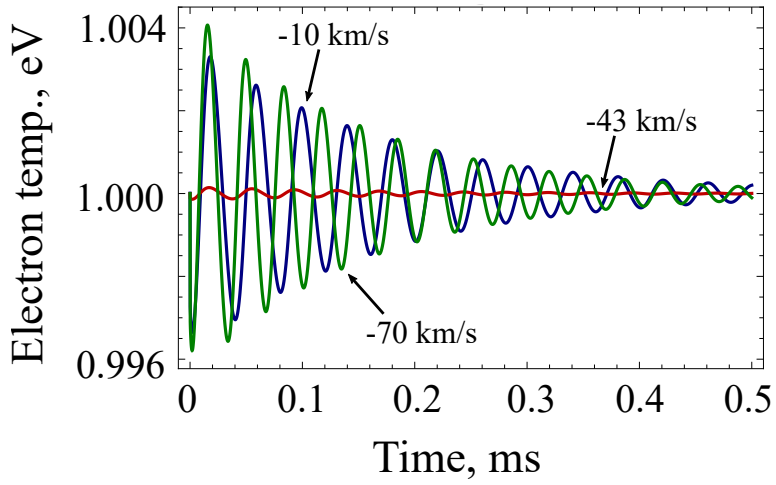

Figure 6.4: The normalized time response of the electron temperature for various electron velocities.

A harmonic oscillator is critically damped for $\zeta = 1$, undamped for $\zeta = 0$, and growing for $\zeta < 0$. Figure 6.5 shows these values and demonstrates that they are all positive, and thus the system is stable over a wide range of inputs. The limits in u_e/u_i are dictated by the stiffness of the system, which generally means that the steady-state parameters become unphysical (e.g. $T_e < 0$ eV) or the simulation is numerically unstable outside the plotted domain. This domain therefore represents the range of input parameters of physical interest for the chosen operating condition.

6.4.3.3 Linear Analysis

A linear analysis can be performed using the perturbation forms of Hara et al. [46], yielding the linearized matrix equation shown in Eq. (6.22), where β is the power relating ξ_{iz} to linear perturbations in T_e, and some "effective electron energy relaxation frequency" Λ is defined in Eq. (6.23).

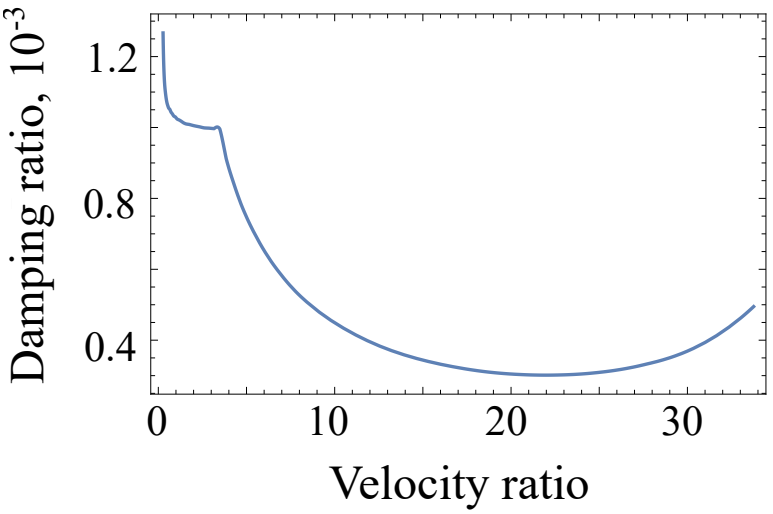

Figure 6.5: The damping ratio of the time response of the system for varying absolute ratios of the electron velocity to the ion velocity.

$$\begin{bmatrix} -i\omega & -n\xi_{iz} & \frac{n}{L_{ch}} & -n\frac{u_i}{L}\frac{\beta}{T_e} \\ \frac{u_i}{L} & -i\omega + \frac{n_{n,0}}{n_{n,0}-n_n}n\xi_{iz} & 0 & n\frac{u_i}{L}\frac{\beta}{T_e} \\ -i\omega u_i & 0 & n\left(-i\omega + \frac{2u_i}{L}\right) & 0 \\ -i\omega\frac{3}{2}T_e & n\xi_{iz}\chi\epsilon_{iz} & 0 & n\left(-i\frac{3}{2}\omega + \Lambda\right) \end{bmatrix} \begin{bmatrix} \tilde{n} \\ \tilde{n_n} \\ \tilde{u_i} \\ \tilde{T_e} \end{bmatrix} = \mathbf{0} \tag{6.22}$$

$$\Lambda \equiv \frac{3}{2}\frac{\epsilon_w}{T_e}\nu_w + \frac{u_i}{L}\frac{\beta}{T_e}\chi\epsilon_{iz} + \frac{5}{2}\frac{u_e}{L} \ . \tag{6.23}$$

The resulting polynomial given by the determinant of the linearized matrix is fourth order, which generally precludes any analytical judgment of stability. Alternatively, the growth rate and real frequency can be computed numerically for a given thruster and operating condition.

Fig. 6.6 shows representative numerical results for the SPT-100. All roots were damped, so only those with definite real and complex parts are shown. The only

independent variable is the electron-ion velocity ratio, and it can clearly be seen that the growth rate is always negative and asymptotically approaching zero for stationary electrons. Previous work by Hara et al. [46] showed similar plots as a function of electron temperature, and although this may highlight that the model nearly predicts a region of positive growth, it is clear from Fig. 6.7 that the steady state T_e line never intersects the growing region. A linear perturbation analysis by definition is only valid around the steady state condition, thus the model does not predict linear growth for this case. However, because this system is intractable to evaluate analytically, it cannot be said that the system is stable for all conditions. It is also important to note that the range of u_e/u_i shown in the figure is far wider than that considered typical from the current utilization efficiencies expected for a SPT-100 or more modern Hall thrusters.

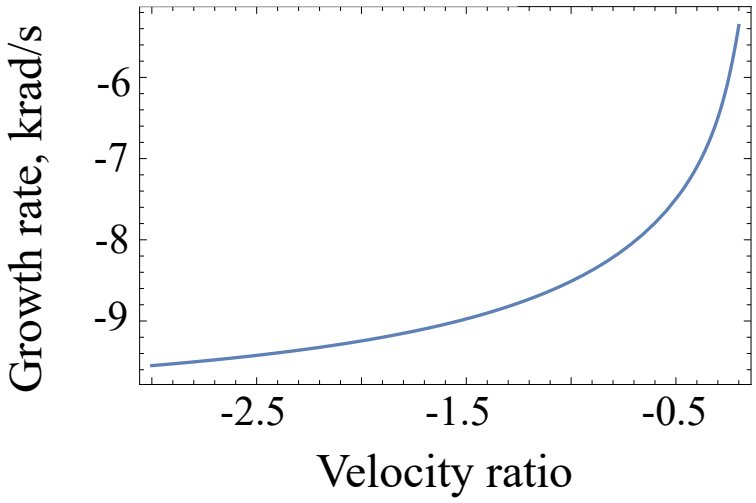

Figure 6.6: The growth rate as a function of the electron-ion velocity ratio..

6.4.4 Case IV

To improve the coupling of T_e to the rest of the system, Ohm's law can be added to the model. This allows the electric field to be expressed in terms of electron velocity and the total collision rate, which is a function of several time-dependent parameters.

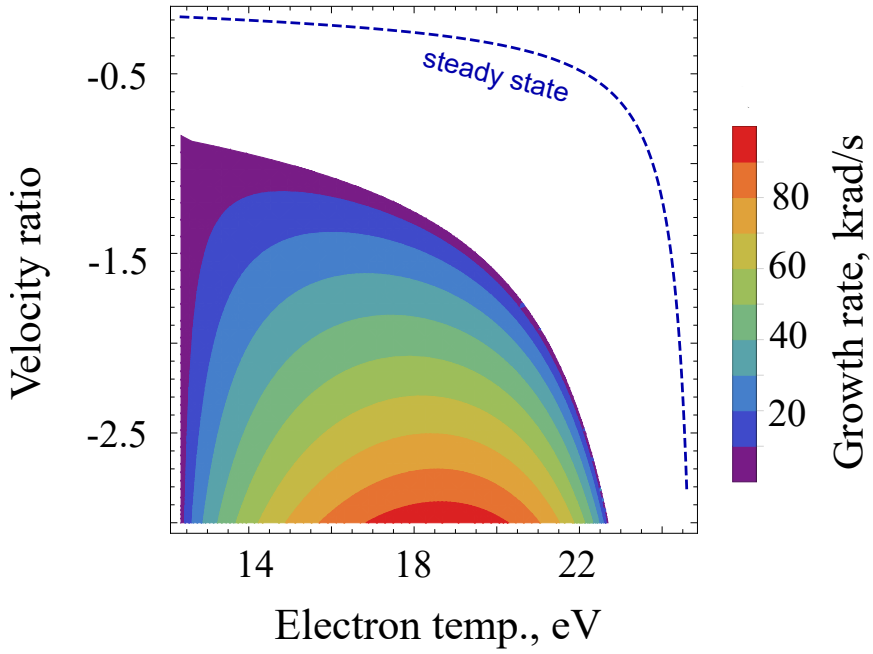

Figure 6.7: The growth rate as a function of the electron-ion velocity ratio (colored region), and the steady-state electron temperature (blue line). The white region corresponds to zero or negative growth rates.

In this way, E_z becomes a fluctuating quantity, introducing another potential source of instability.

6.4.4.1 Preliminary Numerical Simulations

Figure 6.8 shows the time response of the system as a function of u_e and the electron transport factor α. The behavior is damped for these sample cases. Figure 6.9 shows the T_e response normalized, as in Fig. 6.4. The curves show very small oscillation amplitudes, indicating that T_e coupling is not improved. This suggests that even including Ohm's law does not induce large perturbations in T_e, and including perturbations in E_z does not induce instability.

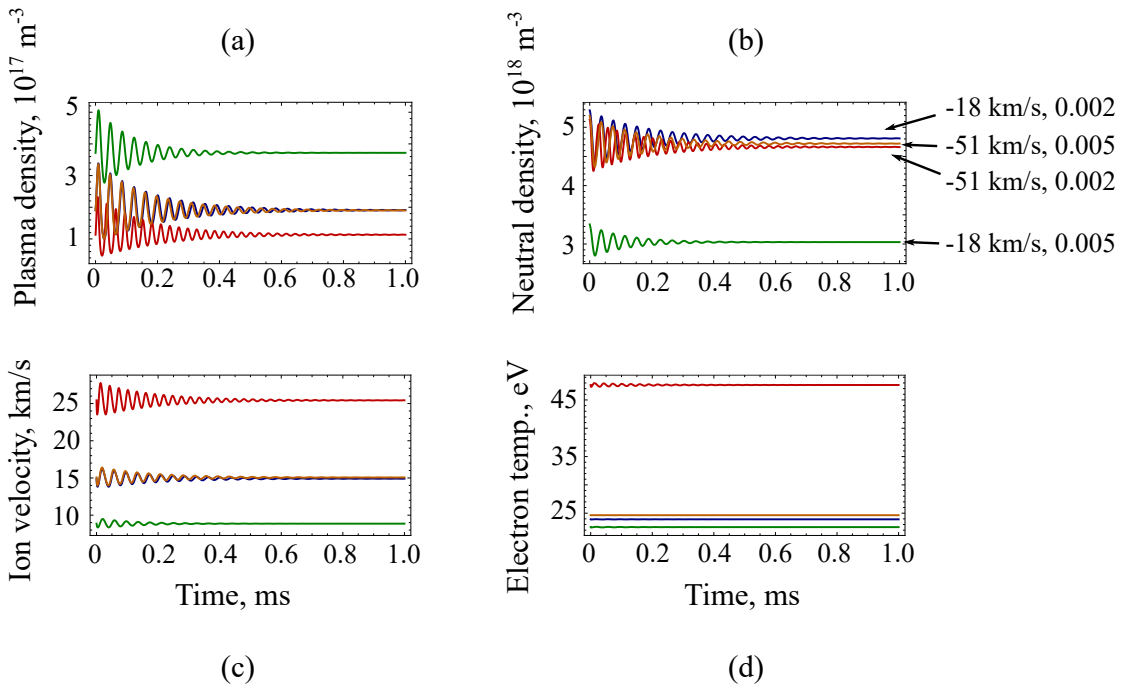

Figure 6.8: The time response of the system in terms of plasma density (a), neutral density (b), ion velocity (c), and electron temperature (d) with Ohm's law included. The response for various electron velocities and transport factors α, denoted in (b), are shown.

6.4.4.2 Extensive Numerical Map

By defining a nominal discharge current, current continuity couples u_e to u_i and n such that α is a function of u_e. As a result, only one input parameter, u_e, is required for this model with a given discharge current. Figure 6.10 shows this relationship for a SPT-100 at 4.5 A. The limits of u_e in this plot are dictated by the stiffness of the system of equations. Figure 6.10 also shows the damping ratio for a range of u_e and α that are close to those for a nominal discharge current of 4.5 A. Everywhere the response is damped, and thus the system is everywhere stable. The discharge current curve is superimposed on the damping ratios in Fig. 6.10 for context. It should be noted that the damping ratios do not cover the full extent of the discharge current curve because the simulations became numerically unstable in certain extremes of this range. Even so, we conclude from Fig. 6.10 that including Ohm's law into the

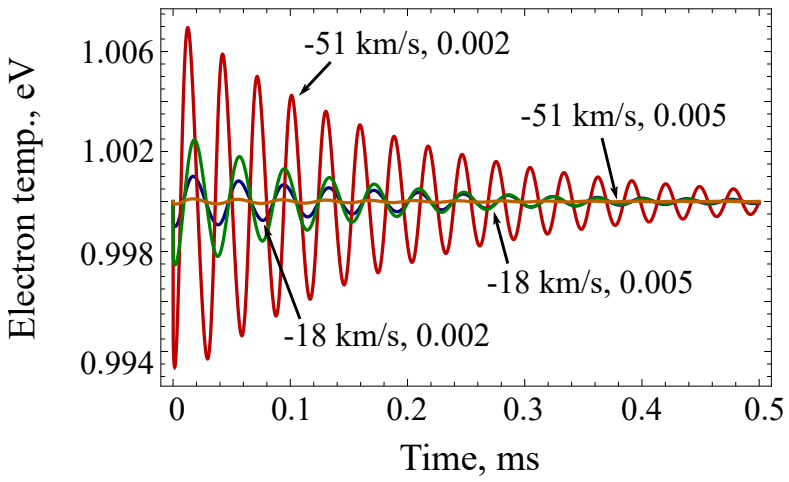

Figure 6.9: The normalized electron temperature response of the system with Ohm's law included.

temperature-dependent model does not induce instability for a nominal discharge current in this case.

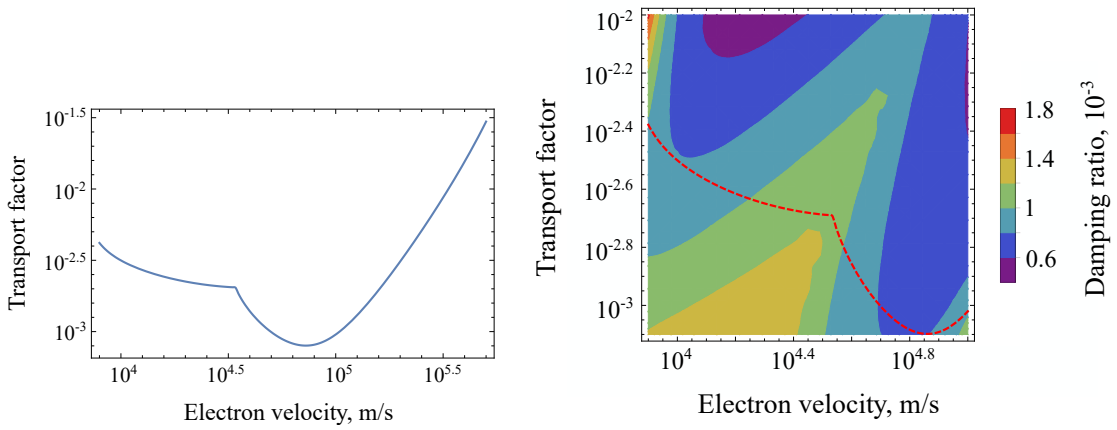

(a) (b)

Figure 6.10: (a) The logarithm of the anomalous collision frequency scaling factor α as a function of the logarithm of u_e in m/s for a nominal discharge current of 4.5 A. (b) The damping ratio of the ion density as a function of the logarithm of u_e in m/s and α, in the vicinity of those values that correspond to the nominal discharge current (red dashed line).

6.4.4.3 Linear Analysis

The linear analysis for this system is similar to that of Case III, except the Ohm's law definition of E_z introduces perturbation terms to the linearized matrix. For ranges of u_e and α similar to the numerical simulation map in Fig. 6.10, the growth rate yielded by the linear analysis is nowhere positive. To demonstrate this, the growth rate of roots with finite positive real frequency is shown in Fig. 6.11. It is clear that the linear oscillations are always damped, supporting the findings of the numerical simulations.

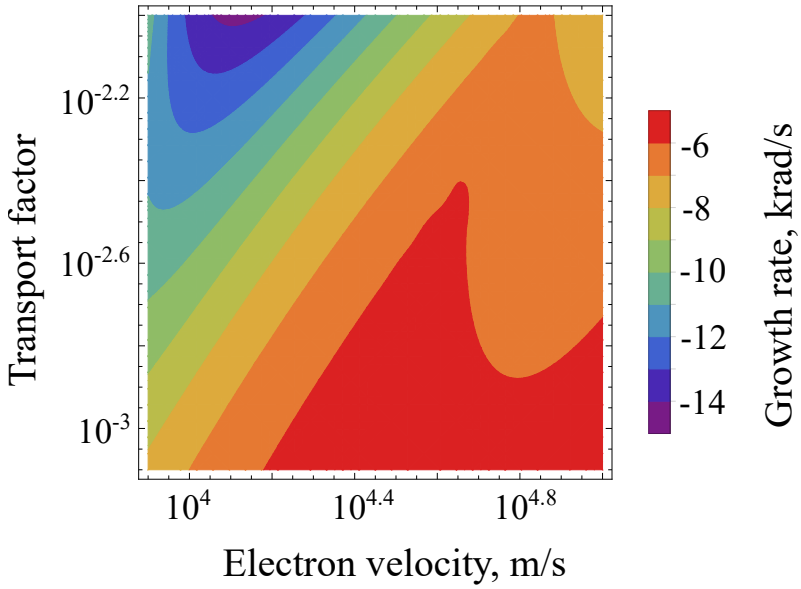

Figure 6.11: The growth rate of linear perturbations as a function of the logarithm of u_e in m/s and α. Only solutions with a positive real frequency are chosen.

6.4.5 Case V

A model incorporating time-dependent T_e and E_z terms was incapable of producing instability for a range of input parameters corresponding to a nominal discharge current. And based on the spatial dependence of many of the parameters for this model, any unstable marginal cases for the SPT-100 conditions considered here are not expected to be meaningful. The next step would be to include ionization length

perturbations in the model of Case IV. However, this would further complicate an already analytically intractable model, so the electron energy conservation equation (which contains E_z perturbations) and the damping ion momentum conservation equation are removed before including a L_{iz} perturbation form. The rationale for this approach is as follows: if perturbations in L_{iz} alone are shown to make the system unstable, any additional physical processes are not of primary importance for capturing the breathing mode and may only serve to add conditions to the instability; conversely if the system is stable, destabilizing it by adding more fluctuation quantities will not yield a transparent growth mechanism. Another possibility is that any growing linear fluctuations due to $\tilde{L}_{iz}$ may be damped by including electron energy conservation and ion momentum into the model; since these added equations presumably increase the fidelity of the model, any growth seen in a simpler model should be ignored. However, beyond attempting to keep the system analytically tractable, we are also looking for inspiration into physical mechanisms that can be compared to the measurements of Chapter V and used to develop a new theory in Chapter VII. For this reason, even a fluctuation quantity like L_{iz} that may destabilize the system in only simple cases would be insightful. As a result, instead of adding L_{iz} perturbations to the model of Case IV, only the ion and neutral continuity equations are retained, as in Case I. This is done to make the system more amenable to linear perturbation analysis.

6.4.5.1 Preliminary Numerical Simulations

A sample numerical simulation of the full nonlinear equations is shown in Fig. 6.12. As can be observed, within 1 ms all quantities are oscillating and growing continuously, and the frequency is approximately 14 kHz at the end of the simulation. The nonlinear oscillations in ionization length and ion density are in phase, which is consistent with results from more sophisticated simulations [28]. Since this system is observed to be unstable and is simple enough for analytical linear analysis, a more

extensive set of numerical simulations is unnecessary.

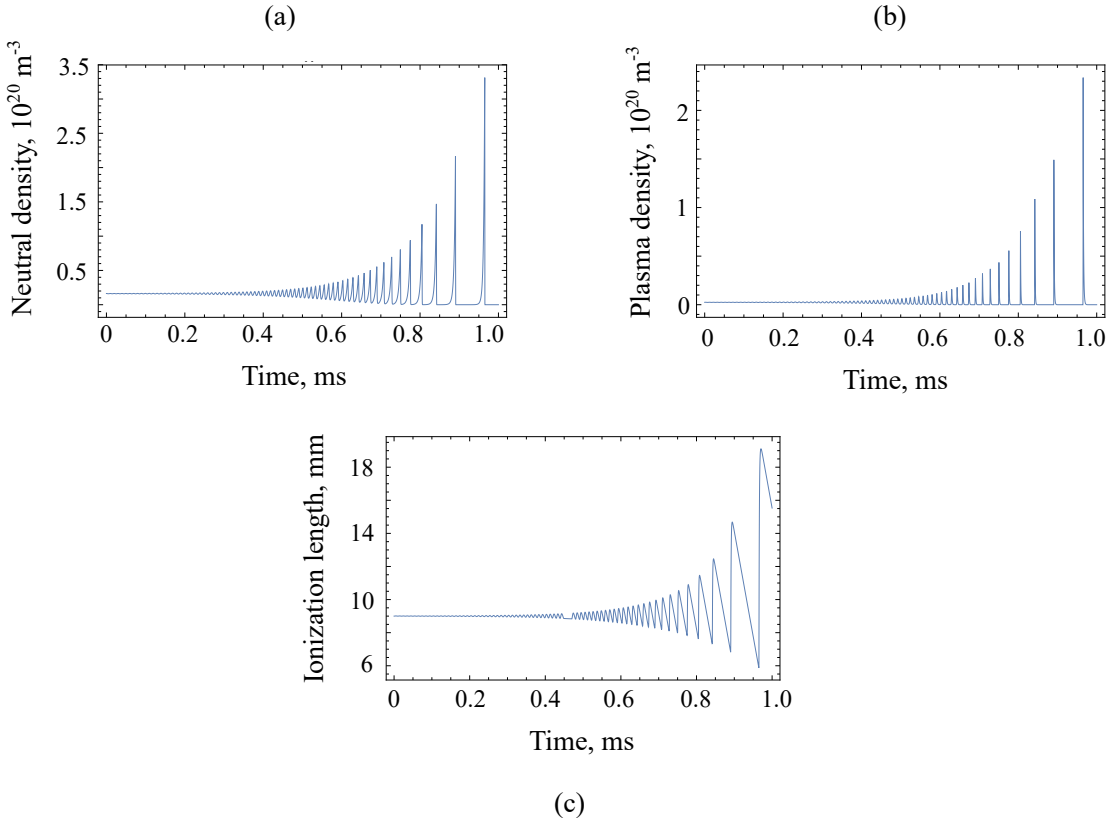

Figure 6.12: Time response of neutral density (a), ion density (b), and ionization length (c) for representative plasma conditions.

6.4.5.2 Linear Analysis

The linearized matrix equation based on this system is shown in Eq. (6.24), where $\rho \equiv n_{n,0}/n_n$ and $L^* \equiv L_n/L_{iz}$. All quantities are steady-state. The roots of the determinant of the matrix must be found, and this determinant is given by Eq. (6.25). An exact analytical form for the roots of ω based on Eq. (6.25) exists but is much too complicated to be useful for judging the stability of the system.

$$\begin{bmatrix} \dfrac{\rho u_n}{L_{iz}} - i\omega & \dfrac{u_i}{L_{iz}^2\omega}\left(\dfrac{1}{L_{iz}} - i(1-\rho)L^* u_n\right) \\ \dfrac{(1-\rho)u_n}{L_{iz}} & \dfrac{i(1-\rho)L^* u_i u_n}{L_{iz}^2\omega} - i\omega \end{bmatrix} \begin{bmatrix} \tilde{n_n} \\ \tilde{n} \end{bmatrix} = \mathbf{0} \tag{6.24}$$

$$i(\rho-1)L^*u_iu_n^2+(\rho-1)(L^*-1)L_{iz}u_iu_n\omega+i\rho L_{iz}^2u_n\omega^2+L_{iz}^3\omega^3=0 \tag{6.25}$$

However, for the polynomial $a_0+a_1s+a_2s^2+s^3$, the Routh-Hurwitz criteria for stability are $a_0>0$, $a_2>0$, and $a_1a_2-a_0>0$. For Eq. (6.25) these criteria become,

$$0<-\frac{(\rho-1)L^*u_iu_n^2}{{L_{iz}}^3} \tag{6.26a}$$

$$0<\frac{\rho u_n}{L_{iz}} \tag{6.26b}$$

$$0<\frac{(\rho-1)u_iu_n^2(\rho(L^*-1)-L^*)}{{L_{iz}}^3}\ . \tag{6.26c}$$

Given that $\rho>1$ and $L^*>0$, these criteria cannot be satisfied and thus the system is always unstable or metastable. However, whether it is purely exponential (such that $\Re(\omega)=0$) and thus nonlinearly periodic cannot be determined.

In order to examine the linear stability numerically, we considered a test case with $u_n\sim 100$ m/s, $u_i\sim 10$ km/s, and $L_{iz}\sim 1$ cm. Fig. 6.13 shows the growth rate as a function of the logarithm of ρ and L^* for reasonable ranges of those values, assuming $\rho\sim 10$ and $L^*\sim 1$, where the latter implies that neutral density drops significantly throughout the entire ionization region. As it shows, the growth rate is everywhere positive. At small L^*, the growth rate is insensitive to ρ; at large L^*, the growth rate is proportional to ρ. It should be noted that the real frequency for the positive growth region is everywhere zero, indicating the the linear growth is purely exponential and thus any oscillations are a nonlinear effect. The previous numerical simulations seem to confirm this.

Although these analytical results are promising, it is important to compare this proposed effect to our experimental measurements to see if it is physically realizable. In Chapter V we found that n is nearly in phase with I_d (Figs. 5.18a and 5.14c)

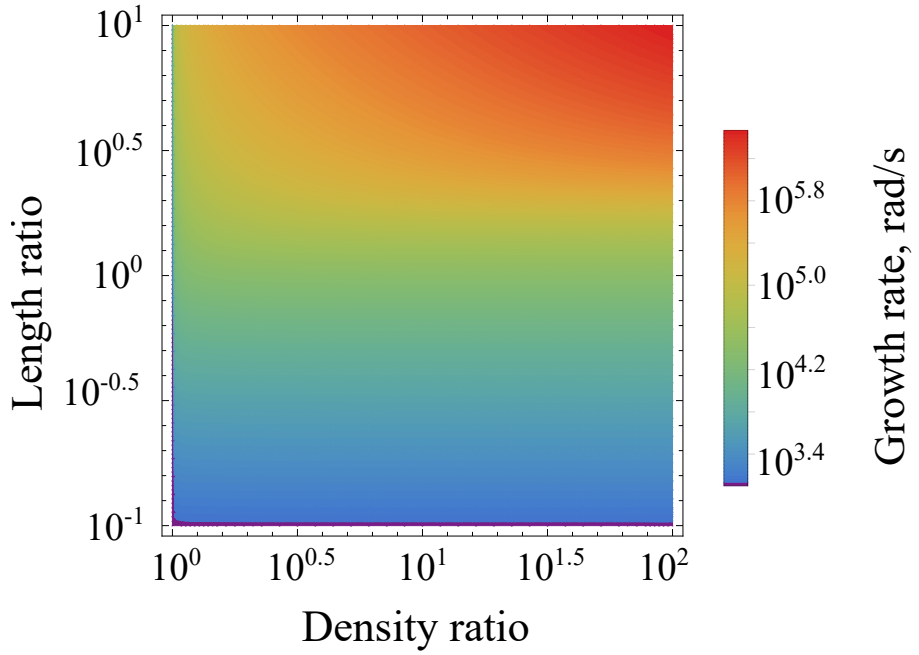

Figure 6.13: Logarithm of the growth rate in rad/s as a function of the neutral density ratio ρ and neutral-ionization length ratio b.

while the upstream edge of the ionization region slightly lags I_d (Fig. 5.17a), which collectively implies that the phasing of the mechanism in this case may be realistic. However, a closer examination as in Fig. 6.14 shows that the ionization region upstream half-width only slightly lags n, and in fact we calculate the phase to be only about 15°. It appears, then, that although this variation of the predator-prey model may produce growing solutions, they are not experimentally supported.

6.4.6 Case VI

This apparent success in destabilizing the system without overly complicating it encourages us to explore a similar variation of the predator-prey model. Whereas in Case V we incorporated fluctuations of L_{iz} into the continuity equations, now we presume that $n_{n,0}$ fluctuates. In particular, we assume $\tilde{n}_{n,0} = \mathcal{N}_{n,0}\tilde{n}$, where $\mathcal{N}_{n,0}$ is a complex amplitude. Physically, this assumption implies that the neutral flow entering the 0D ionization region is modulated with some phase offset relative to fluctuations in

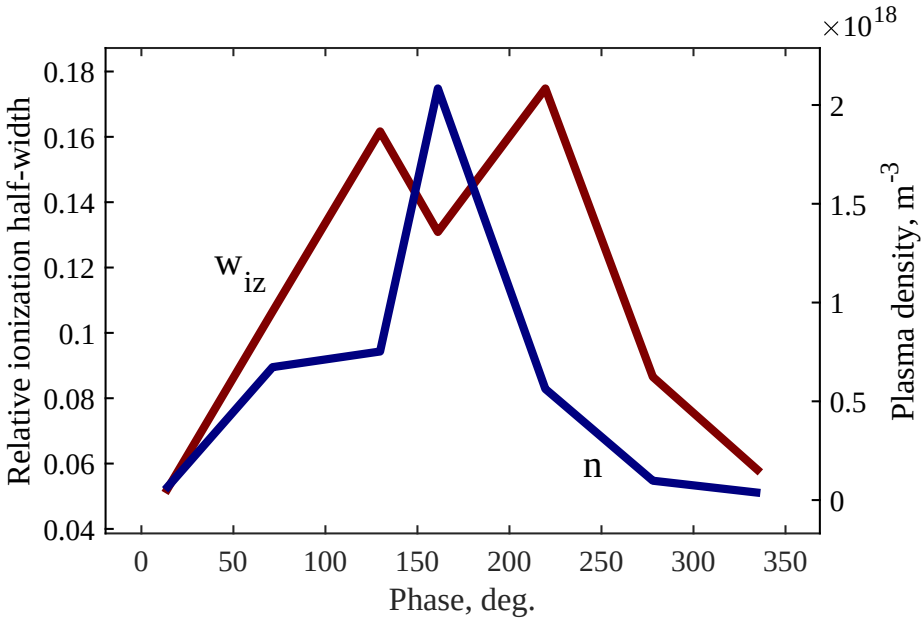

Figure 6.14: The plasma density in the ionization region and relative ionization zone half-width (normalized by L_{ch}) as a function of breathing phase.

plasma density. We could have just as easily assumed that $n_{n,0}$ fluctuated proportional to $\tilde{n}_n$ – the choice here is made arbitrarily as at this point there is no physical insight into this upstream modulation of the neutral density, only that $n_{n,0}$ indeed fluctuates.

6.4.6.1 Preliminary Numerical Simulations

To examine this model, we use steady state conditions typical for a high-power thruster like the H9 instead of the SPT-100 conditions from other cases. We also arbitrarily assume that $\tilde{n}_{n,0}$ is 180° out of phase with $\tilde{n}$ for numerical simplicity; in our following linear analysis (§6.4.6.2) we find that this assumption is justified. We show the time evolution of the full nonlinear continuity equations for several breathing cycles in Fig. 6.15. This plot depicts the plasma density, resident neutral density, and inflowing neutral density as all unstable. The fluctuations in these quantities grow significantly over these few breathing periods, suggesting that γ is likely comparable in order of magnitude to $\Re(\omega)$.

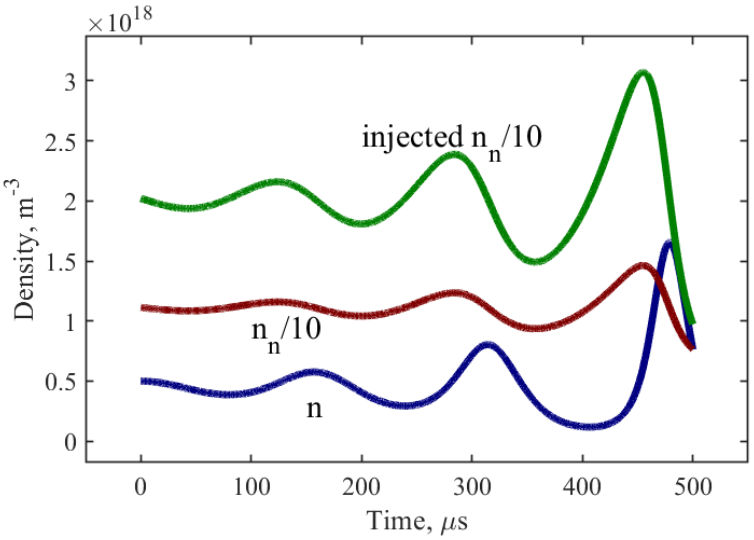

Figure 6.15: A full nonlinear 0D simulation of the predator-prey process with $n_{n,0}$ fluctuations.

6.4.6.2 Linear Analysis

Since the baseline predator-prey model has only one imaginary term, the growth rate must either be zero or, by physical constraints, negative. This suggests that other fluctuation terms out of phase with plasma and/or neutral density fluctuations, $\tilde{n}$ and $\tilde{n}_n$, must be included to allow for growth purely on analytical grounds. In the previous section, we showed that allowing $n_{n,0}$ to fluctuate completely out of phase with n produced growth. More generally, if we presume that the incoming neutral density $n_{n,0}$ is fluctuating such that $\tilde{n}_{n,0} = \mathcal{N}_{n,0}\tilde{n}$, where $\mathcal{N}_{n,0}$ is a complex amplitude, the linear perturbation quadratic becomes

$$\omega^2 + \frac{i\rho u_n \omega}{L} - (\rho - 1)u_n \frac{u_i - \mathcal{N}_{n,0}u_n}{L^2} = 0 \ , \tag{6.27}$$

where $\rho \equiv n_{n,0}/n_n$. This quadratic has a closed form solution but isolating the imaginary frequency $\Im(\omega)$ is quite difficult, so the Routh-Hurwitz theorem can be employed to provide criteria for stability of the oscillations based on the number of

stable and unstable roots:

$$0 < \frac{i\rho u_n}{L} \tag{6.28a}$$

$$0 < -(\rho - 1)u_n \frac{u_i - \mathcal{N}_{n,0} u_n}{L^2} \ . \tag{6.28b}$$

The system is not stable if $u_i > u_n \Re(\mathcal{N}_{n,0})$ and/or $\Im(\mathcal{N}_{n,0}) < 0$, where we assume $\rho > 1$ and $u_n > 0$. Physically, these conditions suggest the oscillations *may* grow if $n_{n,0}$ fluctuates weakly in phase with n, out of phase with n, or leads n by any amount. In short, fluctuations of the incoming neutral density to the ionization-acceleration region may be sufficient for a predator-prey description of the breathing mode to predict growth. This is physically sensible because, even in the absence of any predator-prey process, injecting varying amounts of propellant into a thruster will leading to corresponding fluctuations in ionization. Here, we simply show that these fluctuations exacerbate any feast-famine cycle existing in the ionization zone.

This result, like that in the previous case, is somewhat unprecedented in studies of 0D breathing models. It indicates that complicated physics do not need to be piled onto the traditional predator-prey model to yield growth. Rather, more fluctuating terms are only required to achieve this. In this case, experimental evidence of modulation of the neutral flow, as shown in Fig. 5.15d, guided us and suggests that this variation of the predator-prey model may be physically realstic. However, this result is deceptively simple in that the process producing fluctuations in n_n needs to be modeled and incorporated into the 0D predator-prey framework to describe this effect *ab initio*.

6.5 Identification of Important Quantities

Having explored six variations of the predator-prey model, we now discuss the most salient features or quantities necessary to produce growth. Of those cases, the

fifth is definitely unstable and the sixth is possibly unstable. In the former, we assume the location of the upstream edge of the ionization zone oscillates over a breathing cycle, while in the latter we assume the neutral density entering the ionization region is modulated by some upstream process. In either case, we fundamentally rely on the ion and neutral continuity equations and simply relate some other term – L_{iz} or $n_{n,0}$ – to other fluctuations quantities.

As much as these case studies have highlighted important features of the predator-prey model to explore, they likewise inform us which parameters do not need to be examined so closely. Since the addition of the ion momentum equation in Case II did not allow for growth, it is clear that ion transit through the ionization-acceleration region is fast enough to not have a primary impact on the breathing mode in a 0D framework. Likewise, the evolution of electron energy in Cases III and IV does not yield growth, and so electron dynamics within the ionization region are likely of secondary importance. Finally, even incorporating a simplified Ohm's law with an anomalous electron transport component does not make the linear system unstable, which implies that a more nuanced description of the electron transport in the acceleration region is not necessary in a predator-prey-like model. This is not surprising considering many Hall thruster codes are able to resolve low-frequency oscillations while implementing very different electron transport models.

6.6 Summary

In the previous chapter, we found that the predator-prey model scaled fairly well with experimental observations of the breathing mode, but dynamically its traditional zero-dimensional implementation was inconsistent with our data. Ultimately, this can be traced back to the fact that the predator-prey model by itself does not have a clear energy source – it cannot predict growth – and thus is missing certain dynamic effects. In this chapter, we expanded the traditional predator-prey model with additional

physical relationships in hopes of introducing a growth mechanism. As part of this, we included zero-dimensional ion momentum conservation, electron energy conservation, and Ohm's law. All of these variations appeared to be stable, indicating that none of this increased fidelity allowed for linear growth.

However, we also explored two spatial effects: deformation of the ionization zone (Case V) and modulation of the incoming neutral flow (Case VI). In the former, we presumed that the location of the upstream edge of the ionization region will fluctuate as if it were a "flame front," and we found that this effect is sufficient to allow for growth of the predator-prey process. In the latter, we presumed that the neutral density entering the zero-dimensional ionization region is modulated with some phase offset compared to the resident plasma density, and we found it to be conditionally unstable. The success of these two variations of the predator-prey model suggests that including spatial effects are important for the growth of this process. Naturally, this indicates that a one-dimensional model may most faithfully describe the breathing mode, as sacrifices to include necessary spatial effects into a 0D framework would not be required.

Leveraging the experimental data from the previous chapter, we were able to show that the fluctuation of the ionization region is not consistent with our modeling in Case V but that there is strong evidence of neutral density waves consistent with Case VI. We therefore propose that modulation of the neutral gas flow is a sufficient and physically probable mechanism by which the predator-prey model may grow. What remains is a theoretical justification for this proposal, which we pursue in the following chapter.

CHAPTER VII

Two-Zone Breathing Model

7.1 Introduction

In this chapter, we try to expand on the origin of the neutral flow modulation in a physically-meaningfully and self-consistent way. In essence, we are searching for a means by which the downstream plasma can communicate to the upstream neutral flow. In the last chapter, we proposed two possible mechanisms that could fill this role: oscillation of the ionization region and modulation of the upstream neutral flow. We found, though, that only the latter effect was detected experimentally. Recent work by Chapurin et al. has also proposed that ion flow toward the anode can serve this purpose [133], but again in our experiments we found no evidence of this effect. Instead, we propose that this modulation is a result of periodic ionization near the anode. We note that this is contrary to the typical picture of a Hall thruster in which near-anode ionization is unimportant [78], but it has parallels in other discharges where there can be high-ionization near the electrodes, like the cathode and anode glow regions of a Geissler tube [134]. If ionization within/near the anode Debye sheath is periodically enhanced, out of phase fluctuations in neutral density would slowly travel downstream, consistent with Fig. 5.15d. We hypothesize that this oscillating near-anode ionization is the result of coupled instabilities near the anode and in the traditional downstream ionization region. An increase in ionization downstream

would increase electron flux at the anode, relatively boosting ionization there. As a result, fewer neutrals would leave the near-anode region, producing a decrease in ionization downstream after some lag dictated by the neutral speed. This process would repeat and may grow depending on the ionization rates and neutral gas properties. In essence, coupled predator-prey action would be occurring in two locations with some lag between them. As a secondary effect, studies on Hall thruster anode sheath physics have indicated that both positive and negative sheaths can form [135], in which the former can lead to increased ionization due to the additional energy gained by electrons falling through the sheath [136]. It can be imagined that a drop in f_{iz} in the traditional ionization region could produce a drought of electrons at the anode, leading to the formation of a positive (or at least less negative) anode fall. The electrons streaming to the anode gain additional energy, resulting in greater ionization in that vicinity. In turn, a trough in the neutral density develops and advects downstream. The process is reinforced via predator-prey action when this neutral trough reaches the ionization region.

7.2 Methodology

Encouraged by the analytical results of the previous chapter, we develop a new model based on the premise described in the previous section, and we evaluate it theoretically and numerically. After deriving the model, we use the experimental measurements obtained in Chapter V to a evaluate the linearized model over a wide parameter space. Following this preliminary examination of the behavior of the system, a narrower set of steady-state conditions are inferred from our data to explore more relevant solutions of the model. From this we can judge this new model against the traditional predator-prey description and explore its predictive capabilities. In total, this process encompasses the following steps:

(i) *Provide a physical description of the proposed process*: A new physical process to explain the breathing mode is proposed based on the experimental data and the performance of the modified predator-prey models considered previously.

(ii) *Compare this description to experimental evidence*: The proposed process is compared to our experimental data as a cursory assessment of whether it is physically consistent.

(iii) *Formulate a new model and analyze its stability*: A zero-dimensional model is developed to capture the proposed breathing process. A linear perturbation analysis is conducted on the new model to explore its theoretical stability. Various assumptions are considered and applied to render the model more analytically pliable. The growth and real frequency of the oscillations predicted by this model are estimated and compared to the traditional predator-prey model. Experimental data is used to infer steady-state parameters, and this information is then used to numerically study the stability of the linear model.

(iv) *Simplify the model to assess its predictiveness*: Simplifying assumptions are applied to the new model so that a straightforward analytical expression for ω can be found. The result is related to high-level thruster parameters to produce a "phenomenological" model of the breathing mode. The predictions of the model are then compared to empirical trends from the literature.

The tools for formulating and investigating the stability of the new model have already been discussed in §6.2, so instead we will cover the details of calculating the steady-state parameters needed to validate the new model in §7.5.2.1. This includes the equations involved and the assumptions necessary. We further consider the ramifications of these assumptions and what physical expectations we can use to assess their impact. Finally, we will give a brief overview of root locus analysis in §7.5.2,

specifically discussing the interpretation of root locus maps like those considered in Step (iii).

7.3 Physical Description

We now provide a description of a hypothetical physical process based on the proposal in §7.1, and then we explore it experimentally, theoretically, and numerically in the following sections. We presume that a predator-prey-like ionization instability should exist in the traditional ionization zone. As the plasma density increases during rampant ionization, an excess of electrons stream to the anode. Ionization in the near-anode region is enhanced by this increase in electron flux. As a result, the neutral population is reduced, so a dearth of neutrals drift downstream. There is also a concomitant excess of ions due to this enhanced ionization which presumably recombine on the anode, but we ignore this population for now. The sparse neutrals reach the ionization region while the ionization rate there is already dropping due to typical predator-prey action, which exacerbates the drop. Once the plasma thins, a dearth of electrons stream to the anode, leading to an excess of neutrals drifting to the ionization region. In this way, the process repeats itself. A diagram of this process is provided in Fig. 7.1, where the two columns represent local predator-prey cycles that are slightly out of phase and connected by particles drifting between the two regions with some phase lag.

Fundamentally, this model proposes that there are two coupled ionization cycles, one in the traditional ionization region and one near the anode. It is the interplay between them that allows the predator-prey-like mechanism in the former to grow. The energy for the instability is therefore derived from the electrons – it is the energy stripped from them during impact ionization events near the anode that supports fluctuations in the upstream neutral density, which in turn fuels the downstream predator-prey oscillations. An important aspect of this process is the delay

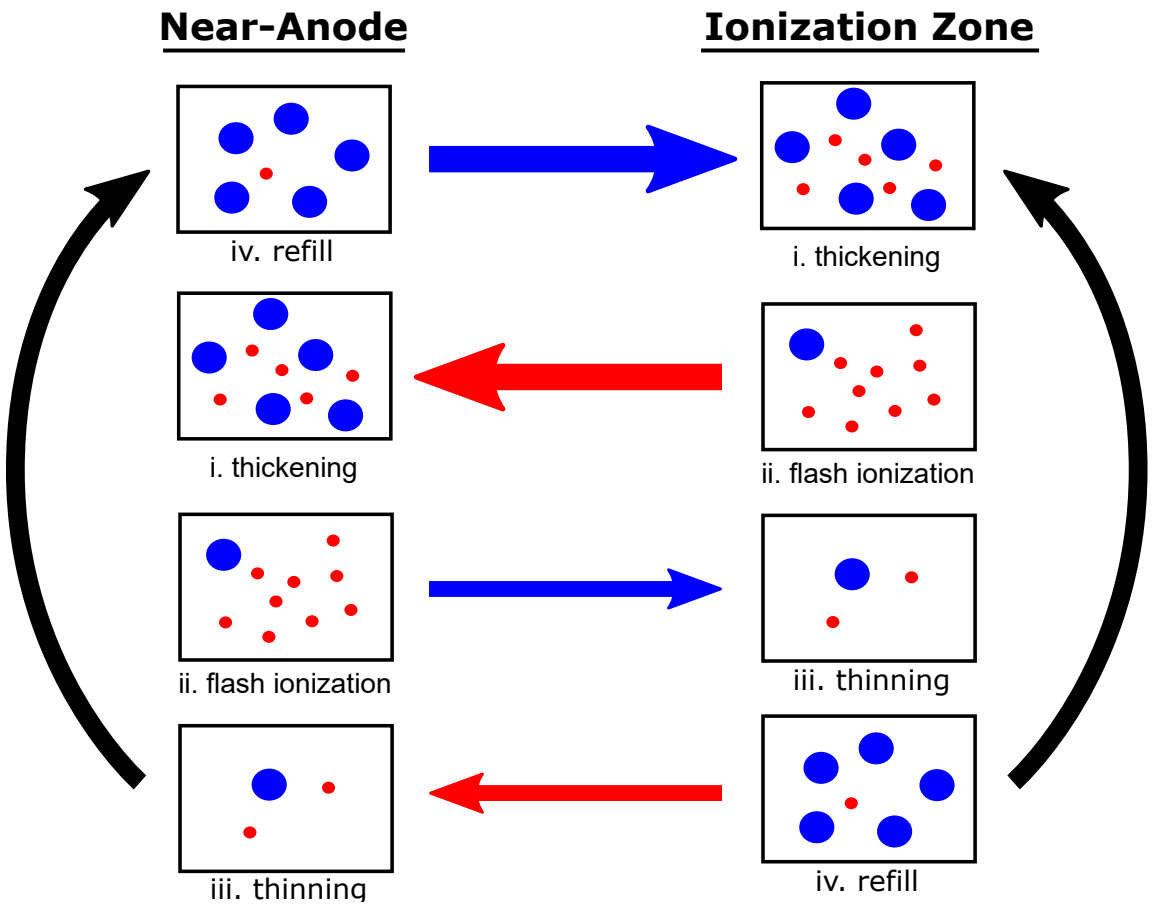

Figure 7.1: A diagram of the physical process proposed for the two-zone model, where electrons are shown in red and neutral gas is shown in blue. The righthand cycle represents the typical predator-prey process in the ionization region, and the lefthand cycle represents a similar phenomenon near the anode. The arrows between the two reflect the coupling between the two instabilities.

in electrons reaching the anode from the ionization region and the delay of neutrals reaching the ionization region from the anode. Presumably these quantities play a significant role in setting the pace and growth of breathing oscillations. The electron transit time is hard to predict in the near-anode region and is often determined non-classically. This adds an unfortunate complication to an otherwise very simple model. The implications of this will be discussed later in §7.5.2.3.

7.4 Experimental Evidence

Before developing a quantitative model to underpin this proposed physical process, we first look for evidence of it in the experimental measurements of Chapter V. We have previously noted the presence of neutral drift waves in the channel, and in Chapter VI we showed that modulation of the neutral flow can destabilize the 0D predator-prey model. However, the nature of those drift waves and their role in the breathing process can be explored further. In this section, we experimentally consider the dynamics of electrons/neutrals, the anode sheath, ion recombination, and ionization in relation to the proposed model.

7.4.1 Electron and Neutral Gas Dynamics

Unfortunately, the near-anode plasma was inaccessible to LIF measurements in this study, and in general this is a difficult region to probe owing to Hall thruster geometry. However, the proposed modified predator-prey model can be tested to some extent using the phase information of Fig. 5.18a. First, since the phase of n_n at the ionization region should be dictated by the phase delay of electron/neutral holes/excesses across the channel (from anode to ionization region), we can estimate this total phase delay θ_{n_n} and compare it to the directly measured phase of n_n. According to our near-anode ionization instability hypothesis, the phase delay relative to n in the ionization zone is given by the following:

$$\theta_{n_n} = (\theta_n - \theta_{I_d}) + \pi/2 + t_{n_n}\Re(\omega) \ , \tag{7.1}$$

where in general θ is the phase of a given quantity and t_{n_n} is the transit time of neutrals from the anode to the ionization region. Physically, the first term on the righthand side is the phase lag due to electrons drifting from the ionization region to the anode; the second term is the phase lag between n and n_n due to ionization

Table 7.1: An accounting of the lag processes according to the proposed modified predator-prey model.

Process	**Measured Lag**
electron upstream drift	6°
near-anode ionization	90°
neutral downstream drift	231°
total	147 ± 29°

at the anode; and the third term is the phase lag accrued by neutrals drifting from the anode to the ionization region. Based on electron and neutral continuity in the near-anode region (introduced later as Eqs. (7.2)), the phase difference in n and n_n is given by the argument of $n_{n,0}u_n/n_n\lambda_D - i\omega$, where as always $n_{n,0}$ is the injected neutral density. Assuming that oscillations are much faster than neutral transport, n lags n_n by $\pi/2$. As a result, this term is added to θ_{n_n} to account for the ionization phase offset near the anode. The average neutral transit phase delay $t_{n_n}\Re(\omega)$ can be calculated from the neutral and ion LIF data of Chapter V, and we find it to be approximately 231°. The phase delay of an electron traveling to the anode can be found from $\theta_n - \theta_{I_d}$, calculated to be about 6°. Altogether, this yields a total phase difference between plasma density in the ionization region and neutrals arriving there of $\theta_{n_n} - \theta_n = 147° \pm 43°$. The measured value of $\theta_{n_n} - \theta_n$ is $129° \pm 57°$ according to Fig. 5.18. These quantities agree within uncertainty and thus the phase of n_n in the ionization region is consistent with the proposed model. Note though that the $\pi/2$ term added to θ_{n_n} assumes the electron density near the anode is greater than that leaving the ionization zone, which may not be realistic but is consistent with the simple model we have proposed here. Further, the assumption of fast oscillations compared to near-anode neutral transport is made without physical evidence, since the near-anode zone could not be thoroughly interrogated in our experiments. In any case, this comparison is summarized in Table 7.1.

7.4.2 Anode Sheath Dynamics

Another aspect of this hypothesis is that the anode polarity may change during breathing oscillations, contributing to the enhanced near-anode ionization. If this were so, the delay between a n hole traveling from the ionization region to the anode should be completely in phase with the conventional sheath voltage V_s. Physically, this means that a decrease in electron density at the anode – by itself reducing the ionization rate – should also be accompanied by a negative sheath potential such that electrons lose energy as they traverse the sheath, reducing ionization even further. Determining the anode sheath potential is not trivial. It is tempting to use the fluctuations in discharge voltage $\tilde{V}_d$ as a proxy for variation in the sheath potential, but in fact V_d is the sum of the sheath potential V_s, accelerating voltage V_a, and the cathode-coupling voltage V_{cc}, all of which may be oscillating. We illustrate this voltage composition in Fig. 7.2.

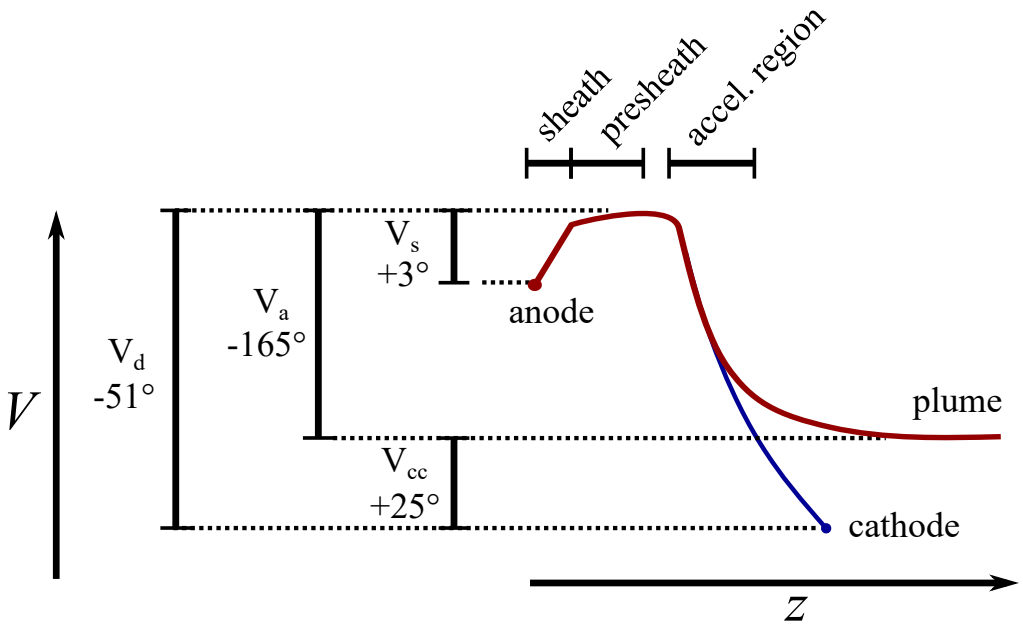

Figure 7.2: A diagram of the spatial distribution of voltage in the discharge, along with measured/inferred phase lags relative to the discharge current signal. The blue curve is followed by electrons headed toward the channel.

In this study, V_d was measured as part of the usual thruster telemetry with a

high-speed high-voltage differential amplifier, and was found to lead I_d by about 51°. By integrating the inferred E_z profile over axial position, V_a was calculated to lead I_d by about 165°. Finally, V_{cc} was measured using the electrostatic probe data and discharge current telemetry, and was found to lag I_d by about 25°. Altogether, the resulting V_s signal lags I_d by only about 3°, such that the difference between its phase and the phase delay of n for electrons traveling to the anode is only 13° ± 1°. This is also summarized in Fig. 7.2. Physically, this means an increase in electron density at the anode is accompanied by an increase in sheath potential with a mere 13° lag. This is mostly consistent with anode sheath polarity fluctuations contributing to near-anode ionization in the modified predator-prey system. It is important to note though that this effect is not necessary for the proposed growth mechanism of the predator-prey model but rather is a natural result of it. Further, the complexity of modeling these sheath variations will lead us to neglect them in the 0D model we later develop. However, oscillation of the sheath polarity may still be an important secondary effect in the breathing mode, and we have discussed it here as a possible route for increased ionization near the anode.

7.4.3 Ion Recombination Dynamics

We previously noted that enhanced ionization near the anode will not only modulate the neutral density but the ion density as well, and that these ions (presumably) swiftly recombine at the anode. This presents a challenge to the physical process we have proposed: if ions recombine at the anode and return as neutrals much faster than the breathing frequency, neutral density fluctuations will be attenuated. We illustrate this in Fig. 7.3, in which we depict a recombination rate $\gg \omega$ such that the neutral flow is essentially uninterrupted by near-anode ionization. To evaluate the severity of this effect, we assume that the "neutral replenishment time" is given by $\lambda_D/u_{i,a}+\lambda_D/u_n$, which physically represents the time it takes new ions to fall through

the sheath and the resulting neutrals to return to the sheath edge, since recombination is itself very fast [134]. The ions produced inside the sheath will presumably not be at the Bohm velocity, so we assume their motion is dictated by a constant sheath electric field. We estimate the sheath potential to be ∼10 V, and further we loosely estimate the Debye length as ∼0.1 mm. We also know the neutral velocity from the Xe I LIF measurements to be about 165 m/s. Together, this produces a lag of ~ 0.1 μs, or about 0.6° for the experiment of §5.4.2.3.

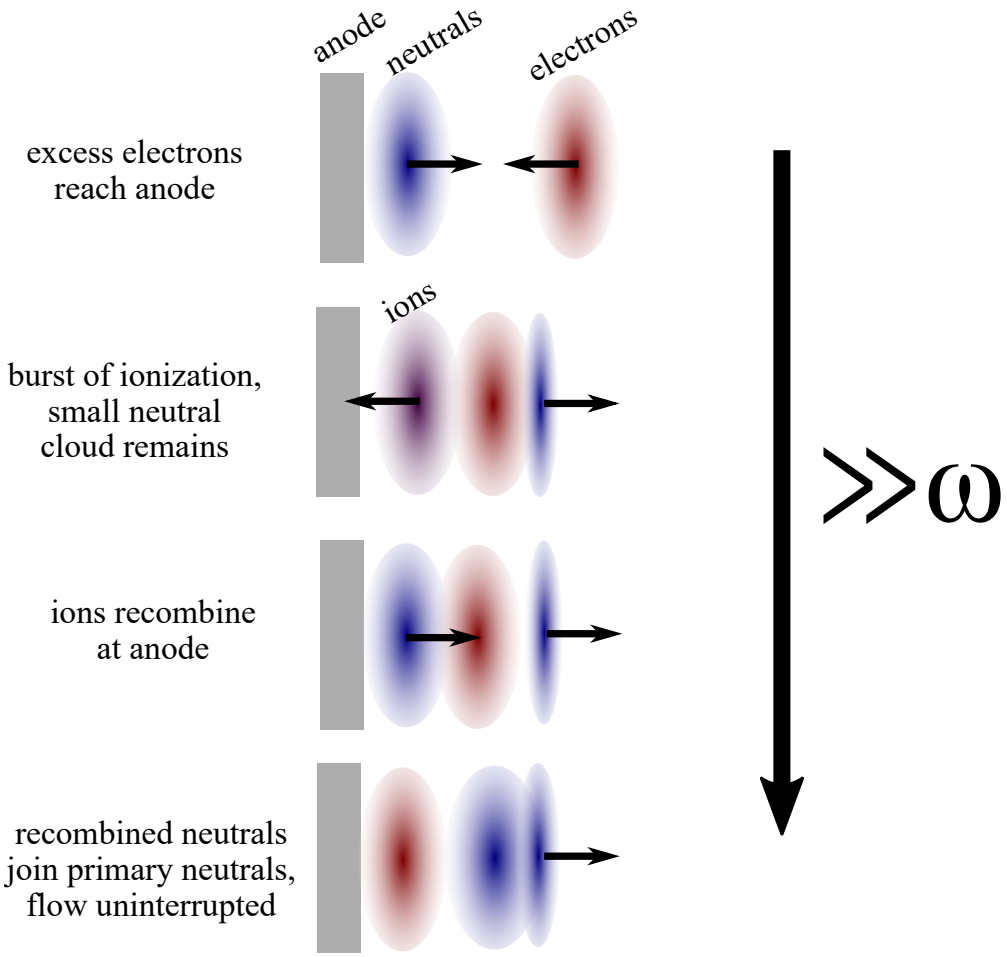

Figure 7.3: A diagram of the fast ion recombination process, where a burst of electrons arriving at the end ultimately does not interrupt the neutral flow due to rapid neutralization of ions on the anode.

For oscillations in the primary neutral population $\tilde{n}_n$, the fluctuations in the entire population (recombined and primary neutrals) for some small recombined neutral lag

θ_r is $i\theta_r\tilde{n}_n$. For our estimated θ_r, this means a nearly 100x reduction in n_n oscillation amplitude and an additional 90° lag. We have previously found that the near-anode ionization process we proposed is consistent with experimental phase data when we ignore this recombination effect (§7.4.1), and we also suspect that the sheath polarity may be fluctuating during a breathing cycle (§7.4.2). A physical picture reconciling these points now becomes clear: a positive sheath enhances ionization and repels local ions such that the lack of recombination exacerbates the (already) reduced neutral density, and a negative sheath reduces ionization and attracts local ions such that recombination boosts the (already) excess neutral density. The alternation of the sheath polarity during the breathing process could therefore minimize the role of ion recombination, explaining the apparently strong and phase-consistent neutral fluctuations we inferred with IBIS. For this reason, we ignore this effect for the models derived later in this chapter. Similarly, we do not consider the ramifications of ions streaming away from the anode when there is a positive sheath.

7.4.4 Ionization Dynamics

Finally, we investigate whether the neutral waves entering the ionization region coincide with the ionization rate. To reiterate, the proposed modified predator-prey mechanism is sustained when neutral holes cause a decrease of ionization in the traditional ionization region, which then consequently sends an electron hole toward the anode. According to this model, θ_{n_n} should lead the ionization rate phase $\theta_{\dot{n}}$ by 90°. In this experiment, θ_{n_n} was found to be 43° and $\theta_{\dot{n}}$ 146°, such that the neutral density fluctuations lead those in ionization rate by 103° ± 60°. Although the uncertainty in this measurement is large, it is nevertheless consistent with our modified predator-prey description. Again, we have found that the physical process we propose is consistent with our experimental observations.

7.4.5 Limitations

In the previous sections, we established three points: the delay in neutral density observed at the ionization region is consistent with electron and neutral transit to/from the anode; the fluctuation in discharge voltage is consistent with electron transit to the anode; and the fluctuation in ionization rate is consistent with neutral transit from the anode. However, the uncertainty on the computed phases makes these observations tenuous, and regardless only circumstantial evidence of this mechanism has been presented.

A foremost inconsistency with this hypothesis is that it is unclear whether the near-anode process prescribed by it is realistic. There is little direct experimental characterization of the Hall thruster anode region [136], and different numerical studies tend to treat this boundary differently and often inflexibly [135]. First, the electron density and temperature in this region are both expected to be small, so a true predator-prey like ionization cycle here is unlikely to occur, as there will never be a "critical mass" of hot electrons to rapidly deplete the neutral gas. However, this is not entirely necessary for the process we proposed: the ionization rate near the anode will fluctuate in response to the downstream predator-prey cycle, even if it is not sustained/reinforced by a local predator-prey process. As we speculated previously, we suspect that it is the phase lag accrued by neutrals and electrons drifting between the two regions that drives the breathing mode, which is ignorant of the nature of the ionization oscillations in either region. Similarly, large-scale sheath potential fluctuations seem unlikely but again this is not absolutely necessary for our hypothesis: small oscillations in V_s can exacerbate near-anode ionization fluctuations due to phasing even without changes in polarity. In this way, these inconsistencies are a matter of scale: the magnitude of ionization and sheath potential fluctuations near the anode is unclear, not their existence. Interestingly, a spectroscopy study by Meezan et al. on a low-power slitted Hall thruster did indicate the presence of strong

low-frequency near-anode neutral gas fluctuations [31].

Additionally, a potential inconsistency with this description pertains to the variation in V_s. Although the calculated phase offset between the sheath potential and the electron density oscillations at the anode were consistent with the modified predator-prey description proposed presently, there is considerable uncertainty unaccounted for in the estimation of V_a and V_{cc}. In particular, V_a is based on the inferred profiles of E_z, which when integrated tend to yield $V_a > V_d$ due to the relatively large axial spacing of LIF measurements compared to the relevant length scales of E_z. Further, $V_{cc} \equiv V_p - V_{c2g}$ relies on high-speed telemetry for V_{c2g} as well as Langmuir probe measurements in the near-plume to provide V_p, but the relevant location to measure the latter is hard to determine. As a result, there is likely considerable uncertainty in V_{cc} that is conceptually difficult to quantify.

Another inconsistency is that numerical simulations of Hall thrusters often assume a constant discharge voltage (with the exception of recent work by Brieda et al. [69]) yet are able to reproduce low-frequency oscillations. It is speculated in this work that the additional ionization resulting from the anode sheath switching polarity, and thus V_d changing, may be an important part of the breathing process. Further, codes often implement sheath conditions differently but again are able to demonstrate breathing. For example, HPHall-2 can "force" the Bohm condition at walls but in general its satisfaction is dependent on the mesh and the macroparticle weighting [137]. One possibility is that the oscillations produced in these simulations are not actually physical or at least do not correspond to the experimental breathing mode. Alternatively, here we have simply proposed that there is a spatial aspect to the predator-prey mechanism that drives it. In this way, we still assume that the breathing mode is fundamentally the result of periodic neutral depletion and refill of the thruster channel. Hall thruster codes may therefore be simulating the same process but with a different energy source, and thus can produce qualitatively similar breathing oscil-

lations without reproducing this near-anode process and accompanying neutral flow modulation. Imposing unrealistic boundary conditions may be one way to fuel these predator-prey oscillations. For example, with Dirichlet potential boundaries at the anode and cathode (cf. Refs. 138 and 139) in the absence of sheath modeling, and for a constant cathode plasma resistance R_c so that $V_a = V_d - V_{cc} = V_d - R_c I_d$, it can be shown that the relationship $\tilde{u_i} \propto$ -$\tilde{n}$ is implied such that the traditional predator-prey model of §6.4.1 is conditionally unstable if $V_{cc} > (m_i/e)u_i u_n \alpha$. In general, $V_{cc} \sim V_d/10$ and $\alpha \equiv n_{n,0}/n_n \sim 10$ such that this inequality will likely hold under some realistic circumstances. This example is not meant to provide real insight into the breathing mode but rather it emphasizes how unphysical conditions could lead to relatively simple growth mechanisms with the predator-prey model framework.

In total, there is some indirect evidence that this anode-related breathing process exists but there still remain some inconsistencies. In general, this process incorporates some of the dynamics of the predator-prey model – in that the production of electron holes and excesses is governed by electron-impact ionization in the ionization zone – but also includes the near-anode ionization that allows for growth by reinforcing fluctuations of the neutral gas.

7.5 Two-Zone Theory

We implement this hypothetical process as a two-zone predator-prey model. That is, we consider two coupled 0D sets of continuity equations, for ions and neutrals in the traditional ionization zone, and for electrons and neutrals near the anode. The evolution of the plasma and neutral populations is largely ignored between these zones, and instead we represent the transit of electrons and neutral particles between the zones with phasors $\mathcal{N}_e \angle \theta_n$ and $\mathcal{N}_n \angle \theta_{n_n}$. It is important to note that this implementation implies a physically unrealistic configuration of the discharge. In particular, we expect that the near-anode plasma density is less than the downstream density, but

since we consider the plasma between the anode and ionization region to be "frozen" here, the electron density will increase near the anode due to ionization.

For plasma density, neutral density, electron velocity, and ionization rate coefficient near the anode denoted n_a, $n_{n,a}$, $u_{e,a}$, and $\xi_{iz,a}$, respectively, the relevant 0D continuity equations assuming quasi-neutrality are as follows:

$$\frac{dn}{dt} = \xi_{iz} n n_n - n\frac{u_i}{L_{iz}} \tag{7.2a}$$

$$\frac{dn_n}{dt} = -\xi_{iz} n n_n + (n_{n,a} - n_n)\frac{u_n}{L_{iz}} \tag{7.2b}$$

$$\frac{dn_a}{dt} = \xi_{iz,a} n_a n_{n,a} + (n - n_a)\frac{u_{e,a}}{\lambda_D} \tag{7.2c}$$

$$\frac{dn_{n,a}}{dt} = -\xi_{iz,a} n_a n_{n,a} + (n_{n,0} - n_{n,a})\frac{u_n}{\lambda_D} \tag{7.2d}$$

Here, we assume that the neutral velocity does not vary spatially, that no ionization or acceleration occurs between the two regions, and that the near-anode region is contained roughly within the anode sheath. The assumption of quasi-neutrality breaks down near the anode but we ignore that here under the assumption that the sheath potential will be somewhat low so only a small disparity in densities exists. Also, it is important to note that the electron continuity equation pertains solely to electrons produced in the ionization region – electrons streaming from cathode to anode are ignored. In reality, recombination at the walls and other effects may limit the number of electrons that belong to this neglected group, or may enhance the neutral density throughout the channel. We expect that the current utilization efficiency is a good representation of the ratio of channel-born to cathode-born electrons; these efficiencies are usually around 80% for modern thrusters [8], which indicates that in fact a minority of electron flux in the channel is sourced from the cathode.

Linearizing these equations yields the following system:

$$\begin{bmatrix} -i\omega & (1-\rho_1)\frac{u_n}{L_{iz}} & 0 & 0 \\ \frac{u_{e,a}}{{}_{iz}L} & -i\omega + \frac{u_n}{L_{iz}} & 0 & -\mathcal{N}_n\angle\theta_{n_n}\frac{u_n}{L_{iz}} \\ -\mathcal{N}_e\angle\theta_n\frac{u_{e,a}}{\lambda_D} & 0 & -i\omega + (2-\rho_2)\frac{u_{e,a}}{\lambda_D} & (1-\rho_3)\frac{u_n}{\lambda_D} \\ 0 & 0 & (1-\rho_2)\frac{u_{e,a}}{\lambda_D} & -i\omega + \rho_3\frac{u_n}{\lambda_D} \end{bmatrix} \times \begin{bmatrix} \tilde{n} \\ \tilde{n}_n \\ \tilde{n}_a \\ \tilde{n}_{n,a} \end{bmatrix} = 0 \quad (7.3)$$

Here, the ρ quantities are density ratios: $\rho_1 \equiv n_{n,a}/n_n > 1$, $\rho_2 \equiv n/n_a < 1$, and $\rho_3 \equiv n_{n,0}/n_{n,a} > 1$. Physically, ρ_1 is the ratio of neutral density near the anode to that in the ionization region, which should be above unity due to ionization. Correspondingly, ρ_2 is the ratio of plasma density in the ionization region to that near the anode, where it should be below unity due to ionization. Finally, ρ_3 is the ratio of neutral density coming from the anode to that near the anode, which we anticipate to be slightly above unity.

The solution of this system is a fourth-order polynomial in ω. Although closed-form solutions for polynomials like this exist, they are notoriously complicated and in this case would not avail an insightful solution. However, assuming $\rho_1 \gg 1$, $\rho_2 \ll 1$, and $\rho_3 \approx 1$, the following somewhat simplified equation results:

$$\begin{aligned} 0 = &\left\{ \frac{\rho_1 u_{e,a} {u_n}^2}{{\lambda_D}^2 L^2}[u_i(3\rho_3 - 1) + u_{e,a}\mathcal{N}_\urcorner\angle\theta_n\mathcal{N}_n\angle\theta_{n_n}] \right\} \\ &-i\omega \left\{ \frac{\rho_1 u_n}{{\lambda_D}^2 L^2}[L u_{e,a} u_n(3\rho_3 - 1) + u_i\lambda_D(2u_{e,a} + u_n\rho_3)] \right\} \\ &-\omega^2 \left\{ \frac{u_n}{{\lambda_D}^2 L^2}[L^2 u_{e,a}(3\rho_3 - 1) + L\lambda_D\rho_1(2u_{e,a} + u_n\rho_3) + \rho_1{\lambda_D}^2 u_i] \right\} \\ &+i\omega^3 \left\{ \frac{1}{\lambda_D L}[L(2u_{e,a} + u_n\rho_3) + u_n\lambda_D\rho_1] \right\} \\ &+\omega^4 \end{aligned} \quad (7.4)$$

It is immediately apparent that several common terms appear in these coefficients. Further, there are some physical relationships between the quantities involved that

may simplify the coefficients even further. In particular, we consider $u_{e,a} > u_i \gg u_n$, and we define $L^* \equiv \lambda_D / L$. Finally, since the phasor quantities appear together and if we assume that the transit of particles between zones is lossless, we combine them as $\angle\theta$. This reduces the equation to the following:

$$\begin{aligned} 0 = & \left\{ \frac{\rho_1 u_{e,a} {u_n}^2}{{L^*}^2 {L_{iz}}^4} [u_i(3\rho_3 - 1) + u_{e,a}\angle\theta] \right\} \\ & -i\omega \left\{ \frac{\rho_1 u_{e,a} u_n}{{L^*}^2 {L_{iz}}^3} [u_n(3\rho_3 - 1) + 2u_i L^*] \right\} \\ & -\omega^2 \left\{ \frac{u_n u_{e,a}}{{L^*}^2 {L_{iz}}^2} [(3\rho_3 - 1) + 2\rho_1 L^*] \right\} \\ & +i\omega^3 \left\{ \frac{1}{L^* L_{iz}} [2u_{e,a} + u_n \rho_1 L^*] \right\} \\ & +\omega^4 \end{aligned} \tag{7.5}$$

7.5.1 Stability Analysis

The stability of this model can be evaluated aided by certain additional assumptions. First, we examine the low-growth limit $\Re(\omega) \gg \Im(\omega)$. Without making any assumptions on θ, the real component of Eq. (7.5) is a sparse quartic and the imaginary component a sparse cubic. Even though the latter is more tractable, complications still arise. For example, at a minimum the discriminant Δ of the polynomial can reveal the nature of any possible roots but here the sign of Δ is not immediately clear because the first-order coefficient has a different sign than the zeroth and third. However, an order of magnitude analysis suggests that $\Delta \ll 0$, which means that there is only one valid root to the cubic in this case. A large ω contradictorily yields $\omega = 0$, but a small ω compared to the zeroth order coefficient assuming $u_{e,a} \gg u_i$ and assuming $\rho_1 L^*$ is relatively small yields

$$\Re(\omega) = \sqrt[3]{\frac{\rho_1 u_{e,a} {u_n}^2}{2L^* {L_{iz}}^3}} \ . \tag{7.6}$$

This expression bears some similarities to the traditional predator-prey model. For instance, there is scaling with u_n/L_{iz}, although here it is ${u_n}^{2/3}$ rather than ${u_n}^{1/2}$. Further, this expression roughly indicates the breathing frequency is the geometric mean of the near-anode electron transit frequency and the ionization zone neutral transit frequency, where the latter is double-weighted. In the traditional predator-prey model, this mean involves the ionization zone ion transit frequency.

In summary, the only readily available solution for Eq. (7.5) in the limit of small growth requires $\sin(\theta)$ must be relatively large. This suggests that neutral particles must significantly lead/lag in phase while traveling from the anode to the ionization zone. However, note that we have assumed $\Im(\omega)$ is small compared to $\Re(\omega)$, which itself is small compared to the zeroth order term of Eq. (7.5). We will return to this assumption in §7.5.2.3.

Next, the limit of high growth is investigated, $\Re(\omega) \ll \Im(\omega)$. In this case, the polynomial is a full and real quartic. To make any analytical progress, we assume θ is near $\pm 90°$; that is, the neutral particles accrue a considerable lead/lag in phase traveling through the channel. As a result, only the zeroth-order coefficient of Eq. (7.5) has an imaginary component. In fact, $\sin(\theta)$ must be zero in this case, which violates the starting premise that there is considerable lag/lead. Over all, then, the high growth limit is either unphysical or requires completely in-phase or out-of-phase θ, which is not consistent with the argument developed in Eq. (6.27). As a result, it seems likely that the growth rate predicted by this two-zone predator-prey model must be small or comparable to the real frequency.

7.5.2 Numerical Study

We have derived a linear model of this two-zone process and shown that it is largely too complicated to easily evaluate its stability. As a result, we now explore the model numerically to evaluate its stability for reasonable input parameters. Although this

approach is less universal than determining analytical stability criteria, it requires fewer model assumptions and anchors the analysis with realistic parameters.

In studying the stability of the proposed model numerically, we generate root locus plots. For a linear perturbation analysis of the model, ω is described with a polynomial with complex roots. We plot these roots in the complex plane, where they trace out trajectories as a function of an independent variable. On this plot, the left half-plane is stable and the right half-plane is unstable. The lower half-plane, corresponding to negative real frequencies, is not unphysical but represents linear perturbations 180° out of phase. When examining these plots, we are mostly trying to determine the number of unstable roots and the real frequencies that correspond with them. Further, we are interested in whether the loci cross quadrants, as this may provide onset criteria of the instability. A notional example of a root locus plot is shown below in Fig. 7.4 with some characteristic loci.

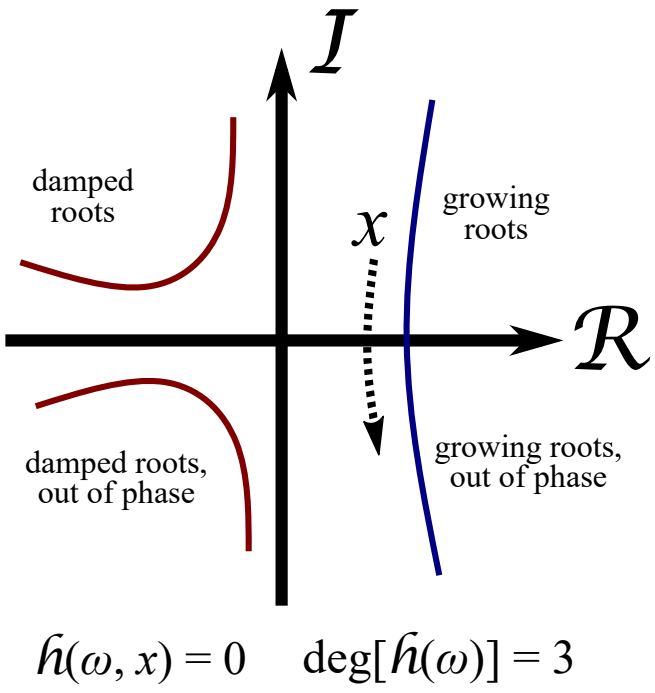

Figure 7.4: An example of a root locus plot with characteristic loci for some third-order polynomial h in ω that is dependent on some other quantity x.

In some cases, we plot the real frequency or growth rate of the fastest growing root as a function of other independent quantities. Here, the root locus plot is a heat map that helps define the stability of the model as a whole with the variation of other parameters.

7.5.2.1 Steady-State Parameters

To evaluate the linear model numerically, relevant steady-state parameters must be known. With the information yielded by IBIS and supplemented by the analyses of §5.3.3.1 and §5.4.2.5, we can calculate these parameters. Specifically, plasma and neutral properties can be averaged spatially within the ionization-acceleration region and temporally throughout a breathing cycle to yield realistic values with which to evaluate the model. These include ion and neutral velocities and densities. Further, densities upstream of the ionization region can be estimated via heavy particle continuity and current continuity, where $\dot{m}$ is the mass flow rate injected at the anode:

$$\dot{m} = A(u_n n_n + u_i n) \ , \tag{7.7}$$

$$I_d = eAn(u_i + u_e) \ . \tag{7.8}$$

One aspect to validating the new model based on the physical premise presented in §7.1 involves experimentally determining the phase lag accrued in the density of electrons and neutrals while transiting the channel, θ_n and θ_{n_n}. The density phase can be determined either directly with TRLIF data or with the phase information extracted from the IBIS results. In the first case, u_n can be integrated across the spatial domain to determine an average transit time from the anode to the ionization region. In the second case, we assume that fluctuations in discharge current respond to changes in density originating in the ionization region such that the phase of n in the ionization region relative to I_d can be used as an approximation of the transit

phase lag of electrons.

Although densities near the anode can be determined with continuity equations, estimating the electron velocity near the anode $u_{e,a}$ is challenging, even given the wealth of information yielded by IBIS. The major difficulty in specifying $u_{e,a}$ is that the sheath conditions at the anode are unclear. We begin by assuming a negative anode sheath such as shown in Fig. 7.5, where ions enter at the Bohm speed u_B and electrons are slightly repelled, as is typical for a warm non-equilibrium plasma [134]. Assuming quasineutrality and a uniform radial distribution of discharge current, the electron velocity can be directly computed anywhere within the LIF domain as

$$u_e = \frac{I_d}{enA} - u_i \ . \tag{7.9}$$

The anode presheath (i), where $u_i = 0$, was often within the TRLIF spatial domain; u_e at this point is perhaps the simplest estimate of the near-anode electron velocity. For our TRLIF experiment on the H9, it was found to be $u_e = 5.7$ km/s. At the sheath edge (ii), quasineutrality no longer holds but by assuming a negative collisionless sheath we can apply $n_e \approx 0.61n$ and $u_i \approx u_B$ [134] to Eq. (7.9) to estimate u_e. Finally, assuming a Maxwellian electron distribution, quasineutrality at the presheath edge, and negligible electron drift compared to T_e, the total sheath potential can be estimated. If the sheath is collisionless, this can then yield a estimate of the electron velocity at the anode (iii). This value is anticipated to be large because only the few fastest electrons manage to reach the anode surface but must carry more than the discharge current to compensate for backstreaming ions.

The phase and zonal information yielded by TRLIF-IBIS also permits an estimate of the average $u_{e,a}$ between the anode and the ionization region as $(\theta_n - \theta_{I_d}) z_{iz} \omega / 2\pi$, where $\theta_n - \theta_{I_d}$ is the phase difference between n and I_d, and z_{iz} is the location of the ionization region. Again here we assume that fluctuations in density in the ionization

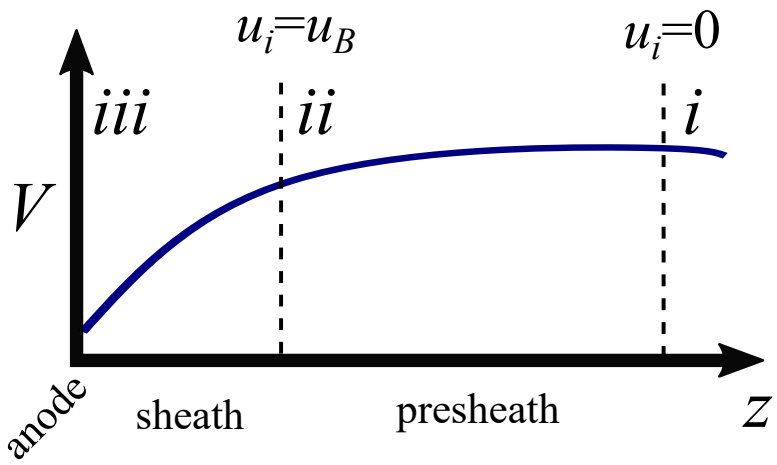

Figure 7.5: A diagram of the anode sheath, with three locations where u_e can be estimated denoted: the presheath edge (i), the sheath edge (ii), and the anode surface (iii).

region are carried to the anode by electrons and correspond to discharge current fluctuations. The instantaneous value will likely be close to this in the presheath but much higher than this in the Debye sheath and at the anode. Nonetheless, it provides a point of comparison for the values of $u_{e,a}$ calculated with the methods outlined previously.

7.5.2.2 Broad Study

Now that we have established how to estimate steady-state quantities, we will now proceed to make these estimates for application to hte two-zone model. For operation at 300 V and 15 A with 15 mg/s of xenon flow – a standard condition for the thruster used in our time-averaged LIF experiments – the ion terminal velocity is roughly 20 km/s based on energy conservation and a typical voltage utilization efficiency of 93% [8]. For a symmetric E_z profile, u_i in the "center" of the acceleration region is closer to $1/\sqrt{2}$ times the terminal velocity, or 14 km/s. Previous studies in similar thrusters have shown neutral velocities to be close to 300 m/s throughout much of the channel [101]. The electron velocity in the ionization-acceleration region is difficult to estimate, but following the approach of Hara et al. and assuming a current utilization

efficiency η_I of about 80%, $u_e \approx (u_i/\eta_I)(1 - \eta_I/\sqrt{2})$, or roughly 7.8 km/s. A similar approach cannot be taken near the anode, and as we discussed before estimating $u_{e,a}$ is quite difficult. As a result, we consider it a free variable in this numerical study. With this information, the steady-state forms of Eqs. (7.2), combined with current continuity, yield downstream neutral and ion densities of 1.9×10^{18} m^{-3} and 2.8×10^{17} m^{-3}, and near-anode neutral and ion densities of 1.3×10^{19} m^{-3} and 3.1×10^{17} m^{-3}. This then means that ρ_1 is 7.0, ρ_2 is 0.9, and ρ_3 is 1.1, which agrees with our previous assessment about their comparison with unity.

Based on the previous discussion and the derivation of the previous section, the free variables in this numerical analysis are θ_n, θ_{n_n}, and $u_{e,a}$. For simplicity, we assume $\theta_n \to 0$, as we expect electrons to travel rapidly from the ionization region to the anode. We can then examine how the real and imaginary components of ω, dictated by Eq. (7.5), evolve as a function of θ_{n_n} and $u_{e,a}$. Figure 7.6 shows this for the fastest-growing of the quartic's four roots. Both the real frequency and growth rate vary several orders of magnitude over the domain of θ_{n_n} and $u_{e,a}$, and the appearance of discontinuities suggest that the root locus structure may contain loops or intersections (multiple roots grow equally fast at some points).

It is interesting to note that there is a region of considerable growth for $u_{e,a}$ near 2 km/s where the real frequencies are close to the anticipated order of magnitude. However, the real frequency and growth rate appear to be independent of θ_{n_n} in this area. But if we examine it closer, as in Fig. 7.7a, very clear trends become apparent. For $u_{e,a}$=2 km/s, the real frequency is clearly directly proportional to $\sin(\theta_{n_n})$, and the growth rate weakly proportional to $\cos(\theta_{n_n})$. Physically, this indicates that the growth is strong regardless of θ_{n_n} but the mode does not support linear oscillations when the neutral density fluctuations are completely in phase or out of phase during transit between zones. The fact that such simple trends appear in an otherwise complex root locus map suggests that a simplified version of the two-zone model, as

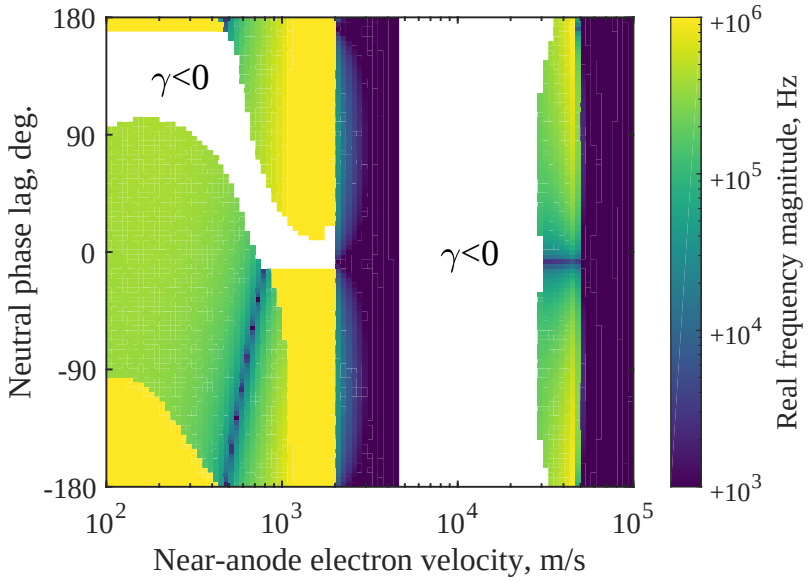

(a)

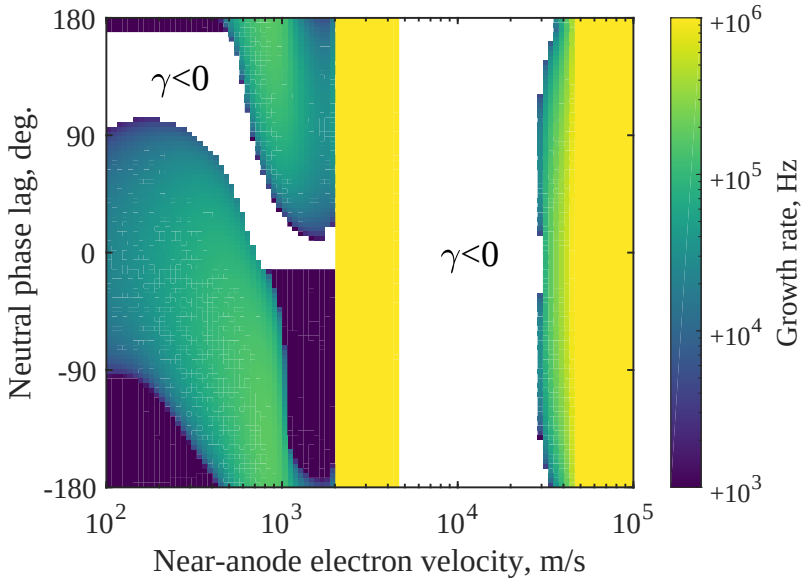

(b)

Figure 7.6: The real frequency (a) and growth rate (b) as a function of neutral density phase lag and near-anode electron velocity. Damped regions are indicated on both plots with red dashed lines.

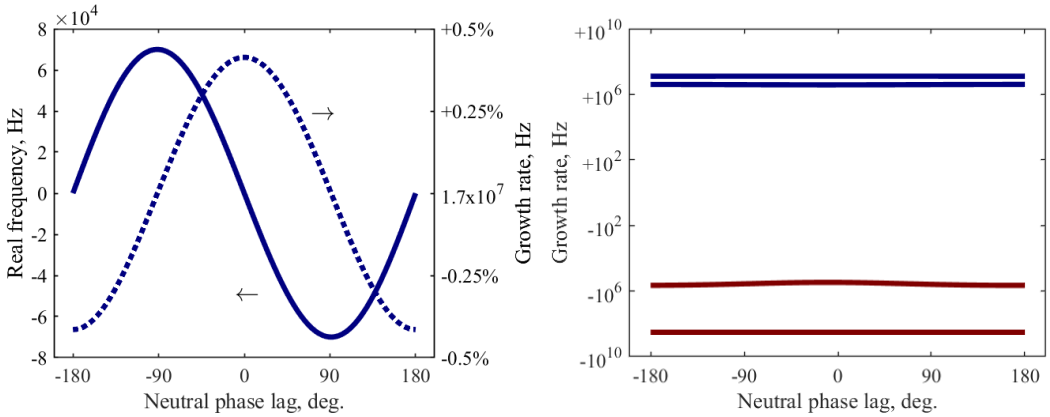

Figure 7.7: The real frequency and growth rate as a function of the neutral density phase lag (a), and the root loci of the two-zone model (b). Both plots assume $u_{e,a}$=0. In (a), the growth rate varies very little with θ_{n_n}, so the ordinate scale is in percentage change from the mean value. In (b), a signed logarithmic scale is used.

we explore in §7.6.

Figure 7.7b shows the root locus curves for $u_{e,a}$ of 2 km/s. All four roots are always complex, with the limiting case that some of them become purely imaginary for θ_{n_n}=0. Further, it is interesting to note that there are in fact two growing roots. Although it is not apparent from Fig. 7.7b, the slower-growing root has higher real frequencies for a given θ_{n_n}, typically around twice as large as those of the fastest-growing root.

Alternatively, we can frame Fig. 7.7b in terms of the effective channel length corresponding to a certain neutral phase lag for a constant neutral velocity. Figure 7.8 shows the real frequency and growth rate of growing roots for $u_{e,a} \approx 2$ km/s as a function of this channel length ("plasma width"). There are multiple growing roots and two trajectories are easily distinguishable. Length scales comparable to the geometric L_{ch} correspond to realistic breathing frequencies, ∼10 kHz. As in Fig. 7.7a, the growth rate, here averaging about 12.6 MHz, is mostly insensitive to plasma length.

Altogether, this broad numerical study indicates that this model does allow for

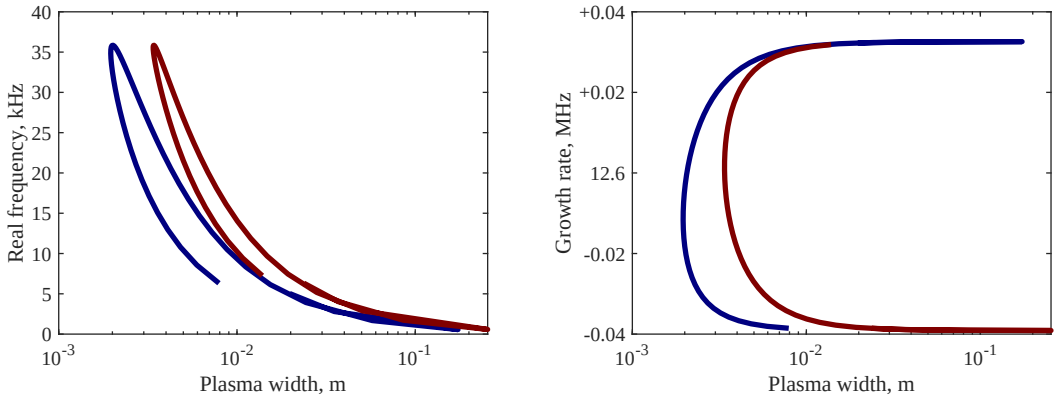

(a) (b)

Figure 7.8: The real frequency (a) and growth rate (b) of growing roots as a function of the effective channel length for $u_{e,a}$ =2 km/s.

growth of the linear instability, and that there are many regions where this growth corresponds to realistic real frequencies. Further, we found simple trigonometric trends in ω for one such region, which suggests that a simpler model may be adequate in some circumstances. This study encourages us that this two-zone model may be a possible explanation of the breathing mode. To increase our confidence in the model, we move on to narrower numerical experiments.

7.5.2.3 Narrow Study

Steady-State Values

With the information of §5.4, the steady-state quantities needed to evaluate the two-zone model can be estimated. That is, plasma and neutral properties can be averaged spatially within the ionization-acceleration region and temporally throughout a breathing cycle to yield realistic values with which to evaluate the two-zone model. The results are summarized in Table 7.2.

Near-Anode Electron Velocity

Estimating the electron velocity near the anode is still challenging, even given the wealth of information yielded by IBIS. In the previous numerical study, we evaluated

Table 7.2: A summary of the steady-state parameters measured or inferred for use with the two-zone model.

u_n	310 m/s
u_i	8.5 km/s
u_e	7.6 km/s
n_n	1.4×10^{19} m^{-3}
n	5.4×10^{17} m^{-3}
$n_{n,a}$	2.2×10^{19} m^{-3}
n_a	1.6×10^{17} m^{-3}

a wide range of $u_{e,a}$, from 0.1 to 100 km/s. However, the results of Chapter V can be used to narrow this region significantly. Following the process described in §7.5.2.1, we can use current continuity and our Xe II LIF measurements to estimate the presheath electron velocity as 5.7 km/s. At the sheath edge, we apply $n_e \approx 0.61n$ and $u_i \approx u_B$ to Eq. (7.9) such that $u_{e,a}$=11.6 km/s. Finally, the total sheath potential can be estimated as ∼10 V as discussed in §7.4.2. Given that the presheath drop alone should be roughly $2T_e \lesssim 10$V, this seems reasonable. If the sheath is collisionless, this can then yield a estimate of the electron velocity at the anode: $u_{e,a} = 2143$ km/s. To reiterate §7.5.2.1, this value is so large because only the few fastest electrons manage to reach the anode surface but must carry more than the discharge current (to compensate for backstreaming ions).

The phase information of Fig. 5.18a combined with the length data of Fig. 5.16 also permits an estimate of the average $u_{e,a}$ between the anode and the ionization region as $z_{iz}\omega(\theta_n/2\pi)$, where z_{iz} is the location of the ionization region. This value is found to be about 29 km/s, which is plausible given that $u_{e,a}$ is predicted to be lower than this for a large region (presheath) and much higher than this for a small region (sheath). Going forward, we choose to consider $u_{e,a}$ in the presheath, and thus limit the range of possible values from 5.7 to 11.6 km/s.

Density Lag

As discussed in §7.5, one aspect to validating the two-zone predator-prey model

is to experimentally determine θ_n and θ_{n_n}. These are the phase lags accrued by electrons traveling from the ionization region to the anode, and by neutrals traveling oppositely. In analytical terms, this phase lag plays an important role in coupling the downstream and upstream continuity equations. The density phase lags can be determined by Figs. 5.14 and 5.18a. In the former, u_n can be integrated across the spatial domain to determine an average transit time from the anode to the ionization region. This is found to be 862°, or a lag of 142°. In the latter, the phase lag of n from the ionization region relative to I_d can be used as an approximation of the transit phase lag of electrons. From Fig. 5.18a, this lag is roughly 6.5°.

Model Validation

Armed with this information, the steady-state parameters of Table 7.2 can now be used to numerically evaluate the two-zone model. The two-zone model predicts four complex roots for each $u_{e,a}$ used with the given steady-state parameters. In all cases, two roots were damped and two unstable. Of the latter, universally one had a large growth rate but low real frequency, and the other moderate real frequency and growth rate. Figure 7.9a shows the root loci for the average value of $u_{e,a}$, portraying these trends. The moderate growing root is the one of interest in this case, and Fig. 7.9b shows the variation of the real and imaginary part with electron velocity. As it depicts, both quantities are certainly $\sim$10 kHz, averaging about 13 kHz over the studied range of $u_{e,a}$, with the growth rate showing more sensitivity to $u_{e,a}$.

The real frequency predicted by the two-zone model is somewhat lower than the experimentally measured value of 16 kHz but is certainly close enough to be physically plausible. The growth rate is nearly identical to the real frequency, which suggests that neither the high nor low growth limits as discussed in the linear stability study are applicable to the thruster operating condition considered here. However, a moderate growth rate suggests to us that the linear analysis is still meaningful, compared

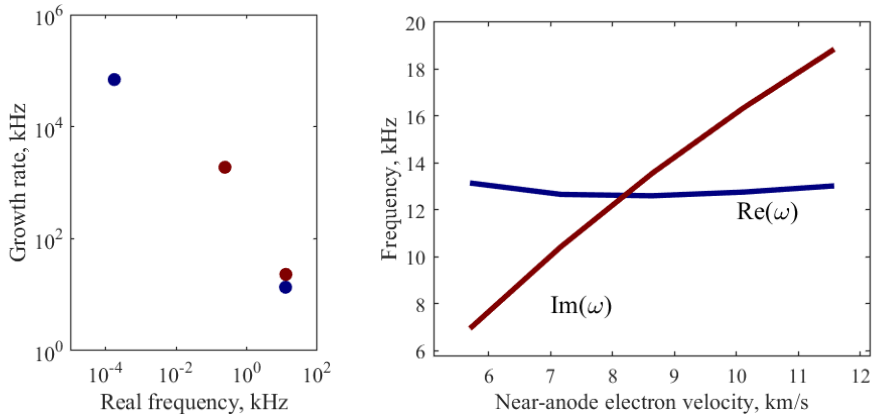

(a) (b)

Figure 7.9: A sample of root loci for one value of $u_{e,a}$ (a), and the variation in the real frequency (blue) and growth rate (red) with electron velocity (b).

to a MHz or GHz growth rate that suggests largely nonlinear development of the instability. In all, this limited experimental validation provides some evidence that the two-zone predator-prey model may be capable of capturing breathing behavior in real thrusters. However, further refinement of the model and/or the experimental validation technique are still needed.

7.6 Simplified Two-Zone Theory

The four-equation two-zone model of the breathing mode encapsulated by Eq. (7.5) clearly allows for unstable solutions (§7.5.2.2) and predicts realistic breathing frequencies for experimentally-derived steady-state inputs (§7.5.2.3). Further, the physical basis for this model is supported by circumstantial experimental measurements (§7.4). However, the complexity of this model limits its predictive capabilities. For instance, only an approximate expression for the real frequency was found, Eq. (7.6). We now present a simplified two-zone model that presents much more tractable analytical expressions for the growth and real frequency of the breathing mode. We follow this with a brief numerical study, and finally we compare this model with high-level trends in low-frequency oscillations.

7.6.1 Linear Analysis

The traditional predator-prey model considers only two types of populations: inflowing and resident/outflowing. The former are entering the 0D box, and the latter exist inside the box and advect out of it. Specifically, the model considers an incoming neutral flow given by $n_{n,0}$ and a resident/outflowing population given by n_n. Likewise, there is a resident/outflowing population of ions given by n. In the two-zone model, we allow for inflowing electrons near the anode. In that model, we connect the outflowing neutrals at the anode to the inflowing ones at the ionization zone, and similarly connect the outflowing electrons at the ionization zone to the inflowing ones at the anode. It therefore becomes less meaningful to draw the distinction between inflowing and resident populations, since the outflowing particles of one region become the inflowing particles of another. As a result, we can effectively remove one continuity equation in each region such that we only consider neutral continuity at the anode and ion continuity at the ionization region, where $\tilde{n}_a = \mathcal{N}_e \tilde{n}$ and $\tilde{n}_n = \mathcal{N}_n \tilde{n}_{n,a}$. Following notation we have used before, $\mathcal{N}_e$ and $\mathcal{N}_n$ are complex amplitudes where $\arg(\mathcal{N})$ represents the electron and neutral transit phase lags, θ_n and θ_{n_n}. In this way, we relate n_n and n_a to $n_{n,a}$ and n such that only these latter quantities must be known. In doing this, we are ignoring differences in neutral densities and plasma densities (and ionization rate coefficients) between the near-anode and ionization regions, and thus we concede some physical accuracy (as in the full two-zone model of §7.5) for simplicity. The system then includes the following equations:

$$\frac{dn}{dt} = \xi_{iz} n n_{n,a} - n\frac{u_i}{L_{iz}} \tag{7.10a}$$

$$\frac{dn_{n,a}}{dt} = -\xi_{iz} n n_{n,a} + (n_{n,0} - n_{n,a})\frac{u_n}{\lambda_D} \tag{7.10b}$$

As before, n is the plasma density in the ionization zones while $n_{n,a}$ is the neutral density near the anode. These equations are not dissimilar to §6.4.1 except we assume

$n_a = n$ and $n_n = n_{n,a}$ in the steady state, and each equation acts on different length scales.

With this approach, we linearize Eqs. (7.2):

$$\begin{bmatrix} -i\omega & -\mathcal{N}_n \frac{u_n}{\lambda_D}(\rho_1 - 1) \\ \mathcal{N}_e \frac{u_i}{L_{iz}} & -i\omega + \frac{u_n}{L_{iz}} + \frac{u_n}{\lambda_D}(\rho_1 - 1) \end{bmatrix} \times \begin{bmatrix} \tilde{n} \\ \tilde{n}_n \end{bmatrix} = 0 \ . \tag{7.11}$$

Note that a distinction in length scales between the two regions is still made: the near-anode length is approximated as the Debye length λ_D and the ionization region length is defined as L_{iz}. The determinant of the square matrix in Eq. (7.11) yields a quadratic in ω,

$$L_{iz}\lambda_D\omega^2 + iu_n[L_{iz}(\rho_1 - 1) + \lambda_D] - \angle\theta u_i u_n(\rho_1 - 1) = 0 \ , \tag{7.12}$$

where like in Eq. (7.5) the $\mathcal{N}_e$ and $\mathcal{N}_n$ terms collapse into the phasor angle $\angle\theta$. Assuming that $\rho_1 \gg 1$ and $\Re(\omega) \sim \Im(\omega) \sim u_n/L_{iz}$, where this last similarity is justified empirically in §5.3.3.3 and §7.5.2.3, we find

$$\Re(\omega) \approx \frac{u_i}{L_{iz}} \sin\,\theta \ , \tag{7.13a}$$

$$\Im(\omega) \approx \frac{u_i}{L_{iz}} \cos\,\theta \ . \tag{7.13b}$$

Further, assuming that θ is dominated by the transit of neutral particles across the channel, we can substitute it as $\Re(\omega)L_{ch}/\langle u_n\rangle - 2\pi\mathrm{N}$ where $\langle u_n\rangle$ is the average neutral velocity in the channel, L_{ch} is the distance between the anode and the ionization region (considered here an effective rather than geometric channel length), and N is some integer that accounts for the fact that it may take multiple breathing cycles for neutrals to transit the channel. Assuming strong growth, we expand the trigonometric

part of Eqs. (7.13a) and (7.13b) to zeroth order and find

$$\Re(\omega) \approx 2\pi \mathrm{N} \frac{u_n}{L_{ch}} \ , \tag{7.14a}$$

$$\Im(\omega) \approx \frac{u_i}{L_{iz}} \ . \tag{7.14b}$$

Here we have assumed that the ratio $(u_i/L_{iz})/(u_n/L_{ch})$ is much greater than unity. This is not unreasonable, as physically it is the ratio of the ion transit rate through the ionization region, $\sim$100 kHz, to the neutral transit rate across the channel, $\sim$1 kHz. Equation (7.14a) physically implies that the real frequency scales like the neutral transit rate through the channel, which mirrors the scaling of the traditional predator-prey model (Eq. (3.3)). Equation (7.14b) physically implies that the growth rate scales like the ion transit rate through the ionization region.

7.6.2 Limitations

This simplified two-zone theory is attractive for its predictive power and simplicity. However, there are several caveats to consider. First, this model is essentially a "stretched out" version of Fife et al.'s predator-prey process with additional phasing between densities, so we assume that the plasma properties near the anode (the upstream side of the stretched 0D domain) are identical to those near the ionization-acceleration zone (the downstream side of the stretched 0D domain). In reality, we expect the plasma at either end of the thruster channel to be significantly different.

Second, although we have presented several arguments couched in experimental measurement for it, there is no direct evidence that significant ionization occurs in the near-anode zone. Further, the simplified model we derived depends trigonometrically on $\theta \approx \theta_{n_n}$, and so some physical configurations implied by this model are indistinguishable. That is, a long L_{ch} such that $\theta \approx \theta_{n_n} > 2\pi$ will yield the same ω as $\theta \approx \{\theta_{n_n} \bmod 2\pi\}$, which corresponds to a much shorter L_{ch}. In this way,

any apparent agreement between the simplified two-zone model and our experimental measurements does not suggest that there is in fact non-negligible ionization near the anode, but rather offers the possibility that there is a closer upstream zone where the neutral flow is being modulated. It is imaginable, then, that this two-zone model could capture coupling between the peaks of a bifurcated (downstream) ionization zone. However, within the scope of the measurements described in the previous chapter, and without further evidence, this remains speculation.

Finally, there is the risk that this model has sacrificed too much fidelity in the name of simplicity. For instance, we have assumed there is strong positive growth such that θ is small but this is a numerical convenience here, not a physical feature of this model. It is possible, then, that Eqs. (7.13a) and (7.13b) require additional expansion, or even that the assumptions leading to those equations are unjustified. In general, this touches upon the question of whether a zero-dimensional model is even capable of sufficiently describing the breathing mode. Although it is desired to describe this phenomenon as simply as possible, it is not guaranteed that an intuitive and analytically transparent model is possible. Many assumptions have been made in deriving this simple two-zone model, and even so we expect many more spatial effects to exist in the channel that were not addressed at all. If nothing else, then, the simplified two-zone model suggests that a spatial component of some form is necessary to describe the breathing mode with any remote accuracy, and thus it indicates that a one-dimensional model is likely required at a minimum to rigorously capture the breathing mode.

7.6.3 Model Predictions

Even though the fidelity of the simplified two-zone model may be poor, we can still examine its predictions in terms of the frequency scaling it dictates and the physical trends it implies. In this way we can still evaluate the usefulness of this new model,

even if we suspect that it is not a complete description of the breathing mode.

7.6.3.1 Frequency Scaling

Armed with our simplified expressions for ω given by Eqs. (7.14), we can evaluate the frequency scaling of the two-zone model compared to our experimental data, as in §5.3.3. Figure 7.10 shows this comparison for various N. The predicted frequencies for N=2 are quite close to our measurements and the model is apparently more sensitive to CFF than we found for other models in Chapter VI, with a slope of nearly 0.2 Hz/Hz. For each N, the correlation coefficient is >0.99 with a null probability of 3%. This means that the correlation between predicted and measured frequencies is very strong and significant. In fact, of the breathing mode theories examined in this work, the two-zone model is only bested in terms of correlation by the neutral drift transit frequency, but unlike that quantity, Eqs. (7.14) allows for growth. The difference in magnitude between the predicted and measured frequencies is likely in part due to the fact that Xe I LIF data was not taken all the way to the ionization zone, so our estimate of u_n is incorrect.

7.6.3.2 Dynamic Behavior

In Chapter V, we not only considered the frequency scaling of each existing theory but also the dynamic criteria for them. In the case of this simplified two-zone model, we have already extensively examined the evidence supporting its existence in §7.4. Here, we will review this evidence as it applies to the simplified model. The criteria for the two-zone model distilled from §7.4 are as follows: the phase of neutrals entering the ionization region is consistent with electron transit to the anode, ionization at the anode, and neutral transit to the ionization region; recombination at the anode is slower than the characteristic neutral transit time there; and neutral density fluctuations should lead those in ionization rate by 90° in the ionization region.

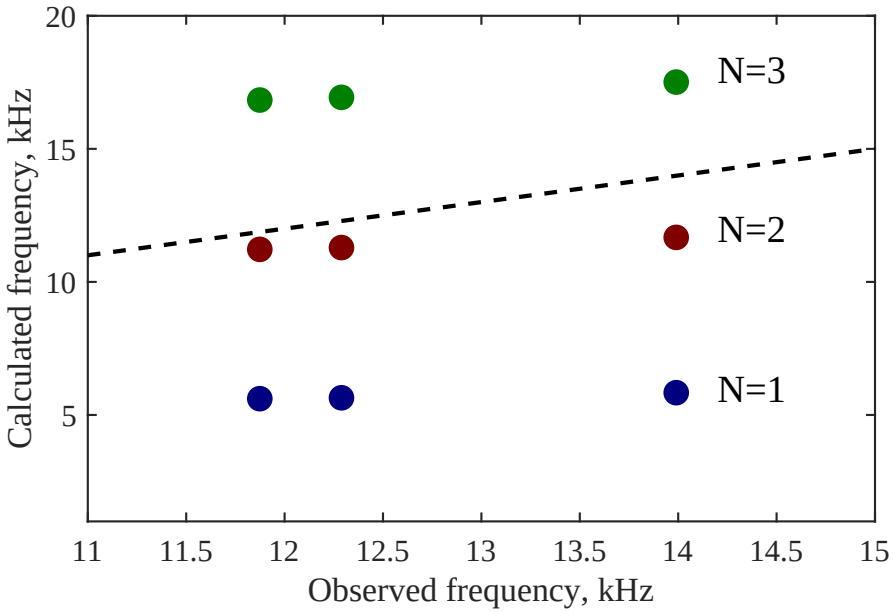

Figure 7.10: A comparison of the measured breathing frequencies and those predicted by the two-zone model, to scale and with a line of perfect correlation.

First, knowing θ_n, θ_{I_d}, and $u_n(z)$, we were able to calculate the phase lag associated with electrons/neutrals streaming across the channel, and found it be 147°±29°. Our direct measurement of $\theta_{n_n} - \theta_n$ was 129°±57°, and thus our experimental data is consistent with the phase of particles transiting the channel according to the two-zone model.

Next, we considered ion recombination at the anode, which we proposed would attenuate ionization there by $i\theta_r\tilde{n}_n$. By estimating the relevant quantities, recombination should contribute a 100x reduction in n_n oscillations and an additional 90° lag. In short, this indicates that we predict recombination to not be much slower than neutral transit through the near-anode region. In this way, this criterion is not met. However, our simplified two-zone model does not account for sheath potential fluctuations, and as we discussed in §7.4, this effect may be sufficiently strong to reduce the impact of recombination. As a result, although this criterion is not technically met, we believe that it may not be physically significant.

Finally, based on our measurements of θ_{n_n} and $\theta_{\dot{n}}$ we estimated the phase lag

between the two to be 103°±60°. Although the uncertainty on this value is quite high, it is consistent with the anticipated 90° lag, and thus this criterion is met within the certainty of our experimental data.

7.6.3.3 High-Level Trends

We now give some thought to the predictive power of Eqs. (7.14a) and (7.14b). First, the real frequency should increase with neutral speed, which likely will scale with anode temperature. So operating conditions with a higher steady-state thruster temperature – typically those at higher voltages – will lead to faster breathing oscillations. Second, L_{ch} is dictated by the position of the ionization region, which is typically upstream somewhat of the acceleration region, which itself is near the maximum radial magnetic field strength. In this way, the physical channel geometry and magnetic field topography dictates a nominal breathing frequency. However, studies have shown that the discharge can shift due to local pressure effects [64] and changes in magnetic field strength [140]. The exact mechanisms behind these trends are not well understood, so it is hard to relate this back to Eq. (7.14a) to more fully describe the high-level influence of L_{ch}. However, we assume that $L_{ch} \propto P^{-1}$, such that higher pressures push the discharge inward, reducing the effective channel length.

The growth rate is a function of the ion velocity and ionization region length, and if we assume the linear growth is representative of the nonlinear oscillation amplitude, we can estimate the strength of the breathing mode as a function of these parameters. The ion velocity is largely controlled by the discharge voltage, although the anode sheath conditions, cathode coupling, and ionization-acceleration region overlap presumably also play a role. In general we can speculate that a higher discharge voltage will lead to stronger breathing, while increased cathode coupling voltage (due perhaps to cathode placement) will reduce breathing strength. The length of the ionization region, like its location, is hard to predict, and thus the effect of L_{iz} on the growth

rate is unclear.

It is important to clarify the factors dictating the location of the ionization zone and its width, as these are two parameters that are intimately linked to the results of the simplified two-zone model. This is a non-trivial problem, and although rules of thumb exist [78], there are few rigorous descriptions of the structure of the Hall thruster discharge. Instead of tackling this problem completely, we present here a rudimentary description of the ionization region location and width for the purpose of comparison with the simplified two-zone breathing mode model. First, we presume that the acceleration region is located at the position of maximum radial magnetic field. The separation between this region and the ionization zone is likely a function of the widths of both regions, the discharge voltage, and other parameters, but here we assume that it is mostly an inverse function of the discharge current $z_{iz} \sim {I_d}^{-1}$. Physically, for a given current utilization efficiency a certain amount of ion current must be generated in the acceleration zone (where electron current is low) to sustain the discharge. As the discharge current increases, more ion current must be generated, which may be accomplished by less overlap (more separation) between the ionization and acceleration zones. In this way, more ions are fully accelerated, producing more current.

The width of the ionization region can be described as the ionization mean free path, $u_n n_n / n f_{iz}$. We can further define $n f_{iz}$ by assuming that electron current is much greater than ion current in the ionization zone ($I_d \approx I_e$) and that I_e is largely dictated by the advancement of electrons along magnetic field lines with ionizing collisions. In this way, $I_e \approx e n f_{iz} r_L$, where r_L is the electron Larmor radius, equal to the incremental advancement of electrons per ionization event. The ionization region width then becomes

$$L_{iz} \sim \frac{I_d B_r}{u_{th}} \ , \tag{7.15}$$

where u_{th} is the electron thermal velocity. We assume that u_{th} is a function of V_d,

since ${u_{th}}^2 \propto T_e \approx V_d/10$ [78] for temperatures in eV. Altogether, the ionization region length varies $\sim I_d B_r/V_d$. Note that we have ignored the order of dependence on these quantities (e.g. V_d rather than $\sqrt{V_d}$) since in many cases the exact functional relationship is unclear so retaining the dependence is arbitrary.

7.6.3.4 Phenomenological Model

If we combine all of the high-level scaling trends, we can produce a rough phenomenological breathing mode model:

$$\Re(\omega) \sim V_d(T_n) I_d(L_{ch}) P(z_{iz}) \ , \tag{7.16a}$$

$$\Im(\omega) \sim \frac{V_d(u_i, L_{iz})}{V_{cc}(u_i) B_r(L_{iz}) I_d(L_{iz})} \ . \tag{7.16b}$$

There are some immediate successes apparent in these phenomenological forms. First, assuming that $\Im(\omega)$ is representative of the amplitude of low-frequency oscillations, we see that $\gamma \sim {B_r}^{-1}$, which agrees with the universal trend that breathing oscillations weaken with increasing magnetic field strength [14]. Second, we recover the direct proportionality of the real frequency and pressure, as we observed ourselves by varying the CFF. Third, there may be some evidence for $\Re(\omega) \sim V_d$ scaling in the literature [36, 123], although admittedly different trends have be found in different studies [14]. Likewise, $\gamma \sim V_d$ may be true for the H9 in some cases [123].

Despite the simplicity of this streamlined two-zone model, there are still many terms in Eqs. (7.16) that are not simple to estimate or cannot easily be compared to trends identified in the literature. This challenge is likely not at all related to the fidelity of the simplified two-zone model but rather to the fact that most plasma and neutral parameters of interest in a Hall thruster are expected to be inter-related and have complicated functional dependencies, so producing such a phenomenological model for any given parameter – let alone ω – may be analytically intractable.

Nonetheless, we do find some successes in Eqs. (7.16a) and (7.16b), which may warrant further investigation.

7.7 Summary

In this chapter, we proposed a physical process by which the neutral gas flow is modulated in the Hall thruster channel, leading to the growth of a predator-prey-like process in the ionization zone. Specifically, we promulgated a "two-zone" description, in which there are coupled ionization fluctuations near the anode and in the traditional ionization zone. In this physical picture, we imagine that the phase lag of electrons upstreaming and neutrals downstreaming is critical for the communication between these regions, and that this communication drives the breathing mode.

Following our qualitative presentation of this process, we provided experimental evidence for its existence. We examined electron and neutral phasing, anode sheath dynamics, recombination at the anode, and ionization phasing. We found that in most cases our measurements supported this two-zone process. However, our experimental data could not confirm that this process drives the breathing mode.

Our next step, then, was to derive a zero-dimensional two-zone model and examine its stability analytically and numerically. We found that such a model, although complicated, could yield some analytical approximations for ω. Further, broad numerical studies revealed that this model widely predicted growth, and a narrower study informed by our experimental data produced realistic ω.

Finally, we simplified our two-zone model to allow for more extensive linear analysis. We derived a simple expression for ω that, although slightly insensitive, accurately reflects observed trends in breathing frequency. We related this model to high-level thruster parameters and likewise found good correspondence between empirical trends and the model. Altogether, we find that the two-zone process is experimentally-justified, the resulting model is a realistic representation of the breathing mode, and

meaningful predictions of oscillation trends are possible with this model.

CHAPTER VIII

Conclusions and Future Work

8.1 Summary of Work

We have conducted an investigation of the Hall thruster breathing mode. In doing this, we have examined this phenomenon from a theoretical and experimental perspective, and have leveraged simple numerical studies to evaluate our findings. We now summarize these efforts.

To start, we conducted experimental studies of the breathing mode to better characterize its dynamic properties. A sample-and-hold TRLIF setup was implemented for measuring ion and neutral VDFs on the timescale of the breathing mode. We developed a method for determining various plasma parameters from this information, referred to as IBIS. However, this approach requires very precise determination of velocity moments (measured with LIF), as well as a careful numerical analysis to avoid singular solutions. We were able to demonstrate that the TRLIF system successfully captured the evolution of the IVDF in a Hall thruster over a breathing cycle, and further that the IBIS method could be used to meaningfully infer additional plasma parameters.

Once we had established the TRLIF-IBIS approach as sufficient for characterizing the breathing mode, we conducted several experiments to both evaluate existing breathing mode theories and yield insight into the physical processes occurring in a

Hall thruster discharge. First, we took time-averaged LIF data for xenon neutrals and ions while varying the cathode flow fraction of the thruster to induce changes in the breathing frequency. Using IBIS, we were able to estimate a wide range of steady-state plasma and neutral properties for each condition, such that we could predict the breathing frequency according to different existing theories of the instability. In comparing these predicted frequencies to those experimentally measured, we could judge the accuracy of each proposed mechanism. We found that a traditional predator-prey and neutral gas instability were both in rough agreement with the measured frequencies, both in terms of magnitude and trend with varying cathode flow fraction, but were fairly insensitive. A neutral drift instability showed the best correlation but has little theoretical justification.

Next, we performed time-resolved studies of the thruster at a single oscillatory operating condition. Using both xenon neutral and ion LIF supplemented with IBIS, we inferred a wide variety of plasma and neutral parameters as a function of axial position and breathing cycle phase. Not only did this data indicate which quantities fluctuated in response to the breathing mode but also the phase relationships between them and the spatial evolution of fluctuations. Altogether, this data provided further evidence to suggest that the traditional predator-prey process and resistive instability were inadequate descriptions of the low-frequency oscillations. We also observed significant fluctuations in the neutral density upstream of the ionization zone. This experimental finding later became the foundation for more theoretical work.

Next we reviewed existing theories for the breathing mode and chose one of the most prominent and successful, the predator-prey model, as a starting point for theoretical study based on our experimental findings. We identified the major shortcomings of this model – in particular a lack of linear growth – and devised several variations of the model to explore possible mechanisms for incorporating this growth. The model was examined as found in the literature (ion and neutral continuity), and

then cumulatively by adding ion momentum conservation, electron energy conservation, and Ohm's law. None of these models were found to be linearly unstable for physically meaningful steady-state input parameters. However, two more cases were examined: with deformation of the ionization region using an "ionization front" model, and with modulation of the neutral inflow density. Linear perturbation analysis and 0D numerical simulation indicates that both of these models can be unstable.

Based on this experimental and theoretical evidence, we proposed a physical process by which this neutral flow modulation could occur. Specifically, we suggested that two coupled ionization instabilities – one near the anode, the other near the traditional ionization zone – could be responsible for the breathing mode. We referred to our experimental phase measurements for support of this hypothesis, and found good agreement between the measured neutral density phase at the ionization zone and the corresponding phase that would result from this so-called "two-zone" model. We then proceeded to develop a zero-dimensional theory to correspond with this physical description. Using four continuity equations coupled by an electron lag $\mathcal{N}_e$ and neutral lag $\mathcal{N}_n$, we were able to derive an approximate expression for the real frequency, and observed that it bore much of the same scaling as the traditional predator-prey model. Unlike its predecessor, numerical studies of this model using a wide estimated range of parameters as well as a more narrow experimentally-derived set of values demonstrated that this system could be linearly unstable. Further, estimating ω using experimental steady-state values yielded a real frequency very close to that measured, adding further support that this model could describe the breathing mode. Finally, a simpler form of this model was derived and expressions for the real frequency and growth rate determined.

8.2 Implications of Work

The ramifications of this work can be described in three ways. First, the experimental techniques developed and applied in this investigation hold promise for new and varied experiments beyond those pertaining to the breathing mode. Second, we have systematically found evidence that existing breathing mode theories are inaccurate for the device and operating conditions we explored, and have provided an alternative that matches our experimental measurements. And third, we have presented a qualitative and analytical framework with which to increase our predictive understanding of low-frequency oscillations.

8.2.1 Experimental Techniques

In Chapter V we summarized our evaluation of existing high-speed diagnostics for the purpose of characterizing the breathing mode. A major challenge for many diagnostics is that they must be able to access the thruster channel plasma, which requires them to have adequate spatial resolution yet also minimally perturb the thruster. Not unsurprisingly, of the three diagnostics considered, two could not meet this requirements. However, we developed a new approach, IBIS, using time-resolved laser-induced fluorescence to yield a wide variety of plasma parameters that are otherwise inaccessible. Although this approach has precedence in a study by Pérez-Luna et al., until the present work it had never been applied in a time-resolved sense nor had it been extended to measure plasma density. In the course of Chapter V, we showed how IBIS can be used to determine phase relationships between quantities and how the spatial structure of the plasma evolves in time. We even demonstrated that this method can be used in a time-averaged sense for identifying the ionization and acceleration regions. In parameter studies, this method can then be used to quantify the spatial reorganization of the discharge as operating parameters are varied.

This diagnostic technique could easily be applied to other experiments or with

other LIF setups. For instance, in Appendix H we show how electron transport can be characterized non-invasively using the IBIS technique, and further that it can be done in a time-resolved sense. In this way, novel measurements can be made, like in this example the time-varying anomalous electron collision frequency. But even mundane measurements can benefit from this work. As Pérez-Luna et al. demonstrated, not accounting for ionization when determining the electric field strength from LIF data can lead to noticeable error. Alternatively, using the numerical techniques developed in the present work, IBIS can be used to determine the electric field strength and ionization frequency simultaneously with no additional experimental burden.

8.2.2 Theoretical Understanding of the Breathing Mode

Collectively, the experimental and analytical work of Chapters V and VII have increased our understanding of the Hall thruster breathing mode from a theoretical standpoint. First, the frequency scaling study and the time-resolved data indicated that the traditional predator-prey model, the prevailing qualitative explanation of the breathing mode in the literature, and a resistive instability, an alternate description that has been studied periodically, do not accurately portray the breathing mode. In and of itself, this is a significant result, as we have shown in the case of the predator-prey model that it is fundamentally incompatible with the measured oscillatory behavior of a Hall thruster discharge. Even though there are several studies in the literature that point out the theoretical shortcomings of the predator-prey model, our work is the first direct experimental evidence of the model's limitations.

However, we have also proposed a new model that retains the fundamental physics of the predator-prey process – which generally leads to accurate predictions of $\Re(\omega)$ – but incorporates the physical effects illuminated by our experiments to overcome the limitations we found in the traditional model. Further, we have found evidence in our experimental data that the process encapsulated by this model does in fact

occur. In judging the stability of this model, we showed numerically that it not only *can* predict growth but in fact predicts realistic real frequencies and a growing linear oscillation when evaluated for experimentally-determined steady-state input parameters. In short, we have proposed an alternative breathing mode process, supported it with experiments, and showed that a linear model of this process agrees with measured oscillatory behavior. In this way, we have provided the foundation for a new explanation of low-frequency oscillations in Hall thrusters that does not stray too far from the widely-embraced predator-prey model but agrees with experimental measurements in ways that the traditional model does not. Although the fidelity of this model is questionable, if nothing else its success by inclusion of a spatial effect serves as an indication that a one-dimensional description of the breathing mode is necessary. One of the ultimate goals of this work was to increase our understanding of the stability of Hall thrusters by exploring the breathing mode, and in producing this new model, we believe we have provided a more accurate and insightful physical description of this instability.

8.2.3 Predictive Understanding of the Breathing Mode

Another goal of this work was to increase the predictive capabilities of our current understanding of the breathing mode. In a sense, the first line of defense against unreliable performance of a thruster is to design it with some cognizance of when low-frequency oscillations will emerge. The traditional predator-prey model of Fife et al. provides a very simple expression for a real frequency but none for the growth rate, hindering its predictive power. Moreover, even the real frequency can only be vaguely estimated, as the model relies on an unclear length scale that may be insensitive to the plasma (e.g. the channel length) or intimately related to it (e.g. the ionization mean free path). In the final section of Chapter VII, we derive a simplified two-zone model of the breathing mode that yields analytically tractable expressions of the real

frequency and growth rate. Although this model does not provide an onset criterion ($\gamma = 0$), it does allow the growth rate to be estimated in terms of well-defined plasma parameters that, although not known in the design phase, can be easily measured. This result is the first step toward a more comprehensive predictive understanding of the breathing mode. In practice, this information can be used to steer thruster design toward operating conditions that suppress the breathing mode, and to conduct experiments under facility conditions that do the same. For instance, the scaling of $\Im(\omega)$ found in the previous chapter implies that the breathing mode diminishes for low voltage and high current, such that high-thrust conditions may be less oscillatory than high-I_{sp} ones for a given discharge power.

It is worth noting that we were also able to provide a high-level description of the growth of the breathing mode. Although our phenomenological expressions largely agree with experimental trends in the literature, their inherent ambiguity still limits their usefulness. By this we mean that some quantities like u_i can easily be connected to operating parameters like V_d, but others are anticipated to have a more varied and complicated dependencies. For example, the ionization region length L_{iz} should strongly control γ according to Eq. (7.14b), but even though L_{iz} is defined relatively well, we expect it to depend on many other aspects of the discharge/thruster, which inhibits our ability to couch it in high-level parameters. In this way, there are still major gaps in our predictive understanding of the breathing mode because of this dichotomy between plasma properties and macroscopic thruster operating parameters. However, the present work has elucidated the role of low-level plasma parameters in the breathing process, which has put us in a more favorable position for attempting to close this final gap.

8.3 Future Work

Having identified the impact of the current work on the study of low-frequency oscillations in Hall thrusters, we now present several possible directions that the research presented herein could be taken. Some of these ideas are supplementary studies to resolve "loose ends", such as theoretical inconsistencies or missing experimental data that could benefit the conclusions made from this work; while others are complementary studies outside of the scope of this investigation, such as high-fidelity simulation; and yet still more are avenues of investigation based on recent developments reported in the literature.

8.3.1 Supplementary Studies

8.3.1.1 Direct Interrogation of Neutral Properties

In Chapter V, we described the way in which neutral properties were inferred. Although we performed LIF on the neutral population as part of the experiments in that chapter, we were not able to determine the neutral density from this data. Instead, the neutral density was calculated as a consequence of continuity using the ionization rate found from IBIS with Xe II LIF. Although extensive numerical experimentation was performed concerning the boundary conditions for the computed neutral density, it would be preferable to directly measure n_n to avoid any ambiguity. Ideally, such an investigation could confirm the presence of neutral density fluctuations upstream of the ionization zone.

Unfortunately, there are not many direct techniques to make these measurements. For example, there is a resonant Xe I LIF scheme that could be used to estimate density [101] but the signal tends to be distorted too close to thruster surfaces, so it cannot be used far into the channel. Aside from this approach, typical *in situ* pressure probes that use an ionization gauge or heat flux sensor are expected to be too slow

or bulky [115]. Further, injecting a pitot probe into the channel would be excessively perturbative, and even if a long pitot probe is used to reach into the channel, the reduced gas conductance would severely limit the bandwidth of any attached pressure gauge. In summary, the diagnostic challenge of directly measuring neutral density fluctuations may make it an interesting but worthwhile study to supplement the present work.

8.3.1.2 TRLIF Improvements

Since the TRLIF system used in the present experiments was purpose-built, attempts were made to optimize it for studying low-frequency oscillations. However, it would be helpful to continue improving this setup. First, no averaging was done sample-to-sample with the sample-and-hold hardware used in these experiments, as a result of the limited trigger rate of the device. Consequently, the only averaging of fluorescence samples at a given phase occurred in the LIA, and thus the number of samples in this average was something like 100. Ideally, the sample-and-hold circuit would output a running average of the fluorescence signal within each chop. This could reduce noise in the measured VDFs, which would improve the accuracy of the calculated moments. Although the trends in the first moment of the neutral population depicted in Chapter V are fairly clear, we were not able to find any consistent fluctuations in this moment. If the moments could be calculated more accurately, though, it is possible that small fluctuations could be detected.

Additionally, the sample-and-hold approach to TRLIF inherently cannot capture transient behavior and requires a very coherent reference signal (i.e. discharge current) to achieve usable SNR. In our experiments, we had to operate the thruster in off-nominal conditions to achieve this coherence, and even then long LIA integration times were required to produce clean VDFs. The various types of TRLIF implementations were discussed in Chapter V, where we noted that we chose the sample-and-hold

approach due to its simplicity. However, it might be worthwhile to explore some of the alternatives so that better SNR could be achieved, which would allow for greater certainty in the IBIS results.

Finally, there are several fundamental aspects of the LIF setup that could be improved. Firstly, we never directly accounted for Zeeman splitting or hyperfine broadening of the Xe II VDFs, having argued that these effects are small. However, it would be interesting to evaluate this firsthand for experiments like those conducted in the present work. Secondly, we only performed perfunctory saturation studies as part of this work, but it could be insightful to explore this matter further, especially with regard to temporal saturation effects. That is, it is possible that on average saturation was not significant but at certain phases of a breathing cycle the targeted metastable population was severely depleted and thus the VDF broadened. There is evidence for this effect in the work of Romadanov et al. [116] but in the present experiments it was ignored because of the excessive time it would take to conduct such a study.

8.3.1.3 Diagnostic Validation

As much as we relied on IBIS in this work, we did not dedicate any experiment to validating it. By producing realistic and repeatable profiles we merely verified that the technique was performing as expected but could say nothing about its systematic accuracy. Within the scope of the present investigation, where we are more interested in the fluctuation of plasma and neutral parameters rather than their absolute magnitudes, using an unvalidated diagnostic is not unconscionable. However, we suggested in §8.2.1 that the TRLIF-IBIS technique could be extended for other research purposes, in which case it may be critical to validate it.

The challenge in validating the IBIS method is that few diagnostics are capable of reproducing its wide range of measurements for comparison. Injected probing, as

discussed in Chapter V, is highly perturbative and thought to shift the discharge subtly [81]. On the other hand, wall probes – small electrodes embedded in the ceramic channel walls [141] – can be used to estimate centerline plasma potential and electron temperature in unshielded thrusters by tracing magnetic field lines and assuming they are equipotential and isothermal [9]. There do exist other non-invasive techniques that have been applied to a Hall thruster channel plasma, but often their measurements are not specific enough to be helpful here. For example, Hall current tomography could yield the perpendicular electric field but plasma density must also be known [86]; similarly, Fabry-Pérot spectroscopy could provide an approximate measurement of ion density, but these measurements are line-integrated and require numerical modeling [142]. Alternatively, high-fidelity simulation could be used for some degree of verification, but as there are no self-consistent Hall thruster codes to date, the simulation itself would need to be validated in other ways.

One approach to validating IBIS would be to compare its results to high-level operating parameters. For example, the accelerating voltage inferred with IBIS, given as $\int E_z dz$, could be compared to the discharge voltage and far-field cathode coupling voltage. Although this technique would not be exact, if for no other reason than it does not account for the anode sheath voltage, it could reveal any egregious errors in the determination of E_z with IBIS. Likewise, the total ion production rate $\int n f_{iz} A_{ch}/u_i dz$ could be used to determine the ion mass flow rate $\dot{m}_i$ which could be compared to near-field Faraday probe measurements, assuming negligible losses of ions to processes unmodeled with IBIS like recombination. However, even this approach is difficult because it would require vast LIF maps.

8.3.2 Complementary Studies

8.3.2.1 High-Fidelity Simulation

In this work, we only perform zero-dimensional numerical studies, either of full nonlinear conservation equations (Chapter VI) or of a linearized system (Chapter VII). We found in §5.3.3.1 that a zero-dimensional description of the predator-prey process was incompatible with our measurements, and so we developed the two-zone model to incorporate the spatial effect we believe plays a role in the breathing mode. Yet, we expect that there are many higher-order effects ignored by this model, and so dedicated 1D simulations could be helpful in clarifying the two-zone breathing process. For instance, we were only able to speculate on fluctuations in anode sheath potential and the impact of this on near-anode ionization, while a 1D numerical study could potentially resolve this feature.

There do in fact exist many 1D and 2D Hall thruster codes that reproduce low-frequency oscillations, but unfortunately we expect many of them are not completely capturing the two-zone process. This is because hybrid/fluid codes (as discussed in §2.5.1) have varied treatments of the anode boundary with equally diverse degrees of physical accuracy. We speculate that this means these codes are producing low-frequency oscillations in some other way, perhaps related to the nature of the artificial anomalous electron transport included in the code. Full PIC codes have also exhibited low-frequency oscillations [143] but again often sheaths are not resolved self-consistently and are simply imposed. Constructing a high-fidelity simulation to properly capture the anode sheath behavior could therefore be insightful in studying this two-zone breathing process.

8.3.2.2 Extensive Parametric Studies

The reported trends in low-frequency oscillations in Hall thrusters often conflict study to study, which indicates that the high-level parameters varied in these experiments may have an influence on the discharge that depends on facility effects, thruster geometry and materials, and discharge power. To elucidate these trends and provide comparisons for a predictive model (§7.6.3), extensive parametric studies on a single thruster with accompanying diagnostic work (such as with TRLIF-IBIS) could be conducted. For example, when varying the discharge voltage one might naively assume that primarily only u_i is increasing, which according to Eq. (7.14a) does not directly effect $\Re(\omega)$. And yet, studies have reported observing changes in the breathing frequency with V_d. However, the discharge voltage may also be influencing the thruster temperature and thus neutral velocity, as well as the spatial structure of the discharge, which would all affect the real frequency according to Eq. (7.14a). In this way, blind parametric studies reported in the literature may obscure the intricate web of interdependence between plasma and neutral properties, which limits their usefulness when assembling a high-level breathing mode model.

8.3.3 Recent Developments

Finally, there are some reason developments in the study of the Hall thruster breathing mode that could present new avenues of investigation. For example, recent work by Chapurin et al. involved 1D hybrid and full fluid Hall thruster simulations in which they observed a process similar to the two-zone one described in the present work [133]. However, they found that ions recombining at the anode are the source of the upstream neutral flow modulation, not enhanced ionization near the anode as we have proposed. In their work, they find that the ionization region shifts close to the anode presheath edge during a breathing cycle, and thus a large amount of ions are ingested by the sheath and ultimately must recombine at the anode. In our

experimental work, we find that the ionization region displaces very little during a breathing cycle and the ionization rate is relatively low in the vicinity of the anode presheath, which suggests a relatively small ion flux toward the anode. Further, ion recombination would present different phase relationships than as we described in §7.3 because the ion transit time to the anode will likely be much longer than for electrons, and thus the transit phase lag θ should be larger than we found experimentally. However, we admit that these two mechanisms are phenomenologically similar enough that both are plausible. As a result, further theoretical study of the recombination mechanism and an experimental search for evidence of it are warranted.

APPENDICES

APPENDIX A

Implementation and Evaluation of Optical Emission Spectroscopy

Introduction

In contrast to electrostatic probing, we also attempted a much less perturbative technique, optical emission spectroscopy. This is a passive diagnostic approach in which the light spectrum emitted from a plasma is used to infer the plasma's state. We start with a discussion of previous work on this diagnostic, narrowing the wide body of literature to that concerning xenon spectroscopy. We briefly discuss the emission model we used, although most of the details are reserved for Appendix B. We finish by describing the implementation of our system, including the spectroscopy hardware, the analysis techniques, and the electrostatic probe setup used to validate our low-speed spectroscopy measurements.

Previous Work

Optical emission spectroscopy (OES), in which plasma parameters are related to the relative intensity of atomic emission lines due to spontaneous transitions in the

plasma, previously has been applied with some success to Hall thrusters operating on xenon [144, 31, 145, 146]. Initial efforts made use of models assuming corona equilibrium, where collisional excitation from the ground state is exactly balanced by spontaneous emission from all transitions of interest. Manzella et al. applied such a model to measurements of a SPT-100 plume [144]. He also assumed the plasma was in Boltzmann equilibrium but found that this assumption led to poor electron temperature predictions based on a comparison of the emission intensities as a function of energy to the underlying theory. Meezan et al. interrogated a HET discharge channel with OES to examine high-speed oscillations [31]. This work made further use of the corona equilibrium assumption, and although the oscillations seen in ion saturation current could also be meaningfully resolved from optical emission line ratios, the electron temperatures computed from the model did not agree with those found with this *in situ* electrostatic probe. This disagreement was attributed to a highly non-Maxwellian distribution, as expected for the discharge channel plasma.

Karabadzhak et al. developed a collisional-radiative model that accounted for excitation from metastable states, greatly improving on the corona equilibrium model that preceded it [147]. Considerable care was made in choosing emission lines related to states that were short-lived enough so as to have little collisional de-excitation but long-lived enough to adequately populate and emit intensely for easy measurement. This model was improved in collaboration with Chiu and Dressler to become the Karabadzhak-Chiu-Dressler (KCD) model [148]; this model was unique in relying more directly on experimental cross sections and in incorporating ion impact excitation effects. Comparisons were made to plasma measurements far from an anode layer thruster (TAL) and eight-line least-squares extractions led to deviations of the modeled intensity ratios with experimental ratios of only about 28%. Dressler et al. improved the model further by incorporating experimental emission cross sections reported by Jung et al. and theoretical cross sections by Zatsarinny et al. and Srivas-

tava et al. [149], which we refer to as BSR-RDW-Jung, leading to deviations of only about 12% from far-field TAL measurements reported by Karabadzhak. However, few comparisons were made between the temperatures predicted by these models and those measured with other diagnostics, and so mainly the self-consistency of the models was evaluated in these works.

More recently, the KCD model was applied by Gonzales et al. to stroboscopically measure line ratios and predict time-resolved electron temperatures in the plume of a BHT-600 operated in an oscillatory condition [146]. In this case, a spectrometer was used in conjunction with a gated intensified charge-coupled device (CCD) with custom timing electronics that allowed photon collection at specific phases of a periodic signal.

Model

Fundamentally, a collisional-radiative emission model assumes that the intensity of light emitted at a certain transition wavelength is related to the rate at which particles excite to the upper energy state of that transition. In theory, this excitation is a result of collisional excitation from lower states, and cascade effects where particles in higher states transition down to the given state. Additionally, radiation trapping — in which emitted photons are reabsorbed and excite particles — can contribute to the population of a given state either directly or by cascade. Light emission decreases due to diffusion losses and collisional de-excitation of the transition upper state. Since the latter requires considerable effort to model accurately and cross-section data for xenon is sparse, emission lines for states that are short-lived must be used. Diffusion can also be neglected for short-lived states, such that emission intensity is solely a function of excitation rate. However, excitation can be due to electron impact or ion impact, with the latter having an increasingly significant role as electron temperature decreases [148]. Additionally, not only can the lower state for these excitations be the ground state but it may also be metastable states, which are long-lived enough

to experience particle collisions before spontaneous emission. Ignoring metastables as in the corona equilibrium assumption greatly simplifies the model, but unfortunately metastables have a non-negligible influence on emission either through excitation or metastable diffusion losses, as the success of the KCD model attests [148]. In this work, we implemented the KCD model with BSR-RDW-Jung cross-sectional data [148], described further in Appendix B.

Aside from the choice of emission model, the manner in which it will be applied to experimental data must also be considered. The most thorough method is to perform a least-squares fit of normalized intensities as a function of temperature for all modeled emission lines. For the KCD and BSR-RDW-Jung models, this involves extracting the temperature corresponding to the best fit for eight modeled emission lines compared to the experimental intensities. However, as few as two intensities is sufficient, for the sake of normalization so as to remove density dependence and the effect of the spectral response of the optical system [149]. In some cases, using fewer lines may be preferable as a subset of the modeled emission lines may have greater accuracy than the entire eight-line extraction under certain circumstances; Dressler et al. noted this for the 834 and 828 nm NIR Xe I lines using the KCD model [149]. In this experiment, we chose to consider only three Xe I emission lines: 823.2, 828.0, and 834.7 nm.

Implementation

The optical emission spectroscopy system was implemented using a high-speed camera and dielectric bandpass filters. A Photron FASTCAM SA5 operated at 75,000 fps was used for these experiments. The FASTCAM has a CMOS sensor that can image 256×256 pixels at this frame rate. The camera acted as the trigger source for an oscilloscope used to record the discharge current signal. The delay between the trigger signal and the first frame recorded by the camera was nominally <0.35 μs.

A Nikon Nikkor ED AF 80-200 mm zoom lens was used to image the thruster at a distance of 5 m with f/2.8 aperture. With this setup, only portions of the thruster could be imaged at a time. For plume imaging, the camera was at a distance of approximately 4 m from the plume axis. However, to image certain portions of the plume at less extreme angles, a 19 $\times$ 27 cm silvered glass mirror was used to redirect the optical path, lengthening it to nearly 6 m.

Although characterization of the full lineshape of the modeled emission lines with a spectrometer is ideal, these devices are often too slow to capture breathing oscillations, and thus dielectric filters are used here. The choice of filters and their characterization is also a non-trivial portion of the OES setup. The collision-radiative model dictates the relative intensities of emission lines as a function of T_e, and the light passed through a filter with a known (unique) spectral response is a function of those intensities, and thus the ratio of light intensity passed through different filters is a unique function of T_e. In this experiment, we found that a minimum of two filters can be used estimate electron temperature with the previously described model. For simplicity, we used common off-the-shelf 820-nm and 830-nm Fabry-Perot thin dielectric stack filters, each 25 mm in diameter and with a 10-nm full-width half-maximum (FWHM). The spectral response of the camera-filter system based on discrete component measurements with an Ocean Optics HR4000 spectrometer (fitted with a 200-1050 nm grating) for unit emissions at the modeled wavelengths is shown in Fig. A.1a; this response curve accounts for sensor response, lens transmittance, filter transmittance, and natural and collisional line broadening. Also included in Fig. A.1b is the variation in emission intensity with temperature according to the KCD model. This plot shows that with increasing temperature all line intensities increase rapidly, peak, and then slowly decrease. The high temperature accuracy of the model is expected to be poor, but encouragingly the observed trend agrees with the shape of the relevant excitation cross sections. These two plots can be combined to yield Fig.

A.2, which shows the ratio of filter intensities as a function of effective Maxwellian electron temperature. The filter ratio is a unique function of temperature using either the KCD or BSR-RDW-Jung model, which is necessary for the estimation of electron temperature from the filtered light but not guaranteed for any conceivable set of filters and modeled emission lines.

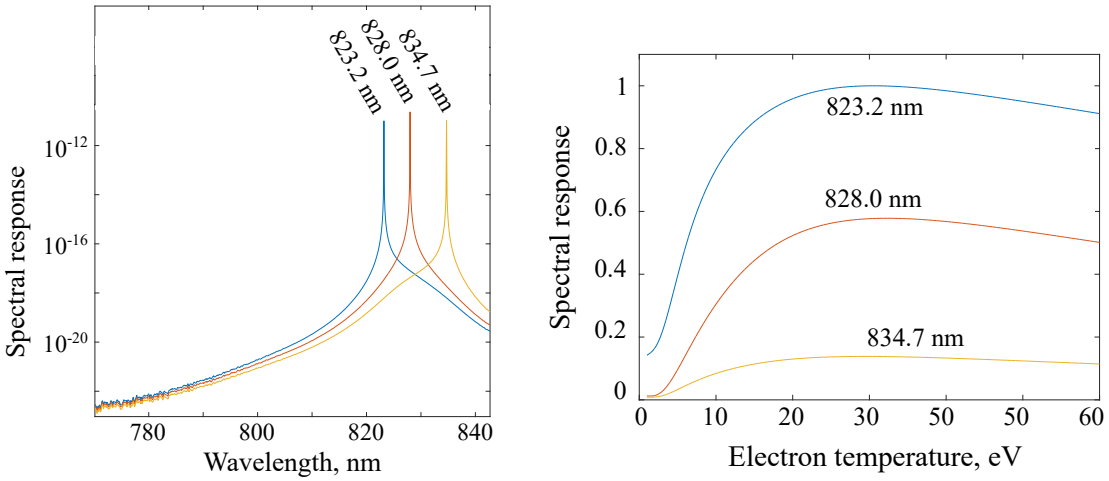

Figure A.1: The spectral response of the camera, filter, and lens system for unit emissions near 820 and 830 nm (left), and the normalized emission intensity for the same lines as a function of temperature (right).

For low-speed optical emission plume measurements, Langmuir probe data was also acquired within the field of view of the camera for comparison. A dual cylindrical Langmuir probe with a 10 mm by 0.6 mm diameter tungsten tip was located 1.6 m downstream of the thruster, on thruster centerline and aligned axially with the thruster. The probe was sinusoidally swept at 10 Hz from -20 to 50 V using an Agilent 33220A arbitrary waveform generator and a Krohn-Hite 7500 amplifier, and the collected current was measured by comparing voltage across two low-inductance resistors trimmed to within 0.1 Ω. Although having a dual probe is not necessary at such low sweep rates, it was included to allow for faster sweeping if desired. Voltages were acquired with a pair of AlazarTech ATS9462 16-bit, 180 MHz PCIe digitzer

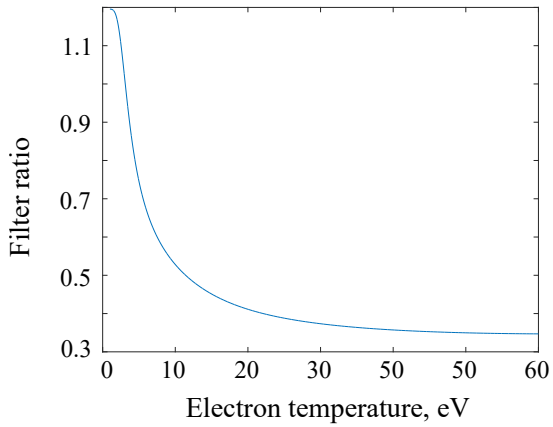

Figure A.2: The filter ratio according to the KCD model is a unique function of electron temperature, allowing it to be used for diagnostic purposes. The slope approaches zero as temperature increases, meaning that the model is less effective in that limit.

cards. Approximately twenty I-V traces were collected per acquisition and averaged within 0.1 V bins to mitigate signal noise.

Evaluation

For this experiment, we performed optical emission spectroscopy on the X3 operating in the LVTF with the inner channel at 300 V and roughly 4 kW. We first describe the experimental setup used in these studies. Then we present the oscillatory characteristics of the thruster in this condition as well as in other multi-channel firing configurations, as determined from the discharge current signal and high-speed image analysis. Next, we review a low-speed OES study of the thruster plume in which we compare the optical results to an *in situ* Langmuir probe. Finally, we attempt to perform OES at high-speed for the thruster channel.

Experimental Setup

This experiment was conducted in the LVTF, described completely in §4.4.1. The device under test was the X3, a 100 kW-class nested-channel Hall thruster developed

by the University of Michigan in collaboration with NASA and the Air Force Office of Scientific Research. This thruster like the H9 has been extensively studied and its record-breaking operation is described in Ref. [150]. The OES study was part of a 30-kW characterization of the X3 [151] but the data was taken with only the inner channel operating at 300 V and roughly 4 kW. At this condition, relatively strong and coherent low-frequency oscillations were observed without manipulation of the magnetic field. The pressure near the thruster measured with a Varian 571 ionization gauge was about 4 μTorr-Xe for this experiment. A photograph of the X3 installed in the chamber and operating in three-channel mode is shown in Fig. A.3.

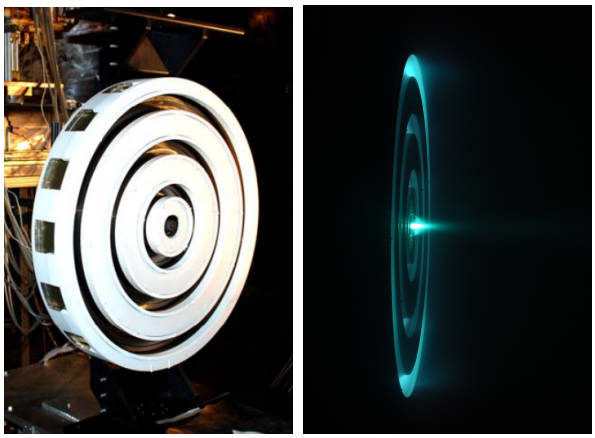

(a) (b)

Figure A.3: The X3 before first firing (a) and during low-power operation (b).

Discharge Channel Oscillations

An inspection of the discharge current signals for all configurations of the 300 V operating condition examined as part of this work leads to the conclusion that the breathing mode was likely dominant in all cases. Figure A.4 is a sample of the intensity surface and discharge current during breathing, produced by the high-speed video analysis techniques developed by McDonald et al. [36], in which pixel intensity of the channel images are normalized and plotted as a function of azimuthal position over time.

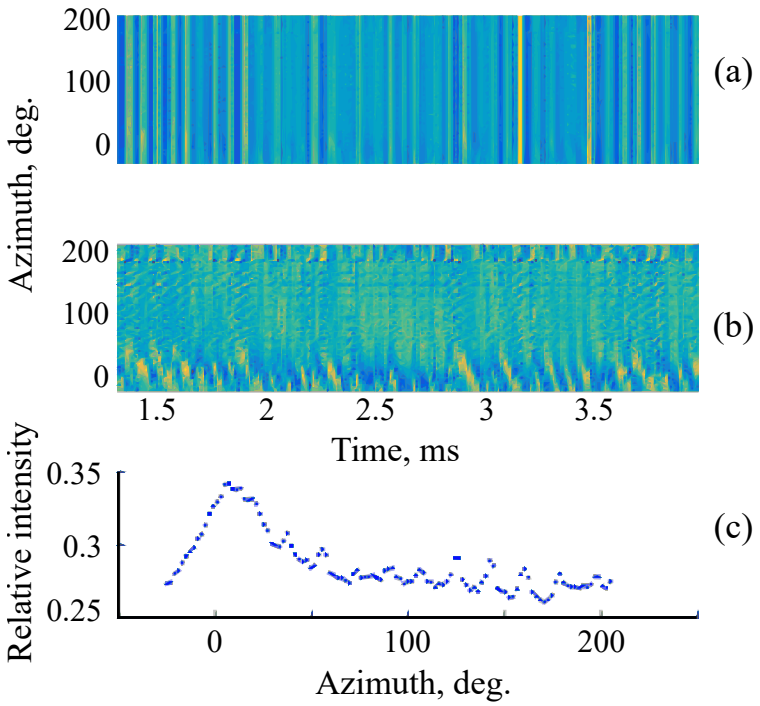

Figure A.4: An example of the breathing mode for the X3 middle channel operating at 4 kW, as the intensity map (a), spatially-normalized intensity (b), and oscillation RMS amplitude azimuthal uniformity (c).

The strong vertical features of Fig. A.4a indicate significant global (breathing) oscillations. The breathing frequency was found to be 14.5±0.4 kHz according to both the discharge current and high-speed video, and the RMS oscillation amplitude was 22.7% the mean value with relatively good uniformity according to Fig. A.4c. Figure A.4b shows the spatially-normalized image intensity (global features removed), where spoke-like features are apparent at certain angles. In other firing configurations spokes are more apparent, and in some turbulent local features are present (and may either be aliased spokes or camera artifacts), and still in a few cases there is only noise in the normalized intensity surface. Table A.1 qualitatively summarizes the local features present in each channel configuration, labeling them as artifacts ("art."), unresolved turbulent features ("turb."), noise, or spokes ("CCW" or "CW" for spoke propagation direction). The outer channel consistently has observable spokes, despite

also experiencing some of the clearest breathing of all channels. This may simply be due to the fact that it was often the brightest channel imaged, so fine features like spokes were easier to distinguish. In total, Table A.1 demonstrates that the X3 is rich with low-frequency oscillations in all configuration without manipulation of the magnetic field. We discuss the oscillatory properties of multi-channel operation further in Appendix I.

Table A.1: The qualitative local features that can be discerned from the normalized intensity surfaces for all configurations. Local turbulent features are denoted "turb.", local artifacts are denoted "art.", and spokes are denoted by their propagation direction.

Case	I	M	O
I	turb.	-	-
M	-	art.	-
O	-	-	CCW
I+M	noise	noise	-
M+O	-	art.	CCW
I+O	noise	-	CCW
I+M+O	noise	art.	art.

Low-Speed Filtered Imaging

To evaluate the suitability of the FASTCAM for emission spectroscopy, time-averaged measurements of the plume were made initially. This condition is well-suited to the KCD and BSR-RDW-Jung models, and by comparing to Langmuir probe measurements, served as an excellent benchmark for our OES setup. The unfiltered images of the plume during inner channel bake-out near 4 kW are shown in Fig. A.5, captured by the FASTCAM at 60 fps without using a mirror. Also included are the 820-nm and 830-nm filtered images acquired sequentially over the course of several minutes. These images show that the Langmuir probe and its stand were within the field of view of the camera. In this configuration, the camera was rotated 28° about the vertical axis and 29° about the chamber axis, so these raw images contain some angular distortion that could be avoided with a mirror. Pixel intensities normalized

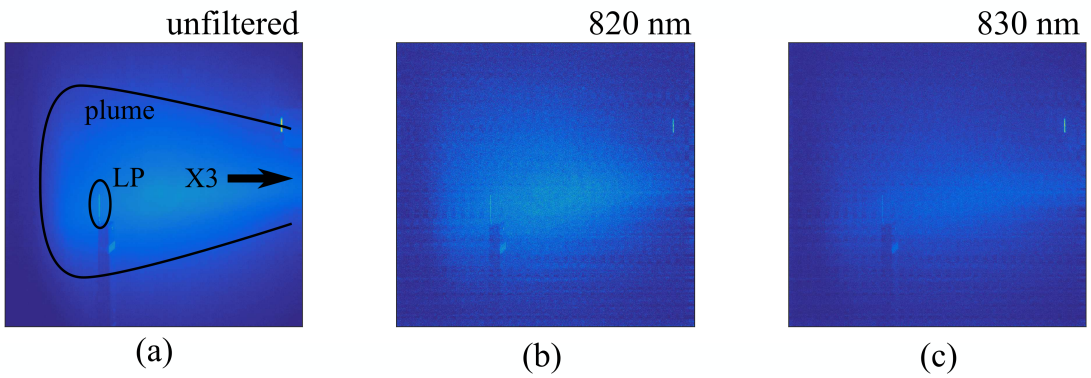

Figure A.5: Images of the X3 inner channel plume operating during bakeout near 4 kW, captured by the FASTCAM SA5 unfiltered with annotations (a), filtered around 820 nm (b), and filtered around 830 nm (c). The graininess of each image is an indication of its intensity, but otherwise the intensity is scaled during plotting.

to bit depth at this condition averaged 0.047, 0.0033, and 0.0041 for the three cases respectively, and the average RMS noise normalized to the bit depth over 100 frames was 0.0022, 0.0015, and 0.0016. This indicates that, without taking extra measures to reduce sensor noise, the signal is fairly noisy and may require smoothing to account for isolated noisy pixels. As expected, the filters appear to cut out a considerable amount of light, although it is likely that the small filter size (encompassing <10% of the lens area) was by itself blocking out a significant portion of incoming light.

A Langmuir probe acquisition made just prior to the FASTCAM imaging is shown in Fig. A.6. For the digitizer voltage range used here, the ion saturation current was below the noise floor, which contributes a small uncertainty to inferred plasma properties. Additionally, the collected current was noisy trace to trace, indicating that considerable averaging is required. The binned and averaged I-V curve and logarithmic I-V curve based on the acquisition shown in Fig. A.6 is displayed in Fig. A.7. As the logarithmic electron current plot shows, a very linear electron retarding region is apparent. Fitting a line to this region yields an estimate of electron temperature of 3.8 $\pm$ 0.5 eV assuming a Maxwellian energy distribution.

Figure A.8 shows the raw filter ratio map and the angle-corrected temperature

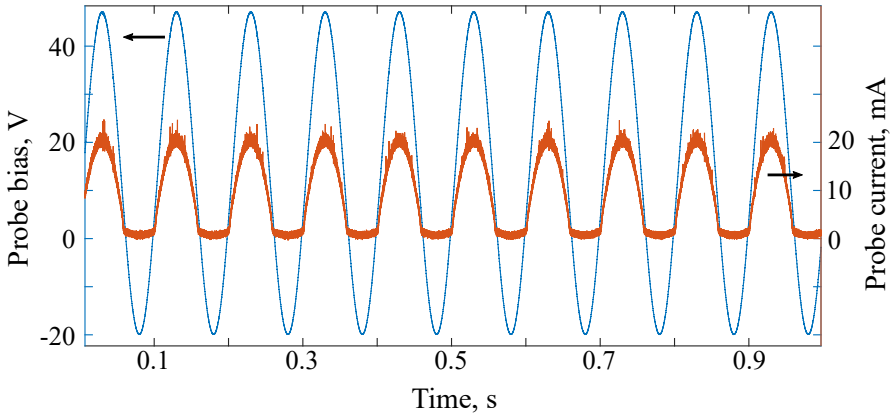

Figure A.6: A sample of the Langmuir probe data acquired over 1 s, encompassing roughly ten sweep cycles or twenty I-V curves. Note the probe bias did not reach the waveform generator limits due to voltage drops across the shunt resistors. There is noticeable noise in each trace, and the low-current regions of each I-V curve appear to consist entirely of noise.

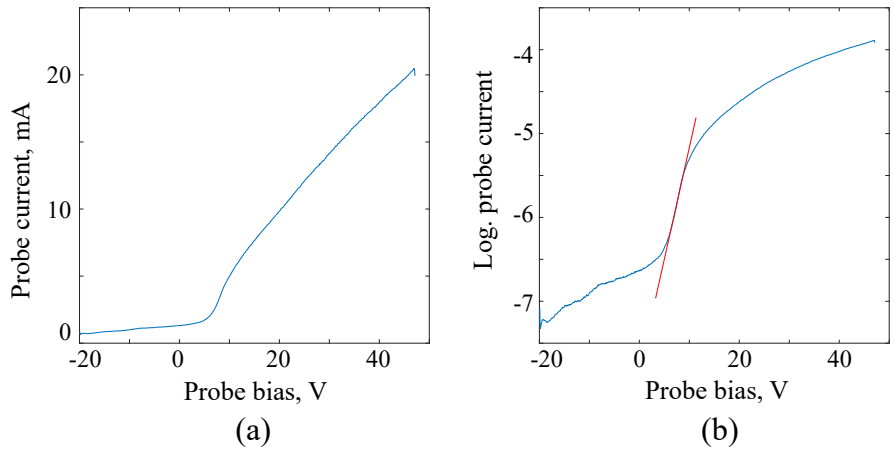

Figure A.7: The probe current as a function of applied voltage after 0.1-V binning (a), and neutral logarithmic electron current as a function of applied voltage after the same binning (b). The curves appear very smooth except toward low voltages, where the measured signal was mostly DAQ noise. Slight deviations at the ends of either curve are due to the binning algorithm, and have no bearing on the temperatures determined from these curves. The linear fit to calculate temperature is shown in red.

map using the KCD model, spatially binned and averaged into 8×8 mm squares. The KCD model was used here as it gave better performance than the BSR-RDW-Jung model. The probe was located in the lower left corner of the maps, and averaging

100 pixel temperatures around that edge yields a temperature of 2.99 ± 0.03 eV. The uncertainty on this temperature is due only to noise, as the systematic uncertainty of the camera measurements is hard to determine, and the uncertainty related to the fidelity of the OES model is likewise difficult to quantify. In any case, there appears to be fair agreement between the two diagnostics, with an error of 20.4%. The uncertainty of both measurements may be large enough (relative to the actual temperatures measured) that the agreement is not particularly impressive; in fact, the uncertainty of the Langmuir probe measurement alone is at least 12.8% of the computed temperature. Further, this only shows agreement for very low temperatures (a small region of the imaged area), which is the ideal case for the KCD model; again, this means that the agreement is not surprising. The trend of increasing temperature toward the right (toward the thruster) is reasonable. On the other hand, the high temperatures at the rightmost extent of the map do not seem plausible. By examining the raw temperature map, shown in Fig. A.9, it becomes clear where these high temperatures originate. The data is fairly sparse close to the thruster, and there are a few data points in that region with erroneously high temperatures according to the OES model. It is likely that these high-temperature points — corresponding to very low filter ratios — are a result of sensor noise, defective pixels, or residual charge in the sensor electronics between frames. In general, the sparsity of data is a result of pixels with filter ratios outside those predicted by the KCD model, again potentially due to sensor noise or defects.

High-Speed Filtered Imaging

Having met success with plume OES, we then attempted to image the discharge channel in the same way. Figure A.10 shows the unfiltered and filtered raw images captured by the camera at 75,000 fps for inner channel operation of the X3 at 300 V and 4 kW. These images show that nearly the entire discharge channel could be

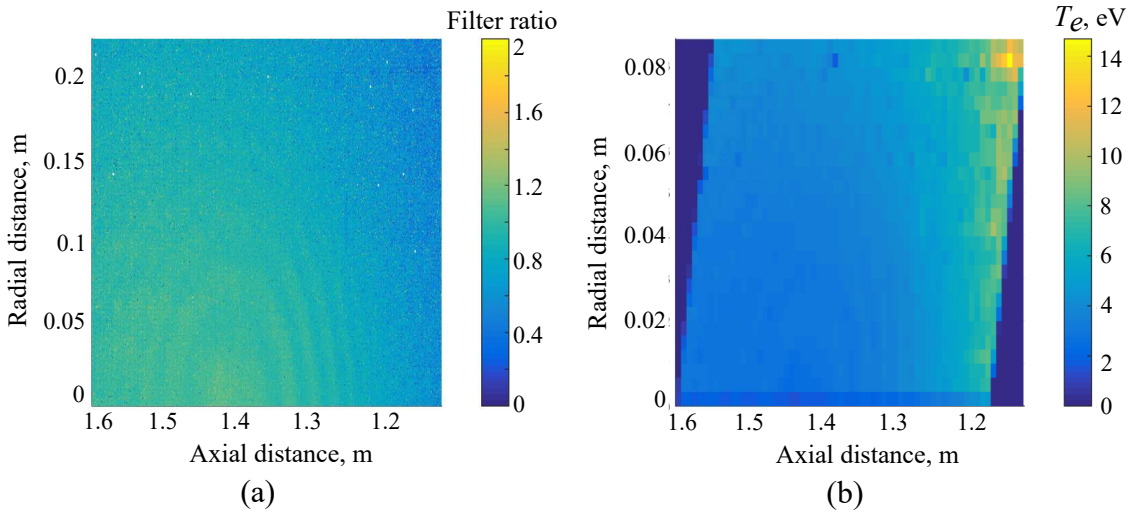

Figure A.8: A map of raw 820-nm to 830-nm filter ratios (a) and corresponding smoothed temperatures according to the KCD model (b) for the plume of the X3 inner channel operating near 4 kW. The filter ratio map is not corrected for angular distortion and is not binned, while the temperature map is both corrected and binned. Ratios over 2 were removed from the filter ratio map so that the scaling was meaningful.

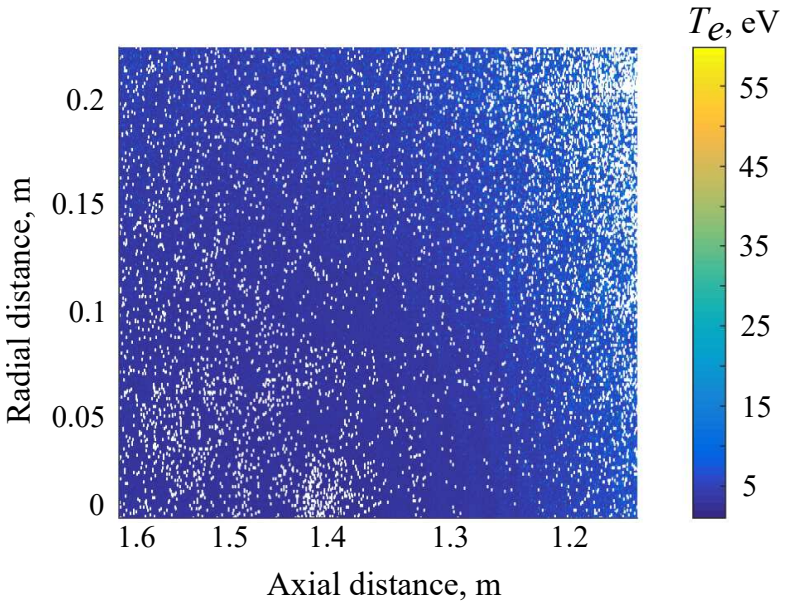

Figure A.9: The raw temperature map using the KCD model. This map is uncorrected for angular distortion and all filter ratios that are too high or low for the KCD model are displayed as white. Data is sparse near the top right and bottom left corners, while large swathes are continuous toward the middle of the map.

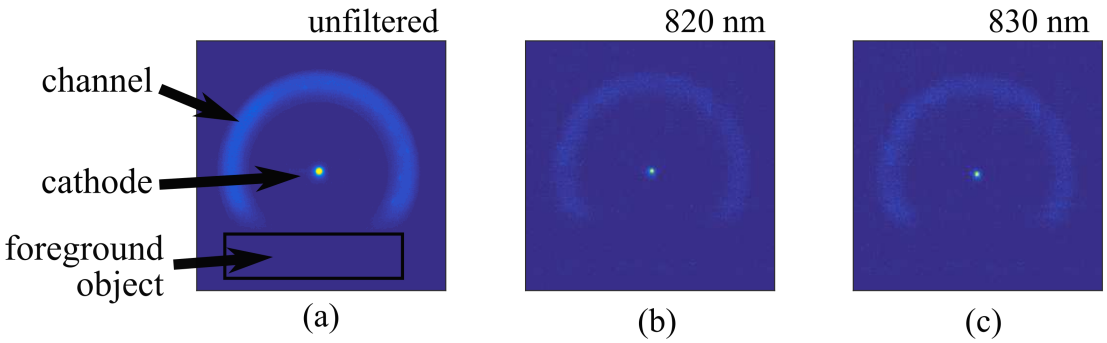

Figure A.10: Time-averaged images of the X3 inner channel during bakeout near 4 kW, captured by the FASTCAM SA5 unfiltered with annotations (a), filtered around 820 nm (b), and filtered around 830 nm (c). Note that there is considerable loss in image intensity when filters are added, although the channel is still discernible and the cathode is still particularly brilliant. Although only 204° of the channel was visible, the azimuthal bin size was small enough to discern several spatial modes with the 2D discrete Fourier transform.

imaged and the signal was usable even when filtered. Note here that the graininess of the filtered images indicates that the sensed intensities are much lower than for the plume images due to the much higher shutter speed. The mean pixel intensities normalized to the bit depth are 0.016, 0.0011, and 0.0010 for the unfiltered, 820-nm filtered, and 830-nm filtered images, respectively. The sensor dark noise pixel intensity normalized to the bit depth over 1000 frames was about 0.00078, 0.00068, and 0.00063. On average, this implies that a meaningful filtered signal is sensed, but this does not necessarily guarantee it can be successfully applied to the KCD model.

The unfiltered DC-coupled pixel intensity as a function of time and discharge channel azimuthal position was produced using the high-speed image analysis techniques mentioned previously and is shown in Fig. A.11. Neither the breathing mode nor spoke mode was strong in this operating condition, although there is some spoke-like feature from 0° to 20°. Although the nominal 4 kW operating condition for the X3 inner channel demonstrated strong breathing as shown before, this experiment was conducted during bakeout for the condition, in which the high-speed behavior of the thruster is anticipated to be erratic. This represents one of the worst possible

conditions for sequential filtered imaging, as was implemented in this experiment. However, the spectrum of the unfiltered channel image as shown in Fig. A.12 indicates that there is still detectable breathing (m=0) near 5 kHz. The spectra for the 820-nm and 830-nm filtered images similarly contain peaks in that vicinity. However, the noisiness of the filtered spectra may skew the prediction of the peak center. Indeed, the unfiltered, 820-nm filtered, and 830-nm filtered peaks based on 10,000 frames were identified as being 4.50±0.43 kHz, 3.94±0.02 kHz, and 4.92±1.80 kHz. The uncertainties on these values indicate that over the course of an acquisition the breathing frequency was fairly steady and sinusoidal, but spectral noise filter-to-filter leads to disagreement between the peak frequency, increasing it for the 830-nm filter (blue noise) and decreasing it for the 820-nm filter (pink noise).

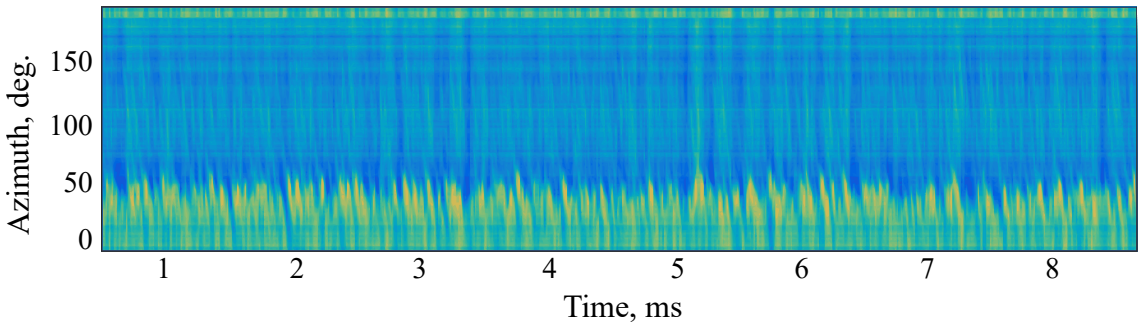

Figure A.11: The unfiltered time-resolved intensity map for the inner channel operating near 4 kW. No strong global features are prominent, although turbulent local features do appear at small angles. Some of these features may be artifacts due to reflections off of the viewport and sacrificial glass, while others may be genuine plasma features. Sharp fixed-pattern features (those that are present at all times) are likely camera artifacts.

The phases of the dominant spectral peak as calculated with a Fourier transform can be used to align the filtered videos and compute the filter ratio, assuming that the phase was nearly constant during the acquisition time. The offset between the two filtered videos was found in this way to be 16 μs, or roughly one frame. Figure A.13 shows the time-resolved variation of this ratio; a short timescale is used to highlight the strong high-frequency noise in this signal. Fig. A.14 shows the frequency

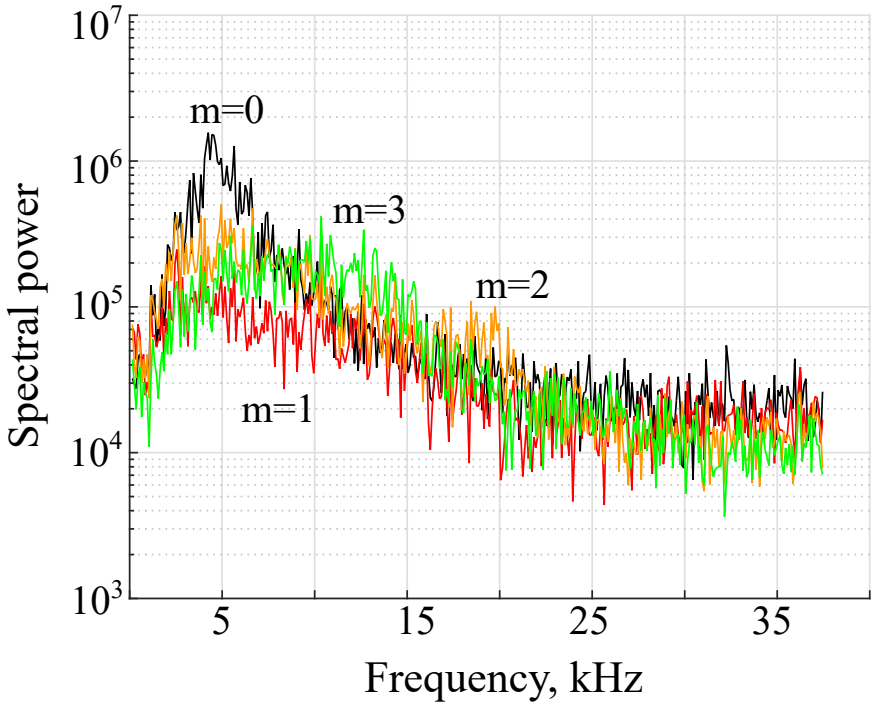

Figure A.12: The power spectral density for the unfiltered imaging of the inner channel near 4 kW. A strong breathing mode is present, even though it was not apparent in the intensity map. Higher order modes also appear to be fairly strong, especially the m=3 mode. However, the higher order features are so wide that little meaningful analysis can be performed.

spectrum for the ratio signal. The time-averaged filter ratio for the entire acquisition is 1.12, which corresponds to a KCD electron temperature of 2.40 eV. This value is unreasonably low for the discharge channel plasma, which indicates that either the KCD model is inappropriate for that region or our filter setup failed in some way. The former may be due to a fundamental breakdown of the model, such as if collisional de-excitation becomes prominent in the discharge channel, or it may be due to the infiltration of unmodeled lines. Investigation with a spectrometer could be used to evaluate that possibility.

Although the signal itself appears very noisy, a peak near 5 kHz is apparent in the frequency spectrum, as are half-integer harmonics. The presence of harmonics is not unexpected for the ratio of two periodic signals, although the multitude of them was

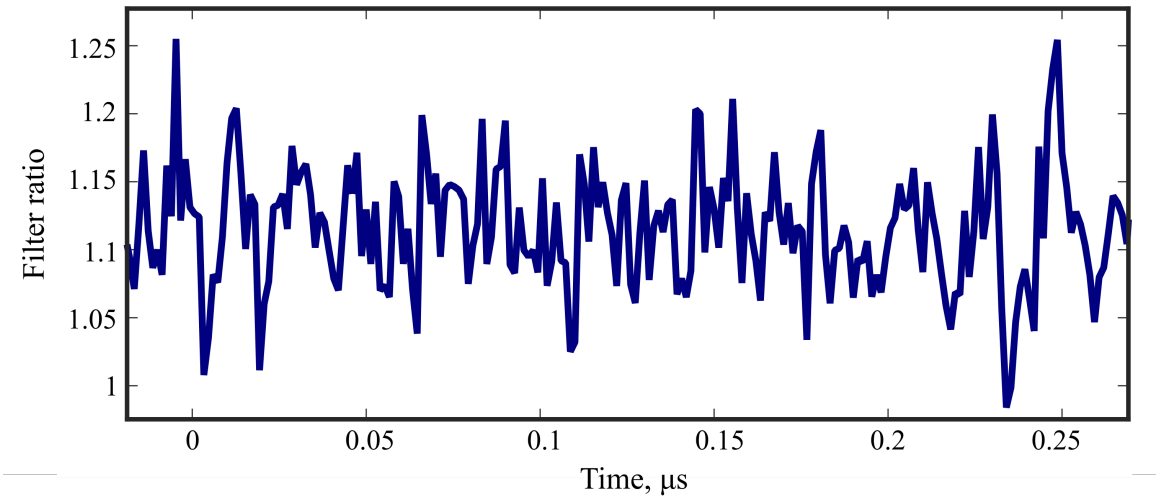

Figure A.13: A sample of the time-resolved filter ratio signal. The signal appears to be composed entirely of noise.

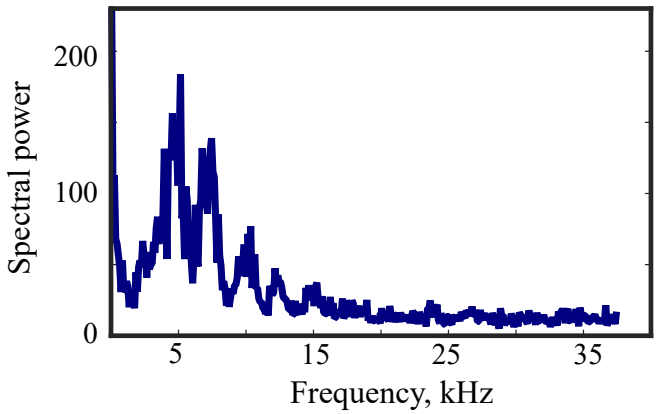

Figure A.14: The power spectral density for the filter ratio signal. Considerable power is located at low frequencies, due to the DC offset of the signal. The sharpest AC peaks occur at 5 kHz and every half-integer harmonic.

not anticipated. In any case, strong harmonics may be an indication here that the two filtered image intensity signals are out of phase. This suggests that the spectra are too noisy for the phase correction to be effective, or the phase varies significantly in time. In total, then, a meaningful signal may have been measured, but the lack of strong periodic features and the poor performance of the model means that no usable information can be extracted from the sequential high-speed filtered imaging. It is unlikely, then, that this technique could successfully be used to characterize the

breathing mode.

APPENDIX B

Collisional-Radiative Model for Optical Emission Spectroscopy

In Chapter V, we implemented and evaluated an optical emission spectroscopy system for characterizing the breathing mode. As part of this, we used an emission model from the literature to relate line intensities to plasma properties, in this case electron temperature. The derivation of this model relies on a strong understanding of atomic physics, so here we present a brief description of it that focuses on the practical aspects of its application.

The KCD model can be described in terms of its collisional-radiative model formulation as well as the lines to which the model is tailored. As for the former, the KCD model fundamentally assumes that the intensity of light emitted at a certain wavelength J_λ is a function of the particle excitation rates from lower states due to electron collisions κ_{ep}^{λ} and from the ground state due to ion collisions κ_1^{λ}, assuming optical thinness. Naturally, the electron collision term depends on the target state density n_p and the electron density n_e, while the ion collision term depends on the neutral density n_n and the ion density n_i. This is shown as Eq. (B.1). For now, the emission lines of interest are associated with neutral excited states, although the exact states themselves do not need to be determined yet. It is assumed here that

the transition of interest that emits at wavelength λ is short-lived enough such that all depopulation is by spontaneous emission. Additionally, the formulation presented here only includes excitation from singly-ionized particles since Karabadzhak et al. noted that the influence of doubly-charged ions is small, even though their formulation retained the doubly-charged ion terms [148].

$$J_\lambda = \frac{hc}{4\pi\lambda} n_n n_e \left(\sum_p \frac{n_p}{n_n} \kappa_{ep}^\lambda + \frac{n_i}{n_e} \kappa_1^\lambda \right) \tag{B.1}$$

If it is assumed that most ions are energized to the thruster discharge voltage, the excitation rate due to ion collisions can be simplified. Additionally, if quasi-neutrality is assumed such that the ratio of singly-charged ion density and electron density α is constant, Eq. (B.2) results. Notice that the first term in Eq. (B.1) has been replaced with a ground state term and a metastable state term, where the latter depends on the electron collision excitation rate from the metastable state κ_{em}^λ and the metastable state density n_m.

$$J_\lambda = \frac{hc}{4\pi\lambda} n_n n_e \left(\kappa_{e0}^\lambda + \frac{n_m}{n_n} \kappa_{em}^\lambda + \alpha \kappa_1^\lambda \right) \tag{B.2}$$

Since comprehensive cross sections for Xe I metastables are rare, a specific set of emission lines had to be defined to advance Eq. (B.2) further. Several near-infrared (NIR) lines associated with the Xe I $2p_i$ (Paschen notation) states are very intense for HET plasmas, and so the KCD model uses the emission lines associated with transitions down from these states. It was noted that three of these lines, $2p_1$, $2p_3$, and $2p_5$, are only weakly coupled to nearby metastable states and instead de-excite to the $1s_2$ and $1s_4$ resonant states. This allows these states to be modeled without considering metastable densities or cross sections, eliminating the middle term in Eq. (B.2). However, the strongest $2p_i$ lines are dipole-coupled to metastable states and therefore depend on metastable properties. The KCD model approximates metastable density

by forming an equilibrium rate equation in which the metastable state is populated by spontaneous emission from all states that de-excite to the metastable state and is depopulated by collisional de-excitation and diffusion. Diffusion losses can be shown to be insignificant compared to collisional de-excitation for all but very low temperatures [148]. The rate of collisional de-excitation is estimated from the collisional excitation cross sections out of the metastable state, weighted by the branching ratio $\mathbb{P}$ of the resulting upper state to nearby states that resonate to ground. That is, de-excitation of the metastable state is the average rate of collisional excitation such that a particle cannot enter the metastable state without re-exciting from the ground state. With these approximations, the ratio of metastable density to ground state neutral density is given by Eq. (B.3).

$$\frac{n_m}{n_n} = \frac{\sum_i \left(\kappa^i_{e0} + \alpha\kappa^i_1\right)}{\sum_i \mathbb{P}_i \kappa^i_{em}} \tag{B.3}$$

The rate coefficient for excitation from the metastable state is approximated as proportional to the degeneracy of the higher energy state scaled by the branching probability for the $2p_i$ end state to the metastable state [148]. The constant of proportionality does not need to be determined since the metastable density ratio is also proportional to degeneracy through the κ^i_{em} term.

Work by Dressler et al. removed the metastable approximations of the KCD model by applying a combination of experimental cross sections from Jung [152] and theoretical cross sections produced with the Breit-Pauli B-Spline R-matrix (BSR) method and relativistic distorted wave (RDW) method. The same equilibrium rate equation was used to determine metastable density ratio, except the relevant experimental or theoretical rate coefficients were used instead of weighted rate coefficients. Likewise, the metastable rate coefficient did not need to be estimated from the degeneracy but could be directly calculated from experimental and theoretical cross-sections. The resulting model, which showed better eight-line extractions to Karabadzhak et al.'s

TAL data than the KCD model, is called the BSR-RDW-Jung model.

APPENDIX C

Implementation and Evaluation of High-Speed Langmuir Probing

Introduction

The first diagnostic technique we will discuss is high-speed electrostatic probing. We begin by reviewing previous development and application of this technique. We then discuss our particular implementation of it, including the electronics and translation stage involved. We conclude with an overview of the analysis of high-speed Langmuir probe traces, focusing on our contributions.

Previous Work

Electrostatic probing of plasmas, and particularly Langmuir probing, has an extensive history of application [153] and theoretical study [154]. As a brief review, a Langmuir probe is an electrode inserted into a plasma and biased so that it collects ion and electron current. As the voltage is reduced far below the plasma potential, the probe predominantly collects ions. Due to sheath expansion, the ion saturation

current can be estimated by accounting for Coulombic trajectories of ions (orbital motion limited theory) to yield a saturation ion current $I_{i,s}$ collected by a probe of area A_p for a given plasma potential V_p and ion mass m_i of

$$I_{i,s} = \frac{\sqrt{2}}{\pi} enA_p \sqrt{\frac{eV_p}{m_i}} \ . \tag{C.1}$$

As the voltage increases, the more mobile electrons quickly begin to contribute current:

$$I_e = \frac{1}{4} enA_p u_{th} \exp\left(\frac{V_b - V_p}{T_e}\right) \text{ for } (V_b - V_p) < 0 \ , \tag{C.2}$$

where u_{th} is the electron thermal speed and V_b is the probe bias relative to ground. At some voltage V_f the ion and electron current balance and the probe is said to "float."

Langmuir probes can also characterize non-Maxwellian plasmas. For example, the Druyvesteyn method [155] allows the electron energy distribution function f_e to be calculated from the electron current:

$$f_e = \text{-}\frac{2}{e^2 A_p} \sqrt{2m_e e\left(V_p - V_b\right)} \frac{d^2 I_e}{dV_b{}^2} \ . \tag{C.3}$$

Other theories [156, 157] exist for the calculation of the EEDF from the first derivative of the electron current, for varying assumptions and probe geometries.

Although high-speed plasma probes operating on these principles have existed for as long as high-speed electronics [158, 159], the use of fast electrostatic probes to characterize Hall thrusters is a relatively recent development. Previously, floating probes have been used to detect the presence of oscillations [22] or negatively-biased probes to estimate ion density [32], but the amount of information yielded with these techniques was limited.

One of the major limitations in measuring high-speed plasma properties with

an electrostatic probe is that often the probe bias must be swept to infer many plasma parameters. One exception is the triple-probe [160], which makes use of two electrodes biased relative to a third such that there are three distinct plasma currents collected at any given time, allowing electron temperature and density to be estimated instantaneously. However, these probes have no capacity for characterizing non-Maxwellian plasmas and are particularly susceptible to noise [89], so for these reasons as well as the inherent additional electronics and poor spatial resolution, swept probes have remained most prominent. As a result, most Langmuir probe circuits are limited by the sweep rate that can be applied.

As the rate of voltage sweep is increased, reactance of the probe and cabling quickly leads to the collection of spurious current that can obscure the plasma-related signal. It has long been suggested to use a filter with a rapidly-swept probe to minimize its reactance [161]. This basic concept has been applied to Langmuir probes for fusion applications [162, 163, 164] with success. For Hall thruster research, studies have been performed with phase-averaged probing [165] relying on well-matched cabling, as well as moderately fast unfiltered probing necessitated during reciprocating probe injection using high-speed actuators [166, 167]. A significant amount of pioneering work with high-speed Langmuir probe operation was performed by Lobbia [168].

As Lobbia and Gallimore demonstrated [87], the theoretical bandwidth for a Langmuir probe very close to a Hall thruster is generally limited to below 100 kHz by the stray capacitance of the probe cabling; otherwise, the limit may be $\sim$1 MHz or higher. As a result, Lobbia and Gallimore developed a high-speed dual Langmuir probe configuration in which the differential current between two identical (parallel) probes – one with a plasma-wetted tip and one without – removes any accumulated reactive current [59]. Specifically, an active probe cabled with capacitance C and swept at a rate dV/dt collects both plasma current I_p and capacitive current such

that $I_a = I_p + CdV/dt$, while an unexposed "null" probe collects only the (identical) capacitive current. As a result, the differential current should be equal to the true plasma current, $\Delta I = I_a - I_n = I_p$, which should be relatively undistorted up to a few megahertz. Lobbia's thesis work demonstrated the successful application of this diagnostic technique to Hall thruster plumes [168] and the technique was applied further by Sekerak et al. [169]. More recently, an alternative but similar system using variable capacitors was built and applied fruitfully for studying a different E×B device by Skoutnev et al. [170]. The techniques used to analyze HSLP data do not depart far from traditional Langmuir probe analysis and are discussed in Ref. [168]; a few modifications we contributed to this procedure are reserved for Appendix D.

Implementation

As part of evaluating possible diagnostic techniques for characterizing the breathing mode, we implemented a high-speed Langmuir probe (HSLP) as part of a high-speed axial reciprocating probe (HARP) setup in the style of Haas et al. [79]. The probe was attached to a Aerotech linear motor system that included a brushless servomotor and a Renishaw incremental encoder that was used to maintain positional accuracy $\leq$1 mm. This system was used to produce speeds up to 1.8 m/s and accelerations up to 4.6 g, reducing the residence time of the probe inside the thruster below 50 ms. The planar Langmuir probe was equipped with an exposed (active) electrode, a hidden (null) electrode, and a large reference electrode, where the active electrode was a tungsten collector approximately 1.1 mm by 0.5 mm in size. The reference electrode was included to shorten the return path for plasma current. The probe was injected as far as 5 mm into the discharge channel at a range of radial locations from 2 mm inward to 1 mm outward from the injection origin, located on channel centerline azimuthally between 3 and 6 o'clock. The axial probe position was measured from the center of the probe collecting surface. The probe collecting surface normal was

oriented mostly in the radial direction to prevent the collection of ram current from the electron E×B drift, as shown in a diagram of the setup in Fig. F.1.

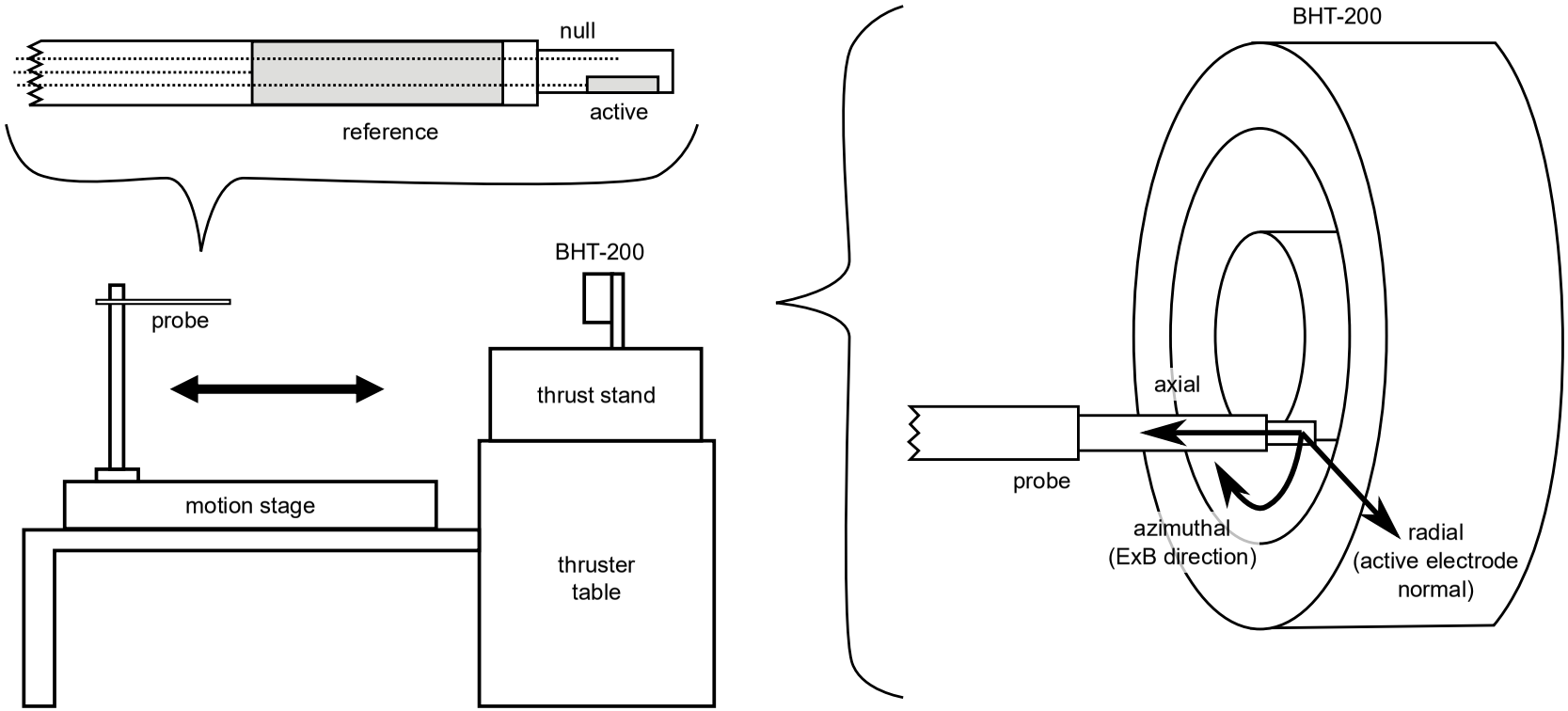

Figure C.1: A diagram of the experimental configuration for high-speed Langmuir probing.

The hardware of the HSLP setup included an Agilent 33600A waveform generator, a Krohn-Hite 7500 wideband power amplifier, several API 610-10-2 oscilloscope probes, and a Tektronix TCP312 current sensor paired with a Tektronix TCPA300 amplifier, as shown in Fig. F.2. All high-speed signals were recorded with Gage CSE1642 digitizer cards, recording with 16-bit depth at 200 MS/s and 125 MHz bandwidth. Motion stage position data was stored in the Aerotech Soloist HLe controller's onboard memory, triggering with the digitizer cards from a signal produced by a SRS DG535 pulse generator.

During the experiment, several probe configurations were tested. First, the probe was equipped with a large reference electrode near the tip electrode, and the probe was connected to the Krohn-Hite amplifier via a transformer. This would in theory allow the HSLP to operate like a double probe, floating to higher voltage as the probe approached the thruster, but also permitting the measurement of electron saturation due to the size disparity of the reference and tip electrodes. In practice, it was found that to preserve current continuity the probe would float to very low voltages, such that only ion saturation was reached. Next, the probe was ground-referenced and the biasing sine wave was superimposed on a low-frequency ramping voltage so that the sweep would never extend too far above the plasma potential (identified by large collected current) but still approach ion saturation for the entire measurement envelope. These two contrasting configurations are shown in Fig. F.2. In the ground-referenced setup, the differential current between the active and null probe lines was measured first with a pair of 50-Ω shunts and a Lecroy DA1855 differential amplifier, but it was found that the common-mode range of the amplifier was too limited to accommodate the sweep range for the entire probing envelope. Finally, the configuration was switched so that current was measured with the Tektronix TCP312 Hall sensor by counter-wrapping the active and null probe lines multiple time around the sensor. This increased the sensitivity of the sensor and yielded the differential

current without additional active electronics.

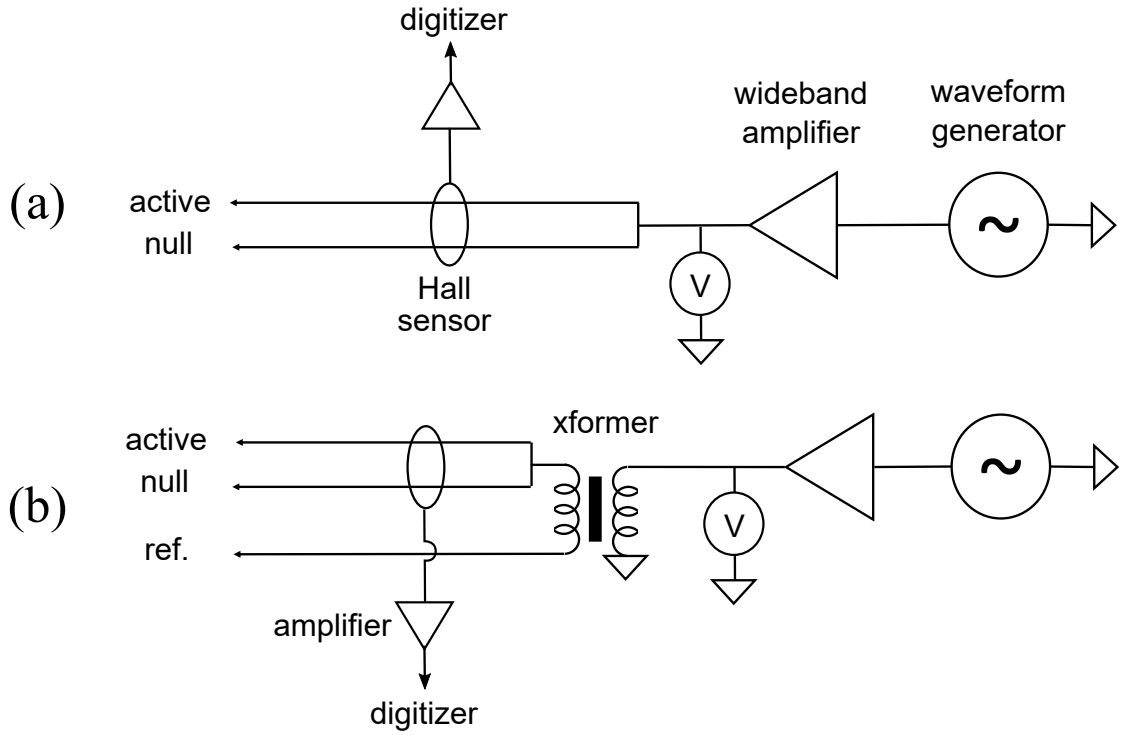

Figure C.2: A schematic of two variations of the high-speed Langmuir probe setup: (a) ground-referenced and (b) floating.

Evaluation

We also experimentally evaluated a high-speed Langmuir probe setup for interrogating the near-field plasma in a low-power Hall thruster. Specifically, an axially-injected high-speed Langmuir probe was evaluated in the SPEF chamber on a BHT-200 thruster for two oscillatory conditions: nominal magnetic field strength and half strength. For both conditions, there were strong oscillations at 24 kHz corresponding to the breathing mode. We examined not only the probe signal and the plasma parameters inferred from it but also the spectral response of thruster telemetry during a probe injection. In this way, aside from characterizing the near-field and internal plasma, we could also examine the perturbative effect of the probe injection.

Experimental Setup

The experiments in this evaluation work were conducted in the Space Environment Facility (SPEF) at the Air Force Research Laboratory, Edwards Air Force Base. The SPEF is a stainless steel sphere 9.1 m in diameter, equipped with six 122-cm oil diffusion pumps with LN_2-cooled baffles. This facility has a xenon pumping speed above 300 kL/s. It is equipped with a beam dump similar to LVTF, and likewise has equivalent water-handling and viewports.

The high-speed Langmuir probe experiments in SPEF were conducted on a BHT-200, a small commercial 200-W Hall thruster; an iteration of this device is described in Ref. [171]. This thruster has a nose cone that extend roughly 7 mm beyond the exit plane, a channel width of 16 mm, and a similar channel length. The thruster was operated at 150 V at a nominal magnetic field strength (200 W discharge) and at half strength (270 W discharge). At the nominal condition, the RMS oscillation amplitude was <5% of the mean discharge current, while at the half-strength condition they were closer to 20% – this is consistent with the onset of the breathing mode.

Transient Behavior

Figures F.3 and F.4 show the variation in discharge current with radial and axial probe position during high-speed injections for two different operating conditions: nominal (200 W) and half magnetic field strength (270 W). The exit plane is z=0, with z increasing positive in the downstream direction.

In agreement with other studies, the mean discharge current $\bar{I}_d$ increases as the probe approaches the thruster. However, the RMS discharge current $\tilde{I}_d$ only momentarily spikes. For the half-magnet condition shown in Figure F.4, the transition occurs outside the exit plane and it can be observed that $\tilde{I}_d$ drops below its nominal value as the probe enters the thruster. The response of I_d to the probe presence is therefore significant and nuanced.

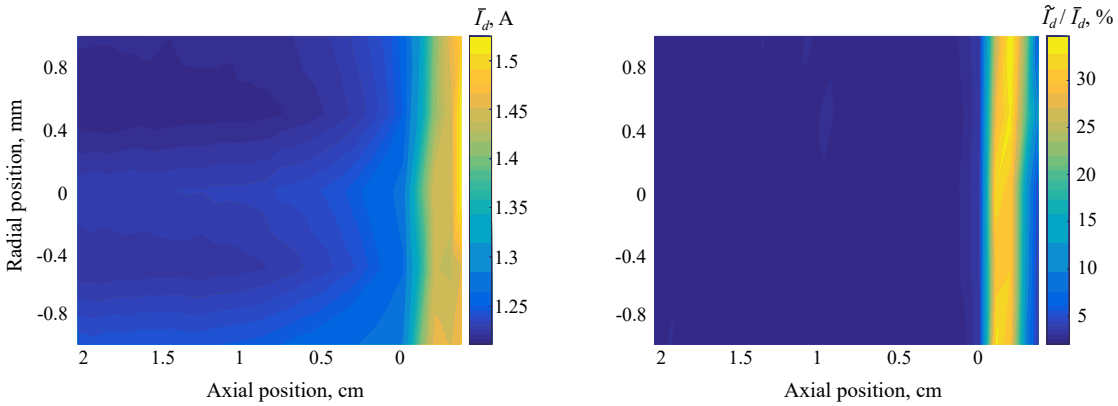

Figure C.3: The variation of $\bar{I}_d$ (a) and $\tilde{I}_d$ (b) is shown as a function of axial and radial position for nominal operation. The narrowness of the radial range mostly precludes its use in identifying spatial trends but can still serve as an indication of the consistency of the probe injections.

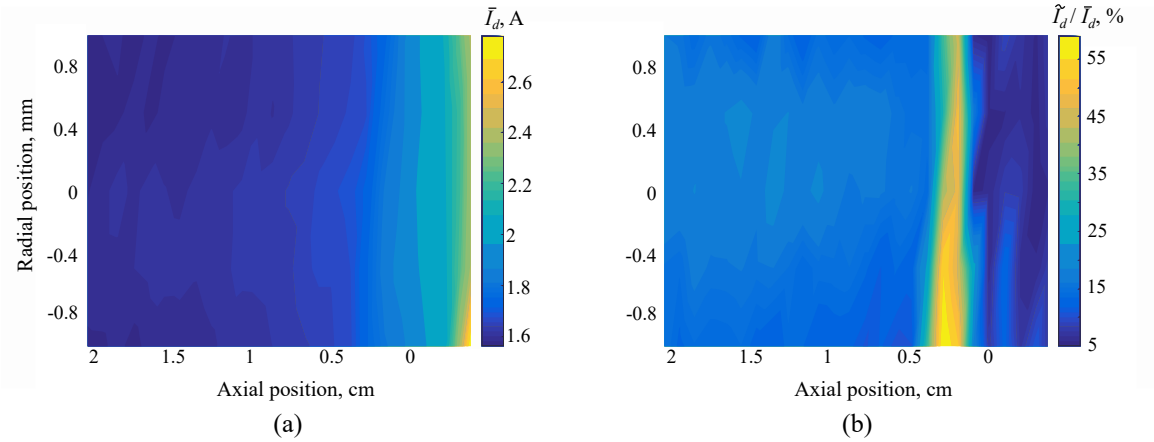

Figure C.4: The variation of $\bar{I}_d$ (a) and $\tilde{I}_d$ (b) is shown as a function of axial and radial position for half-magnet operation. The narrowness of the radial range mostly precludes its use in identifying spatial trends but can still serve as an indication of the consistency of the probe injections.

Several plasma parameters extracted from the HSLP I-V traces are shown in Figs. F.5-F.8 for the nominal and half-magnet cases. Note that the data for the nominal case only extends to the exit plane and for the half-magnet case to several mm downstream of the exit plane. This is due to the probe signals suddenly becoming unusable at these boundaries, as if due to some thruster mode transition. Otherwise, the trends in V_p, T_e, and n are as expected. The plasma potential was determined

with a polynomial-fitting algorithm to find a plateau in dI_e/dt, and after that the one-dimensional electron energy density functions (1D EEDFs) could be calculated following Ref. 157. The EEDFs are shown in Fig. F.9. From those surfaces, n and (effective) T_e spatial profiles were calculated by taking moments.

The nominal case shows no remarkable features in the oscillation amplitude of these parameters, other than perhaps a slight increase in amplitude toward the exit plane (shown clearly by n). The half-magnet case similarly shows reasonable DC trends, although T_e curiously appears to hit a maximum around 3 mm. Additionally, the oscillation magnitudes for V_p and T_e show a sharp decline starting at 10 mm. In both cases, the majority of the acceleration region is not captured as E_z is small and still increasing at the deepest point probed.

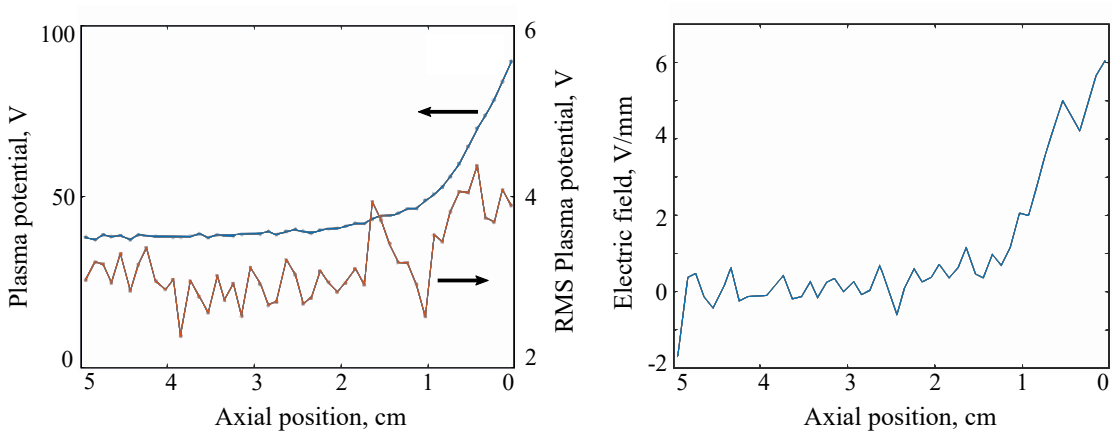

(a) (b)

Figure C.5: Time-averaged plasma potential and its oscillation amplitude was determined from the HSLP for the nominal case. Results were binned and averaged every mm. The electric field magnitude was computed from the plasma potential as its second-order numerical derivative.

Spectral Behavior

Figures F.10 and F.11 show the power spectra of the discharge current and cathode-to-ground voltage V_{c2g} as a function of axial position. There is a sudden change in the spectra at positions that correspond with the transition seen in Figs.

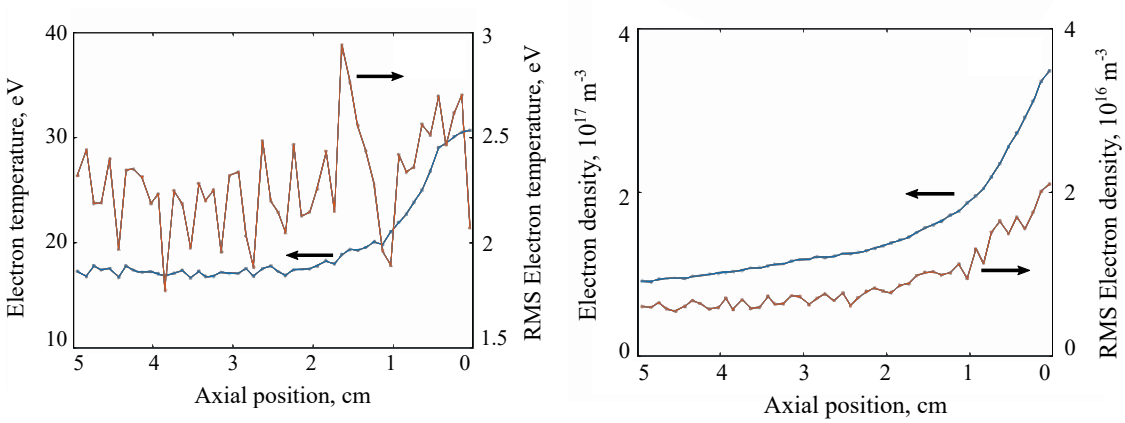

(a) (b)

Figure C.6: Time-averaged electron temperature and density and their oscillation amplitudes were determined from the HSLP for the nominal case. Results were binned and averaged every mm.

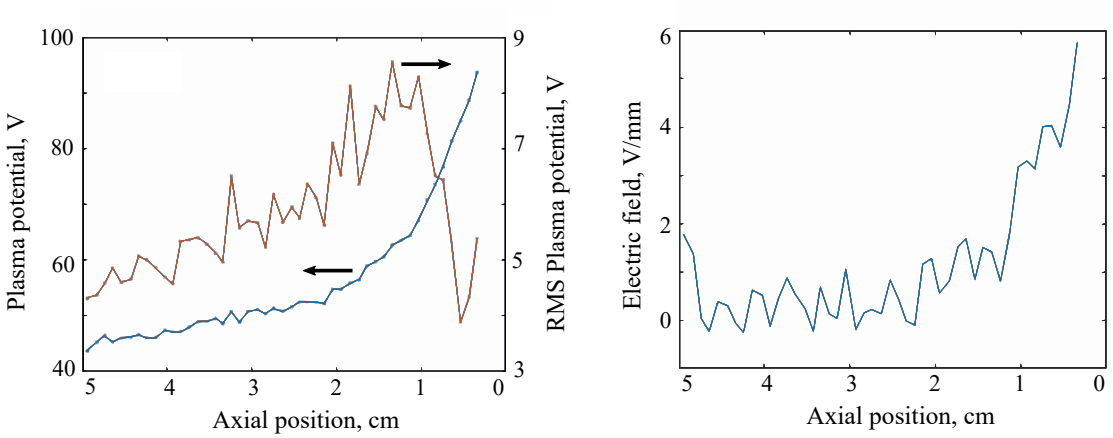

(a) (b)

Figure C.7: Time-averaged plasma potential and its oscillation amplitude was determined from the HSLP for the nominal case. Results were binned and averaged every mm. The electric field magnitude was computed from the plasma potential as its second-order numerical derivative.

F.3 and F.4. While the probe is far from the thruster, there are diffuse oscillations centered ∼10 kHz; when the probe is near the exit plane, the oscillations suddenly become more defined closer to 100 kHz; as the probe continues into the channel, there are no strong low-frequency oscillations. Interestingly, there are weak but remarkably consistent oscillations above 1 MHz that are present on either side of the transition threshold. Similarly, the V_{c2g} spectra show features above 100 kHz that appear com-

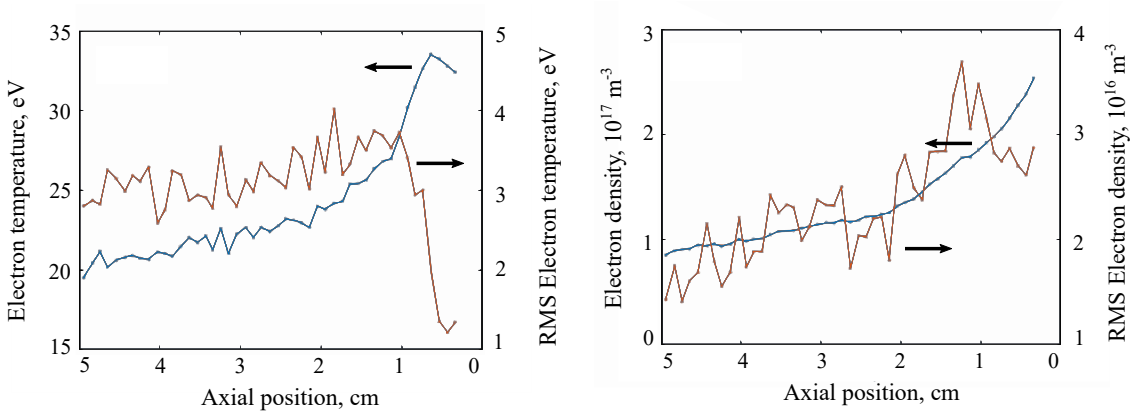

Figure C.8: Time-averaged electron temperature and density and their oscillation amplitudes were determined from the HSLP for the nominal case. Results were binned and averaged every mm.

pletely undisturbed by the probe. It is interesting to note that although the oscillation amplitudes of V_p and T_e for the half-magnet case showed a decrease near -10 mm, the I_d spectrum appears unchanged. This indicates that either the decrease in amplitude from the HSLP data is erroneous and an artifact of the analysis process, or that all oscillations were weakening without otherwise changing character. This latter effect should be unnoticeable in Fig. F.11 since the spectra are all normalized.

Figure F.12 shows a few representative spectra from Figs. F.10 and F.11, with considerable smoothing applied to clarify their differences. As seen in the full spectral plots for nominal operation, there is a broad peak centered near 24 kHz before the transition region; during the transition, the peak becomes more defined and increases toward 59 kHz; after the transition, there is a broad peak at a similar frequency but relatively weaker. As noted before, there is a 4.7 MHz feature that is common to both stable spectra. For half-magnet operation, there are broad peaks at 8 and 24 kHz before transition, and a 27 kHz peak during and after transition. There is a 4.7 MHz feature that appears in all regions. The exact values of these peaks are not meaningful due to the noisiness of the raw spectra but the clear shifting of features corresponding with probe position is indicative of perturbation of the discharge. We

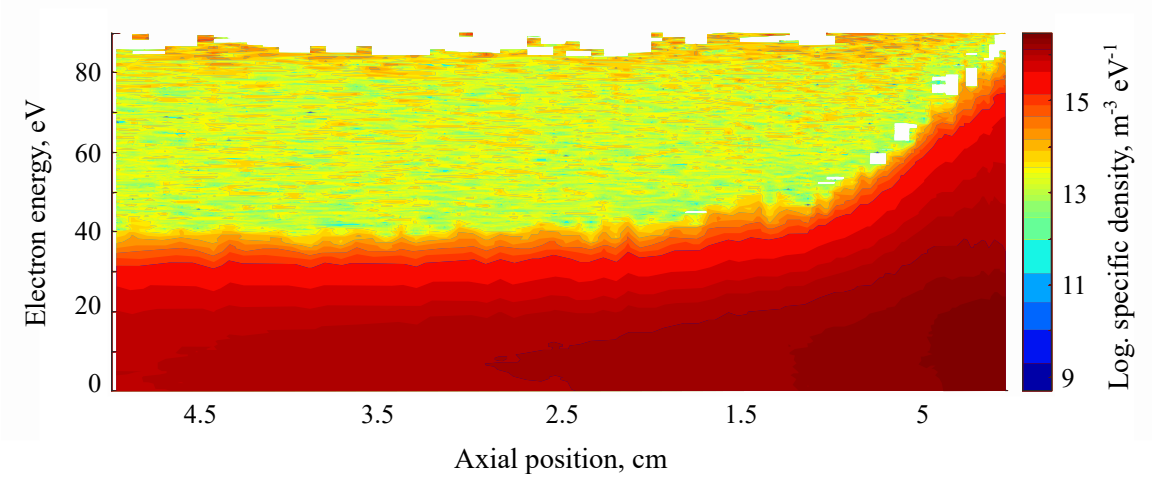

(a)

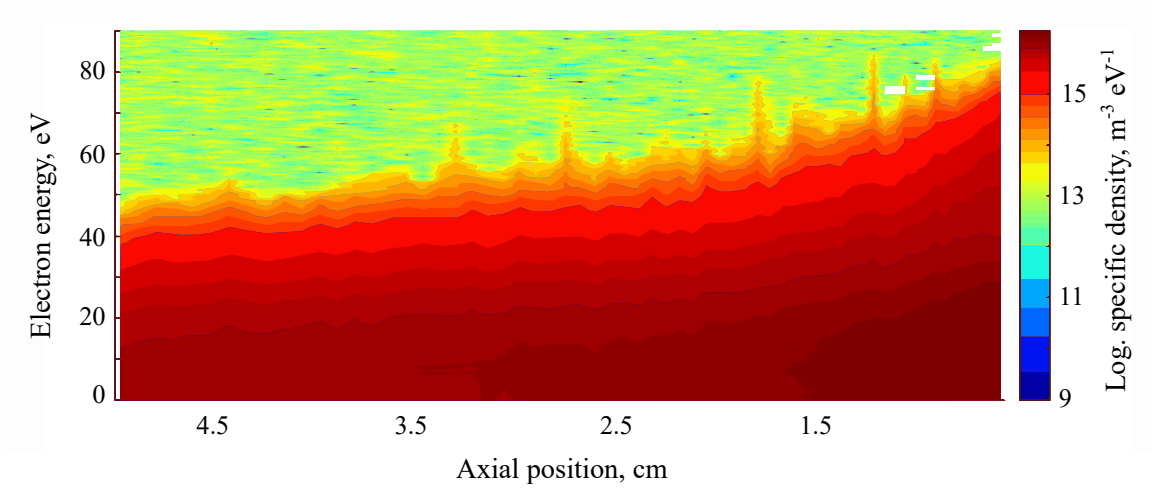

(b)

Figure C.9: The 1D EEDF can be calculatd from the HSLP data. The nominal case is shown on top and the half-magnet case below.

speculate on the nature of these effects in Appendix E, but it suffices to say here that they suggest high-speed Langmuir probing will not be a satisfactory diagnostic for characterizing the breathing mode.

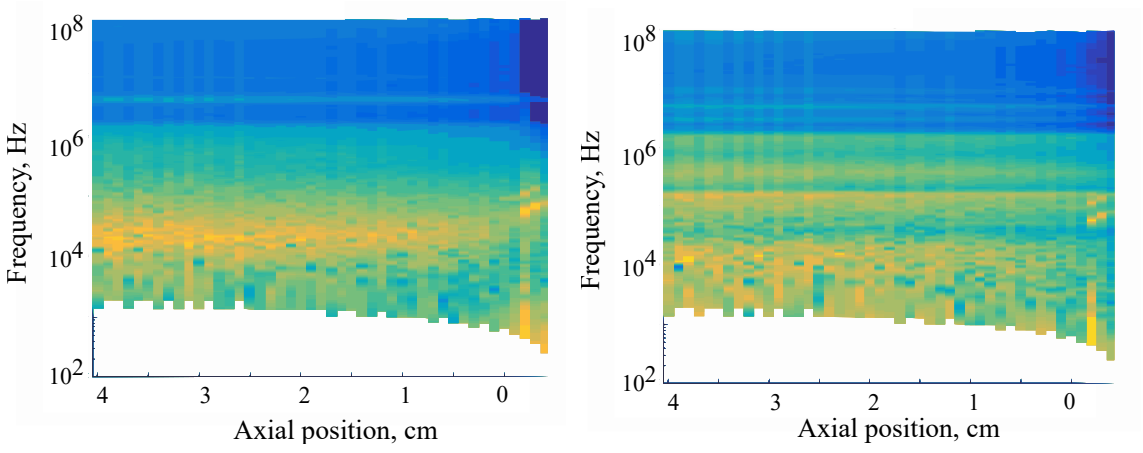

(a) (b)

Figure C.10: The relative power spectra of I_d (a) and V_{c2g} (b) are shown as a function of axial position for nominal thruster operation. Hotter colors indicate greater logarithmic spectral power. The range of each spectrum (vertical slice) varies due to the differing amounts of time the probe spent at each location while decelerating. Quantization artifacts observable at alternating light and dark bands are non-physical.

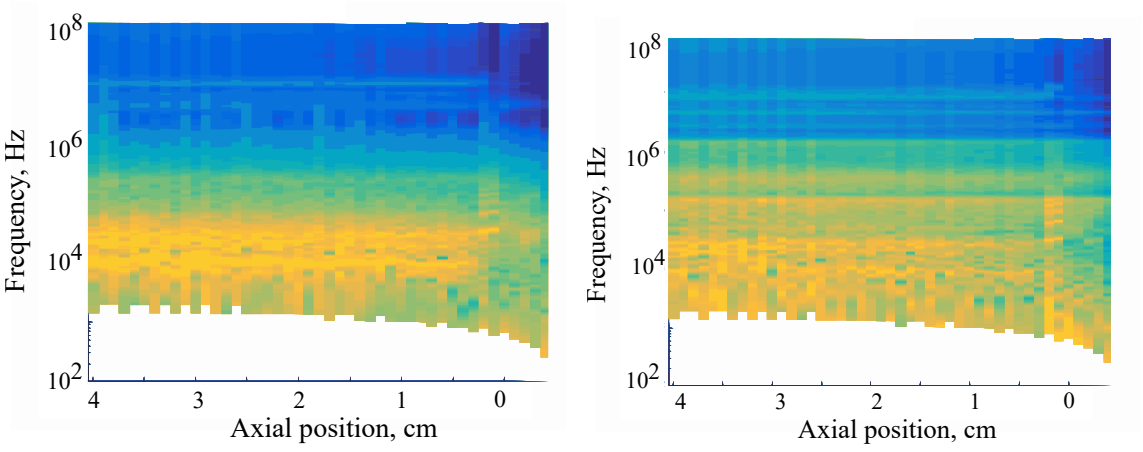

(a) (b)

Figure C.11: The relative power spectra of I_d (a) and V_{c2g} (b) are shown as a function of axial position for half-magnet thruster operation. Hotter colors indicate greater logarithmic spectral power. The range of each spectrum (vertical slice) varies due to the differing amounts of time the probe spent at each location while decelerating. Quantization artifacts observable at alternating light and dark bands are non-physical.

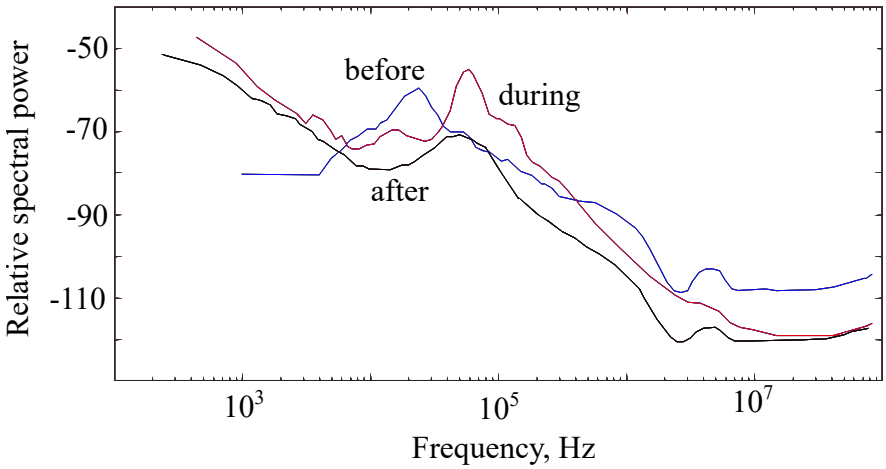

(a)

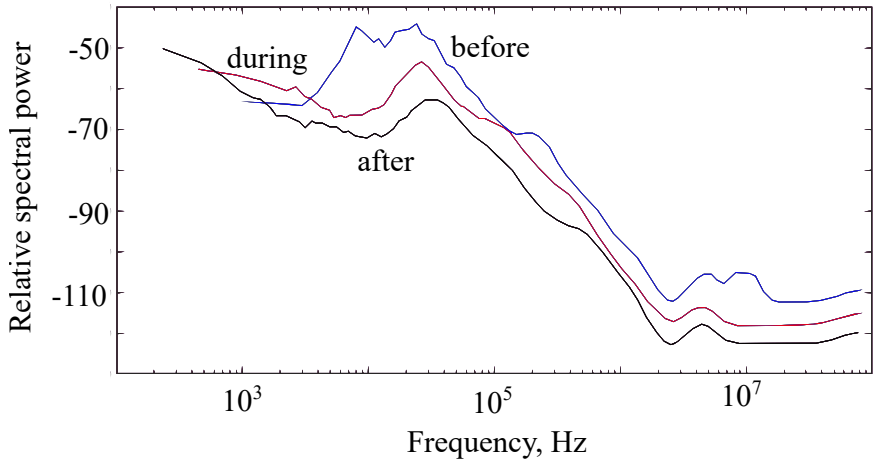

(b)

Figure C.12: Selected relative power spectra of I_D are shown for the nominal (top) and half-magnet (bottom) conditions. Five-point linear Savitzy-Golay smoothing was applied to the spectra, which was binned and averaged logarithmically with a width of 0.05 orders of magnitude.

APPENDIX D

High-Speed Langmuir Probe Analysis

The analysis of HSLP data is similar to that for a traditional Langmuir probe once the differential current is known. Algorithms for Langmuir probe analysis are widely available [89] and will not be focused on here. However, two major aspects of the analysis procedure that were developed as part of this work and described in the following sections are the phase correction of the current and voltage signals by considering transmission line effects, and compensation for sheath capacitance current.

Phase Correction

The major obstacle in operating a Langmuir probe at sweep rates near 100 kHz is the large displacement current generated by the capacitance of the probe cables. However, signal distortion may also be introduced due to transmission line effects. In a typical setup, a 100 kHz sine wave will be sent over roughly 5-10 m of 50-Ω coaxial cable from the voltage source to the probe tip. When the signal wavelength is much greater than the cable length, a standing wave is quickly developed on the line. In this experiment, the digitizer cards were sampling every 5 ns while the signal

traversed the line every 56 ns, and thus the standing wave developed on time scales detectable by the digitizers. Of course, this does not imply that these effects could be meaningfully discriminated by the digitizer, as the time it takes the standing wave to develop is much faster than the period of the biasing signal. However, it does suggest that transmission line effects may be relevant when analyzing the voltage and current signals used to construct I-V traces. One way to account for these effects is by correcting the I-V phase by treating the probe circuit as a low-pass filter, and then separately accounting for line transit delay by time-shifting the signals. For example, a 5-m long cable with 1 pF of uncompensated capacitance conducting 1 mA of plasma current at 100 V will contribute at 100 kHz approximately $\tan^{-1}\{-CV\omega/I_p\} = 0.0017°$ phase lag between voltage and current signals, but there will also be a 20-ns round-trip propagation delay along the cables. Although this method may effectively align the probe current and bias signals, it greatly simplifies the electrical properties of the probe cabling and as a result may not appropriately remove phase distortion.

Alternatively, for an ideal transmission line there is a phase distortion k that describes the linear change in phase of the signal. Note that in transmission line terminology this is the imaginary component of the propagation constant of the line, but in fact is is simply a line propagation wavenumber. As a simplistic approach, the phase offset between the voltage and current signals in the HSLP setup can be estimated by tracking how "far" the signals travel relative to each other. First, a voltage signal is generated at the amplifier and travels one line length, L_c, before reaching the probe tip. The time required for sheath formation may not be insignificant compared to the sampling rate of the digitizer [87] but it may be assumed that the sheath begins forming immediately, and thus the current signal (albeit representative of an incompletely developed sheath) is generated immediately. Next, the plasma current signal travels back to the amplifier. In this sense, the voltage signal of interest has traveled L_c compared to the measured voltage signal, while the measured current

signal has traveled L_c compared to the desired current signal. Thus, the signals are out of phase by $2kL_c$. For the cable discussed in the previous example, a 1-mΩ line resistance, perfect isolation, and no inductance would yield a k of 0.022 rad/km. Note that this rudimentary approach to accounting for phase distortion has ignored wave reflections from the probe tip, which may be significant depending on the impedance of the plasma and probe sheath. In practice, placing 50-Ω shunt resistors near the amplifier can reduce secondary reflections, but a matching network would be needed to properly remove primary reflections from the load.

Sheath Capacitance Effects

The capacitance of the sheath that forms at the probe tip may also skew the current signal measured with a HSLP by introducing displacement current. An analytical expression for sheath capacitance, C_{sh}, as a function of probe bias V_b, plasma potential V_p, and Debye length λ_D has been derived by Chen [172] and is shown in Eq. (D.1), where $V^* \equiv -(V_b - V_p)/T_e$. For typical near-field HET plasma parameters, C_{sh} will be at most $\sim$10 pF, which may be comparable to the mismatch in line capacitance between the active and null probe cables in a HSLP. A major difference is that line capacitance mismatch will produce displacement current 90° out of phase with the bias signal, while sheath capacitance current has a more complicated variation, indicated by Eq. (D.2). In this way, the bias signal waveform can be designed such that the line capacitance current is strongest in ion saturation, which impacts the resulting I-V trace little since this region already may not be reliably measured with high-speed digitizer cards. In contrast, the impact of sheath capacitance current may be greatest in the electron retarding region, which can significantly skew extracted plasma parameters.

$$C_{sh} = A_p \frac{\epsilon_0}{\lambda_D} \frac{1}{\sqrt{2}} \frac{(1+2V^*)^{-1/2} - \exp(\text{-}V^*)}{\sqrt{\sqrt{1+2V^*} + \exp(\text{-}V^*) - 2}} \tag{D.1}$$

$$I_{sh}(t) = C_{sh}(t) \frac{d[V_b(t) - V_p(t)]}{dt} + [V_b(t) - V_p(t)] \frac{dC_{sh}(t)}{dt} \tag{D.2}$$

One approach to removing the sheath capacitance effect is to analyze the I-V trace to estimate V_p and λ_D, use these values to estimate C_{sh} according to Eq. (D.1), and then compute I_{sh} according to Eq. (D.2). The resulting sheath capacitance current can be subtracted from the probe current signal, and the process can be repeated. This continues iteratively until the plasma parameters extracted from the I-V trace are consistent with the sheath capacitance correction used in producing that trace.

The former approach assumes that the sheath capacitance effect is small enough to begin with such that the I-V trace can be effectively analyzed. Figure D.1 demonstrates how severe trace hysteresis due to sheath capacitance can be with a large probe. As an alternative, one can average sequential I-V traces. Traces with different signs for dV_b/dt will either add or subtract sheath capacitance current, so the average of sequential traces will have the sheath capacitance effect removed. This method assumes that plasma properties are not changing drastically trace-to-trace. Although this approach halves the sampling rate of the HSLP, it does not rely on Eq. (D.1), which carries with it the assumption of a Maxwellian plasma and *a priori* knowledge of the plasma parameters.

Additionally, this sequential averaging analysis technique yields an estimate for I_{sh} as half the difference between the traces, and so Eq. D.3 can be applied to compute the sheath capacitance. For a sufficiently Maxwellian plasma, Eq. (D.1) can then be used to estimate T_e and n. In this way, a variety of plasma parameters can be simultaneously calculated via the traditional I-V analysis procedure and with this capacitance method. Further, the plasma potential can be estimated using the

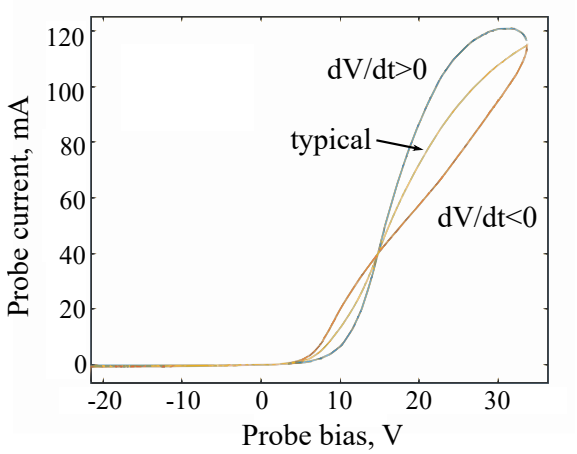

Figure D.1: Probe hysteresis due to sheath capacitance, compared to an ideal trace generated by taking the average of two skewed sequential traces.

computed sheath capacitance. When the probe is biased to plasma potential, it will have no sheath and thus it will have no sheath capacitance, and so the voltage at which the experimental C_{sh} curve drops to zero can serve as an estimate of the plasma potential. As Eq. (D.3) shows, this method relies on numerical integration of the current data instead of differentiation like the traditional I-V analysis method, which reduces noise.

$$C_{sh}(t) = \frac{\int_{t_0}^{t} I_{sh}(t')dt'}{V_b - V_p} \tag{D.3}$$

Since V_p as estimated with the sheath capacitance technique is very sensitive to the alignment of the current and voltage signals, checking the consistency of the V_p values for the low-pass filter and transmission line phase correction methods can be used to compare them. For a set of sample HSLP data, the plasma potential was found in the traditional I-V trace manner ($V_{p,IV}$) by identifying the maximum of the first derivative of the collected electron current, and in the new sheath capacitance way ($V_{p,sh}$) by identifying the zero-crossing of the integral of the current due to sheath capacitance. The resulting V_p values were averaged over >18,000 traces spanning about 180 ms to yield DC values for easy comparison. In one test case involving a

<100 W hollow cathode plume-mode plasma (from which Figure D.1 was extracted), the low-pass filter alignment technique yielded $V_{p,IV}$=14.5 V and $V_{p,sh}$=8.8 V, while the transmission line technique yielded $V_{p,IV}$=15.3 V and $V_{p,sh}$=15.2 V. Given that the uncertainty of these values is about ±1 V, this indicates that the transmission line method yields plasma potential values that are much more consistent than the low-pass filter method. Altogether, this shows that the transmission line technique discussed previously is superior than the standard low-pass filter method, and that with it the plasma potential can be easily estimated from the sheath capacitance.

APPENDIX E

Probe Perturbation Effects

Probe Effects

In the present study, many of the characteristic probe perturbation features documented in previous work were observed. For instance, a sudden mode change was observed in which $\bar{I}_d$ had a sustained increase and $\tilde{I}_d$ had a momentary increase. This indicates that operating a HSLP in the very-near-field of a HET is comparable to doing so with traditional diagnostics from a perturbation perspective. However, the inability to measure usable I-V traces beyond the mode transition point indicates that there is a unique interaction between the thruster and HSLP. Based on previous work, this likely means the HSLP can only be used up to the perturbed electric field maximum, which will be downstream of the nominal electric field maximum. Assuming the interaction of the HSLP with the thruster is not particular to this experiment, for a typical HET a HSLP will become unusable close to and beyond the exit plane. As a result, the acceleration and ionization region will largely be off limits to this diagnostic.

Beyond demonstrating that a HSLP can be used in the very-near-field of a HET, the data yielded by the HSLP can be used to compare the perturbative effects of

the probe in this experiment to other investigations. Previous LIF studies of a BHT-200 showed the electric field maximum for the nominal conditions occurs about 2 mm upstream of the exit plane, and for a 75% magnetic field strength condition 1.5 mm upstream of the exit plane [99]. In the present study, the mode transition due to perturbation occurred at the exit plane for the nominal case and roughly 3 mm downstream of the exit plane for 50% magnetic field strength. These values are approximate, since the discharge current began gradually increasing over several centimeters before jumping drastically. The transition point is judged with the discharge current signal because spatial variations in plasma parameters measured with the HSLP may mask variations due to mode transition. Assuming these positions are close to the electric field maximum, these results are consistent with previous investigations: the discharge was shifted downstream due to the presence of the cold probe, and the probe was measuring this perturbed discharge. Unfortunately, V_p could only be measured up to the point of mode transition, which prevents the electric field maximum from being truly resolved in this experiment.

Although the transition point indicated by the discharge current agrees with trends in previous work, when comparing the magnitude of the electric field measured via HSLP and LIF [99], it appears that the discharge displaced 2-3 mm upstream, which would put the electric field maximum roughly 4-5 mm upstream of the exit plane. This does not correspond with the transition point determined from the discharge current signal, nor does this trend agree with previous work.

For the half-magnet case, the position of the unperturbed electric field maximum is unknown, other than that it should be downstream of +1.5 mm. Again, the probe measurements were unreliable near the transition point, so it cannot be directly concluded if the transition point corresponded with the perturbed electric field maximum. However, it can be postulated that the unperturbed discharge should be downstream of the 75%-magnet case for which LIF measurements are available, and

thus the perturbed electric field maximum should be downstream of the 75%-magnet unperturbed maximum. Again, though, the electric field magnitudes yielded by the HSLP are small and correlate best to a shift of the discharge upstream by 3-4 mm.

The most likely cause of this discrepancy is the HSLP itself. Namely, the time-resolved I-V traces become very noisy close to the HET, which makes the trace analysis much more uncertain. The data was binned with a resolution of 1 mm, allowing 50-200 trace results to be averaged for each bin. But note that each trace was analyzed and the results averaged, instead of the traces being averaged and then analyzed. This is done because the presence of instabilities close to the sweep rate of the HSLP may make trace-averaging unreliable.

However, it is important to note that Grimaud et al. showed floating probes could lead to either upstream or downstream shifts of the discharge depending on the probe geometry [82]. That is, a large floating probe produced a downstream shift while a smaller floating probe produced an upstream shift. This suggests that the observed upstream shift of the discharge may not be evidence of poor probe performance but is instead a function of the probe geometry or operation.

Discharge Shift Mechanism

Work by Staack et al. and Grimaud et al. has shown that probe material and heating have an effect on perturbation due to probe injection, which suggests that secondary electron emission (SEE) is the mechanism behind the perturbation [80, 82]. Jorns et al. postulated that, due to the proportionality between axial electric field strength and collision frequency ν_e, a perturbation in ν_e could lead to mode transition [81]. When a probe is injected into the channel, SEE will lead to the production of cold electrons, lowering T_e and thus ν_e, encouraging mode transition. However, this does not reconcile the shifting of the discharge with the sudden mode transition observed once the probe reaches the electric field maximum. Further, it does not

explain what controls the direction of the discharge shift, nor does it predict that such a shift occurs.

The characteristics of the discharge shift remain incompletely explored. Data collected by Jorns et al. with wall probes shows the T_e maximum – and presumably the maximum electric field location – moves gradually downstream as the probe approaches the thruster, rather than the discharge "snapping" between locations [81]. With this in mind, Jorns' data indicates that the discharge moves downstream until the probe tip reaches the electric field maximum, at which point it stops moving even though the probe body is still immersed in the plasma and the probe tip is still moving toward the anode. In Jorns et al.'s experiment, the discharge stops shifting soon after the probe has passed the wall probes. This could be interpreted two ways: the wall probes were coincidentally placed near the perturbed maximum electric field location, or the perturbation is a local effect.

The latter option seems unlikely because it would suggest that during probe injection the thruster can develop multiple ionization and acceleration regions, and sustain them over many electron channel residence periods. The former option suggests that the probe is fundamentally reshaping the potential structure in the discharge channel as it approaches the thruster. A probe body will contribute low-temperature electrons along its entire length, depleting local higher-energy populations of electrons. An equilibrium temperature along each isothermal magnetic field line impinging on the probe is reached when the SEE-mediated electron cooling is balanced by the thermalization of incoming electrons that have hopped onto the field line. A cooler electron population will promote collisions that allow electrons to cross field lines, and thus the probe will increase mobility in a way that is dependent on the equilibrium temperature.

The electric field maximum typically corresponds with the location of minimum mobility, which occurs where the radial magnetic field strength is greatest. But when

a probe is present, a new equilibrium temperature profile will form and dictate a new mobility profile. Due to the nonlinearity of SEE effects, especially when space charge saturated sheaths can form such as in a HET discharge channel, the influence of the magnetic field on electron mobility may be outweighed in certain places, allowing the electric field maximum to shift away from the radial magnetic field maximum. Although this postulation has been entirely qualitative, it presents a possible mechanism for discharge shifts due to probe interaction. Moreover, it suggests that perturbation due to probe injection can fundamentally alter the operation of the thruster, and is dependent on the probe materials and its interaction with the plasma, which we believe implies that perturbation of the discharge can only be minimized, not avoided completely.

APPENDIX F

Evaluation of Time-Resolve Laser-Induced Fluorescence and IBIS

Introduction

The first diagnostic technique we will discuss is high-speed electrostatic probing. We begin by reviewing previous development and application of this technique. We then discuss our particular implementation of it, including the electronics and translation stage involved. We conclude with an overview of the analysis of high-speed Langmuir probe traces, focusing on our contributions.

Previous Work

Electrostatic probing of plasmas, and particularly Langmuir probing, has an extensive history of application [153] and theoretical study [154]. As a brief review, a Langmuir probe is an electrode inserted into a plasma and biased so that it collects ion and electron current. As the voltage is reduced far below the plasma potential, the probe predominantly collects ions. Due to sheath expansion, the ion saturation

current can be estimated by accounting for Coulombic trajectories of ions (orbital motion limited theory) to yield a saturation ion current $I_{i,s}$ collected by a probe of area A_p for a given plasma potential V_p and ion mass m_i of

$$I_{i,s} = \frac{\sqrt{2}}{\pi} enA_p \sqrt{\frac{eV_p}{m_i}} \ . \tag{F.1}$$

As the voltage increases, the more mobile electrons quickly begin to contribute current:

$$I_e = \frac{1}{4} enA_p u_{th} \exp\left(\frac{V_b - V_p}{T_e}\right) \text{ for } (V_b - V_p) < 0 \ , \tag{F.2}$$

where u_{th} is the electron thermal speed and V_b is the probe bias relative to ground. At some voltage V_f the ion and electron current balance and the probe is said to "float."

Langmuir probes can also characterize non-Maxwellian plasmas. For example, the Druyvesteyn method [155] allows the electron energy distribution function f_e to be calculated from the electron current:

$$f_e = -\frac{2}{e^2 A_p} \sqrt{2m_e e\left(V_p - V_b\right)} \frac{d^2 I_e}{dV_b{}^2} \ . \tag{F.3}$$

Other theories [156, 157] exist for the calculation of the EEDF from the first derivative of the electron current, for varying assumptions and probe geometries.

Although high-speed plasma probes operating on these principles have existed for as long as high-speed electronics [158, 159], the use of fast electrostatic probes to characterize Hall thrusters is a relatively recent development. Previously, floating probes have been used to detect the presence of oscillations [22] or negatively-biased probes to estimate ion density [32], but the amount of information yielded with these techniques was limited.

One of the major limitations in measuring high-speed plasma properties with

an electrostatic probe is that often the probe bias must be swept to infer many plasma parameters. One exception is the triple-probe [160], which makes use of two electrodes biased relative to a third such that there are three distinct plasma currents collected at any given time, allowing electron temperature and density to be estimated instantaneously. However, these probes have no capacity for characterizing non-Maxwellian plasmas and are particularly susceptible to noise [89], so for these reasons as well as the inherent additional electronics and poor spatial resolution, swept probes have remained most prominent. As a result, most Langmuir probe circuits are limited by the sweep rate that can be applied.

As the rate of voltage sweep is increased, reactance of the probe and cabling quickly leads to the collection of spurious current that can obscure the plasma-related signal. It has long been suggested to use a filter with a rapidly-swept probe to minimize its reactance [161]. This basic concept has been applied to Langmuir probes for fusion applications [162, 163, 164] with success. For Hall thruster research, studies have been performed with phase-averaged probing [165] relying on well-matched cabling, as well as moderately fast unfiltered probing necessitated during reciprocating probe injection using high-speed actuators [166, 167]. A significant amount of pioneering work with high-speed Langmuir probe operation was performed by Lobbia [168].

As Lobbia and Gallimore demonstrated [87], the theoretical bandwidth for a Langmuir probe very close to a Hall thruster is generally limited to below 100 kHz by the stray capacitance of the probe cabling; otherwise, the limit may be $\sim$1 MHz or higher. As a result, Lobbia and Gallimore developed a high-speed dual Langmuir probe configuration in which the differential current between two identical (parallel) probes – one with a plasma-wetted tip and one without – removes any accumulated reactive current [59]. Specifically, an active probe cabled with capacitance C and swept at a rate dV/dt collects both plasma current I_p and capacitive current such

that $I_a = I_p + CdV/dt$, while an unexposed "null" probe collects only the (identical) capacitive current. As a result, the differential current should be equal to the true plasma current, $\Delta I = I_a - I_n = I_p$, which should be relatively undistorted up to a few megahertz. Lobbia's thesis work demonstrated the successful application of this diagnostic technique to Hall thruster plumes [168] and the technique was applied further by Sekerak et al. [169]. More recently, an alternative but similar system using variable capacitors was built and applied fruitfully for studying a different E×B device by Skoutnev et al. [170]. The techniques used to analyze HSLP data do not depart far from traditional Langmuir probe analysis and are discussed in Ref. [168]; a few modifications we contributed to this procedure are reserved for Appendix D.

Implementation

As part of evaluating possible diagnostic techniques for characterizing the breathing mode, we implemented a high-speed Langmuir probe (HSLP) as part of a high-speed axial reciprocating probe (HARP) setup in the style of Haas et al. [79]. The probe was attached to a Aerotech linear motor system that included a brushless servomotor and a Renishaw incremental encoder that was used to maintain positional accuracy $\leq$1 mm. This system was used to produce speeds up to 1.8 m/s and accelerations up to 4.6 g, reducing the residence time of the probe inside the thruster below 50 ms. The planar Langmuir probe was equipped with an exposed (active) electrode, a hidden (null) electrode, and a large reference electrode, where the active electrode was a tungsten collector approximately 1.1 mm by 0.5 mm in size. The reference electrode was included to shorten the return path for plasma current. The probe was injected as far as 5 mm into the discharge channel at a range of radial locations from 2 mm inward to 1 mm outward from the injection origin, located on channel centerline azimuthally between 3 and 6 o'clock. The axial probe position was measured from the center of the probe collecting surface. The probe collecting surface normal was

oriented mostly in the radial direction to prevent the collection of ram current from the electron E×B drift, as shown in a diagram of the setup in Fig. F.1.

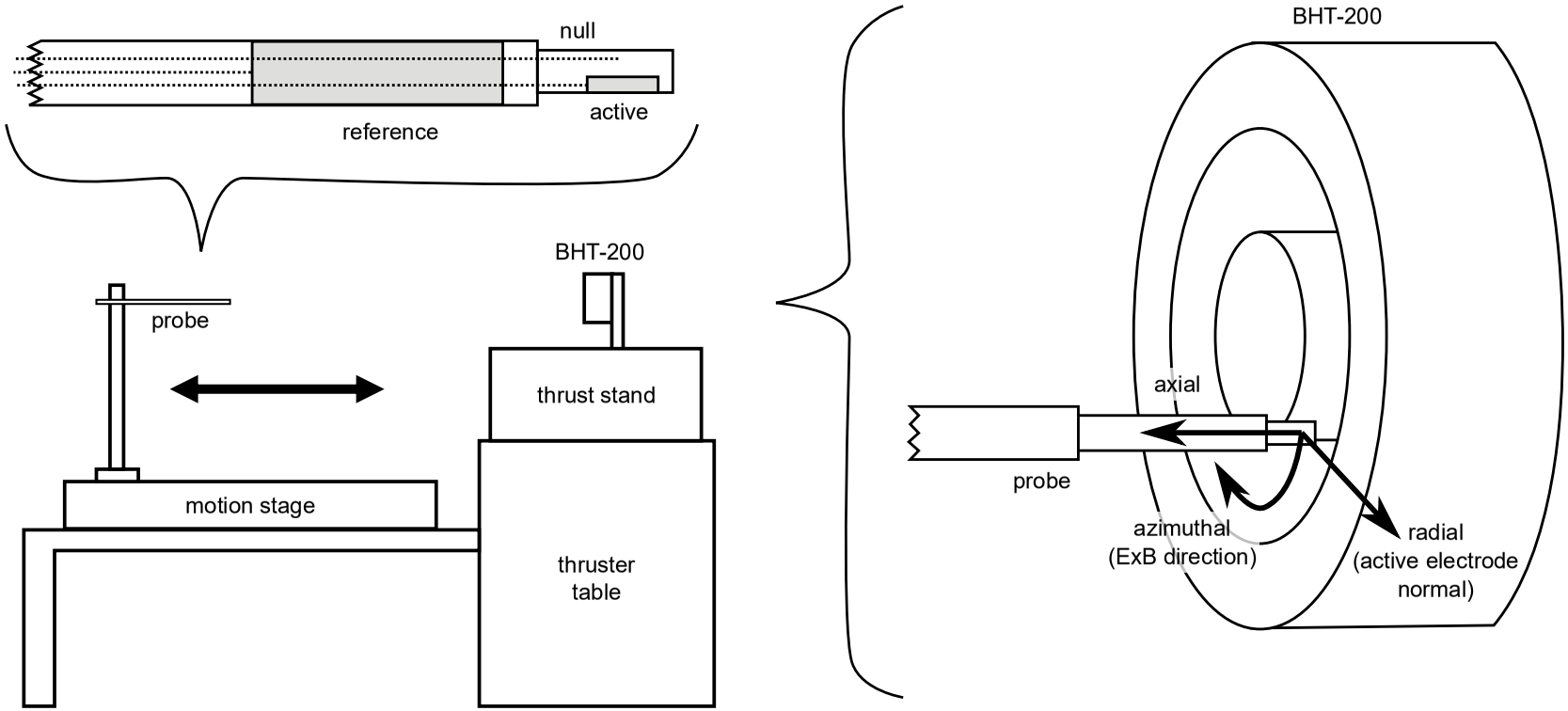

Figure F.1: A diagram of the experimental configuration for high-speed Langmuir probing.

The hardware of the HSLP setup included an Agilent 33600A waveform generator, a Krohn-Hite 7500 wideband power amplifier, several API 610-10-2 oscilloscope probes, and a Tektronix TCP312 current sensor paired with a Tektronix TCPA300 amplifier, as shown in Fig. F.2. All high-speed signals were recorded with Gage CSE1642 digitizer cards, recording with 16-bit depth at 200 MS/s and 125 MHz bandwidth. Motion stage position data was stored in the Aerotech Soloist HLe controller's onboard memory, triggering with the digitizer cards from a signal produced by a SRS DG535 pulse generator.

During the experiment, several probe configurations were tested. First, the probe was equipped with a large reference electrode near the tip electrode, and the probe was connected to the Krohn-Hite amplifier via a transformer. This would in theory allow the HSLP to operate like a double probe, floating to higher voltage as the probe approached the thruster, but also permitting the measurement of electron saturation due to the size disparity of the reference and tip electrodes. In practice, it was found that to preserve current continuity the probe would float to very low voltages, such that only ion saturation was reached. Next, the probe was ground-referenced and the biasing sine wave was superimposed on a low-frequency ramping voltage so that the sweep would never extend too far above the plasma potential (identified by large collected current) but still approach ion saturation for the entire measurement envelope. These two contrasting configurations are shown in Fig. F.2. In the ground-referenced setup, the differential current between the active and null probe lines was measured first with a pair of 50-Ω shunts and a Lecroy DA1855 differential amplifier, but it was found that the common-mode range of the amplifier was too limited to accommodate the sweep range for the entire probing envelope. Finally, the configuration was switched so that current was measured with the Tektronix TCP312 Hall sensor by counter-wrapping the active and null probe lines multiple time around the sensor. This increased the sensitivity of the sensor and yielded the differential

current without additional active electronics.

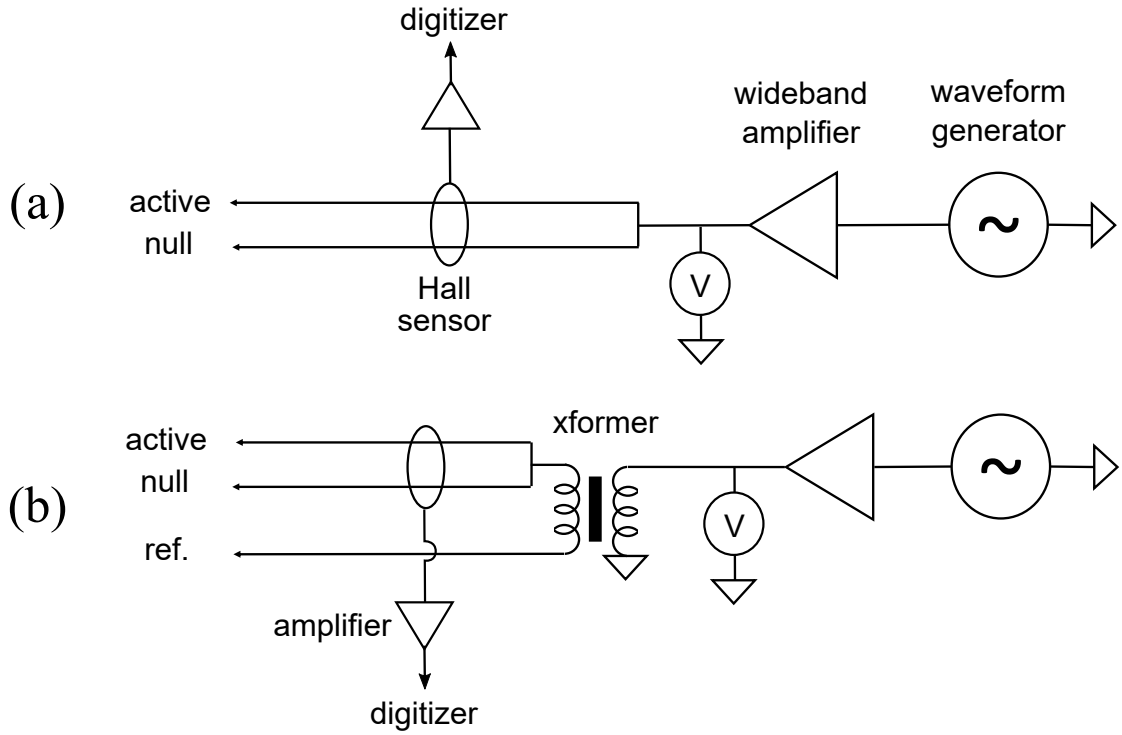

Figure F.2: A schematic of two variations of the high-speed Langmuir probe setup: (a) ground-referenced and (b) floating.

Evaluation

We also experimentally evaluated a high-speed Langmuir probe setup for interrogating the near-field plasma in a low-power Hall thruster. Specifically, an axially-injected high-speed Langmuir probe was evaluated in the SPEF chamber on a BHT-200 thruster for two oscillatory conditions: nominal magnetic field strength and half strength. For both conditions, there were strong oscillations at 24 kHz corresponding to the breathing mode. We examined not only the probe signal and the plasma parameters inferred from it but also the spectral response of thruster telemetry during a probe injection. In this way, aside from characterizing the near-field and internal plasma, we could also examine the perturbative effect of the probe injection.

Experimental Setup

The experiments in this evaluation work were conducted in the Space Environment Facility (SPEF) at the Air Force Research Laboratory, Edwards Air Force Base. The SPEF is a stainless steel sphere 9.1 m in diameter, equipped with six 122-cm oil diffusion pumps with LN_2-cooled baffles. This facility has a xenon pumping speed above 300 kL/s. It is equipped with a beam dump similar to LVTF, and likewise has equivalent water-handling and viewports.

The high-speed Langmuir probe experiments in SPEF were conducted on a BHT-200, a small commercial 200-W Hall thruster; an iteration of this device is described in Ref. [171]. This thruster has a nose cone that extend roughly 7 mm beyond the exit plane, a channel width of 16 mm, and a similar channel length. The thruster was operated at 150 V at a nominal magnetic field strength (200 W discharge) and at half strength (270 W discharge). At the nominal condition, the RMS oscillation amplitude was <5% of the mean discharge current, while at the half-strength condition they were closer to 20% – this is consistent with the onset of the breathing mode.

Transient Behavior

Figures F.3 and F.4 show the variation in discharge current with radial and axial probe position during high-speed injections for two different operating conditions: nominal (200 W) and half magnetic field strength (270 W). The exit plane is z=0, with z increasing positive in the downstream direction.

In agreement with other studies, the mean discharge current $\bar{I}_d$ increases as the probe approaches the thruster. However, the RMS discharge current $\tilde{I}_d$ only momentarily spikes. For the half-magnet condition shown in Figure F.4, the transition occurs outside the exit plane and it can be observed that $\tilde{I}_d$ drops below its nominal value as the probe enters the thruster. The response of I_d to the probe presence is therefore significant and nuanced.

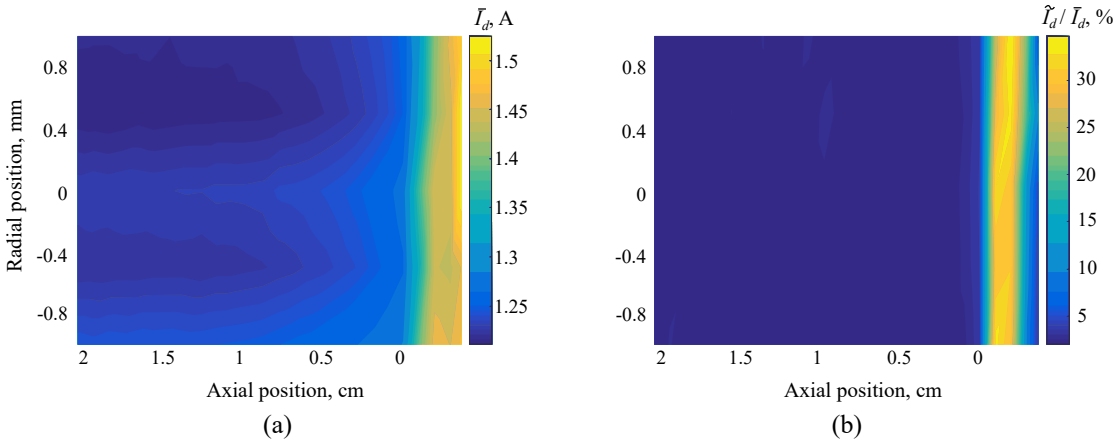

Figure F.3: The variation of $\bar{I}_d$ (a) and $\tilde{I}_d$ (b) is shown as a function of axial and radial position for nominal operation. The narrowness of the radial range mostly precludes its use in identifying spatial trends but can still serve as an indication of the consistency of the probe injections.

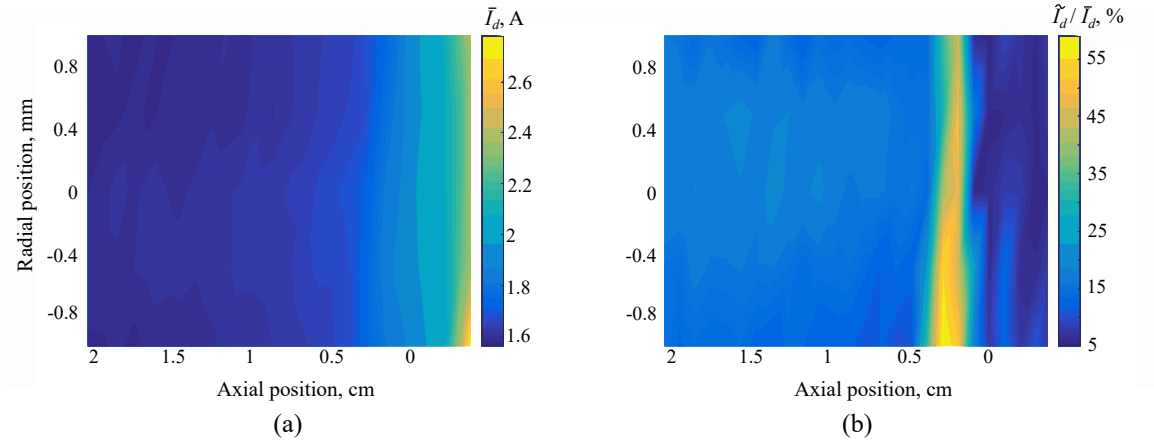

Figure F.4: The variation of $\bar{I}_d$ (a) and $\tilde{I}_d$ (b) is shown as a function of axial and radial position for half-magnet operation. The narrowness of the radial range mostly precludes its use in identifying spatial trends but can still serve as an indication of the consistency of the probe injections.

Several plasma parameters extracted from the HSLP I-V traces are shown in Figs. F.5-F.8 for the nominal and half-magnet cases. Note that the data for the nominal case only extends to the exit plane and for the half-magnet case to several mm downstream of the exit plane. This is due to the probe signals suddenly becoming unusable at these boundaries, as if due to some thruster mode transition. Otherwise, the trends in V_p, T_e, and n are as expected. The plasma potential was determined

with a polynomial-fitting algorithm to find a plateau in dI_e/dt, and after that the one-dimensional electron energy density functions (1D EEDFs) could be calculated following Ref. 157. The EEDFs are shown in Fig. F.9. From those surfaces, n and (effective) T_e spatial profiles were calculated by taking moments.

The nominal case shows no remarkable features in the oscillation amplitude of these parameters, other than perhaps a slight increase in amplitude toward the exit plane (shown clearly by n). The half-magnet case similarly shows reasonable DC trends, although T_e curiously appears to hit a maximum around 3 mm. Additionally, the oscillation magnitudes for V_p and T_e show a sharp decline starting at 10 mm. In both cases, the majority of the acceleration region is not captured as E_z is small and still increasing at the deepest point probed.

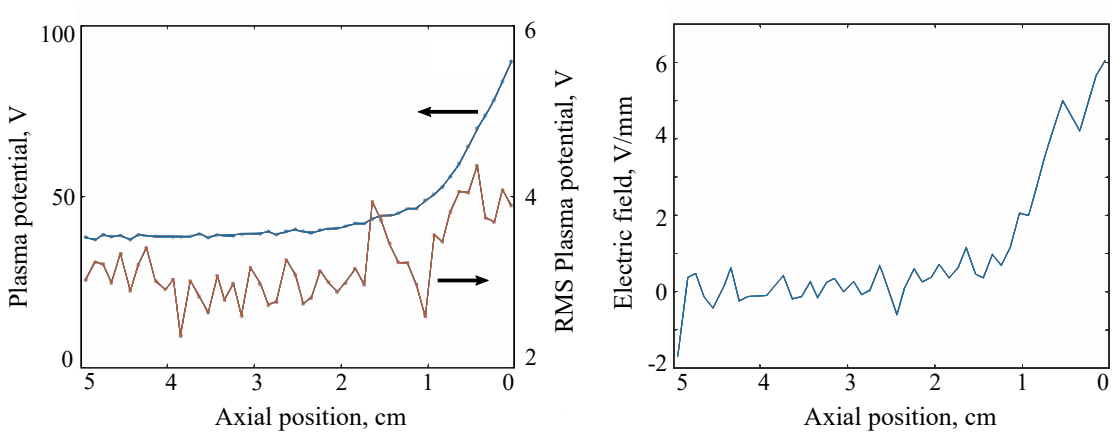

(a) (b)

Figure F.5: Time-averaged plasma potential and its oscillation amplitude was determined from the HSLP for the nominal case. Results were binned and averaged every mm. The electric field magnitude was computed from the plasma potential as its second-order numerical derivative.

Spectral Behavior

Figures F.10 and F.11 show the power spectra of the discharge current and cathode-to-ground voltage V_{c2g} as a function of axial position. There is a sudden change in the spectra at positions that correspond with the transition seen in Figs.

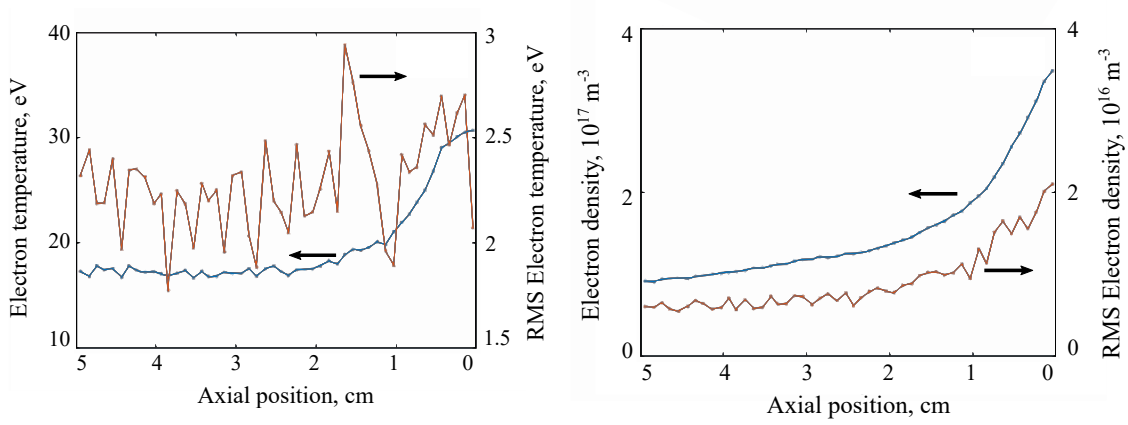

(a) (b)

Figure F.6: Time-averaged electron temperature and density and their oscillation amplitudes were determined from the HSLP for the nominal case. Results were binned and averaged every mm.

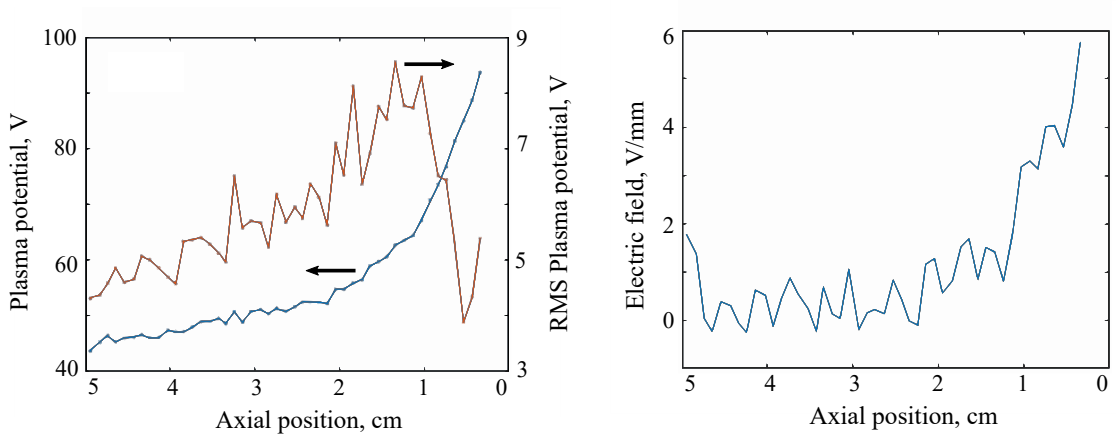

(a) (b)

Figure F.7: Time-averaged plasma potential and its oscillation amplitude was determined from the HSLP for the nominal case. Results were binned and averaged every mm. The electric field magnitude was computed from the plasma potential as its second-order numerical derivative.

F.3 and F.4. While the probe is far from the thruster, there are diffuse oscillations centered ∼10 kHz; when the probe is near the exit plane, the oscillations suddenly become more defined closer to 100 kHz; as the probe continues into the channel, there are no strong low-frequency oscillations. Interestingly, there are weak but remarkably consistent oscillations above 1 MHz that are present on either side of the transition threshold. Similarly, the V_{c2g} spectra show features above 100 kHz that appear com-

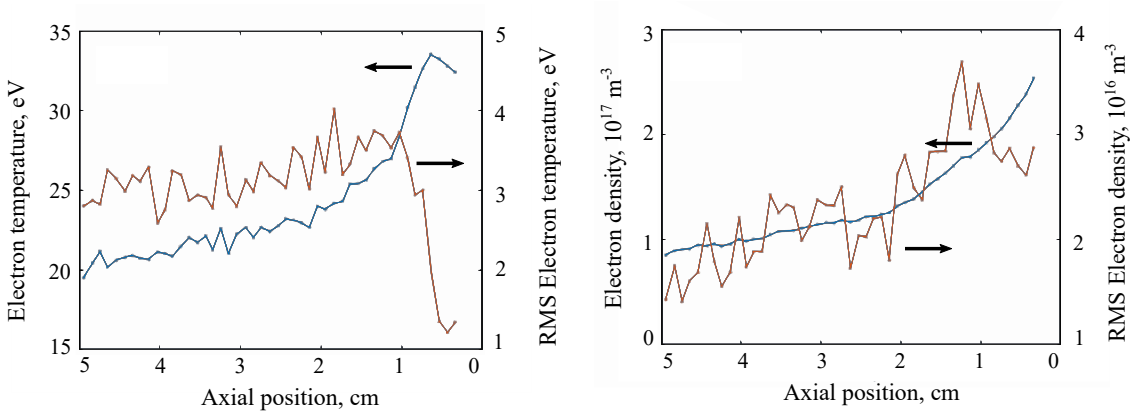

(a) (b)

Figure F.8: Time-averaged electron temperature and density and their oscillation amplitudes were determined from the HSLP for the nominal case. Results were binned and averaged every mm.

pletely undisturbed by the probe. It is interesting to note that although the oscillation amplitudes of V_p and T_e for the half-magnet case showed a decrease near -10 mm, the I_d spectrum appears unchanged. This indicates that either the decrease in amplitude from the HSLP data is erroneous and an artifact of the analysis process, or that all oscillations were weakening without otherwise changing character. This latter effect should be unnoticeable in Fig. F.11 since the spectra are all normalized.

Figure F.12 shows a few representative spectra from Figs. F.10 and F.11, with considerable smoothing applied to clarify their differences. As seen in the full spectral plots for nominal operation, there is a broad peak centered near 24 kHz before the transition region; during the transition, the peak becomes more defined and increases toward 59 kHz; after the transition, there is a broad peak at a similar frequency but relatively weaker. As noted before, there is a 4.7 MHz feature that is common to both stable spectra. For half-magnet operation, there are broad peaks at 8 and 24 kHz before transition, and a 27 kHz peak during and after transition. There is a 4.7 MHz feature that appears in all regions. The exact values of these peaks are not meaningful due to the noisiness of the raw spectra but the clear shifting of features corresponding with probe position is indicative of perturbation of the discharge. We

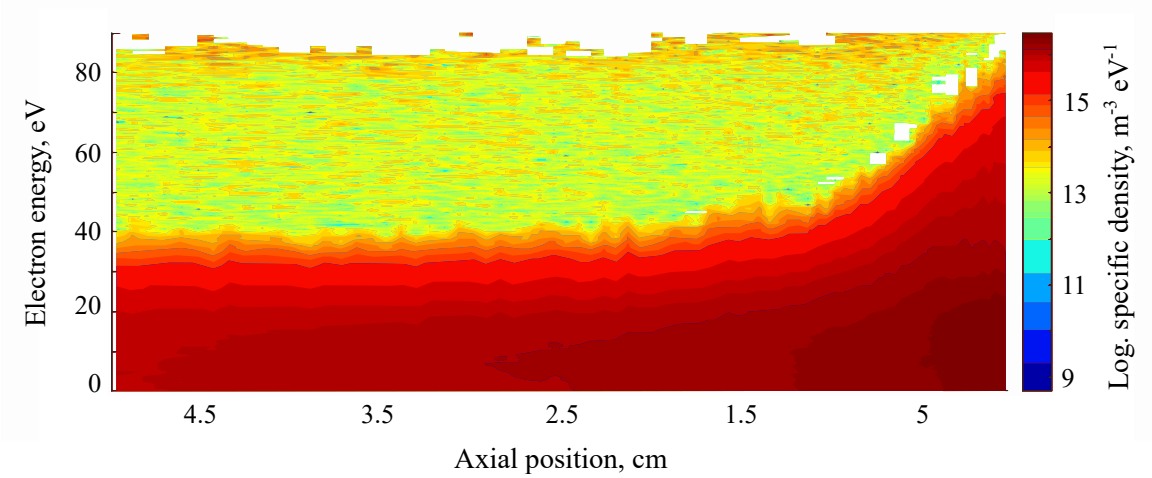

(a)

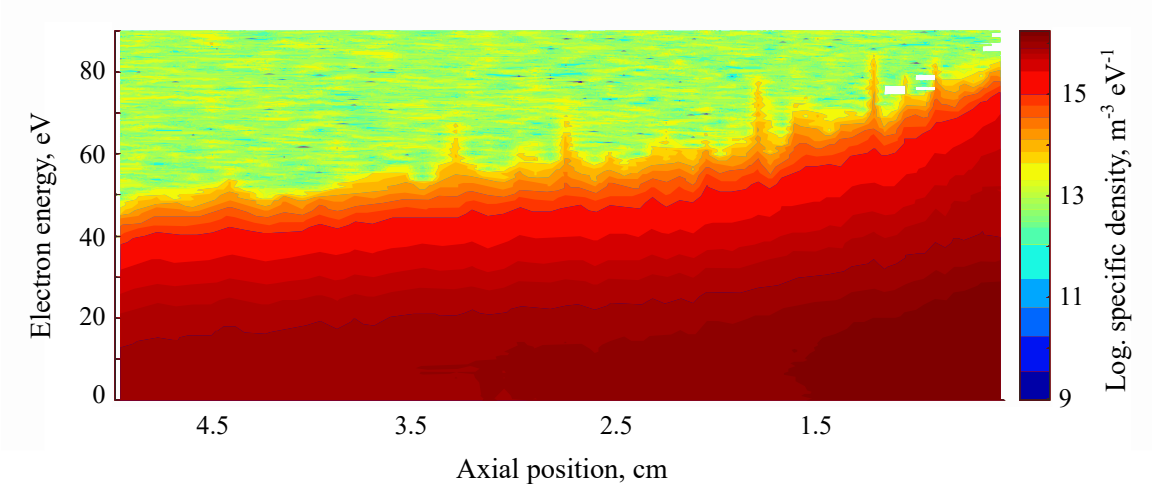

(b)

Figure F.9: The 1D EEDF can be calculatd from the HSLP data. The nominal case is shown on top and the half-magnet case below.

speculate on the nature of these effects in Appendix E, but it suffices to say here that they suggest high-speed Langmuir probing will not be a satisfactory diagnostic for characterizing the breathing mode.

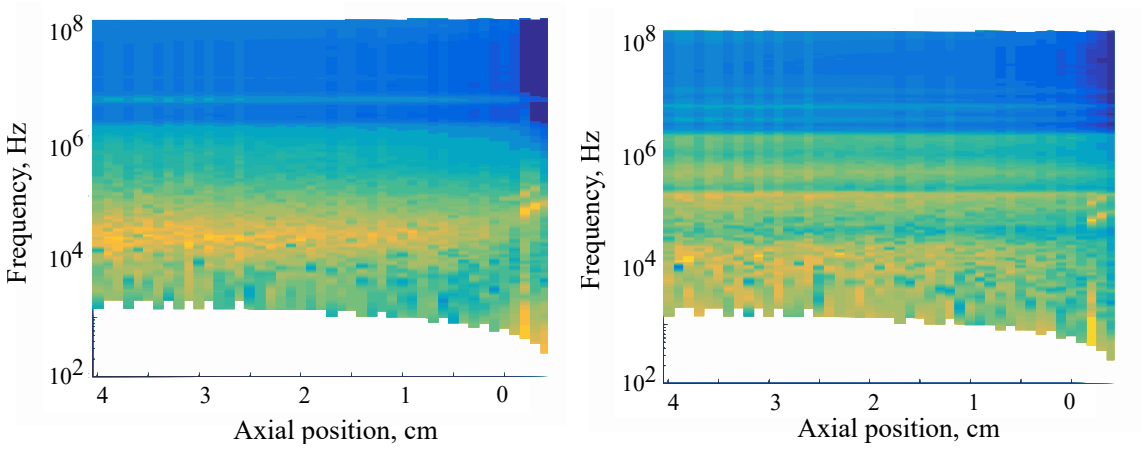

(a) (b)

Figure F.10: The relative power spectra of I_d (a) and V_{c2g} (b) are shown as a function of axial position for nominal thruster operation. Hotter colors indicate greater logarithmic spectral power. The range of each spectrum (vertical slice) varies due to the differing amounts of time the probe spent at each location while decelerating. Quantization artifacts observable at alternating light and dark bands are non-physical.

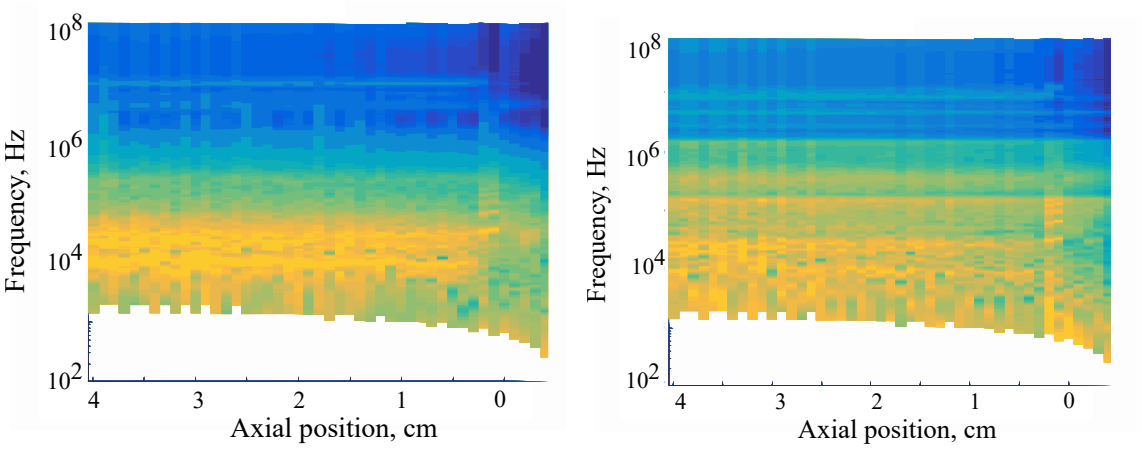

(a) (b)

Figure F.11: The relative power spectra of I_d (a) and V_{c2g} (b) are shown as a function of axial position for half-magnet thruster operation. Hotter colors indicate greater logarithmic spectral power. The range of each spectrum (vertical slice) varies due to the differing amounts of time the probe spent at each location while decelerating. Quantization artifacts observable at alternating light and dark bands are non-physical.

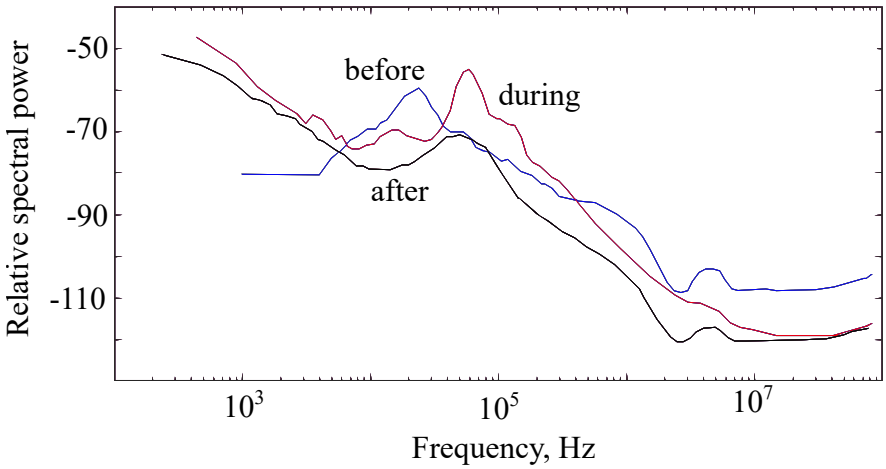

(a)

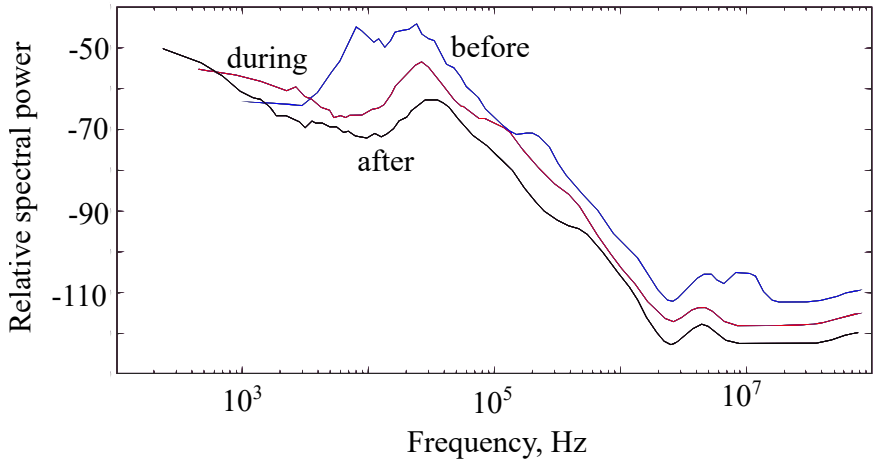

(b)

Figure F.12: Selected relative power spectra of I_D are shown for the nominal (top) and half-magnet (bottom) conditions. Five-point linear Savitzy-Golay smoothing was applied to the spectra, which was binned and averaged logarithmically with a width of 0.05 orders of magnitude.

APPENDIX G

Pseudo-Deconvolution of Neutral Xenon Lineshapes

In Chapter V, we discussed an alternative to full deconvolution of measured Xe I lineshapes, in which we capture the stationary broadening with a finite number of Gaussians and from them calculate a correction term for raw velocity moments. We now present the details of that process.

To measure a cool stationary xenon population, we probed a Hamamatsu Laser Galvatron optogalvanic (OG) cell with the same homodyning approach as in typical Xe I LIF. Here, we use a voltage output from the OG cell as a measure of excitation of the neutral population rather than fluorescence. Figure G.1 shows the measured lineshape of the OG cell without an applied magnetic field. It also shows a five-Gaussian fit, which apparently captures the shape of the broadening quite well. It is important to note here that so few Gaussians – as opposed to the multitude of individual split lines – can capture the lineshape because the Doppler broadening in a relatively cool gas, here room temperature, effectively dominates many of these lines. Table G.1 summarizes the properties of the fit Gaussians.

Since we are interested specifically in broadening here, it was critical to ensure that we were not saturating the targeted transition by injecting too much laser power.

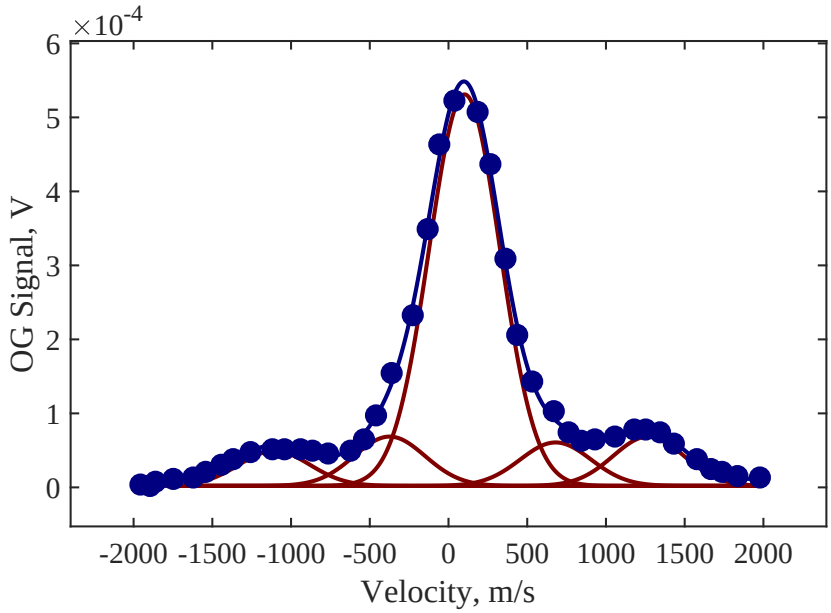

Figure G.1: The measured stationary Xe I lineshape (blue dots), the fit Gaussians (red), and the sum of the fit Gaussians (blue line).

Table G.1: The mean and amplitude of the four ancillary Gaussians relative to the central (largest) one in Fig. G.1, enumerated with increasing mean velocity. The mean frequencies are relative to the mean of the central Gaussian, and the amplitudes are normalized by the amplitude of the central Gaussian.

Gaussian	Relative Mean (GHz)		Relative Amplitude	
1	-1.40	+0.08 -0.05	0.1261	+0.0242 -0.0170
2	-0.69	+0.12 -0.10	0.1109	+0.0318 -0.0255
4	0.57	+0.13 -0.10	0.1259	+0.0494 -0.0422
5	1.45	+0.09 -0.06	0.0892	+0.0232 -0.0181

Figure G.2 shows the peak signal intensity as a function of input power estimated with a Thorlabs PDA36A silicon photodetector. At high power, the photodetector itself saturates but below that the intensity gradually becomes linear. The lineshape of Fig. G.1 is taken with <2 mW of input power to reduce saturation as much as possible while still resolving the lineshape.

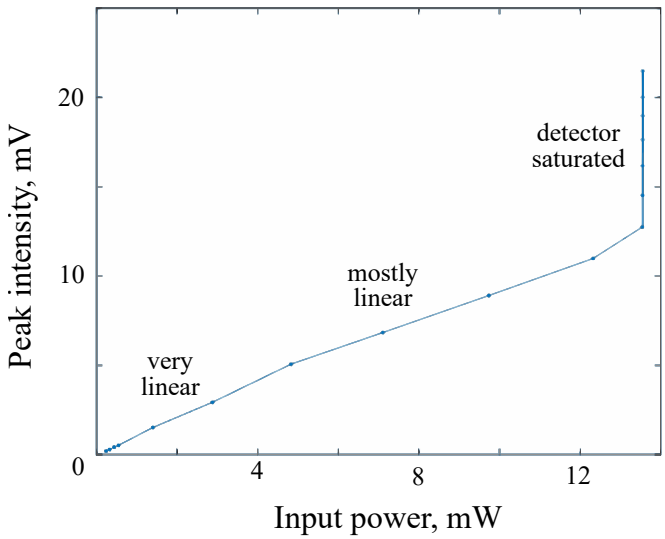

Figure G.2: Peak OG cell signal intensity as a function of input laser power. At high power the photodetector is saturated, then it becomes mostly linear, and finally it appears very linear.

In Chapter V, we showed that the correction of Eq. (4.6) can be encapsulated with a subtractive factor $\Delta\overline{u}$. Using the information of Table G.1, we find this factor to be about 132.3 m/s. This means the first velocity moment of a measured Xe I lineshape will be 132.3 m/s larger than the true deconvolved lineshape. Figure G.3 shows a sample OG cell trace, which has a raw first moment of 125 m/s and a correct one of -7 m/s, which is indistinguishable from 0 m/s with the given velocity resolution. Since the gas inside the OG cell is known to be stationary, this correction is clearly critical in calculating velocity moments from raw Xe I lineshapes.

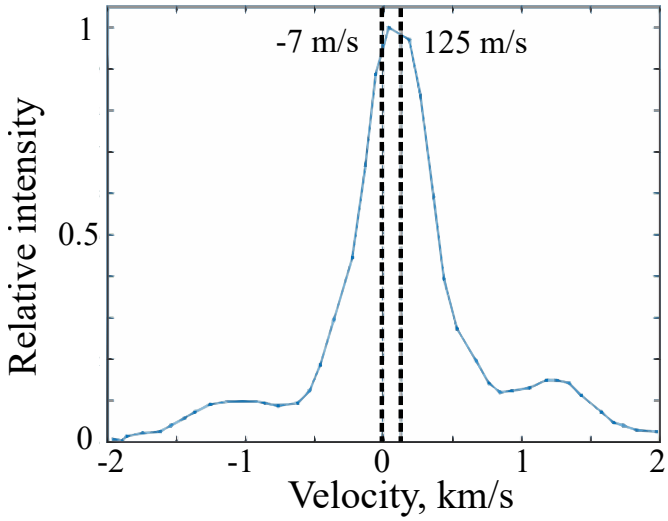

Figure G.3: A sample OG cell trace showing the raw first moment (125 m/s) and the corrected value (-7 m/s).

APPENDIX H

Characterizing Electron Transport with IBIS

Theory

Hydrodynamic representations of Hall thrusters treat electrons as a fluid where conservation of momentum neglecting electron inertia is encapsulated by Ohm's law:

$$\vec{E} = \eta_e \vec{j_e} + \eta_e \Omega \vec{j_e} \times \hat{B} - \frac{\nabla p_e}{n} + \eta_i \vec{j_i} \ . \tag{H.1}$$

Here, $\hat{B}$ is the magnetic field unit vector, η_e is the electron resistivity, η_i is the resistivity due to classical ion collisions, j_e is electron current density, and j_i is ion current density. The resistivities are generally defined as $m\nu/q^2 n$, and the current densities as qnu. The Hall parameter Ω is the ratio of the cyclotron frequency $\omega_{ce} \equiv qB/m_e$ and total electron collision frequency ν_e. The electron pressure p_e is given by enT_e where T_e is the electron temperature in eV. We assume the electric field $\vec{E} \approx E_z \hat{z}$ is mostly axial and the magnetic field $\vec{B} = B\hat{B} \approx B_r \hat{r}$ is mostly radial. The balance of forces in Ohm's law includes the electric force, pressure, Lorentz force, and a collisional drag. This drag is classically the result of electron-ion and electron-neutral collisions. Anomalous transport can be represented in Ohm's law as an additional

drag force $\vec{F_a}$ formulated such that $\vec{F_a} = (m_e/q^2)n\nu_a\vec{j_e} \equiv \eta_a\vec{j_e}$, where the anomalous drag is ascribed to an anomalous collision frequency ν_a. The total drag in Eq. (H.1) is therefore $(\eta_e + \eta_a)\vec{j_e} \equiv \eta_t\vec{j_e}$, where the total resistivity η_t is a function of ν_e, the sum of classical collisions ν_{class} and so-called anomalous collisions ν_a. Anomalous transport can be directly characterized within this framework if the total electron collision frequency and the classical collision frequency can be measured.

To determine the total collision frequency, the axial component of Eq. (H.1) is taken:

$$E_z = \eta_e j_e(1 + \Omega^2) - \frac{\nabla p_e}{n} + \eta_i j_i \ . \tag{H.2}$$

The first term on the righthand side is the resistivity due to electron collisions in the presence of a magnetic field; the second term is the electron pressure gradient, which generates an electric field when there are large electron density or temperature gradients, such as near the magnetic barrier in a Hall thruster; and the last term is ion resistivity due to ion collisions. Eq. (H.2) is a quadratic in ν_e such that

$$\nu_e = \frac{\mathcal{E} \pm \sqrt{\mathcal{E}^2 - (2u_e B_r)^2}}{2\frac{m}{e}u_e} \ , \tag{H.3}$$

where u_e is the electron velocity and we have defined $\mathcal{E} \equiv E_z + \frac{\nabla p_e}{n} - \eta_i j_i$. Physically, $\mathcal{E}$ represents the electric field due solely to electron collisional resistivity according to Eq. H.2. If ion resistivity and electron pressure were neglected, $\mathcal{E}$ would be identical to E_z. The total collision frequency given in Eq. (H.3) includes all collisions that electrons may undergo while transiting the thruster: anomalous collisions, electron-neutral collisions ν_{en}, and electron-ion collisions ν_{ei}.

Armed with Eq. (H.3), we can evaluate the total collision frequency if plasma density, electron temperature, electron and ion velocity, axial electric field, and radial magnetic field are known. While there are standard techniques for determining most of these properties, to date it has not been possible in Hall thrusters to measure the

electron velocity directly. As an alternative approach following the work of Linnell [173], we instead make a series of approximations that allow us to relate this parameter to the more easily measured values of ion and discharge currents. To this end, noting that radial currents in a Hall thruster are small or symmetric [174] and assuming radial symmetry within the channel such that gradients in the radial direction are small on centerline, we can treat the ion and electron continuity equations as effectively one dimensional in the axial direction. This allows us to express the electron current density in the axial direction as the difference in total (discharge) current density and ion current density, $j_e = j_d - j_i$. The ion current density can be calculated from the plasma density and ion mean velocity $\overline{u}$, which can be measured directly and assumed one-dimensional due to the ballistic nature of ions and small divergence of the ion beam in the near field. The discharge current density j_d can be calculated from the discharge current I_d and the known channel area A if it is assumed that current is carried uniformly across the channel, i.e. $j_d = I_d/A$. Alternatively a non-uniform shape to the current distribution could be inferred from numerical simulations or otherwise assumed, but without knowing the distribution and its evolution over a breathing cycle exactly, such an approach could be just as inaccurate as assuming a uniform distribution. This assertion will be discussed later in this appendix. With these approximations, Eq. (H.3) thus reduces to

$$\nu_e = \frac{\mathcal{E} \pm \sqrt{\mathcal{E}^2 - \left[2\left(\frac{j_d}{n} - \overline{u}\right) B_r\right]^2}}{2\frac{m}{e}\left(\frac{j_d}{n} - \overline{u}\right)} \ . \tag{H.4}$$

In this form, it is possible to evaluate the total collision frequency by using standard diagnostic techniques to measure typical plasma parameters in the thruster, e.g. density and electric field. The anomalous collision frequency ν_a in turn can be found by subtracting the classical contributions, ν_{ei} and ν_{en}, from ν_e (c.f. Ref. 78).

The measurement of collision frequency with Eq. (H.4) already has been done with

physical probing techniques in a time-averaged way [173]. However, as we discussed in Chapter V, these techniques were perturbative and did not yield any information on the dynamic response of the plasma. Our approach to measuring these parameters differs in the present investigation in that we use the weakly-invasive IBIS technique to acquire them.

Sample Results

The total collision frequency computed in this way is shown at various phases of the breathing mode in Fig. H.1. Also included at the same ordinate scale is the classical collision frequency at these phases. At the minimum in discharge current (denoted "3"), the total collision frequency is nearly equal to the classical collision frequency, while at the peak in discharge current ("1") there is an order of magnitude or greater difference between them. This indicates that the anomalous collision frequency – the difference between the curves in Figs. H.1b and H.1c – fluctuates significantly throughout a breathing cycle, and even becomes negligible at times. It is also interesting to observe that the local minimum in collision frequency nearly coincides with the peak electric field strength but is consistently upstream of the location of maximum radial magnetic field. The fact that the electric field peak was located upstream of the location of peak magnetic field was also evident in dedicated time-averaged LIF measurements, and this shift in position is much too large to be explained by uncertainty in the axial position of the thruster. This contrasts with steady-state measurements that show the two to be nearly coincident in other thrusters, both shielded like the H6MS [8] and unshielded like the H6 [60], as well as others [82, 175]. The reason why this discrepancy occurs compared to similarly configured devices is not immediately apparent, although previous studies [140] on a 12.5-kW magnetically-shielded thruster have shown the acceleration region to shift upstream as the radial magnetic field increases. This may imply that the magnetic

field used for the operating condition in the present study was relatively strong for the power level.

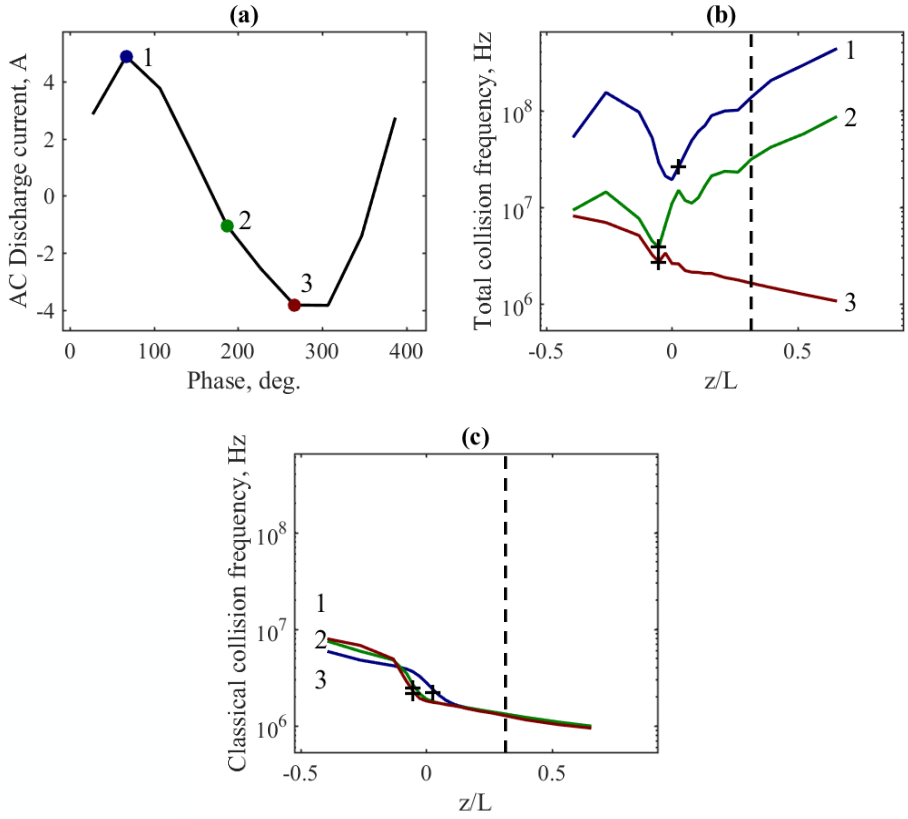

Figure H.1: The discharge current (a), total collision frequency (b), and classical collision frequency (c) at three representative phases of the breathing cycle. The location of maximum radial magnetic field is indicated with a vertical dashed line, and the location of peak electric field strength is indicated with a "+".

Figure H.2 shows several of the constituent quantities used to calculated ν_e. Included are the electric field strength, electron pressure gradient, plasma density, electron temperature, and current densities. It shows the electric field is strongest at the discharge current minimum and weakest at its maximum. In contrast, the total collision frequency and the electron current density are generally weakest at the discharge current minimum. This implies that either resistivity is increasing relatively more than j_e is decreasing, or the electron pressure gradient is increasing dramatically as discharge current reaches a minimum. Figure H.2b indicates the electron pressure

gradient peak magnitude increases with decreasing discharge current, but by only about 200 V/cm at most, while E_z increases by about 400 V/cm in some locations. Thus, changes in resistivity must be contributing significantly to the fluctuation of electric field strength, and therefore resistivity is especially sensitive to the fluctuations of discharge current during a breathing cycle. This observation is a strong piece of evidence that breathing fluctuations are highly correlated with electron transport. Additionally, the plots show that the ion current density fluctuates much less than the electron current density, suggesting that the breathing oscillations have more impact on electron transport than ion transport.

Figure H.3 shows the mean total and classical collision frequency profiles calculated by averaging the time-resolved results over a breathing period. The ν_e curve is surrounded by a region of boot-strapped 95% statistical uncertainty, which is also representative of the error for the data in Fig. H.1. Figure H.3 also shows the average electric field, electron pressure gradient, plasma density, electron temperature, and current densities. A local minimum in the collision frequency exists near the average location of the peak electric field, which agrees with experimental measurements of Linnell and Gallimore [173] and a semi-empirical mobility model synthesized by Koo and Boyd [138]. Further, the total collision frequency appears to begin approaching the classical frequency upstream, which agrees with fluid simulations with the Hall2De code [176]. Finally, the peak mean electron temperature is close to the anticipated value of 30 eV according to a common heuristic that dictates T_e to be approximately 10% the discharge voltage [78].

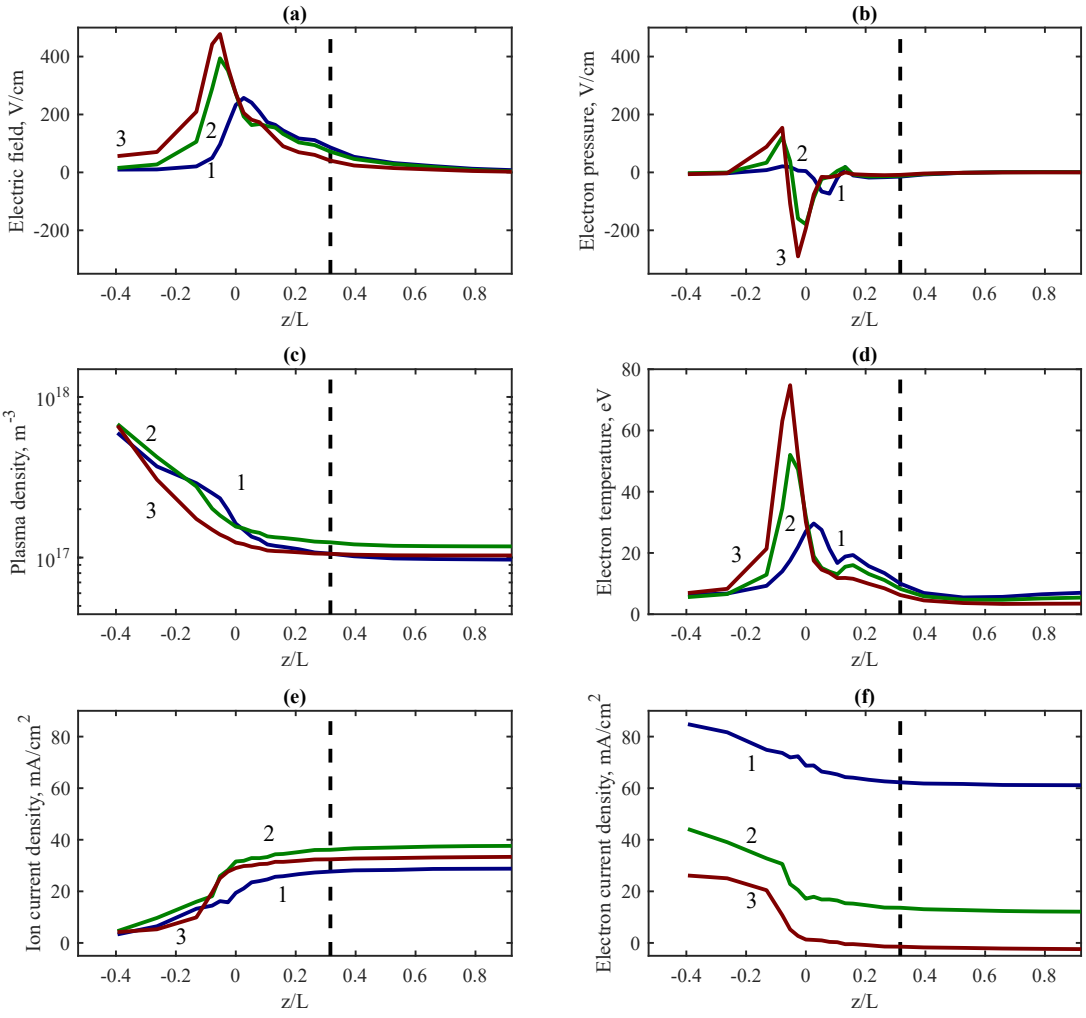

Figure H.2: The (a) axial electric field strength, (b) electron pressure gradient, (c) plasma density, (d) electron temperature, (e) ion current density, and (f) electron current density at phases of the breathing cycle corresponding to those in Fig. H.1. The location of maximum radial magnetic field is indicated with a vertical dashed line.

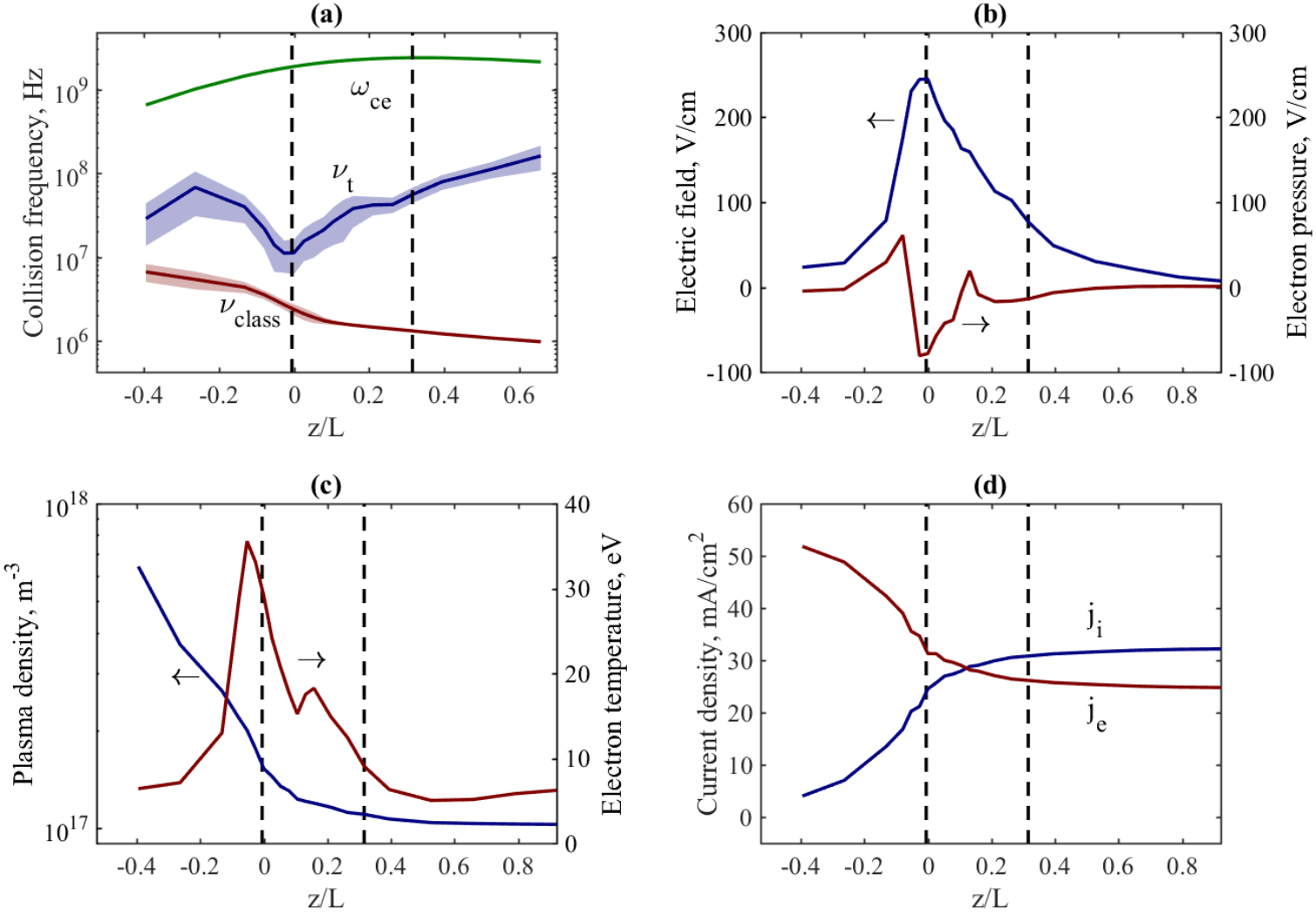

Figure H.3: (a) The mean total and classical collision frequencies and their statistical uncertainty regions, (b) the mean electric field and electron pressure gradient, (c) the mean plasma density and electron temperature, and (d) the mean current densities. The location of maximum radial magnetic field is indicated with the right vertical dashed line, and the average location of peak electric field strength is indicated with the left vertical dashed line. Horizontal arrows indicate the relevant ordinate for each curve.

It is important to note that ν_e shown in Figs. H.1 and H.3 has been given a minimum bound of ν_{class}, but at certain locations and phases Eq. (H.3) yields a raw collision frequency less than the classical value, which implies a negative anomalous electron drag. As this is physically unrealistic, this discrepancy indicates that either the assumptions of IBIS or the previous section are poor, or the uncertainty in ν_e exceeds the classical collision frequency. Although the uncertainty can be large for ν_e, it is not comparable to ν_{class} according to Fig. H.3. The only remaining explanation then is that assumptions underpinning the technique used to compute these quantities have been violated at the points where $\nu_e < \nu_{class}$. This and other limitations will be discussed further in the next section.

Discussion

In this section, we first review the sensitivity of the neutral gas calculations to the chosen boundary values. Next we discuss the validity of other major assumptions in the Boltzmann method proposed and applied in this study. We then discuss the broader ramifications of our findings for approaches to Hall thruster simulations. Finally, we conclude by examining the relationship between breathing and anomalous transport based on the results of the previous section.

Assumptions

There are several major assumptions that must be discussed in context of the results of the previous section. First, we consider the analytical limitations of Eq. (H.3). Given that on physical grounds ν_e must be greater than zero, the form of Eq. (H.3) has two requirements: 1) $\mathcal{E}$ and u_e must have the same sign and 2) $\mathcal{E} \geq 2u_eB_r$ such that ν_e is real. This latter inequality provides a lower bound on the magnitude of $\mathcal{E}$, at which point the total collision frequency for electrons is the cyclotron frequency (demagnetized electrons). Several data points where u_e was computed to

be small in this study violated the first limitation, which suggests that in practice the uncertainty of u_e with this technique will not allow the total collision frequency to be calculated meaningfully at times of negligible electron current. No instances of the second requirement being violated were observed. Consequently, we can conclude the proposed technique for computing ν_e is sensitive to uncertainty in u_e but tolerant of the uncertainty in $\mathcal{E}$, and this sensitivity imposes an analytical obstacle in determining ν_e when u_e is small.

Since the method applied here involves numerically integrating the ion density gradient starting at the boundary established by Faraday probe measurements, another assumption is that the technique is not overly sensitive to uncertainty in those boundary measurements. Here, we examine this sensitivity due to random and systematic variations in the boundary conditions. Physically, this is to say that the boundary density values could be noisy or uniformly skewed in time, which could lead to unstable numerical solutions via the iterative IBIS approach mentioned in Chapter V. With regard to random fluctuations of the boundary value, even though the Faraday probe signal unavoidably carried random noise of up to 5% (capturing 95% of the normally distributed noise), stable solutions for n, E_z, and f_{iz} were still found. This suggests that the numerical scheme was relatively insensitive to random noise in the boundary conditions. This is also true for systematic uncertainty, as demonstrated by Fig. H.4 which shows the mean spatial change in ion density as the boundary density is uniformly varied. The trend is representative of all phases. The figure indicates that the system is a sensitive, nonlinear function of boundary density, yet the smoothness of the curve implies that the numerical solver is still stable over a wide range. If the numerical scheme went unstable for certain systematic increases in the boundary conditions, we might expect the curve in Fig. H.4 to be discontinuous. In total, there is evidence that the numerical scheme is stable in the face of random and systematic variations in the boundary conditions, and thus the computed

quantities are reliable. We also reiterate here that although the breathing frequency was slightly different during the Faraday probing compared to the TRLIF measurements, the oscillations were qualitatively similar so we do not expect the shape of the boundary density signal to be misrepresented.

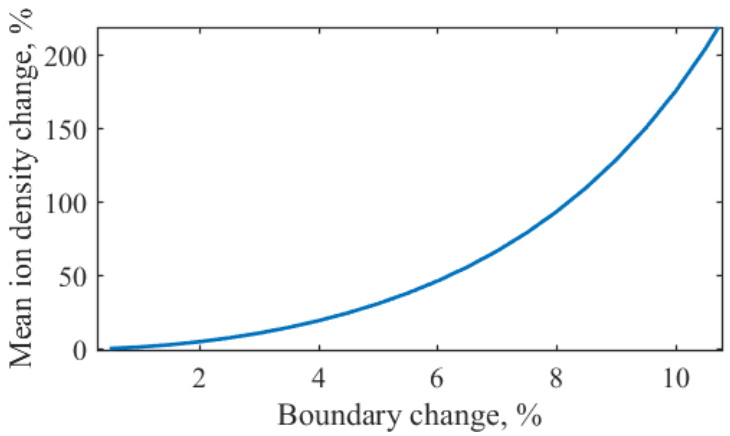

Figure H.4: The mean change in ion density as a function of the uniform increase in the boundary density.

Another assumption that must be evaluated is current continuity – namely, that electron current density can be inferred from the total and ion current densities. This assertion relies on two assumptions: that the total current density can be found by dividing the total discharge current by the channel area and that radial distribution of current is not fluctuating significantly in time. Violations of both of these assumptions may help explain some of our spurious results. As mentioned previously, several values of ν_e were calculated to be below the local classical collision frequency. Some of these physical discrepancies were explainable within the error of the measurements, while others were not. For example, at $z/L = -0.4$ and 188°, the total collision frequency is only 34 kHz below the classical value, which is explainable within the ~10 MHz average uncertainty in ν_e at the location. But at $z/L = -0.05$ and 228°, the difference is several orders of magnitude greater than the local uncertainty. In these cases, the issue stems from the calculation of j_e, which must be close to zero or somewhat negative according to current continuity when ν_e becomes very small. A

possible explanation is that at these points the average total current density is a poor representation of the relevant (centerline) current density. In particular, the fact that j_e is implausibly small at these points indicates that the radial current density profile most likely narrows here such that the total discharge current is distributed over an area smaller than that dictated by the channel geometry. We can assess the impact of this radial uniformity assumption more quantitatively with a sensitivity analysis. Since quasi-neutrality is assumed and n has been measured on centerline, the current distribution controls u_e on centerline via the relation $u_e = j_e/n = (j_d - j_i)/n$. Indeed, in the one-dimensional case we can determine from Eq. (H.3),

$$\frac{\partial \nu_e}{\partial u_e} = \Omega \frac{\omega_{ce}}{u_e} - \frac{\nu_e}{u_e} \ , \tag{H.5}$$

the sensitivity of ν_e to changes in u_e. For the region of interest, $\omega_{ce} > \nu_e$ such that the last term in the above equation can be ignored. In this case, changes in ν_e are inversely proportional to ν_e itself and directly proportional to the fractional change in u_e. This suggests that the lower ν_e values are more susceptible to uncertainty due to a non-uniform current distribution than the larger values for a given uncertainty in u_e since $\partial \nu_e / \partial u_e$ will be large. This may help explain why ν_e was lower than ν_{class} in some instances. Further, it suggests that the lower limit of the measured ν_e is strongly dependent on the assumed current distribution, and thus a more rigorous way of determining the distribution – such as by measuring j_i at multiple radial locations throughout the channel – is necessary to fully resolve the lower extent of the fluctuations in ν_e. To illustrate this, Fig. H.5 shows the time-averaged total collision frequency for three assumed current distributions: uniform, linear from each wall to channel centerline, and Gaussian with a variance of $w^2/4$ where w is the channel width. These cases represent the limits on realistic current profiles: maximum convexity, zero convexity, and in between, respectively. In this way, these cases provide

bounds for the true total collision frequency and illustrate the effect of assuming non-uniform current distributions. Naturally, the greater convexity a profile has the lower the centerline current density can be to achieve a certain discharge current. As a result, more convex profiles have smaller centerline values for j_d and thus smaller j_e and u_e, and so a smaller electron cross-field collision frequency is computed. Although there is considerable variability in ν_e due to the effect exemplified by Fig. H.5, the minimum ν_e occurring at the trough in discharge current is still at most comparable to ν_{class} for any assumed distribution. However, the spatial extent over which $\nu_e \lesssim \nu_{class}$ does vary considerably for different current distributions. At the phase of minimum discharge current (see Fig. H.1), ν_e was within an order of magnitude of ν_{class} for 84%, 37%, and 42% of the measurement domain for the uniform, linear, and Gaussian distributions, respectively. With this in mind, one of the conclusions of the previous section – that classical collisions may dominate at certain phases – still holds for *some* locations in the channel within the certainty of the measurements regardless of the current distribution. Alternatively, a vanishing axial electron current may not be a sign that the assumed current distribution is incorrect but may simply be an indication that the electrons are diverging from centerline within the measurement domain, and thus the one-dimensional Ohm's law used in this technique is inappropriate. This explanation seems likely given that j_e tended to approach zero at the downstream end of the measurement domain, where electrons may still be diverging from the cathode.

Finally, we consider a posteriori the necessity of a generalized Ohm's law, including electron pressure and ion resistivity. As Fig. H.2 shows, the electron pressure gradient is nearly comparable to the accelerating electric field strength at many phases and locations. As a result, $\mathcal{E}$ cannot be approximated with E_z and thus the inclusion of electron pressure is important. However, ion resistivity tends to be small, although it can become important when the electric field weakens far upstream and downstream.

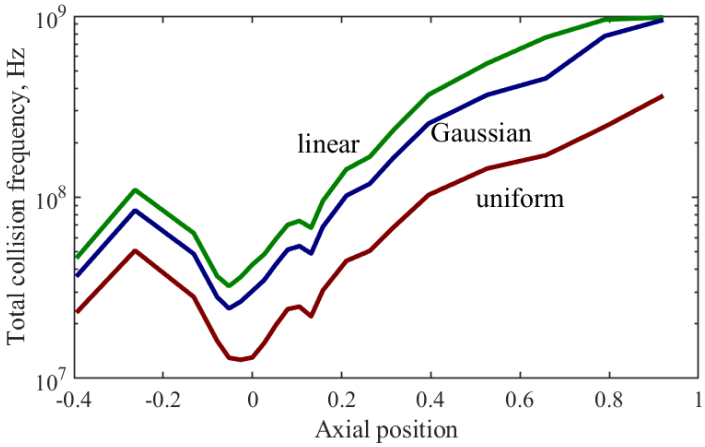

Figure H.5: The time-averaged total collision frequency for different assumed current distributions: uniform, linear, and Gaussian.

Even though it is never a dominating term, this study indicates it is at least non-negligible.

Relation between breathing and anomalous transport

The observation that anomalous transport varies with breathing oscillations agrees with experimental and numerical studies in the literature. Adam et al. observed enhanced transport in an axial-azimuthal PIC simulation which was attributed to the electron cyclotron drift instability (ECDI), a kinetic effect in which energy from the large electron drift velocity in the acceleration region feeds a wave via inverse cyclotron resonance [143]. These simulations also resolved breathing oscillations and demonstrated that the fluctuating electric field due to the ECDI correlated with them. Likewise, PIC simulations by Coche and Garrigues indicated that the cross-field electron mobility profile fluctuates during a breathing cycle, and that the profile increases at peaks in the discharge current that correspond with the onset of azimuthal instabilities (ECDI) [45]. Recently, Tsikata et al. experimentally observed that in some discharge voltage regimes there is strong correlation between discharge current and the strength of the ECDI electric field fluctuations [50]. That study also involved

kinetic simulations that reflected the same trends. Although our present study cannot identify the mechanism behind the quantified anomalous transport, it similarly shows correlation between anomalous transport and the breathing mode, and in fact shows the anomalous collision frequency varying by orders of magnitude over a breathing cycle.

One of the major implications of this relationship between electron transport and low-frequency oscillations is that the anomalous collision frequency must be simulated dynamically to accurately capture electron transport. Many modern fluid electron simulations employ spatially-fixed transport profiles [139, 177]. According to the findings of the present study, that approach – especially when using empirically-derived steady profiles – is not valid. Anomalous transport fluctuates by orders of magnitude on the time scale of breathing oscillations, and thus a steady profile is inappropriate. Further, this study has revealed that many quantities fluctuate significantly during a breathing cycle along with the anomalous collision frequency. For instance, the maximum peak-to-peak variation is 52% for ion density, 142% for ion velocity, 185% for electron temperature, and 346% for electric field. This may suggest that electron transport is sensitive to some of these quantities, which is consistent with ECDI [26].

APPENDIX I

Multi-Channel Breathing Mode Behavior

In the course of applying our optical emission spectroscopy system to the X3, we also studied the thruster's oscillatory properties with multiple channels firing. In these configurations, we were able to compare the frequencies, strengths, and phases of oscillations between channels in any given condition, as well as these properties between conditions. For example, we were able to evaluate how the dominant frequency of the inner channel changes when it is operated with the middle channel or the outer channel. Additionally, the oscillations were measured both through high-speed video and the high-speed discharge current signal, allowing for the detection of spokes as well as verification of our spectral measurements. Although little insight into the nature of these trends was yielded in this study, the tabulation of this data is nonetheless interesting and can be compared *a posteriori* to breathing mode theories.

Experimental Setup

The thruster was operated at 300 V in single-channel, two-channel, and three-channel configurations, where the discharge power of each channel was kept approximately constant such that it operated at 30 kW in the three-channel case. A typical

power achieved for each case is shown in Table I.1, where the inner, middle, and outer channels are denoted "I," "M," and "O," respectively, and cases where they are operated in unison are concatenated with "+". The inner channel is most comparable in size and power to the H6, a laboratory Hall thruster that has been extensively characterized and studied with high-speed diagnostics in both magnetically shielded and unshielded configurations [13].

Table I.1: The 30 kW operating conditions for each X3 configuration, as well as typical xenon-corrected operating pressures for each configuration, measured with a Varian 571 Bayard-Alpert ionization gauge.

Case	I_d (A)	V_d (V)	$\mathcal{P}_d$ (kW)	P (Torr-Xe)
I	13.5	300	4.05	4.38×10^{-6}
M	31.4	300	9.42	9.60×10^{-6}
O	54.9	299	16.4	2.88×10^{-5}
I+M	13.4, 31.9	301, 300	13.6	1.31×10^{-5}
M+O	31.5, 54.8	299, 298	25.8	6.64×10^{-5}
I+O	13.3, 55.3	297, 299	20.5	3.85×10^{-5}
I+M+O	13.6, 32.3, 55	300, 300, 300	30.3	9.43×10^{-5}

The operating pressure of the X3 on xenon in these cases is shown in Table I.1. The background pressure varied dramatically — across almost three orders of magnitude — between conditions, which made it hard to directly compare the operation of a given channel in single- and multi-channel configurations. This problem would be aggravated if the thruster was operated with a constant mass flow rate, in which case the thruster mass ingestion from ambient gas effectively leads to increased discharge current. To make comparisons more meaningful, the thruster was operated at constant channel power, as can be observed by summing the single-channel powers reported in Table I.1. As a result, smaller mass flow rates were required for each channel when multiple channels were operated at once, but the discharge current for each remained the same as it was during single-channel operation. The background pressure was exceptionally high during the three-channel configuration, well exceeding the recommended upper limit for performance evaluation [54]. Although this may

have skewed oscillation measurements for this case, it is assumed that the effect is at least somewhat mitigated by the constant power operation scheme.

Results

For two-channel operation, one might expect that the larger channel – with greater I_d – might have stronger discharge current oscillations. However, we found that the discharge current fluctuation amplitude was sometimes comparable between channels or even slightly greater in the smaller of the two, and other times proportionally greater in the larger of the two. Fig. I.1 shows an example of the former for the inner and middle two-channel configuration at 14 kW, as well as an example of the latter for the inner and outer two-channel configuration at 21 kW. The configuration with the inner and middle channel operating together appears to have much weaker breathing than most cases, such that it may be an example of a transitional case where the thruster is between modes.

Perhaps the only condition where breathing was not clear for all channels was the three-channel configuration at 30 kW. The discharge current for all three channels and the cathode in this configuration is presented in Fig. I.2. In this case, breathing is apparent for the cathode, middle channel, and outer channel, but a more erratic discharge current is exhibited by the inner channel. It seems that the inner channel alone was transitioning between modes while the other channels were exhibiting the breathing mode.

Given that the thruster was exhibiting the breathing mode in all configurations, comparison between single-, two-, and three-channel operation can be achieved through an examination of the breathing frequency and the width of the breathing spectral peak. Table I.2 shows the breathing frequency for each configuration as determined by high-speed image analysis (HIA), with the listed uncertainties ranging the FWHM. Table I.2 also shows the same as determined by high-speed discharge current analysis

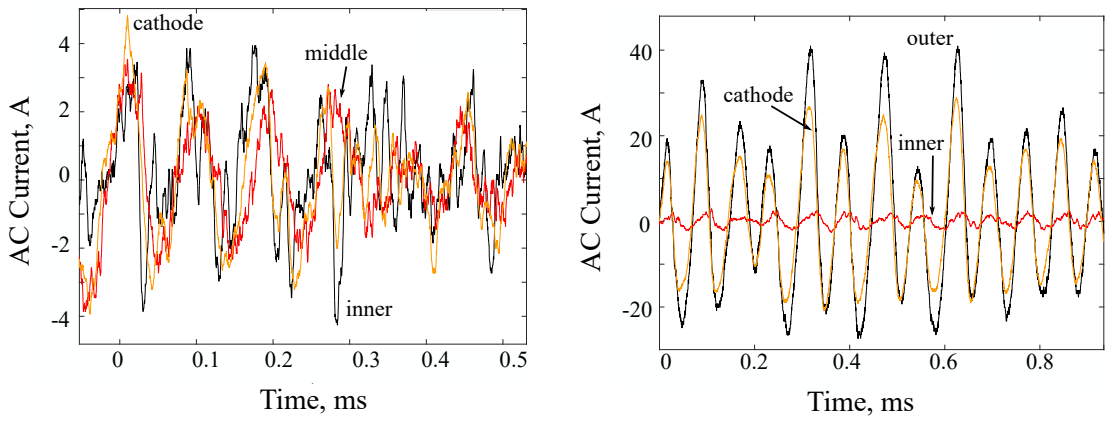

(a) (b)

Figure I.1: An example of a smaller channel having slightly higher current fluctuations than a bigger channel (a) and the opposite (b). The former case shows the inner and middle channels operating together at a total power of 14 kW. In this case the breathing appears very weak, as all AC current signals appear noisy and have low amplitude. The latter case shows the inner and outer channels operating together at a total power of 21 kW. In this case, breathing is very strong, as the clear sinusoidal outer channel AC current signal indicates. The inner channel still appears noisy but breathing oscillations are easily identifiable.

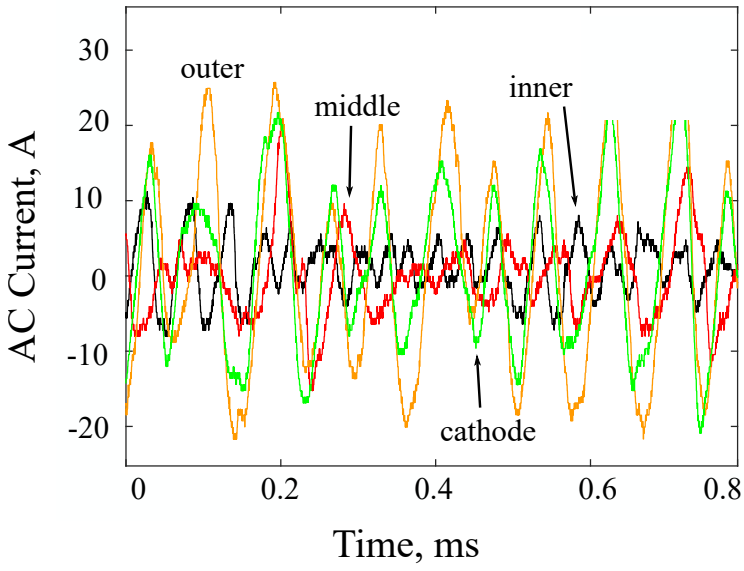

Figure I.2: The cathode current and anode current for all three channels operating in unison at 30 kW. The outer channel and cathode appear to track very closely, and middle channel seems to have a phase delay with them. The inner channel appears very noisy and clearly does not follow the shape of the other signals.

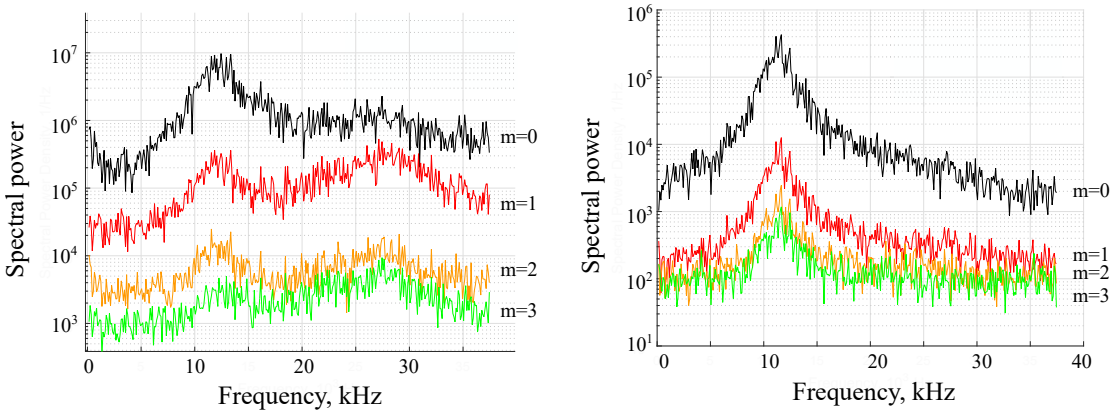

Figure I.3: The power spectral density for the inner channel (a) and middle channel (b) when operated in unison. Note that the m=0 mode dominates at all frequencies for both channels. There are some higher order features perceptible for the inner channel but they are so broad and weak (relative to m=0) that they cannot be taken as a strong indication of spokes.

(HCA). The agreement between the two is excellent, with the largest error amounting to only 320 Hz, well within the uncertainty for most cases. The two-channel frequencies differed noticeably from the respective single-channel values, and in general the frequencies approached each other when operated together. For example, the inner channel slowed down when paired with other slower channels, while the middle channel sped up when paired with other faster channels. However, it is hard to determine if this change is due to the variation in background pressure between the conditions or if it is related to interaction between the channels, as it is known that background pressure can influence the breathing mode [65].

In the three-channel configuration, breathing frequency convergence occurred with the outer and middle channels in that their frequencies are closer than the single-channel cases. The middle channel generally had a lower frequency than the outer channel in all configurations, but in this case the outer channel sped up slightly and the middle channel sped up significantly. The net effect is frequency convergence, although the means by which it happened is puzzling. Nonetheless, this suggests

that there is a strong coupling effect between the outer two channels, regardless of background pressure. On the other hand, the inner channel strongly diverged. There is a weak peak in the inner channel power spectral density, shown in Fig. I.4, at the breathing frequency of the other channels, indicating that there is partial coupling. The inner channel frequency is not a harmonic of the middle/outer frequency, suggesting the channel was breathing very independently aside from the partial coupling. Analytical descriptions of the breathing mode frequency that account for heavy species transport suggest that it is a function of steady state ion and neutral densities in the channel, neutral density at the anode, and the ionization rate coefficient [46]. The fact that the breathing frequency is similar for the two outer channels and that the inner channel has weak breathing at that frequency, then, does not seem likely without coupling effects playing a significant role.

Table I.2: The center frequencies of the breathing mode for each channel and each configuration based on high-speed discharge current and image analysis.

	HCA (kHz)			HIA (kHz)		
Case	I	M	O	I	M	O
I	14.5±0.4	-	-	14.5±0.4	-	-
M	-	9.99±0.01	-	-	9.99±0.01	-
O	-	-	12.0±0.1	-	-	12.0±0.1
I+M	12.5±1.0	11.3±0.5	-	12.2±0.9	11.4±0.5	-
M+O	-	12.2±0.0	12.2±0.0	-	12.2±0.0	12.2±0.0
I+O	12.9±0.1	-	12.9±5.0	12.9±0.1	-	12.9±0.1
I+M+O	19.9±0.7	12.2±0.8	13.7±0.3	19.5±0.6	12.0±0.8	13.6±0.3

The phase delays yielded by high-speed image analysis and high-speed discharge current analysis shown in Table I.3 did not agree well, with an average difference for all configurations of 6.3°. However, they both show similar trends when comparing phase delays between the two-channel cases and the three-channel case. Namely, the inner channel increased in phase for the inner/middle pair, the outer channel decreased in phase for the outer/middle pair, and the inner channel decreased in phase for the inner/outer pair. The phase delay typically decreased when in three-channel operation.

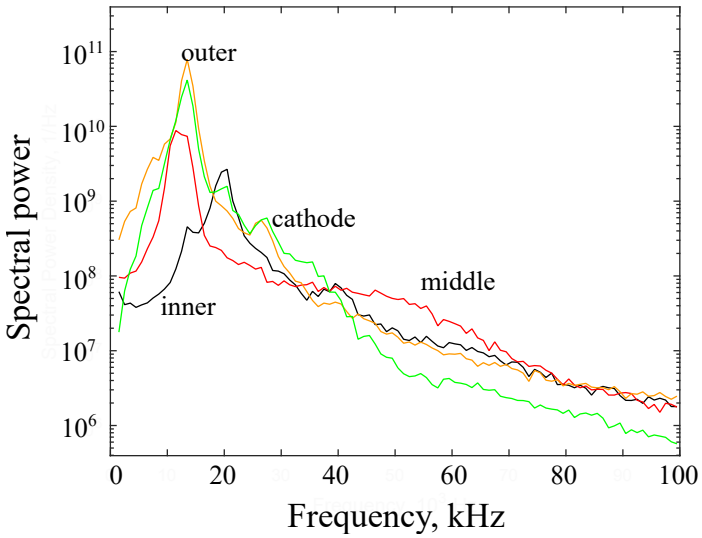

Figure I.4: The power spectral density for three-channel operation, binned to 1 kHz. The cathode and outer channel have nearly the same frequency, while the middle channel is slightly lower and broader. The inner channel has a large peak at a higher frequency and a small peak at the cathode frequency.

Two exceptions to this trend exist for the high-speed image analysis phase delays, for the inner/middle case where there is a slight increase and for the outer/middle case where the uncertainty of the two-channel configuration phase delay is so large that the phase delay may have increased. For the former exception, it is important to recognize that the inner channel was at a much different frequency than the middle channel, so an average phase delay is not meaningful. Similarly, the middle channel was also at a slightly lower frequency than the outer channel, so the phase delay between the two may also be meaningless. In fact, little useful information can be gleaned from the phase delays because of this, and so the similarity in trends between the two diagnostics merely indicates that the discharge current and light emission were well-correlated. A more precise means of evaluating signal phase is required to usefully examine phase delays between channels.

The breathing RMS amplitude also varies for a given channel between the different configurations. Table I.4 shows the RMS amplitude for each configuration. Since

Table I.3: The phase of the breathing mode for each channel and each configuration based on high-speed discharge current and image analysis.

	HCA			HIA		
Case	θ_{IM}	θ_{OM}	θ_{IO}	θ_{IM}	θ_{OM}	θ_{IO}
I+M	-10.1±0.3°	-	-	1.86±0.39°	-	-
M+O	-	23.4±5.8°	-	-	26.1±28.0°	-
I+O	-	-	11.2±1.0°	-	-	24.1±1.3°
I+M+O	-1.74±0.30°	3.82±0.39°	-5.56±0.40°	3.27±0.38°	-11.3±0.4°	14.6±0.5°

discharge current was kept constant, these amplitudes should be comparable between configurations. However, the wildly varying background pressure may have influenced the mode, which would in turn impact the RMS amplitude. In this way, any observable trends cannot entirely be trusted to be independent of pressure effects. In any case, there do not appear to be any strong trends in the discharge current fluctuations. Whereas the inner channel has its largest fluctuations when part of the three-channel configuration, the middle and outer channels vary sporadically. It is likely that the strength of these fluctuations are dependent on a combination of many operating parameters, such that simply operating in the breathing mode — as the thruster was in all configurations — is not enough to specify the strength of fluctuations more than within a broad range. In general, the fluctuation amplitudes were small, most being more characteristic of the spoke mode than the breathing mode. In total, the low fluctuation amplitudes provide evidence that, even though global oscillations were dominant, most operating conditions may have been near the mode transition point.

Discussion

It was previously noted that the inner/middle case may have been transitional given the noisiness and weakness of its discharge current oscillations. The RMS amplitude for the middle channel in this case is especially low, well into the range typically associated with spokes. However, both channels in this configuration showed

Table I.4: The discharge current RMS amplitude for all channels and configurations. Fluctuation currents are shown on the left and relative fluctuations are shown on the right.

Case	$\tilde{I}_I$ (A)	$\tilde{I}_M$ (A)	$\tilde{I}_O$ (A)	Case	$(\tilde{I}/I_d)_I$	$(\tilde{I}/I_d)_M$	$(\tilde{I}/I_d)_O$
I	3.06	-	-	I	22.7%	-	-
M	-	7.51	-	M	-	23.9%	-
O	-	-	17.40	O	-	-	31.7%
I+M	1.66	1.17	-	I+M	12.4%	3.71%	-
M+O	-	5.03	20.45	M+O	-	16.0%	37.3%
I+O	1.16	-	17.47	I+O	8.73%	-	31.6%
I+M+O	3.93	6.71	15.19	I+M+O	28.9%	20.8%	27.6%

only noise in their intensity surfaces. This suggests that the thruster was at least transitioning between modes in this case, although the complete absence of spokes still suggests that it was closer to the breathing mode than the spoke mode. Alternatively, if the spokes were too dim to be detected by the camera, this configuration may have been closer to the spoke mode.

It is interesting to note that the inner channel had higher relative fluctuations than the other channels in the inner and middle two-channel configuration (as discussed previously) and the three-channel configuration. For the latter case, this means that not only was the inner channel breathing much faster than the other channels, is was breathing much harder. In this sense, the high-speed behavior of the inner channel was very different from the others, even though they were qualitatively exhibiting the same mode.

Of note is the inner and middle channel case which appears transitional according to its discharge current signals, as discussed previously. The power spectral density from FASTCAM measurements for this case, shown in Fig. I.3, indicates that global oscillations dominate at all frequencies for both channels. This suggests that even though it may appear transitional and the transient behavior of the discharge current appears noisy (Fig. I.1), most signal spectral power is located in global oscillations. It is possible that the entire image was so dim that spokes, even if they were present,

could not be detected by the camera. This would leave no means to determine the mode other than the discharge current fluctuation amplitude.

BIBLIOGRAPHY

BIBLIOGRAPHY

[1] K.E. Tsiolkovsky. *Study of Outer Space By Reaction Devices*. Mashinotroyenlye Press, Moscow, 1967 edition, 1905.

[2] Raymond Liang. *The Combination of Two Concentric Discharge Channels into a Nested Hall-Effect Thruster*. Ph.D., University of Michigan, Ann Arbor, MI, 2013.

[3] Robert G. Jahn. *Physics of Electric Propulsion*. McGraw-Hill, New York, 1968.

[4] Richard R Hofer. *Development and Characterization of High-Efficiency, High-Specific Impulse Xenon Hall Thrusters*. PhD thesis, University of Michigan, Ann Arbor, MI, 2004.

[5] Ioannis G. Mikellides and Ira Katz. Numerical simulations of Hall-effect plasma accelerators on a magnetic-field-aligned mesh. *Physical Review E*, 86(4):046703, October 2012.

[6] Dan Lev, Roger Myers, Kristina Lemmer, Jonathan Kolbeck, Michael Keidar, Hiroyuki Koizumi, Han Liang, Daren Yu, Tony Schönherr, Jose Gonzalez, Wonho Choe, Riccardo Albertoni, Andrew Hoskins, Shen Yan, William Hart, Richard R Hofer, Ikkoh Funaki, Alexander Lovtsov, Kurt Polzin, and Olivier Duchemin. The Technological and Commercial Expansion of Electric Propulsion in the Past 24 Years. In *35th International Electric Propulsion Conference*, Atlanta, GA, October 2017.

[7] John Brophy. Stationary plasma thruster evaluation in Russia. JPL Publication JPL Pub 92-4, Jet Propulsion Laboratory, February 1992.

[8] Richard Hofer, Dan Goebel, Ioannis Mikellides, and Ira Katz. Design of a Laboratory Hall Thruster with Magnetically Shielded Channel Walls, Phase II: Experiments. In *48th AIAA/ASME/SAE/ASEE Joint Propulsion Conference & Exhibit*, Atlanta, GA, July 2012. American Institute of Aeronautics and Astronautics.

[9] Ioannis Mikellides, Israel Katz, Richard Hofer, and Dan M. Goebel. Magnetic shielding of a laboratory Hall thruster. I. Theory and validation. *Journal of Applied Physics*, 115:043303–043303, January 2014.

[10] E. Y. Choueiri. Plasma oscillations in Hall thrusters. *Physics of Plasmas (1994-present)*, 8(4):1411–1426, April 2001.

[11] C. L. Ellison, Y. Raitses, and N. J. Fisch. Cross-field electron transport induced by a rotating spoke in a cylindrical Hall thruster. *Physics of Plasmas*, 19(1):013503, January 2012.

[12] Michael S. McDonald, Christopher K. Bellant, Brandon A. St Pierre, and Alec D. Gallimore. Measurement of cross-field electron current in a Hall thruster due to rotating spoke instabilities. In *47th AIAA/ASME/SAE/ASEE Joint Propulsion Conference & Exhibit*, San Diego, CA, 2011. American Institute of Aeronautics and Astronautics.

[13] Michael J. Sekerak, Alec D. Gallimore, Daniel L. Brown, Richard R. Hofer, and James E. Polk. Mode Transitions in Hall-Effect Thrusters Induced by Variable Magnetic Field Strength. *Journal of Propulsion and Power*, 32(4):903–917, 2016.

[14] Michael J. Sekerak, Ben Longmier, Alec Gallimore, Wensheng Huang, Hani Kamhawi, Richard R. Hofer, Benjamin Jorns, and James E. Polk. Mode Transitions in Magnetically Shielded Hall Effect Thrusters. In *50th AIAA/ASME/SAE/ASEE Joint Propulsion Conference*, Cleveland, OH, July 2014. American Institute of Aeronautics and Astronautics.

[15] G. S. Janes and R. S. Lowder. Anomalous Electron Diffusion and Ion Acceleration in a Low-Density Plasma. *The Physics of Fluids*, 9(6):1115–1123, June 1966.

[16] S. Yoshikawa and D. J. Rose. Anomalous Diffusion of a Plasma across a Magnetic Field. *The Physics of Fluids*, 5(3):334–340, March 1962.

[17] Andrew T. Powis, Johan A. Carlsson, Igor D. Kaganovich, Yevgeny Raitses, and Andrei Smolyakov. Scaling of spoke rotation frequency within a Penning discharge. *Physics of Plasmas*, 25(7):072110, July 2018.

[18] Y. Sakawa, C. Joshi, P. K. Kaw, F. F. Chen, and V. K. Jain. Excitation of the modified Simon–Hoh instability in an electron beam produced plasma. *Physics of Fluids B: Plasma Physics*, 5(6):1681–1694, June 1993.

[19] Benjamin A. Jorns and Richard R. Hofer. Plasma oscillations in a 6-kW magnetically shielded Hall thruster. *Physics of Plasmas (1994-present)*, 21(5), May 2014.

[20] Ivan Romadanov, Andrei Smolyakov, Yevgeny Raitses, Igor Kaganovich, Tang Tian, and Sergei Ryzhkov. Structure of nonlocal gradient-drift instabilities in Hall ExB discharges. *Physics of Plasmas*, 23(12):122111, December 2016.

[21] Wensheng Huang, Hani Kamhawi, and Thomas Haag. Plasma Oscillation Characterization of NASA's HERMeS Hall Thruster via High Speed Imaging. In *52nd AIAA/SAE/ASEE Joint Propulsion Conference*. American Institute of Aeronautics and Astronautics, July 2016.

[22] Yu.V. Esipchuk and Gennady Tilinin. Drift instability in a Hall-current plasma accelerator. *Sov. Phys. - Tech. Phys. (Engl. Transl.); (United States)*, 21:4, April 1976.

[23] J. Bareilles, G. J. M. Hagelaar, L. Garrigues, C. Boniface, J. P. Boeuf, and N. Gascon. Critical assessment of a two-dimensional hybrid Hall thruster model: Comparisons with experiments. *Physics of Plasmas*, 11(6):3035–3046, May 2004.

[24] Serge Barral, Karol Makowski, Zbigniew Peradzyński, and Michel Dudeck. Transit-time instability in Hall thrusters. *Physics of Plasmas*, 12(7), June 2005.

[25] J. Cavalier, N. Lemoine, G. Bonhomme, S. Tsikata, C. Honoré, and D. Grésillon. Hall thruster plasma fluctuations identified as the ExB electron drift instability: Modeling and fitting on experimental data. *Physics of Plasmas*, 20(8):082107, August 2013.

[26] T. Lafleur, S. D. Baalrud, and P. Chabert. Theory for the anomalous electron transport in Hall effect thrusters. I. Insights from particle-in-cell simulations. *Physics of Plasmas*, 23(5):053502, May 2016.

[27] G.N. Tilinin. High-frequency plasma waves in a Hall accelerator with an extended acceleration zone. *Sov. Phys. Tech. Phys.*, 22(8):974–978, 1977.

[28] J. P. Boeuf and L. Garrigues. Low frequency oscillations in a stationary plasma thruster. *Journal of Applied Physics*, 84(7):3541–3554, October 1998.

[29] John Fife, Manuel Martinez-Sanchez, and James Szabo. A numerical study of low-frequency discharge oscillations in Hall thrusters. In *33rd AIAA/ASME/SAE/ASEE Joint Propulsion Conference & Exhibit*. American Institute of Aeronautics and Astronautics, July 1997.

[30] D. P. Schmidt, N. B. Meezan, W. A. Hargus, and M. A. Cappelli. A low-power, linear-geometry Hall plasma source with an open electron-drift. *Plasma Sources Science and Technology*, 9(1):68–76, January 2000.

[31] N. Meezan, Jr. W. Hargus, D. Schmidt, and M. Cappelli. Optical study of anomalous electron transport in a laboratory Hall thruster. In *35th Joint Propulsion Conference and Exhibit*, Los Angeles, June 1999. American Institute of Aeronautics and Astronautics.

[32] E. Chesta, C. M. Lam, N. B. Meezan, D. P. Schmidt, and M. A. Cappelli. A characterization of plasma fluctuations within a Hall discharge. *IEEE Transactions on Plasma Science*, 29(4):582–591, August 2001.

[33] S. Chable and F. Rogier. Numerical investigation and modeling of stationary plasma thruster low frequency oscillations. *Physics of Plasmas*, 12(3), February 2005.

[34] S. Barral and E. Ahedo. On the Origin of Low Frequency Oscillations in Hall Thrusters. In *AIP Conference Proceedings*, volume 993, pages 439–442. AIP Publishing, March 2008.

[35] S. Barral and Z. Peradzyński. Ionization oscillations in Hall accelerators. *Physics of Plasmas (1994-present)*, 17(1), January 2010.

[36] Michael S. McDonald and Alec D. Gallimore. Comparison of breathing and spoke mode strength in the H6 Hall thruster using high speed imaging. In *33rd International Electric Propulsion Conference*, Washington DC, USA, October 2013.

[37] K.A. Polzin, E.S. Sooby, Y. Raitses, E. Merino, and N.J. Fisch. Discharge Oscillations in a Permanent Magnet Cylindrical Hall-Effect Thruster. In *31st International Electric Propulsion Conference*, Ann Arbor, MI, September 2009.

[38] C.E. Garner, J.R. Brophy, S. Semenkin, V. Garkusha, S. Tverdokhlebov, and C. Marrese. Experimental Evaluation of Russian Anode Layer Thrusters. In *30th Joint Propulsion Conference and Exhibit*, Indianapolis, IN, June 1994. American Institute of Aeronautics and Astronautics.

[39] Ryan Conversano. *Low-Power Magnetically Shielded Hall Thrusters*. PhD thesis, University of California, Los Angeles, Los Angeles, 2015.

[40] S. Mazouffre, S. Tsikata, and J. Vaudolon. Development and experimental characterization of a wall-less Hall thruster. *Journal of Applied Physics*, 116(24):243302, December 2014.

[41] Burak Karadag, Shinatora Cho, and Ikkoh Funaki. Thrust performance, propellant ionization, and thruster erosion of an external discharge plasma thruster. *Journal of Applied Physics*, 123(15):153302, April 2018.

[42] Yuchen Yang, Xue Zhou, Jason X. Liu, and André Anders. Evidence for breathing modes in direct current, pulsed, and high power impulse magnetron sputtering plasmas. *Applied Physics Letters*, 108(3):034101, January 2016.

[43] Alec Gallimore, Mark Reichenbacher, Colleen Marrese, Sang-Wook Kim, and John Foster. Preliminary characterization of a low power end-Hall thruster. In *30th Joint Propulsion Conference and Exhibit*, Indianapolis,IN,U.S.A., June 1994. American Institute of Aeronautics and Astronautics.

[44] Kentaro Hara, Iain D. Boyd, and Vladimir I. Kolobov. One-dimensional hybrid-direct kinetic simulation of the discharge plasma in a Hall thruster. *Physics of Plasmas*, 19(11):113508, November 2012.

[45] P. Coche and L. Garrigues. A two-dimensional (azimuthal-axial) particle-in-cell model of a Hall thruster. *Physics of Plasmas*, 21(2), February 2014.

[46] Kentaro Hara, Michael J. Sekerak, Iain D. Boyd, and Alec D. Gallimore. Perturbation analysis of ionization oscillations in Hall effect thrusters. *Physics of Plasmas (1994-present)*, 21(12), December 2014.

[47] Kentaro Hara, Michael J. Sekerak, Iain D. Boyd, and Alec D. Gallimore. Mode transition of a Hall thruster discharge plasma. *Journal of Applied Physics*, 115(20), May 2014.

[48] O. Koshkarov, A. I. Smolyakov, I. V. Romadanov, O. Chapurin, M. V. Umansky, Y. Raitses, and I. D. Kaganovich. Current flow instability and nonlinear structures in dissipative two-fluid plasmas. *Physics of Plasmas*, 25(1):011604, January 2018.

[49] Kentaro Hara and Ioannis G. Mikellides. Characterization of low frequency ionization oscillations in Hall thrusters using a one-dimensional fluid model. Cincinnati, Ohio, July 2018. American Institute of Aeronautics and Astronautics.

[50] Sedina Tsikata, Anne Heron, and Cyrille Honore. Oscillatory discharge behavior in Hall thrusters: relationships between the discharge current, electric field and microturbulence. pages IEPC–2017–443, Atlanta, GA, October 2017.

[51] Alejandro Lopez Ortega, Ioannis G. Mikellides, and Vernon H. Chaplin. Numerical Simulations for the Assessment of Erosion in the 12.5-kW Hall Effect Rocket with Magnetic Shielding (HERMeS). In *35th International Electric Propulsion Conference, Atlanta, GA, IEPC-2017-154*, 2017.

[52] V. V. Zhurin, H. R. Kaufman, and R. S. Robinson. Physics of closed drift thrusters. *Plasma Sources Science and Technology*, 8(1):R1, 1999.

[53] Serge Barral and Eduardo Ahedo. Low-frequency model of breathing oscillations in Hall discharges. *Physical Review E*, 79(4), April 2009.

[54] T Randolph, V Kim, H Kaufman, K Kozubsky, V Zhurin, and M Day. Facility effects on stationary plasma thruster testing. In *23rd AIAA/AIDAA/DGLR/JSASS International Electric Propulsion Conference*, 1993.

[55] David Y. Oh, John Steven Snyder, Dan M. Goebel, Richard R. Hofer, and Thomas M. Randolph. Solar Electric Propulsion for Discovery-Class Missions. *Journal of Spacecraft and Rockets*, 51(6):1822–1835, 2014.

[56] S. Mazouffre, F. Dubois, L. Albarede, D. Pagnon, and M. Touzeau. Plasma induced erosion phenomena in a Hall thruster. pages 69–74, December 2003.

[57] Benjamin Jorns, Christopher A. Dodson, John R. Anderson, Dan M. Goebel, Richard R. Hofer, Michael J. Sekerak, Alejandro Lopez Ortega, and Ioannis G. Mikellides. Mechanisms for Pole Piece Erosion in a 6-kW Magnetically-Shielded

Hall Thruster. In *52nd AIAA/SAE/ASEE Joint Propulsion Conference and Exhibit*. American Institute of Aeronautics and Astronautics, July 2016.

[58] Maria Choi and Iain D. Boyd. Numerical Simulation of Keeper Erosion in a 6-kW Laboratory. Kobe, Japan, July 2015.

[59] Robert B. Lobbia and Alec D. Gallimore. High-speed dual Langmuir probe. *Review of Scientific Instruments*, 81(7):073503, July 2010.

[60] Wensheng Huang, Brittany Drenkow, and Alec Gallimore. Laser-Induced Fluorescence of Singly-Charged Xenon Inside a 6-kW Hall Thruster. In *45th AIAA/ASME/SAE/ASEE Joint Propulsion Conference & Exhibit*, Joint Propulsion Conferences. American Institute of Aeronautics and Astronautics, August 2009.

[61] S. Mazouffre and G. Bourgeois. Spatio-temporal characteristics of ion velocity in a Hall thruster discharge. *Plasma Sources Science and Technology*, 19(6):065018, 2010.

[62] J. Vaudolon, B. Khiar, and S. Mazouffre. Time evolution of the electric field in a Hall thruster. *Plasma Sources Science and Technology*, 23(2), 2014.

[63] Andrea Lucca Fabris, Christopher V. Young, and Mark A. Cappelli. Time-resolved laser-induced fluorescence measurement of ion and neutral dynamics in a Hall thruster during ionization oscillations. *Journal of Applied Physics*, 118(23), December 2015.

[64] Sarah E. Cusson, Ethan T. Dale, Benjamin A. Jorns, and Alec D. Gallimore. Acceleration region dynamics in a magnetically shielded Hall thruster. *Physics of Plasmas*, 26(2):023506, February 2019.

[65] Kevin Diamant, Rotislav Spektor, Edward Beiting, Jason Young, and Thomas Curtiss. The Effects of Background Pressure on Hall Thruster Operation. In *48th AIAA/ASME/SAE/ASEE Joint Propulsion Conference & Exhibit*, Atlanta, GA, July 2012. American Institute of Aeronautics and Astronautics.

[66] Jonathan A. Walker, Jason D. Frieman, Mitchell L. R. Walker, Vadim Khayms, David King, and Peter Y. Peterson. Electrical Facility Effects on Hall-Effect-Thruster Cathode Coupling: Discharge Oscillations and Facility Coupling. *Journal of Propulsion and Power*, 32(4):844–855, 2016.

[67] Luis R. Pinero. The Impact of Harness Impedance on Hall Thruster Discharge Oscillations. Atlanta, GA, October 2017.

[68] Daren Yu, Chunsheng Wang, Liqiu Wei, Chao Gao, and Guang Yu. Stabilizing of low frequency oscillation in Hall thrusters. *Physics of Plasmas*, 15(11):113503, November 2008.

[69] Lubos Brieda, Justin Koo, and Michelle Scharfe. Influence of a power supply model on simulated Hall thruster discharge voltage oscillations. *AIP Advances*, 9(2):025320, February 2019.

[70] Yevgeny Raitses, Ivan Romadanov, Jacob Simmonds, Andrei Smolyakov, and Igor Kaganovich. Hall thruster with externally driven oscillations. In *AIAA Propulsion and Energy 2019 Forum*, AIAA Propulsion and Energy Forum. American Institute of Aeronautics and Astronautics, August 2019.

[71] O. Buneman. Excitation of Field Aligned Sound Waves by Electron Streams. *Physical Review Letters*, 10(7):285–287, April 1963.

[72] Andrei A. Litvak and Nathaniel J. Fisch. Resistive instabilities in Hall current plasma discharge. *Physics of Plasmas*, 8(2):648–651, January 2001.

[73] E. Fernandez, M. K. Scharfe, C. A. Thomas, N. Gascon, and M. A. Cappelli. Growth of resistive instabilities in ExB plasma discharge simulations. *Physics of Plasmas*, 15(1), January 2008.

[74] Serge Barral and Eduardo Ahedo. Theoretical Study of the Breathing Mode in Hall Thrusters. In *42nd AIAA/ASME/SAE/ASEE Joint Propulsion Conference & Exhibit*, Sacramento, CA, July 2006. American Institute of Aeronautics and Astronautics.

[75] Michael J. Sekerak. *Plasma oscillations and operational modes in Hall effect thrusters*. PhD thesis, National Aeronautics and Space Administration, 2014.

[76] Tyler J. VanderWeele and Ilya Shpitser. On the definition of a confounder. *Annals of Statistics*, 41(1):196–220, February 2013.

[77] Naoji Yamamoto, Kimiya Komurasaki, and Yoshihiro Arakawa. Discharge Current Oscillation in Hall Thrusters. *Journal of Propulsion and Power*, 21(5):870–876, 2005.

[78] Dan Goebel and Ira Katz. *Fundamentals of Electric Propulsion: Ion and Hall Thrusters*, volume 1. John Wiley & Sons, December 2008.

[79] James M. Haas, Alec D. Gallimore, Keith McFall, and Greg Spanjers. Development of a high-speed, reciprocating electrostatic probe system for Hall thruster interrogation. *Review of Scientific Instruments*, 71(11):4131–4138, November 2000.

[80] D. Staack, Y. Raitses, and N. J. Fisch. Shielded electrostatic probe for nonperturbing plasma measurements in Hall thrusters. *Review of Scientific Instruments*, 75(2):393–399, February 2004.

[81] Benjamin Jorns, Dan M. Goebel, and Richard R. Hofer. Plasma Perturbations in High-Speed Probing of Hall Thruster Discharge Chambers: Quantification and Mitigation. In *51st AIAA/SAE/ASEE Joint Propulsion Conference*, Orlando, FL, July 2015. American Institute of Aeronautics and Astronautics.

[82] L. Grimaud, A. Petin, J. Vaudolon, and S. Mazouffre. Perturbations induced by electrostatic probe in the discharge of Hall thrusters. *Review of Scientific Instruments*, 87(4):043506, April 2016.

[83] James Matthew Haas. *Low-perturbation interrogation of the internal and near-field plasma structure of a Hall thruster using a high-speed probe positioning system*. PhD thesis, University of Michigan, 2001.

[84] Shawn Ohler, Brian Gilchrist, and Alec Gallimore. Microwave plume measurements of an SPT-100 using xenon and a laboratory model SPT using krypton. In *31st Joint Propulsion Conference and Exhibit*, San Diego, CA, July 1995. American Institute of Aeronautics and Astronautics.

[85] S. Mazouffre, D. Gawron, and N. Sadeghi. A time-resolved laser induced fluorescence study on the ion velocity distribution function in a Hall thruster after a fast current disruption. *Physics of Plasmas*, 16(4):043504, April 2009.

[86] Carl R. Mullins, Casey C. Farnell, Cody C. Farnell, Rafael A. Martinez, David Liu, Richard D. Branam, and John D. Williams. Non-invasive Hall current distribution measurement in a Hall effect thruster. *Review of Scientific Instruments*, 88(1):013507, January 2017.

[87] Robert B. Lobbia and Alec D. Gallimore. Temporal limits of a rapidly swept Langmuir probe. *Physics of Plasmas (1994-present)*, 17(7):073502, July 2010.

[88] J. P. Sheehan, Yevgeny Raitses, Noah Hershkowitz, and Michael McDonald. Recommended Practice for Use of Emissive Probes in Electric Propulsion Testing. *Journal of Propulsion and Power*, 0(0):1–24, 2016.

[89] Robert B. Lobbia and Brian E. Beal. Recommended Practice for Use of Langmuir Probes in Electric Propulsion Testing. *Journal of Propulsion and Power*, 33(Special Section on Best Practices for Performance and Diagnostic Measurements in Electric Propulsion):566–581, 2017.

[90] J. Perez-Luna, G. J. M. Hagelaar, L. Garrigues, and J. P. Boeuf. Method to obtain the electric field and the ionization frequency from laser induced fluorescence measurements. *Plasma Sources Science and Technology*, 18(3):034008, 2009.

[91] Christopher J. Durot, Benjamin A. Jorns, Ethan T. Dale, and Alec D. Gallimore. Laser-Induced Fluorescence Measurement of the Anomalous Collision Frequency in a 9-kW Magnetically-Shielded Hall Thruster. Atlanta, GA, 2017.

[92] L. Montgomery Smith, Dennis R. Keefer, and S. I. Sudharsanan. Abel inversion using transform techniques. *Journal of Quantitative Spectroscopy and Radiative Transfer*, 39(5):367–373, May 1988.

[93] Stéphane Mazouffre. Laser-induced fluorescence diagnostics of the cross-field discharge of Hall thrusters. *Plasma Sources Science and Technology*, 22(1):013001, 2013.

[94] Vernon H. Chaplin, Ryan W. Conversano, Robert B. Lobbia, Alejandro Lopez Ortega, Ioannis G. Mikellides, Richard R. Hofer, and Benjamin A. Jorns. Laser-Induced Fluorescence Measurements of the Acceleration Zone in the 12.5 kW HERMeS Hall Thruster. Atlanta, GA, October 2017.

[95] Abraham. Savitzky and M. J. E. Golay. Smoothing and Differentiation of Data by Simplified Least Squares Procedures. *Analytical Chemistry*, 36(8):1627–1639, July 1964.

[96] Timothy B Smith. *Deconvolution of ion velocity distributions from laser-induced fluorescence spectra of xenon electrostatic thruster plumes*. PhD thesis, University of Michigan, Ann Arbor, MI, 2003.

[97] N.I. Fisher. *Statistical analysis of circular data*. Cambridge University Press, New York, 1995.

[98] S. Mazouffre, G. Bourgeois, L. Garrigues, and E. Pawelec. A comprehensive study on the atom flow in the cross-field discharge of a Hall thruster. *Journal of Physics D: Applied Physics*, 44(10):105203, 2011.

[99] W. A. Hargus and M. R. Nakles. Ion Velocity Measurements Within the Acceleration Channel of a Low-Power Hall Thruster. *IEEE Transactions on Plasma Science*, 36(5):1989–1997, October 2008.

[100] William A. Hargus and Christopher S. Charles. Near Exit Plane Velocity Field of a 200-Watt Hall Thruster. *Journal of Propulsion and Power*, 24(1):127–133, January 2008.

[101] Wensheng Huang, Alec D. Gallimore, and Richard R. Hofer. Neutral Flow Evolution in a Six-Kilowatt Hall Thruster. *Journal of Propulsion and Power*, 27(3):553–563, May 2011.

[102] Gordon Kemble Woodgate. *Elementary atomic structures*. Oxford science publications. Clarendon Press, 1980.

[103] Derek Ainslie Jackson and M. c. Coulombe. Isotope shifts in the arc spectrum of xenon. *Proceedings of the Royal Society of London. A. Mathematical and Physical Sciences*, 338(1614):277–298, June 1974.

[104] G. D'Amico, G. Pesce, and A. Sasso. Isotope-shift and hyperfine-constant measurements of near-infrared xenon transitions in glow discharges and on a metastable Xeˆ3p_2 beam. *Physical Review A*, 60(6):4409–4416, December 1999.

[105] Masao Suzuki, Katsumi Katoh, and Nobuo Nishimiya. Saturated absorption spectroscopy of Xe using a GaAs semiconductor laser. *Spectrochimica Acta Part A: Molecular and Biomolecular Spectroscopy*, 58(11):2519–2531, September 2002.

[106] E. B. Saloman. Energy Levels and Observed Spectral Lines of Xenon, Xe I through Xe LIV. *Journal of Physical and Chemical Reference Data*, 33(3):765–921, August 2004.

[107] Wensheng Huang, Brittany Drenkow, and Alec Gallimore. Laser-Induced Fluorescence of Singly-Charged Xenon Inside a 6-kW Hall Thruster. In *45th AIAA/ASME/SAE/ASEE Joint Propulsion Conference & Exhibit*, Denver, Colorado, August 2009. American Institute of Aeronautics and Astronautics.

[108] T. B. Smith, B. B. Ngom, and A. D. Gallimore. Optogalvanic spectroscopy of the zeeman effect in singly-ionized xenon. In *The 33rd IEEE International Conference on Plasma Science, 2006. ICOPS 2006. IEEE Conference Record - Abstracts.*, pages 15–15, June 2006.

[109] H. Nyquist. Certain Topics in Telegraph Transmission Theory. *Transactions of the American Institute of Electrical Engineers*, 47(2):617–644, April 1928.

[110] B. Pelissier and N. Sadeghi. Time-resolved pulse-counting lock-in detection of laser induced fluorescence in the presence of a strong background emission. *Review of Scientific Instruments*, 67(10):3405–3410, October 1996.

[111] A. Diallo, S. Keller, Y. Shi, Y. Raitses, and S. Mazouffre. Time-resolved ion velocity distribution in a cylindrical Hall thruster: Heterodyne-based experiment and modeling. *Review of Scientific Instruments*, 86(3):033506, March 2015.

[112] N. A. MacDonald, M. A. Cappelli, and W. A. Hargus. Time-synchronized continuous wave laser-induced fluorescence on an oscillatory xenon discharge. *Review of Scientific Instruments*, 83(11):113506, November 2012.

[113] C. J. Durot, A. D. Gallimore, and T. B. Smith. Validation and evaluation of a novel time-resolved laser-induced fluorescence technique. *The Review of Scientific Instruments*, 85(1):013508, January 2014.

[114] Daniel Eckhardt, Justin Koo, Robert Martin, Michael Holmes, and Kentaro Hara. Spatiotemporal data fusion and manifold reconstruction in Hall thrusters. *Plasma Sources Science and Technology*, 28(4):045005, April 2019.

[115] Lyon B. King and Alec D. Gallimore. Gridded retarding pressure sensor for ion and neutral particle analysis in flowing plasmas. *Review of Scientific Instruments*, 68(2):1183–1188, February 1997.

[116] I. Romadanov, Y. Raitses, A. Diallo, K. Hara, I. D. Kaganovich, and A. Smolyakov. On limitations of laser-induced fluorescence diagnostics for xenon ion velocity distribution function measurements in Hall thrusters. *Physics of Plasmas*, 25(3):033501, March 2018.

[117] E.A. Viges, B.A. Jorns, A.D. Gallimore, and J.P. Sheehan. University of Michigan's Upgraded Large Vacuum Test Facility. In *36th International Electric Propulsion Conference*, Vienna, Austria, September 2019.

[118] Charles Garner, James Polk, John Brophy, and Keith Goodfellow. Methods for cryopumping xenon. In *32nd Joint Propulsion Conference and Exhibit*, Lake Buena Vista, FL, July 1996. American Institute of Aeronautics and Astronautics.

[119] J.F. O'Hanlon. *A User's Guide to Vacuum Technology*. Wiley-Interscience. John Wiley & Sons, New Jersey, 3rd edition, 2003.

[120] B. R. F. Kendall. Ionization gauge errors at low pressures. *Journal of Vacuum Science & Technology A*, 17(4):2041–2049, July 1999.

[121] John W. Dankanich, Mitchell Walker, Michael W. Swiatek, and John T. Yim. Recommended Practice for Pressure Measurement and Calculation of Effective Pumping Speed in Electric Propulsion Testing. *Journal of Propulsion and Power*, 33(3):668–680, May 2017.

[122] R.R. Hofer, S.E. Cusson, R.B. Lobbia, and A.D. Gallimore. The H9 Magnetically Shielded Hall Thruster. In *35th International Electric Propulsion Conference*, volume IEPC- 2017- 232, 2017.

[123] S.E. Cusson, R.R Hofer, R.B. Lobbia, B.A. Jorns, and A.D. Gallimore. Performance of the H9 Magnetically Shielded Hall Thrusters. In *35th International Electric Propulsion Conference*, volume IEPC-2017-239, 2017.

[124] S.E. Cusson, B.A. Jorns, and A.D. Gallimore. Impact of Neutral Density on the Magnetic Shielding ofHall Thrusters. In *36th International Electric Propulsion Conference*, Vienna, Austria, September 2019.

[125] Sarah Elizabeth Cusson. *Impact of Neutral Density on the Operation of High-Power Magnetically Shielded Hall Thrusters*. Ph.D., University of Michigan, Ann Arbor, MI, 2019.

[126] Peter Y. Peterson, Hani Kamhawi, Wensheng Huang, George Williams, James H. Gilland, John Yim, Richard R. Hofer, and Daniel A. Herman. NASA's HERMeS Hall Thruster Electrical Configuration Characterization. In *52nd AIAA/SAE/ASEE Joint Propulsion Conference*. American Institute of Aeronautics and Astronautics, July 2016.

[127] R. R. Hofer, L. K. Johnson, D. M. Goebel, and R. E. Wirz. Effects of Internally Mounted Cathodes on Hall Thruster Plume Properties. *IEEE Transactions on Plasma Science*, 36(5):2004–2014, October 2008.

[128] Ronald Davidson. *Methods in Nonlinear Plasma Theory*. Academic Press, New York, 1st edition, 1972.

[129] Charles Garner, John Brophy, James Polk, and Lewis Pless. Cyclic endurance test of a SPT-100 stationary plasma thruster. In *30th Joint Propulsion Conference and Exhibit*. American Institute of Aeronautics and Astronautics, 1994.

[130] Lord Rayleigh. *The Theory of Sound*, volume 1. Macmillan, London, 1877.

[131] T. E. Sheridan and J. Goree. Langmuir-probe characteristic in the presence of drifting electrons. *Physical Review E*, 50(4):2991–2996, October 1994.

[132] Adolf Hurwitz. On the conditions under which an equation has only roots with negative real parts. In *Selected papers on mathematical trends in control theory*, volume 65, pages 273–284. 1964.

[133] O. Chapurin, A. Smolyakov, G. Hagelaar, J. P. Boeuf, and Y. Raitses. Fluid and hybrid simulations of the ionization instabilities in Hall thruster. In *36th International Electric Propulsion Conference*, Vienna, Austria, September 2019.

[134] Michael A. Lieberman and Allan J. Lichtenberg. *Principles of Plasma Discharges and Materials Processing*. Wiley-Interscience. John Wiley & Sons, Hoboken, New Jersey, second edition edition, 2005.

[135] L. Dorf, V. Semenov, and Y. Raitses. Anode sheath in Hall thrusters. *Applied Physics Letters*, 83(13):2551–2553, September 2003.

[136] Leonid Dorf, Yevgeny Raitses, and N. J. Fisch. Experimental studies of anode sheath phenomena in a Hall thruster discharge. *Journal of Applied Physics*, 97(10):103309, 2005.

[137] F. I. Parra, E. Ahedo, J. M. Fife, and M. Martínez-Sánchez. A two-dimensional hybrid model of the Hall thruster discharge. *Journal of Applied Physics*, 100(2):023304, July 2006.

[138] Justin W. Koo and Iain D. Boyd. Modeling of anomalous electron mobility in Hall thrusters. *Physics of Plasmas*, 13(3):033501, March 2006.

[139] G. J. M. Hagelaar, J. Bareilles, L. Garrigues, and J. P. Boeuf. Two-dimensional model of a stationary plasma thruster. *Journal of Applied Physics*, 91(9):5592–5598, May 2002.

[140] Vernon H. Chaplin, Benjamin A. Jorns, Alejandro Lopez Ortega, Ioannis G. Mikellides, Ryan W. Conversano, Robert B. Lobbia, and Richard R. Hofer. Laser-induced fluorescence measurements of acceleration zone scaling in the

12.5 kW HERMeS Hall thruster. *Journal of Applied Physics*, 124(18):183302, November 2018.

[141] Rohit Shastry. *Experimental Characterization of the Near-Wall Region in Hall Thrusters and its Implications on Performance and Lifetime*. Ph.D., University of Michigan, Ann Arbor, MI, 2011.

[142] D. Gawron, S. Mazouffre, and C. Boniface. A Fabry–Pérot spectroscopy study on ion flow features in a Hall effect thruster. *Plasma Sources Science and Technology*, 15(4):757–764, August 2006.

[143] J. C. Adam, A. Héron, and G. Laval. Study of stationary plasma thrusters using two-dimensional fully kinetic simulations. *Physics of Plasmas*, 11(1):295–305, January 2004.

[144] David H. Manzella. Stationary Plasma Thruster Plume Emissions. Seattle, WA, United States, March 1994.

[145] Jason Sommerville and Lyon King. An Optical Diagnostic for Xenon Hall Thrusters Including Metastable Contributions. In *42nd AIAA/ASME/SAE/ASEE Joint Propulsion Conference & Exhibit*, Sacramento, CA, July 2006. American Institute of Aeronautics and Astronautics.

[146] Ashley Gonzales, Michelle Scharfe, Justin Koo, and William Hargus. Comparison of Numerical and Experimental Time-Resolved Near-Field Hall Thruster Plasma Properties. volume 42, July 2012.

[147] G. Karabadzhak. Improvement of Optical Diagnostic Technique for a Xenon Operating Hall Effect Thruster. volume 555, page 117.1, October 2004.

[148] George F. Karabadzhak, Yu-hui Chiu, and Rainer A. Dressler. Passive optical diagnostic of Xe propelled Hall thrusters. II. Collisional-radiative model. *Journal of Applied Physics*, 99(11):113305, June 2006.

[149] Rainer A. Dressler, Yu-hui Chiu, Oleg Zatsarinny, Klaus Bartschat, Rajesh Srivastava, and Lalita Sharma. Near-infrared collisional radiative model for Xe plasma electrostatic thrusters: the role of metastable atoms. *Journal of Physics D: Applied Physics*, 42(18):185203, August 2009.

[150] Scott J. Hall. *Characterization of a 100-kW Class Nested-Channel Hall Thruster*. Ph.D., University of Michigan, Ann Arbor, MI, 2017.

[151] Scott Hall, Sarah Cusson, and Alec Gallimore. 30-kW Performance of a 100-kW Class Nested-channel Hall Thruster. In *34th International Electric Propulsion Conference*, Kobe, Japan, July 2015.

[152] R. Jung, John Boffard, L. Anderson, and Chun Lin. Electron-impact excitation cross sections from the xenon J= 2 metastable level. *Phys. Rev. A*, 72, August 2005.

[153] H. M. Mott-Smith and Irving Langmuir. The Theory of Collectors in Gaseous Discharges. *Physical Review*, 28(4):727–763, October 1926.

[154] B. E. Cherrington. The use of electrostatic probes for plasma diagnostics—A review. *Plasma Chemistry and Plasma Processing*, 2(2):113–140, June 1982.

[155] M. J. Druyvesteyn. Der Niedervoltbogen. *Zeitschrift für Physik*, 64(11):781–798, September 1930.

[156] R. Claude Woods and Isaac D. Sudit. Theory of electron retardation by Langmuir probes in anisotropic plasmas. *Physical Review E*, 50(3):2222–2238, September 1994.

[157] Scott Knappmiller, Scott Robertson, and Zoltan Sternovsky. Method to find the electron distribution function from cylindrical probe data. *Physical Review E*, 73(6):066402, June 2006.

[158] D.G. Bills, R.B. Holt, and B.T. McClure. Pulsed Probe Measurements. *Journal of Applied Physics*, 33(1):29–33, January 1962.

[159] F. W. Crawford and R. F. Mlodnosky. Langmuir probe response to periodic waveforms. *Journal of Geophysical Research*, 69(13):2765–2773, July 1964.

[160] Sin-Li Chen and T. Sekiguchi. Instantaneous Direct-Display System of Plasma Parameters by Means of Triple Probe. *Journal of Applied Physics*, 36(8):2363–2375, August 1965.

[161] F. F. Chen. Electric Probes. In Richard H. Huddlestone and Stanley L. Leonard, editors, *Plasma Diagnostic Techniques*, Pure and Applied Physics. Academic Press, New York, 1965.

[162] T. F. Yang, Q. X. Zu, and Ping Liu. A dual-cable noise reduction method for Langmuir probes. *Review of Scientific Instruments*, 66(7):3879–3882, July 1995.

[163] G. Chiodini, C. Riccardi, and M. Fontanesi. A 400 kHz, fast-sweep Langmuir probe for measuring plasma fluctuations. *Review of Scientific Instruments*, 70(6):2681–2688, May 1999.

[164] M. Schubert, M. Endler, and H. Thomsen. Spatiotemporal temperature fluctuation measurements by means of a fast swept Langmuir probe array. *Review of Scientific Instruments*, 78(5):053505, May 2007.

[165] L. Albarède, S. Mazouffre, A. Bouchoule, and M. Dudeck. Low-frequency electron dynamics in the near field of a Hall effect thruster. *Physics of Plasmas*, 13(6):063505, June 2006.

[166] James M. Haas and Alec D. Gallimore. Internal plasma potential profiles in a laboratory-model Hall thruster. *Physics of Plasmas (1994-present)*, 8(2):652–660, February 2001.

[167] Y. Raitses, M. Keidar, D. Staack, and N. J. Fisch. Effects of segmented electrode in Hall current plasma thrusters. *Journal of Applied Physics*, 92(9):4906–4911, November 2002.

[168] Robert B. Lobbia. *A Time-resolved Investigation of the Hall Thruster Breathing Mode*. PhD thesis, University of Michigan, Ann Arbor, MI, 2010.

[169] M. Sekerak, M. McDonald, R. Hofer, and A. Gallimore. Hall thruster plume measurements from High-speed Dual Langmuir Probes with Ion Saturation Reference. In *2013 IEEE Aerospace Conference*, pages 1–16, March 2013.

[170] V. Skoutnev, P. Dourbal, E. Rodríguez, and Y. Raitses. Fast sweeping probe system for characterization of spokes in ExB discharges. *Review of Scientific Instruments*, 89(12):123501, December 2018.

[171] V. Hruby, J. Monheiser, B. Pote, P. Rostler, J. Kolencik, and C. Freeman. Development of low power Hall thrusters. In *30th Plasmadynamic and Lasers Conference*. American Institute of Aeronautics and Astronautics, 1999.

[172] Francis F Chen. Time-varying impedance of the sheath on a probe in an RF plasma. *Plasma Sources Science and Technology*, 15(4):773–782, November 2006.

[173] Jesse A. Linnell and Alec D. Gallimore. Hall Thruster Electron Motion Characterization Based on Internal Probe Measurements. In *31st International Electric Propulsion Conference*, volume IEPC-2009-105, Ann Arbor, MI, September 2009.

[174] W. A. Hargus and M. A. Cappelli. Interior and Exterior Laser-Induced Fluorescence and Plasma Measurements within a Hall Thruster. *Journal of Propulsion and Power*, 18(1):159–168, January 2002.

[175] L Grimaud and S Mazouffre. Ion behavior in low-power magnetically shielded and unshielded Hall thrusters. *Plasma Sources Science and Technology*, 26(5):055020, April 2017.

[176] Ioannis G. Mikellides, Benjamin Jorns, Ira Katz, and Alejandro Lopez Ortega. Hall2de Simulations with a First-principles Electron Transport Model Based on the Electron Cyclotron Drift Instability. In *52nd AIAA/SAE/ASEE Joint Propulsion Conference*, Salt Lake City, UT, July 2016. American Institute of Aeronautics and Astronautics.

[177] Richard Hofer, Ira Katz, Dan Goebel, Kristina Jameson, Regina Sullivan, Lee Johnson, and Ioannis Mikellides. Efficacy of Electron Mobility Models in Hybrid-PIC Hall Thruster Simulations. In *44th AIAA/ASME/SAE/ASEE Joint Propulsion Conference & Exhibit*, Hartford, CT, July 2008. American Institute of Aeronautics and Astronautics.